PAL, SATYA

WAKE BOUNDARY LAYER INTERACTION IN TURBOMACHINERY

City University of New York PH.D. 1981

WAKE BOUNDARY LAYER INTERACTION

IN

TURBOMACHINERY

by

SATYA PAL

A dissertation submitted to the
Graduate Faculty in Engineering
in partial fulfillment of the
requirements for the degree of
Doctor of Philosophy,
The City University of New York.

1981

This manuscript has been read and accepted for the Graduate Faculty in Engineering is satisfaction of the dissertation requirement for the degree of Doctor of Philosophy.

May 14, 1981
date

Chairman of Examining Committee

May 15, 1981
date

Executive Officer

Chan M. Tchen

Herbert Weinstein

James R. Steven

Myron Levitsky

Supervisory Committee

The City University of New York

Abstract

WAKE BOUNDARY LAYER INTERACTION IN TURBOMACHINERY

by

Satya Pal

Adviser: Professor Rishi Raj

The wake developed from the trailing edge of a thin and smooth flat plate including the effect of free stream turbulence was studied analytically as well as experimentally. The experimental measurements were taken in a low speed wind tunnel using cross-wire anemometry for three levels of free stream turbulence. Two levels of free stream turbulence were obtained at the leading edge of the flat plate using grids with square bars ($T \sim 5.23$ %) and circular rods ($T \sim 7.23$ %). The third level of free stream turbulence was obtained in the absence of the grid ($T \sim 0.4$ %) because the wind tunnel had turbulence of the order of 0.4 %. The grids were kept at a distance of 273 mm from the leading edge of the flat plate. Experimental results are presented on mean velocity profile, wake center line velocity, half wake width, displacement thickness, momentum thickness, energy thickness, shape factor, components of turbulence intensity and Reynolds stress. It is shown that the free stream

turbulence increases the wake recovery and growth rates. The semi-empirical correlations are developed to predict the foregoing behavior. The analytical investigation also lead to the establishment of two turbulence parameters. These parameters simulate the effect of free stream turbulence on the wake velocity (U_0) and length (L_0) scales. Free stream turbulence increases the turbulence intensity and Reynolds stress in the wake. Correlations are developed to predict the decay behavior of turbulence quantities. These correlations depend upon the trailing edge conditions, free stream turbulence level, drag coefficient and distance downstream from the trailing edge. A self-preservation of wake has been taken as the basis for obtaining the correlations for turbulence quantities.

The wake boundary layer interacted flow was treated as three-dimensional. The order of magnitude analysis, and similarity considerations were used in the theoretical study. Decay laws for the mean velocity and growth laws for length scale were obtained. Theoretical study also lead to the development of three-dimensional turbulence interaction parameters. The wake developed from the trailing edge of a thin and smooth flat plate in the x-z plane interacted with the boundary layer developed on an artifically roughened flat plate in the x-y plane was studied experimentally for three axial spacings between the two plates. Experimental measurements were taken in a

low speed wind tunnel using a triple sensor hot-wire probe. Experimental results are presented on three components of mean velocity, turbulence intensity, Reynolds stress and on wake width. The effect of spacing on the mean and turbulence quantities is also presented. Spectral measurements were taken in the inner region of the wake interacted boundary layer. Frequency energy spectra for three spacings were also measured with the help of a spectrum analyzer. The results on energy spectra are compared with available data on other types of flows. Axial, lateral and normal components of mean velocity defect decrease towards the inner region as well as with increase in spacing due to wake boundary layer interaction. Length scale increases towards the wall, with the increase in downstream distance and with the increase in spacing. Three components of turbulence intensity and Reynolds stress increase towards the wall, decrease towards the outer edge of the wake and with the increase in spacing in the interacting region. Correlation coefficient increases towards the inner region and decreases with the increase in downstream distance and with the increase in spacing.

ACKNOWLEDGMENTS

The author is greatly indebted to Professor Rishi Raj for his valuable suggestions and inspiration during the course of this investigation. The author is grateful to Professors Chan M. Tchen, Herbert Weinstein and James R. Steven for their suggestions during this investigation. The author is also thankful to the City College of the City University of New York for providing the partial financial support through the FRAP grant, by giving the teaching opportunity at the under-graduate level in the department of Mechanical Engineering at the City College of New York and to the National Science Foundation (Grant N.S.F. ENG. 76 - 09611).

I am also thankful to G. Noll and B. Roise for their help in the experimental set-up. I am greatly indebted to my parents and family members for their understanding, inspiration and moral support which I needed most throughout my engineering education. I am also thankful to Ganesh B. Karkal for his association and healthy environment during my stay at the City of New York. Finally, I am thankful to all my friends and colleagues for their help and encouragement.

TABLE OF CONTENTS

LIST OF FIGURES

LIST OF TABLES

NOMENCLATURE

A	Constant (Eqn. 2.12)
a	Constant (Eqn. 7.13)
a_1	Constant
B	Constant (Eqn. 2.12)
b	Constant (Eqn. 7.13)
$\bar{b}$	Bar width of the grid
c_1 to c_{11}	Similarity constants
$\bar{c}_1$ to $\bar{c}_3$	Constants (Eqns. 3.38 to 3.40)
c'_1 to c'_3	Constants (Eqns. 3.35 to 3.37)
c	Chord length of the flat plate
c_d	Drag coefficient
c_{d0}	Drag coefficient in the absence of free stream turbulence
c_f	Local skin friction coefficient
d	Diameter of the grid cylinder
$\bar{D}$	Diameter of the hot-wire sensor
D_i	Calibration constant for the sensor i (Eqn. 5.4)
$\bar{E}_1, \bar{E}_2, \bar{E}_3$	Mean voltages along sensor 1, 2, and 3 directions, respectively
E_i	Instantaneous voltage for sensor i
E_{0i}	Voltages at zero velocity for sensor i
$\overline{e_1^2}, \overline{e_2^2}, \overline{e_3^2}$	Mean square voltages along sensor 1, 2 and 3 directions, respectively
$\overline{e_x^2}, \overline{e_y^2}, \overline{e_z^2}$	Mean square voltages in x, y, and z directions, respectively

e_s, e_d	Output fluctuating voltages of the dual summing unit
F	Energy spectral function
F_1 to F_5	Functional variables
$\bar{f}$	Frequency
$f, \tilde{f}, f_1, f_2, f_3$	Similarity functions
G	Clauser's shape parameter
G_1 to G_3	Functional variable
G_T	Transfer function of the dual summing unit
$\overline{H}$	Similarity function
H	Shape factor
H_1	Non dimensional parameter, δ_1 / δ_b
h_2	Height of the body
I_{xz}	Variable for the interacting flow
I_1, I_2, I_3	Integral constants
K	Kilo Hertz
K_c	Correction factor due to $\ell/\overline{D}$ ratio of the sensor
$\overline{K_1}$ to $\overline{K}_{10}$	Constants (Table VI)
$\overline{K}$	Constant (Eqn. 3.19)
k	Wave number
k_1	von Karman constant
k_r	Height of the roughness element in the boundary layer
ℓ	Length of the sensitive part of the hot-wire sensor
$\overline{\ell}$	Average mixing length
$\tilde{\ell}$	Mixing length

$\tilde{\ell}_\gamma$	Wake value of the mixing length at any streamwise station
L	Dissipation length
$\bar{L}$	Average dissipation length
L_0	Length scale for two-dimensional flow
$\bar{L}_{0i}$	Length scale for the interacting flow
M	Grid spacing
m	Pressure gradient effect
$\bar{n}_1, \bar{n}_2, \bar{n}_3, \tilde{n}_i$	Exponent constants
n_1, n_2, n_3	Hot-wire calibration constants
P	Self-preservation parameter (Eqn. 6.15)
p	Static pressure
$\overline{q_s^2}$	Mean square fluctuating component in the streamwise direction
$\overline{q^2}$	Mean square total turbulence intensity
R	Reynolds number based on the chord length of the flat plate
R_T	Turbulent Reynolds number
R_{ij}	Correlation coefficient (Eqn. 3.30)
$\bar{R}_{ij}$	Correlation coefficient (Fig. 7.18 a or b)
R^+	Reynolds number = $z\, u^+/\nu$
S	Axial distance between two flat plates (Fig. 5.3)
s	Span
T	Turbulence level
T_1	Period
T_2	Taylor's turbulence parameter (Eqn. 2.16)

T_b	Bursting Period
$T_{L.E.}$	Turbulence level at the leading edge of the flat plate producing wake
$T_{umax}, T_{vmax}, T_{wmax}$	Maximum values of components of turbulence intensity along x,y, and z directions, respectively, normalized with respect to $\bar{U}_e$
$\bar{T}_u$, $\bar{T}_v$, $\bar{T}_w$	Components of turbulence intensity along x,y, and z directions, respectively, normalized with respect to $\bar{U}_b$
$T_{uv\ max}, T_{vw\ max}$ $T_{wu\ max}$	Maximum values of Reynolds stress components, normalized with respect to $\bar{U}_e^2$
$\bar{T}_{uv}, \bar{T}_{vw}, \bar{T}_{wu}$	Components of Reynolds stress normalized with respect to $\bar{U}_b^2$
$\bar{U}_1, \bar{U}_2, \bar{U}_3$	Mean velocity components along 1,2,3 axes, respectively
U_0	Wake center line velocity defect
U_∞	Free stream velocity
$U_{d_1}, U_{d_2}, U_{d_3}$	Velocity defects in x,y, and z directions, respectively
U_{d_T}	Total axial component of mean velocity defect at the wake center line for the interacting flow
$\overline{u_1^2}, \overline{u_2^2}, \overline{u_3^2}$	Mean square values of the fluctuating velocities in 1,2,3, directions, respectively
$\overline{u_x^2}, \overline{u_y^2}, \overline{u_z^2}$	Mean square values of the fluctuating velocities in x,y,z, directions, respectively

u_m	Mean value of the turbulence component
$\overline{U}_c$	Mean velocity at the wake center line
$\overline{U}_e$	Local outer edge mean velocity
U_{d_0}	Velocity defect outside the interaction region
$U_{ef,i}$	Effective cooling velocity of sensor i
$\overline{U}$, $\overline{U}_s$	Total mean velocity and streamwise velocity, respectively
$\underline{\overline{U}}$	Actual mean velocity vector (Eqn. 5.6)
$\overline{U}_b$	Local mean velocity at the outer edge of the wake in the interacting flow
u_0	Root mean square value of the turbulence intensity at the arbitrary starting point,
u^*	Frictional velocity $= \sqrt{\tau_{wl}/\rho_{wl}}$
u^+	Mean velocity $= \sqrt{\tau_{max}/\rho}$
$-\overline{u_x u_y}$, $-\overline{u_y u_z}$ $-\overline{u_z u_x}$	Reynolds stress components in Cartesian coordinates axes
$\overline{u_1 u_2}, \overline{u_2 u_3}, \overline{u_3 u_1}$	Reynolds stress components along sensor axes
v_k	Velocity at wave number k
x_ℓ	Axial distance from the leading edge of the first flat plate
x_1	Axial distance from the leading edge of the second flat plate
$\overline{x}$	Axial distance from the grid
x,y,z	Axial, lateral and normal directions, respectively, (Fig. 4.1)

x_0 , x_0'	Virtual origin
y^+	Non-dimensional parameter = $y\, u^*/\nu$

Greek Letters

α	Empirical constant (Eqn. 3.13)
α_i	Empirical constant (Eqn. 4.52)
β	Empirical constant (Eqn. 3.14)
ξ	Similarity variable (Eqn. 4.26)
η , η_1	Similarity variables (Eqn. 4.5 a,b)
ν_{T_i}	Turbulent diffusion coefficient
δ_1	Displacement thickness
δ_2	Energy thickness
δ_b	Boundary layer thickness
δ_w	Wake width
Ω	Angular velocity
π	Profile parameter
ρ	Density
γ	Empirical constant (Eqn. 2.5)
$\bar{\gamma}$	Empirical constant (Eqn. 6.16 to 6.18)
θ	Momentum thickness
θ_1	First transformation angle (Fig. 5.6)
Φ_1 , Φ_2	Velocity and length scale parameters (2d flow)
$\bar{\Phi}_i$, $\bar{\Psi}_i$	Turbulence interacting parameters
ζ_i	Angle of the triple sensor wire (Fig. 5.6)
τ_{ij}	Shear stress
λ_1, λ_3	Wave lengths in x,z directions,

respectively (Fig. 1.3)

λ_3^+ Non-dimensional parameter = $\lambda_3 u^*/\nu$

θ_3 Transformation angle (Fig. 5.6)

$\bar{\Phi}$ Integral constant (Eqn. 2.2)

Subscripts:

c	Center line values
e	Edge values
b	Values referred to the boundary layer
ℓ	Leading edge values
t	Trailing edge values
w	Wake values
w1	Wall values
∞	Free stream values
i	Interaction
0	Non-interaction
1,2,3	Hot-wire sensor coordinates

Superscripts:

$\overline{\quad\quad}$ Mean values

CHAPTER I

INTRODUCTION

1.1 Statement of the Problem:

A better understanding of the wake-boundary layer interaction is necessary to minimize the losses and enhance the reliability of various structures in engineering applications. In general, the phenomenon of the wake - boundary layer interaction occurs downstream of the junction of two bodies, e.g., the stabilizer and the rudder, the wing and the fuselage, an aerofoil with slotted flaps, flow behind the rotor and the stator of a turbomachine near the hub and the tip regions (Fig.1.1). The boundary layer developed on the downstream section of the stabilizer may be markedly affected by the wake shed at the trailing edge of the rudder. The calculation of drag, shear stresses and forces acting on the downstream section of the stabilizer is not possible unless the flow is treated as the interaction of wake and boundary layer. The performance of each part and hence the overall performance of the aeroplane from aerodynamics considerations requires the knowledge of the wake boundary layer interaction.

The wake flow field without any boundary layer interaction effect is generally analyzed for the near wake and the far wake regions. The description of these regions is as follows, Ref. (1):

i) Near Wake: The wake center line velocity defect is

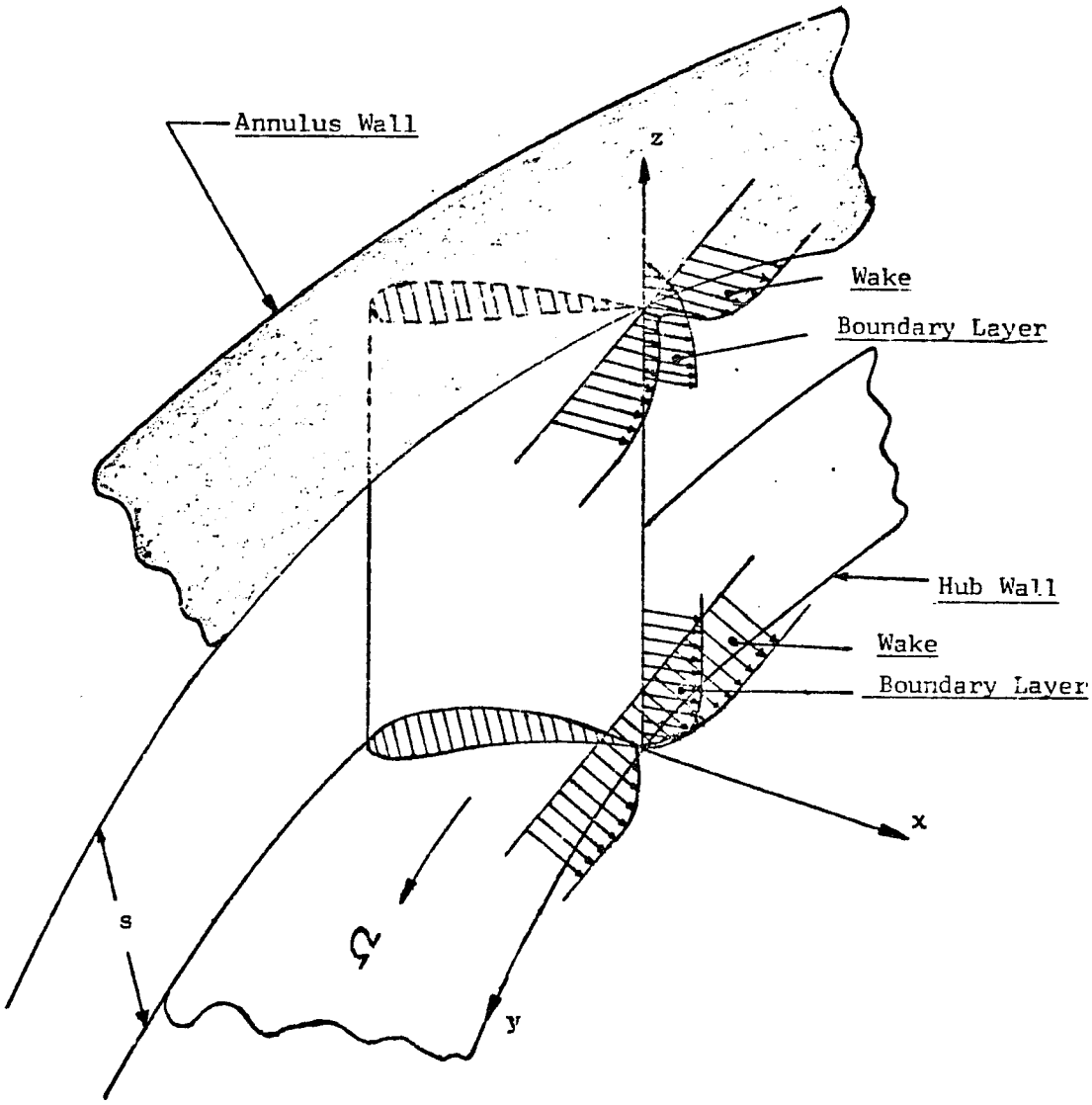

Figure 1.1 Schematic of the Wake and Boundary Layer Interaction Near the Tip and Hub of a Compressor Rotor

almost equal to the wake outer edge velocity. At the wake center line,

$$\overline{u_x^2} > \overline{u_z^2} > \overline{u_y^2}$$

The wake width increases rapidly with the axial distance downstream of the trailing edge.

ii) Far Wake: The wake center line velocity defect is so much smaller as compared to the outer edge velocity that the square of the center line velocity defect is negligible in comparison with the square of the outer edge velocity. At the wake center line,

$$\overline{u_x^2} \sim \overline{u_z^2} \sim \overline{u_y^2}$$

The wake width either grows very slowly or is almost constant.

The turbulent boundary layer is generally analysed for the inner and the outer regions. The outer region is inertia dominated while the inner region is viscosity dominated. The inner region is also known as the wall region. The transition from the inner region to the outer region takes place in a region where both convection and viscous effects are equally strong; such a region is known as a buffer region and its solution is obtained as a limiting case by matching the solution from the inner region and the outer region asymptotically, (Fig. 1.2). The detailed description of these regions is as follows:

i) Inner Region: In the viscous sub-layer, the Reynolds stress is a small fraction of the frictional velocity, the

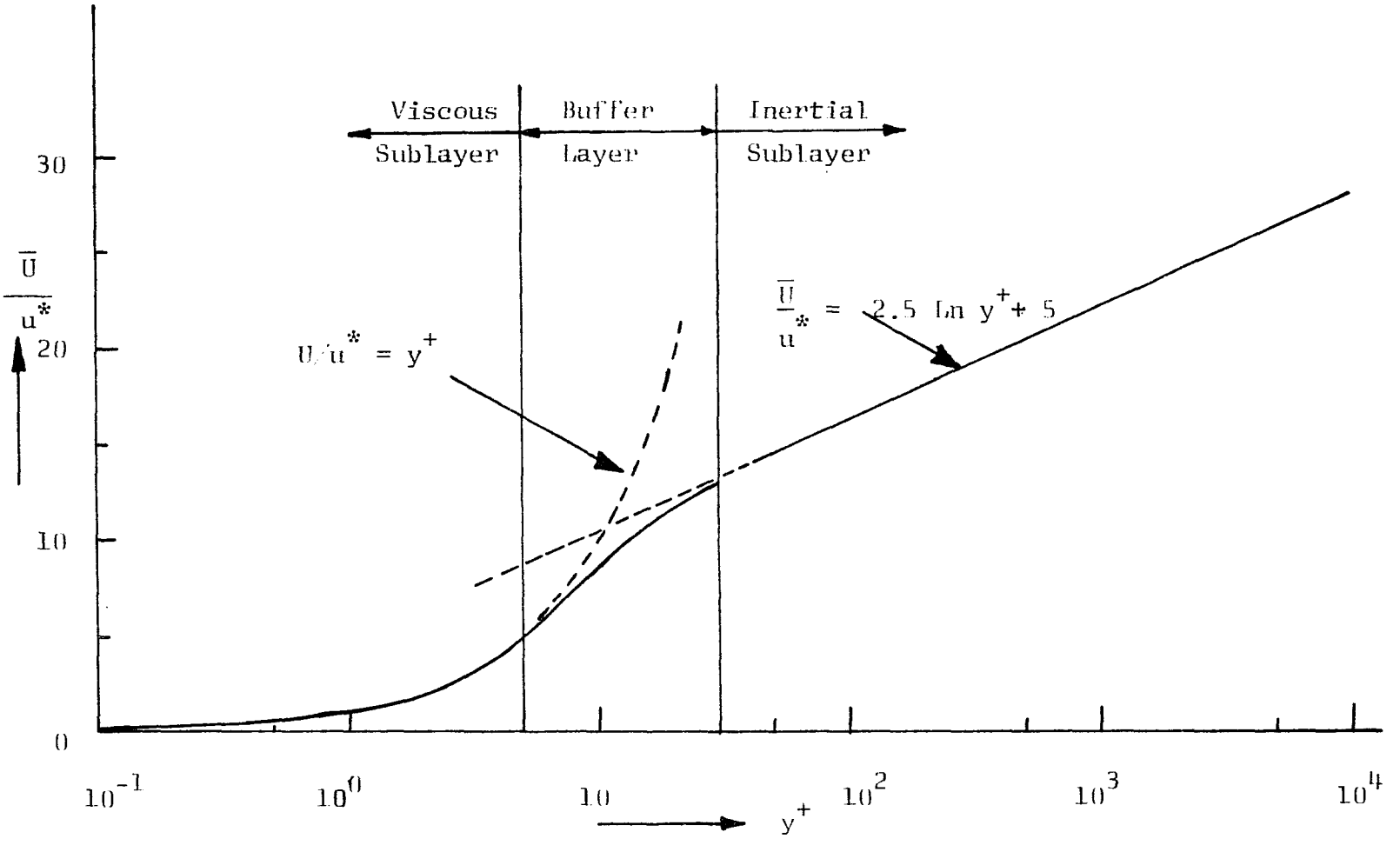

Figure 1.2 Schematic of the Turbulent Boundary Layer on a Flat Plate Showing the Various Layers (Reference 2)

flow is unsteady and the velocity fluctuations are present but do not contribute much to the stress because of the predominant effect of viscosity. Sometimes, the misleading name of "laminar sub-layer" is also associated with this sub-layer. The pressure velocity correlation for the inner region is modeled by Raj (3).

In the wall region, a horse-shoe shaped vortex begins to form. The flow deforms this vortex into an elongated U - shaped loop in the streamwise direction. The tip of the loop moves away from the wall into the regions of ever increasing velocity due to self induction. Thus, due to the stretching process, vorticity increases, giving rise to an outward V component of flow near the tip, creating the in-rush process. A local deceleration is created due to the vortex moving away from the wall. Due to the ejection process, low momentum fluid is transported away from the wall, producing a net positive contribution to shear stress. The instantaneous velocity profile forms a dent with inflection points in addition to the horizontal shear layers. Thus, due to this resultant local inflexional instability and break-down of the fluid surrounding the original tip of the vortex, a turbulence burst (Fig. 1.3) is produced. The pressure waves related to the turbulence burst are propagated through the whole boundary layer. The blob of fluid of high turbulence intensity produced during the burst convects downstream and moves farther away from the wall, increasing the scale by turbulent diffusion. Thus, this blob of fluid

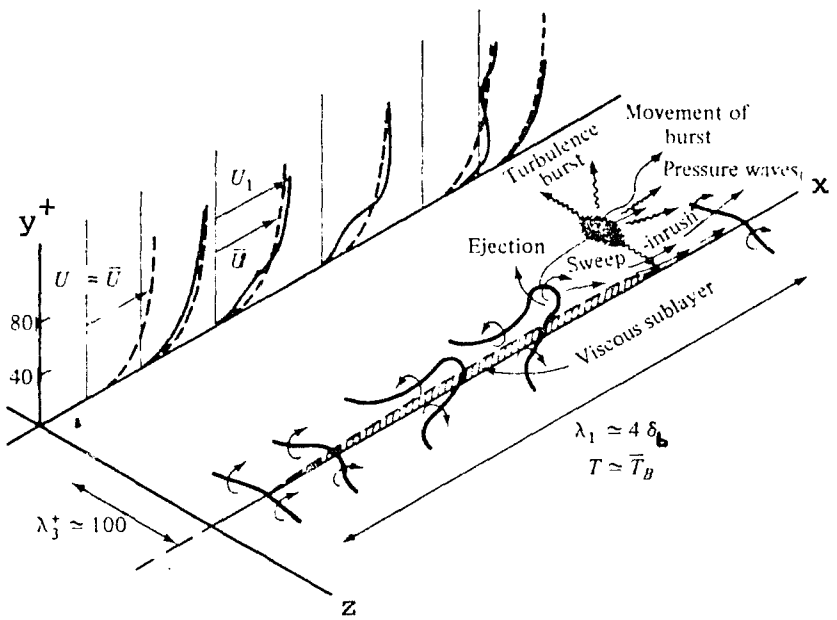

Figure 1.3 Schematic of the " Cyclic " Process of Turbulence Near the Wall (Reference 4)

is convected in an accelerated way in a downstream direction due to the high momentum fluid coming from upstream. Also, the pressure waves generated earlier may add to the movement of the fluid towards the wall creating a sweep - inrush flow, (Fig. 1.3). The sweep inrush flow makes a very small angle of the order of 5^{o} to 15^{o} with the wall, which can be treated as the entry of the high momentum fluid in an almost horizontal direction at the wall. Thus, a tremendous amount of turbulence is produced in the region where $y\, u^{*}/\nu = 10$ to 15 due to the simultaneous cyclic process of ejection, sweep-inrush and turbulent burst. A detailed description of this phenomenon is given in Hinze (4).

The well known laws of the wall for the mean velocity and the Reynolds stress are given below:

$$\frac{\overline{U}}{u^{*}} = f(y\, u^{*}/\nu) \qquad \ldots(1.1)$$

$$-\frac{\overline{u\, v}}{u^{*2}} = g(y\, u^{*}/\nu) \qquad \ldots(1.2)$$

where

u* is frictional velocity, f and g are similarity functions and ν is kinematic viscosity.

Energy spectral function, F, was theoretically obtained by Tchen (5) and is given as:

$$F \sim k^{-7} \sim \tilde{\ell}^{7}$$
$$v_{k} \sim k^{-3} \sim \tilde{\ell}^{3} \qquad \ldots(1.3)$$

where

V_k is the velocity at the wave number k, and $\tilde{\ell}$ is the mixing length.

ii) Outer Region: This region is almost similar to the free turbulent shear flows, particularly regarding the plane wake flows. Here, flow is of intermittent nature but the amplitude of the wavy interface is much smaller as compared to that of the plane wake flow. The outer region is characterized by large eddies, elongated in the main flow direction. The turbulence obtaines its energy mainly by convection and by turbulent transport from the inner region of the upstream part of the boundary layer. Turbulence is also determined by the conditions in the inner region, i.e., by the distribution of the wall shear stress farther upstream. The ratio of the turbulence shear stress to the turbulence kinetic energy across a boundary layer in the outer region is almost constant, (Refs. 2 and 4). The interaction between the inner and the outer region is mainly through the convective distribution, but the pressure effects also give rise to the interaction between the turbulence in the inner and the outer region, though this interaction is much less extended in the main flow direction. In other words, these pressure effects are relatively more local in the streamwise direction, though they are convected mainly with the convection velocities of larger eddies, i.e., roughly, with the average mean velocity across the boundary layer. In channel flow, the outer region is termed as core region.

The dependency of part of the structure of

turbulence on upstream conditions in the outer region points towards longer memory of flow than that in the inner region. Thus, the recovery from any disturbance is much quicker when the disturbance is introduced in the inner region than that if it were introduced in the outer region.

The well known law of the wake, Ref. (6), is given as,

$$\frac{\bar{U}}{u^*} = \frac{\pi}{k_1} h(y/\delta) \qquad \ldots(1.4)$$

where

k_1 is the von Karman constant, h is the similarity function, π is the profile parameter and δ is the thickness of the shear layer.

The energy spectral function, F, for the inertial sub-range, Ref.(5), is given as,

$$F \sim k^{-5/3} \sim \tilde{\ell}^{5/3} \qquad \ldots(1.5)$$

$$v_k \sim k^{-1/3} \sim \tilde{\ell}^{1/3}$$

and

$$F \sim k^{-1} \sim \tilde{\ell} \qquad \ldots(1.6)$$

$$v_k \sim \text{constant}$$

The relation (1.5) is valid for small vorticity and no resonance while the relation (1.6) is valid for large vorticity and strong resonance.

iii) Buffer Region: This region is the most active part as far as production and dissipation of turbulence energy are concerned. In the buffer layer, neither of the stresses

can be neglected. For engineering purposes, the buffer layer is obtained by matching the linear velocity profile in viscous sub-layer to the logarithmic velocity profile in the inertial sub-layer.

The foregoing description of the wake and the boundary layer suggests that the wake-boundary layer problem may be resolved in the following way:

i) Near Wake Interaction: When the distance between the two bodies is very small ($S/c \sim 0.007$) the wake shed from the first body interacts with the outer, buffer and inner regions of the boundary layer developed on the second body.

ii) Far Wake Interaction: When the spacing between the two bodies is large ($S/c \sim 0.7$) the wake shed from the trailing edge of the first body interacts with the outer, buffer and inner regions of the boundary layer developed on the second body.

It is clear from the above description that to resolve the problem theoretically without any experimental input is a fruitless task. The flow field in the tip and the hub regions of the turbomachinery rotor and stator is even more complex. The flow at the tip of the rotor is associated with tip vortices and annulus wall boundary layer. The viscous region downstream of the tip of the rotor is not only affected due to the wake from the trailing edge of the rotor but also due to the boundary layer growth at the

annulus; thus forming the phenomenon of wake boundary layer interaction behind the tip of the rotor. The effect of the shed vortices from the tip of the trailing edge of the rotor may cause the wake-boundary layer interacted flow to be highly inhomogeneous and anisotropic. A similar phenomenon also exists near the hub behind the downstream section of the stator. These interaction effects are unknown at this time experimentally or theoretically.

1.2 Objectives of the Present Investigation:

The objectives of the present investigation were as follows:

i) From scaling considerations, establish trends in the decay or growth rate with distance downstream of the trailing edge of a flat plate for the mean velocity, shape factor, turbulence intensity, Reynolds stress and for the length scale of a wake in the presence of free stream turbulence.

ii) From scaling considerations, establish trends in the decay or growth rate for the mean velocity and the wake width in the wake boundary layer interacted flow.

iii) Experimentally study the two-dimensional turbulent wake of a flat plate with and without free stream turbulence including both the mean and the turbulence quantities.

iv) Experimentally study the wake-boundary layer interacted flow for the near and the far wake regions including both the mean and the turbulence quantities.

v) Correlate the data obtained in (iii) and (iv) with the trends established in studies (i) and (ii), respectively. Also establish the decay or growth rate for the turbulence quantities.

The frequency spectra are also to be obtained at the near and the far wake regions of the wake submerged in the boundary layer. The spectra are to be compared with the theoretical predictions of Tchen (5).

1.3 Method and Means of Investigation:

Realizing the difficulties stated in the previous sections, the problem of the wake-boundary layer interaction was considered in two phases. Phase one included the effect of free stream turbulence on the characteristics of a turbulent wake while the three-dimensional nature of the wake-boundary layer interaction problem was treated in the second phase of the work.

The effect of free stream turbulence was incorporated through two turbulence parameters and using similarity considerations. The decay rate of the wake velocity defect at the wake center line and the growth rate for the wake length scale were derived. The decay rate for the maximum value of longitudinal and lateral components of turbulence

intensity and Reynolds stress of a wake (Chapter III) in the free stream turbulence environment were developed from the self-preservation considerations.

The experimental investigation of the wake in the presence of free stream turbulence (Chapter V) was carried out using single and cross-wire probes. The free stream turbulence was measured by the use of a single sensor hot-wire probe. The measurements of the mean velocity, turbulence intensity and Reynolds stress of the wake in the presence of free stream turbulence were taken using a cross-wire probe. Semi-empirical correlations were obtained for various decay and growth rate using the experimental data (Chapter VI).

For the wake-boundary layer interaction phase of the investigation, the general mean momentum governing differential equations for three dimensional, turbulent and incompressible flow (Chapter IV) were simplified using the high Reynolds number approximation and the scales involved in the geometry of the body under investigation. The turbulent diffusion model was used for the Reynolds stress modeling. The velocity defect laws for the mean velocity components involving similarity functions were introduced. The analytical solution of the governing equations in the similarity variables was obtained. The trends in the decay rate for the wake velocity defect and the growth rate for the length scale were established.

The triple sensor hot-wire probe (Chapter V) was used for the measurements of mean and turbulence quantities in the wake boundary layer interacted flow. A single sensor hot-wire probe was used to check the three sensor hot-wire data (total mean velocity and total turbulence intensity only). The measurements were taken at various axial, radial and lateral locations downstream of the flow field. Semi-empirical correlations were obtained for velocity and length scales. The decay rates for the maximum values of the three components of turbulence intensity and Reynolds stress were also obtained (Chapter VII).

The frequency spectra (Chapter VII) were taken at the near and the far wake regions of the wake interacted boundary layer region. The spectra were transformed into the wave number domain. The energy spectra were compared with the experimental data available on other types of flows.

The conclusions of the free stream turbulence effect on wake and the wake boundary layer interaction are summarized in Chapter VIII.

CHAPTER II

LITERATURE SURVEY

The statement on the wake - boundary layer interaction problem (Chapter I) indicates that the wake-boundary layer problem may be considered as an extension of the problem of the effect of free stream turbulence on the wake and the boundary layer. The difference is that the free stream turbulence effect on the wake or the boundary layer is associated with the extremely weak mean shear in the free stream. It is, therefore, important to study carefully the information available on the effect of the free stream turbulence and infer from it, related information in addition to the available information on the wake-boundary layer interaction. Therefore, the literature search is considered in the following two areas:

I. Effect of free stream turbulence on the turbulent boundary layer and the wake.

II. Wake-boundary layer interaction.

2.1 Effect of Free Stream Turbulence on the Turbulent Boundary Layer and the Wake:

The characteristics of the wake and the boundary layer of a flat plate is an initial input for the study of the wake-boundary layer interaction. Several investigations have been conducted indicating the effect of free stream

turbulence on the growth of the turbulent boundary layer, (References 7 to 14). Very little information is available, however, on the effect of free stream turbulence on wakes, even on the turbulent wake behind a flat plate.

Mc Donald and Kreskovsky (7) performed an overall turbulence energy balance by incorporating the effect of the free stream turbulence level in the turbulent boundary layer equations. The modification in the mixing length due to free stream turbulence as obtained theoretically on the basic formulation of Ref. (15) is

$$\frac{\tilde{\ell}}{\delta_b} = \frac{\tilde{\ell}_\gamma}{\delta_b} \tan\left(\frac{k_1 y}{\tilde{\ell}_\gamma}\right) + \left(1 - \tanh\frac{k_1 \delta_b}{\tilde{\ell}_\gamma}\right)\left(\frac{1 - \cos\frac{y\pi}{\delta_b}}{2}\right) \quad \ldots(2.1)$$

where

$\tilde{\ell}_\gamma$ is the wake value of the mixing length at any particular streamwise station, y is the transverse coordinate, k_1 is the von Karman constant, and δ_b is the boundary layer thickness.

The average mixing length is related to the free stream turbulence as

$$\frac{\bar{\ell}}{\delta_b} = \left[\frac{3\, a_1\, (1 - H_1)}{\bar{\Phi}}\right]^{\frac{1}{2}} T \quad \ldots(2.2)$$

where

$H_1 = \delta_1 / \delta_b$ = displacement thickness/boundary layer thickness

T = Free stream turbulence intensity

$\bar{\Phi}$ = Integral constant

a_1 = constant

But Eqn.(2.2) is valid only if H_1 does not vary appreciably with x and $\bar{\ell}/\bar{L} \sim 1$, where $\bar{L}$ is the average dissipation length.

The expression for the average mixing length can be simplified if the power law type velocity profile, i.e.,

$$\frac{\bar{U}}{U_e} = \left(\frac{y}{\delta_b}\right)^n$$

is assumed; giving $\bar{\Phi} = n/2$, $H_1 = n/(n+1)$

Assuming $a_1 = 0.15$, Eqn.(2.2) can be written as

$$\frac{\bar{\ell}}{\delta_b} = \left[\frac{0.9}{n(n+1)}\right]^{\frac{1}{2}} T \quad \ldots(2.3)$$

In comparison to the 1/7th velocity profile law, only 3 % free stream turbulence level is required to maintain an average mixing length of $0.1\,\delta_b$ which is of the order of the average dissipation length scale.

It is concluded that 5 % increase in the free stream turbulence gives rise to 30 % increase in the heat transfer and the wall friction, as is found in comparison with the available experimental data. In the foregoing analysis, an assumption of the constant streamwise pressure and isotropic free stream turbulence was made. The theory is good for small turbulence levels only. For large turbulence levels, the theory over-predicts the observed effects.

The effect of free stream turbulence level on the heat transfer rates for the various configurations is compiled in Ref. (16).

Charnay, Comte-Bellot and Mathieu (10) studied experimentally the development of turbulent boundary layer on a flat plate in the presence of an external turbulent flow generated by grids of different configuration in a wind tunnel at a mean speed of 10 m/sec. A single sensor hot-wire probe was used in the mean velocity measurement. For the given grid, a lack of self-preservation in the mean velocity profiles at different axial locations is reported. It has been suggested that this is due to the alignment error of a single sensor hot-wire probe in a two-dimensional flow. A cross-wire probe probably could have given better results.

It is found that the usual velocity defect law for a a flat plate,

$$\frac{\bar{U}_e - \bar{U}_s}{u^*} = f(y/\delta_b) \qquad \ldots(2.4)$$

modifies to

$$\frac{\bar{U}_e - \bar{U}_s}{u^* - \gamma\sqrt{\bar{q}_s^2}} = f(y/\delta_b) \qquad \ldots(2.5)$$

in the presence of free stream turbulence.

where $\sqrt{\bar{q}_s^2}$ is the root mean square fluctuating component of

streamwise velocity; γ is the empirical constant; $\bar{U}_s$ is the streamwise velocity; $\bar{U}_e$ is the velocity at the edge of the boundary layer; δ_b is the boundary layer thickness and y is the coordinate normal to the surface.

With the increase of free stream turbulence, the boundary layer grows rapidly, the wall shear stress increases, the turbulent shear stress and the turbulent kinetic energy production increase and the mean velocity profile flattens, while the law of the wake is modified in the outer region of the boundary layer. The results reported in Ref. (11) are of a similar nature as those of Ref. (10). Dryden (17) has shown that increasing the effect of the free stream turbule - nce level causes the forward shift of the transition region for laminar to turbulent flow.

Kline et. al. (18) studied the effect of free stream turbulence on the characteristics of the turbulent boundary layer on a flat plate in a wind tunnel having a 13.7 cm. square test section with a maximum velocity of 45.72 m/sec. The free stream turbulence is generated with variable size rods with a maximum diameter of 1.905 cm.; inserted in a single row in either the horizontal, vertical or crossed position. The horizontal distance between the leading edge of the flat plate and the grid was 22.86 cms.

The experimental results of turbulence intensity are compared with its decay law originally derived by Frenkiel (19):

$$\frac{u}{\bar{U}} = \left[\frac{u_0}{\bar{U}}\,\frac{\bar{b}}{x_0}\right]^{-5/7} \left(\frac{x}{b}\right)^{-5/7} \qquad \ldots(2.6)$$

and later used by Baines and Peterson (20) as

$$\frac{u}{\bar{U}} = 1.12\,\left(x/\bar{b}\right)^{-5/7} \qquad \ldots(2.7)$$

where

$\bar{b}$ is the bar width of the grid; $\bar{U}$ is the local mean velocity; x and u are the distance downstream from the mid-plane of the screen and the root mean square value of the turbulence intensity, respectively and x_0 and u_0 are the corresponding values at the arbitrary starting point.

Eqn. (2.7) is in good agreement with the experimental data of Ref. (20) for high value of $x/\bar{b}$ but a wide scatter in data is indicated in Ref. (18).

It is concluded in Ref. (18) that the increase of free stream turbulence increases the value of wall shear, the boundary layer displacement thickness and the momentum thickness. The velocity profiles with large free stream turbulence do not satisfy the law of the wall. The free stream turbulence changes the law of the wake. The similarity of the velocity profile in the direction of the flow is not maintained. Information on the effect of high free stream turbulence on the skin friction coefficient is unavailable from this investigation. The mean velocity and

the turbulence intensity measurements were made with a single sensor hot-wire probe in a two-dimensional flow and might be the reason for non-existance of similarity in the direction of the flow. The measurements should be made with a cross-wire probe to draw the appropriate conclusions.

Robertson and Holt (21) also studied the effect of free stream turbulence on the turbulent boundary layer. The turbulence was generated with a biplanar circular bar grids of mesh to bar diameter $M/d = 5.3$, and average speed (mostly) of 15.55 m/sec. As the axial distance between the grid and the leading edge of the flat plate was usually very small (about 6.5 cms.), the turbulence generated was anisotropic and did not achieve equilibrium structure.

The decay in the turbulence intensity behind round bar grids was given as (Reference 21) :

$$\frac{u}{\bar{U}_e} = 104 \left(d/x \right)^{0.78} \% \qquad \ldots(2.8)$$

where

d is the bar diameter, u is the r.m.s. value of the velocity fluctuations; $\bar{U}_e$ is the free stream value of the mean velocity and x is the axial distance.

Eqn. (2.8) is found to be valid for the values obtained at a distance greater than 12 d.

It is again concluded in this investigation that the boundary layer thickness increases, the velocity profile

flattens, the shape factor decreases and the skin friction coefficient increases. The turbulence level of 7 % increases the growth rate by 10 %, while the increase in boundary layer thickness is reported as 45 %.

Green (22) compiled the influence of the free stream turbulence on the turbulent boundary layer and concluded that Eqns. (2.4) and (2.5) can be represented in terms of the Clauser's shape parameter G, respectively, as

$$G = \frac{H - 1}{H} \sqrt{2/c_f} \qquad \ldots(2.9)$$

$$G = G_0 \left(1 - \gamma \sqrt{\frac{2}{c_f}} \frac{u}{\overline{U}_e} \right) \qquad \ldots(2.10)$$

where

G_0 is the value of G in the boundary layer of a quiescent flow with zero pressure gradient; generally accepted to be a constant, G_0 is nearly equal to 6.5.

The data of Refs.(10) and (11) can be closely fitted up to a turbulence level of 5 %, to

$$G = G_0 \left(1 - \frac{1}{3} \sqrt{\frac{2}{c_f}} \frac{u}{\overline{U}_e} \right) \qquad \ldots(2.11)$$

where G_0 is taken as 6.4.

Using Eqn. (2.11) and the skin friction relation, (Reference 23),

$$\sqrt{2/c_f} = A \, \mathrm{Ln} \, R_\theta + B + f(G) \qquad \ldots \qquad (2.12)$$

the influence of free stream turbulence on the skin friction

coefficient , c_f; shape factor, H and Reynolds number based on momentum thickness, R_θ , was given by Green (22) as follows:

At constant R_θ

$$\frac{\Delta c_f}{c_f} = 4.8 \frac{u}{\bar{U}_e} \qquad \ldots(2.13)$$

$$\frac{\Delta H}{H} = -\left[2.4 - 0.25\, H\right] \frac{u}{\bar{U}_e} \qquad \ldots(2.14)$$

At constant H

$$\frac{\Delta R_\theta}{R_\theta} = -\left(\frac{0.27}{c_f} - 0.97 \sqrt{\frac{2}{c_f}}\right) \frac{u}{\bar{U}_e} \qquad \ldots(2.15)$$

where $G_0 = 6.4$ and $A = 2.47$ have been used.

In the above derivation it is assumed that the empirical constants in the law of the wall are insensitive to the free stream turbulence. This may be true only for the low level of free stream turbulence, but the constants will change for the high level of free stream turbulence.

Thus, from the above equations, it can be concluded that a free stream turbulence level of 0.2 % increases c_f by 1 %, lowers H by 0.05 %, and increases R_θ by 12 %. It means that a small increase in streamwise root mean square velocity fluctuation has the same effect on the slope of the velocity profile as a fractional increase in Reynolds number, roughly sixty times as great. But nothing has been said about either the importance of turbulence scales or the

influence of pressure gradient.

Hall and Hislop (24) found on the basis of their experimental results, that the Taylor's turbulence parameter correlation, Ref. (25),

$$T_2 = (x/M)^{1/5} \; u_m / \bar{U} \qquad ...(2.16)$$

where

M is the mesh size and u_m is the mean value of the turbulence component,

could not be established. Here, u_m is given by

$$\frac{u_m}{\bar{U}_e} = 100 \; \frac{(\overline{u^2} + \overline{v^2} + \overline{w^2})^{\frac{1}{2}}}{3 \; \bar{U}_e} \; \% \qquad ...(2.17)$$

where

u, v, w are the r.m.s. turbulence velocity components.

But the experimental data of Schaubauer (26) obtained with the grid size of 8.89 cm. and 12.7 cm. were in good agreement with the Taylor's turbulence parameter correlation, implying that the correlation is valid for the turbulence generated due to large grid size.

Hall and Gibbings (27) fitted their experimental data incorporating the effects of free stream turbulence on the start and end of the transition region of the boundary layer developed on a flat plate. These correlations are given as follows, respectively:

$$Ln(R_\theta - 190) = - 103 \; \frac{u_m}{\bar{U}} + 6.88 \qquad ...(2.18)$$

$$\text{Ln}(R_\theta - 320) = - 44.75 \, u_m / \bar{U} + 7.70 \quad \ldots(2.19)$$

where

u_m is given by Eqn. (2.17) and R_θ is the Reynolds number based on momentum thickness, θ.

Further, they concluded that the increase in the free stream turbulence reduces the transition Reynolds number (the transition region reduces). Eqns. (2.18) and (2.19) cannot be treated as the basis for further developments because there is a large scatter in the data at low free stream turbulence (1 % to 3 %). No data is available for turbulence level greater than 3%.

Michel (28) gives good review of Refs.(10, 11, 22 and 27) on the effect of free stream turbulence on the boundary layer parameters. He concluded that the increase in the external turbulence is accompanied by a rapid reduction in the transition Reynolds number, more rapid thickening of the boundary layer, moderate increase of the friction coefficient, fuller velocity profile and reduction of shape parameter. When the fluctuating quantities are referred to the wall friction or the friction velocity, low external turbulence has practically negligible effect near the wall. The velocity defect law in the outer region depends appreciably on the free stream turbulence.

Tsuji and Iida (29) studied experimentally the effect of the free stream turbulence on the velocity

distribution of an incompressible two-dimensional turbulent boundary layer with no pressure gradient. The free stream turbulence was generated with a square mesh grid with a spacing of 50 mm and the rods of cross-section 10 x 10 cm^2. The axial distance between the turbulence generating grid and the test surface was not large enough to obtain isotropic free stream turbulence. It is concluded in this study that the free stream turbulence increases the surface shear stress and mixing length, and decreases the shape factor. The velocity profiles are derived analytically using mixing length and eddy viscosity hypothesis as

$$\frac{\tilde{\ell}}{\delta_b} = \frac{\sqrt{\tau/\tau_{w1}}}{\partial(\bar{U}/u^*)/\partial\eta} \qquad \ldots(2.20)$$

$$K_T = \nu_T/(u^* J \delta_b)$$

$$= \frac{\tau/\tau_{w1}}{J\,\partial(\bar{U}/u^*)/\partial\eta} \qquad \ldots\ldots(2.21)$$

where

τ = shear stress

u^* = $\sqrt{\tau_{w1}/\rho}$ = frictional velocity

$\tilde{\ell}$ = mixing length

K_T = eddy viscosity coefficient

η = y/δ_b = Distance normal to the surface/boundary layer thickness

and J is obtained by integrating the velocity defect along a tangent drawn at $\eta = 0.2$ of the experimental velocity defect profile.

The mixing length and eddy viscosity show large values under free stream turbulence but their values decrease as the turbulence decays. Eddy viscosity is assumed constant throughout the boundary layer which is true only in the outer layer, but not in the inner layer. Thus, the analytical results are of approximate nature only. To get a better understanding of the phenomenon, separate consideration should be given to various regions with appropriate matching of the results.

A preliminary experimental study by Eagleson et. al. (30) on the flat plate turbulent wake contains some passing reference to the effect of free stream turbulence on the wake of a flat plate in water. This study indicated that the wake center line velocity in the presence of high free stream turbulence (7 % to 8 %), may vary as,

$$\frac{\bar{U}_0}{\bar{U}_e} \sim \left(\frac{x}{c} + \frac{x_0}{c} \right)^{-1}, \quad \ldots(2.22)$$

but no information is available on the turbulence quantities. The above velocity defect decay is much faster compared to the velocity defect decay for turbulent wake behind a flat plate without free stream turbulence (Reference 31).

Komoda (32) measured the wake of a 1.0 mm diameter circular cylinder in an air stream of 10 m/sec, with and without free stream turbulence. The cylinder was kept at a distance of 30.5 cm. downstream from the entrance to the

working section, in an Eiffel type wind tunnel, having a 60 x 60 $cm.^2$ closed working section. The measurements of mean and turbulence quantities of Ref. (32) indicate that the wake spreads and the intensity of turbulence increase due to free stream turbulence effect. The structure of small eddies relating to $\overline{(\partial u/\partial x)^2}$ is more affected compared to the large eddies responsible for stress, resulting in a rapid approach towards structural equilibrium. The results reported are only for the turbulence levels of 0.17 % and 3.8 %. No information is available on the theoretical predictions of mean and turbulence quantities.

Experimental study of the wake of a two-dimensional cylinder placed in a fully developed turbulent viscous layer inside a two-dimensional channel was done by Eskinazi (33). Static pressure distribution, decay rates for the mean velocity defect and turbulence intensity etc. were reported. The study does not provide information about the Reynolds stress.

Recently, detailed theoretical and experimental studies of the effect of free stream turbulence on the wake developed from the trailing edge of a flat plate have been reported by Pal and Raj (34, 35).

The effect of free stream turbulence on various parameters of boundary layer based on the foregoing review, is summarized qualitatively and quantitatively in Tables I and II, respectively.

TABLE I

SUMMARY OF THE EFFECTS OF FREE STREAM TURBULENCE (QUALITATIVE) ON VARIOUS PARAMETERS BASED ON REVIEW

S.No.	Parameter/Region	Qualitative Trend	References
1.	Boundary layer thickness	Increases	7,11,18,21,22,28
2.	Mean velocity profile	Flattens	10,11,21,22,28
3.	Displacement thickness	Increases	18
4.	Momentum thickness	Increases	18
5.	Skin friction coefficient	Increases	11,21,22,28,29
6.	Shape factor	Decreases	11,18,21,22,28,29
7.	Transition Reynolds No.	Rapidly Reduces	17,27,28
8.	Reynolds number based on momentum thickness	Increases	22
9.	Heat transfer	Increases	7,16
10.	Production of turbulent kinetic energy	Increases	7,16
11.	Wall shear stress	Increases	7,10,11,18,29
12.	Turbulent shear stress	Increases	10,11
13.	Mixing length	Increases	7,29
14.	Eddy viscosity	Increases	29
15.	Transition region	Shifts Forward	17,27
16.	Law of the wake in outer region	Modifies	10,11,18,29
17.	Law of the wall	Changes	18
		But unchanged for small free stream turbulence	28

TABLE II

SUMMARY OF THE EFFECTS OF FREE STREAM TURBULENCE (QUANTITATIVE) ON VARIOUS PARAMETERS BASED ON REVIEW

S. No.	Parameter	Percentage Increase in Turbulence Level	Percentage Variation in Parameter	References
1.	Boundary layer thickness	11.0	14.3	18
		3.9	50.0	11
		7.0	45.0	21
2.	Mean velocity profile	7.0	10.0	21
3.	Displacement thickness	11.0	4.0	18
		3.9	-9.8	11
4.	Momentum thickness	11.0	10.0	18
		3.9	-1.6	11
5.	Skin friction coefficient	3.9	16.9	11
		0.2	1.0	22
		4.4	15.7	28
		4.1	10.8	29
6.	Shape factor	11.0	-5.5	18
		3.9	-8.5	11
		0.2	-0.5	22
		4.1	-8.7	29
7.	Transition Reynolds No.	2.5	-53.8	17
		0.15	-15.0	27
8.	Reynolds No. based on momentum thickness	0.2	10.0	22
9.	Heat transfer	5.0	30.0	7
10.	Nusselt's No.	3.5	100.0	9
11.	Frictional velocity	3.9	9.4	11
12.	Wall shear stress	5.0	30.0	7
		3.9	19.7	11
13.	Mixing length	4.1	96.0	29
14.	Eddy viscosity	4.1	233.0	29

2.2 Wake - Boundary Layer Interaction:

Experimental data of Love (36) and Armilli (37) on a cylinder wake submerged in the boundary layer of a flat plate indicate that the properties of the wake submerged in the boundary layer are different from the conventional two-dimensional wake.

The theoretical model proposed by Gartshore (38), of simple addition of the wake and the boundary layer defects for the wake-boundary layer interaction using an eddy viscosity model, is valid for two-dimensional and small deficit wakes. Also, it cannot predict the nature of the turbulence quantities.

Counihan, Hunt and Jackson (39) attempted the theoretical and experimental analysis for wakes behind two-dimensional surface obstacles in the turbulent boundary layer by making the following assumptions and approximations:

a) The height of the roughness element in the incident boundary layer, k_r , is less than the height, h_2, of the body, whose wake is under consideration. h_2 is less than the boundary layer thickness, δ_b; i.e.

$$k_r \ll h_2 \ll \delta_b$$

b) Far downstream of the wake, the main velocity of the wake equals its value in the undisturbed boundary layer.

c) In the upstream boundary layer region, the mean velocity profile is represented by the power law:

$$\bar{U}(y) = \bar{U}_{\infty} \left[(y - y_0)/\delta_b \right]^n \quad \ldots.(2.23)$$

where

$\bar{U}_{\infty}$ is the wind speed outside the boundary layer.

The choice of the exponent n gives the best fit over the lowest part of the boundary layer where the wake developes. The value of the exponent n for the best power law fit was found to be 0.125. Near the roughness element (wall region), logarithmic profile, i.e.

$$\bar{U}(y) = \frac{u^*}{k_1} \mathrm{Ln}\left(\frac{y - y_0}{\delta_b} \right) \quad \ldots(2.24)$$

is chosen so as to obtain a better fit to the velocity profile.

d) Far downstream of the body, the region is considered in three different categories, i.e., wall region, mixing region and disturbance region, which is an inviscid perturbation on the boundary layer flow.

The theoretical results have been compared with the available experimental data. The velocity deficit was observed to be in good agreement. But the theory does not adequately describe the distribution of the shear stress and the turbulence intensity across the wake. More accurate and refined measurements of the Reynolds stress, turbulence intensities and scales are required. Moreover, the case

considered in Refs. (38) and (39) is far from being realistic because in the usual practice, the wake boundary layer interacted flow is three-dimensional to start with.

Bradshaw, Dean and Mc-Eligot (40) studied numerically the interacting turbulent shear layers by a simple superposition in a symmetrical duct in which shear stress changes sign when two shear layers interact. It is concluded that good agreement with the usual available experimental data is obtained with the usual empirical input of the boundary layers while the change in empirical constants is essential for high turbulent flows, i.e., free jet flows. In the analysis, eddy length scale is defined only by the conditions at the edge of the simple shear layer, while the shear stress width is the width of the largest eddies. It is more appropriate that the length scale be given by the integral of the shear stress profile. In Ref.(40), the numerical scheme is carried out using the method of characteristics. At all steps except the first, the normal velocity component is calculated directly from the continuity equation instead of from the equation along the normal characteristic. It is also concluded that the interaction does not significantly effect the turbulence structure and if the ratio of the turbulent shear stress to the laminar shear stress is the correct order of magnitude, fairly successful mean velocity predictions are generally obtained.

Morel and Torda (41) applied Bradshaw's interaction hypothesis using kinetic energy and length scale approach for

two-dimensional free shear flows considering the flow with velocity extrema as consisting of several interacting layers. The expression for shear stress, showing that it does not vanish at the velocity extremum, is derived. The analysis is valid for two-dimensional high Reynolds number flow. The interaction hypothesis to a crude approximation is that the two neighboring turbulent flow fields do not interact with each other. The turbulence in each region is shaped by a mean velocity profile, i.e., the structure functions of simple layers are to be little or not at all affected by interaction. The shear stress does not change sign in a simple layer. Thus, it is either a boundary layer or a mixing layer depending upon the boundary conditions. The extension of this analysis to axi-symmetric or three - dimensional flow becomes questionable.

The approach used in Refs. (40) and (41) is a positive step over the eddy viscosity model but cannot predict turbulence quantities. A comprehensive theoretical model is proposed by Raj (42), which requires experimental input.

It is clear from the above survey of literature that there is very little theoretical or experimental information available about the wake-boundary layer interaction.

CHAPTER III

ANALYSIS OF THE EFFECT OF FREE STREAM TURBULENCE ON WAKES

The main objective of the study of free stream turbulence on wakes was to incorporate the effect of free stream turbulence on the wake developed from the trailing edge of a flat plate. As indicated in Chapter (II), the understanding of the free stream turbulence effect on wake may be helpful in the understanding of the wake-boundary layer interaction phenomena because the former is a case of interaction of weak mean shear to strong mean shear, while the latter is a case of interaction of two strong mean shear flows.

The wake of a body is well described by length scale (L_0), wake center line velocity defect (U_0) and shape of the profile (Reference 43). Thus, the incorporation of the effect of free stream turbulence on length scale, wake center line velocity and shape of the profile leads to the description of the free stream turbulence effect of the characteristics of a turbulent wake.

3.1 Scaling Considerations and Similarity Analysis:

3.1.1 Governing Equations:

The governing differential equations in Cartesian and stationary frame of reference for two dimensional, turbulent and incompressible flow after applying boundary layer approximations and neglecting normal stress terms can be written as:

$$\bar{U}\frac{\partial \bar{U}}{\partial x} + \bar{V}\frac{\partial \bar{U}}{\partial y} + \frac{\partial(\overline{uv})}{\partial y} = \bar{U}_e\frac{\partial \bar{U}_e}{\partial x} \qquad \ldots(3.1)$$

$$\frac{\partial \bar{U}}{\partial x} + \frac{\partial \bar{V}}{\partial y} = 0 \qquad \ldots(3.2)$$

Experimental results described later confirm that a self-similarity in the wake mean velocity profile is maintained even in the presence of free stream turbulence. Therefore, it is expected that the presence of free stream turbulence will affect only the velocity (U_0) and length (L_0) scales. If multiples of Φ_1, with U_0 and Φ_2 with L_0 represent the effect of free stream turbulence on the local

velocity and length scales, then Φ_1 will reduce the velocity scale , while Φ_2 will increase the length scale with increase in free stream turbulence level. Note that an increase in velocity scale in a boundary layer due to free stream turbulence (flattening of velocity profile) is equivalent to decrease in wake velocity scale (wake velocity defect at the wake center line).

Considering the foregoing observations and applying arguments similar to the one given in Tennekes and Lumley (2), it is not difficult to see that in the presence of free stream turbulence the wake velocity profile can be expressed as follows:

$$\frac{\bar{U}_e - \bar{U}}{U_0 \Phi_1} = f\left(\frac{y}{L_0 \Phi_2}\right) \qquad \ldots(3.3)$$

where

$\bar{U}_e$ is the wake edge velocity, $\bar{U}$ is the velocity in the wake, U_0 and L_0 are velocity and length scales , respectively, and Φ_1 and Φ_2 are turbulence parameters affecting velocity and length scales, respectively. The form of the parameters Φ_1 and Φ_2 will be determined from the analysis described in Section 3.2.

3.2 Mean Quantities:

3.2.1 Wake Center line Velocity and Length Scale:

Replace $\overline{uv}$ in Eqn. (3.1) with the eddy viscosity model

$$-\overline{u\,v} = \nu_T \frac{\partial \bar{U}}{\partial y} \qquad \ldots(3.4)$$

Substituting Eqns.(3.3) and (3.4) in Eqn. (3.1) and eliminating $\overline{V}$ in the resulting equation by the use of continuity Eqn. (3.2), the following equation can be obtained:

$$\frac{L_0 \Phi_2}{U_0 \Phi_1}\left[\frac{d}{dx}(U_0 \Phi_1)\right] f^2$$

$$- \frac{L_0 \Phi_2}{U_0^2 \Phi_1^2}\left[\frac{d}{dx}(\bar{U}_e U_0 \Phi_1)\right] f$$

$$+ \frac{1}{U_0 \Phi_1}\left[\frac{d}{dx}(\bar{U}_e L_0 \Phi_2)\right] \eta f'$$

$$- \left[\frac{d}{dx}(L_0 \Phi_2)\right] \eta_f f'$$

$$- \frac{1}{U_0 \Phi_1}\left[\frac{d}{dx}(U_0 L_0 \Phi_1 \Phi_2)\right] f' \int f \, d\eta$$

$$+ \left[\frac{\nu_T}{U_0 L_0 \Phi_1 \Phi_2}\right] f'' = 0 \qquad \ldots(3.5)$$

The condition of self-similarity in mean velocity profile is satisfied, only if coefficients of f, f^2, $\eta f'$, $\eta f f'$, $f' \int f \, d\eta$ and f'' are constant. This condition provides a set of equations such that

$$\frac{L_0 \Phi_2}{U_0 \Phi_1} \frac{d}{dx}(U_0 \Phi_1), \qquad \frac{L_0 \Phi_2}{U_0^2 \Phi_1^2} \frac{d}{dx}(\bar{U}_e U_0 \Phi_1),$$

$$\frac{d}{dx}(L_0 \Phi_2) \quad \text{and} \quad \frac{1}{U_0 \Phi_1} \frac{d}{dx}(\bar{U}_e L_0 \Phi_2)$$

are constants and

$$U_0 L_0 \Phi_1 \Phi_2 \propto \nu_T \qquad \ldots(3.6)$$

The similarity condition on the momentum integral of Eqn. (3.1) provides that $U_0 L_0 \Phi_1 \Phi_2$ is identically constant for the non-pressure gradient and is nearly true for the case of pressure gradient (Reference 1).

$$\text{Let,} \qquad U_0 L_0 \Phi_1 \Phi_2 = K_1 \qquad \ldots(3.7)$$

and consider the case when $x/c \simeq 0.1$. The first and third terms in correlations (3.6) become small compared to the other terms because wake center line velocity recovers to about 60 %. Hence similarity is attained if

$$\frac{L_0 \Phi_2}{U_0^2 \Phi_1^2} \frac{d}{dx}(\bar{U}_e U_0 \Phi_1) = K_2 \qquad \ldots(3.8a)$$

and

$$\frac{1}{U_0\ \delta_1}\ \frac{d}{dx}(\ \bar{U}_e\ L_0\ \theta_2\ )\ =\ K_3 \qquad \ldots(3.8b)$$

where K_2 and K_3 are constants.

Substituting Eqn.(3.7) in Eqns.(3.8a) and (3.8b), we get

$$\frac{1}{U_0^3\ \delta_1^3}\ \frac{d}{dx}(\ \bar{U}_e\ U_0\ \theta_2\ )\ =\ \frac{K_2}{K_1}\ =\ K_4 \qquad \ldots(3.9)$$

and

$$\frac{1}{U_0^2\ \delta_1^2}\ \frac{d}{dx}\left[\frac{\bar{U}_e}{U_0\ \delta_1}\right]\ =\ \frac{K_3}{K_1}\ =\ K_5 \qquad \ldots(3.10)$$

where K_4 and K_5 are constants.

Adding Eqn.(3.9) and Eqn.(3.10), we get

$$\frac{1}{U_0^2\ \delta_1^2}\ \frac{d\ \bar{U}_e}{d\ x}\ =\ \frac{K_4\ +\ K_5}{2}\ =\ K_6 \qquad \ldots(3.11)$$

Let $\bar{U}_e\ =\ K_7\ x^{-\ m}$, a type of functional choice dictated by the similarity considerations, Ref.(44), then from Eqn.(3.11), we get

$$U_0\ \delta_1\ =\ K_8\ x^{-(m+1)/2} \qquad \ldots(3.12)$$

and

$$L_0\ \theta_2\ =\ K_9\ x^{(m+1)/2}$$

where K_8 and K_9 are constants.

However δ_1 and θ_2 are not constant and are functions of

x and T, where T is the free stream turbulence. Since the right hand side of Eqn.(3.12) is a monotonic function, and from earlier investigations of two dimensional wakes, (1,2,44) U_0 is also monotonic. Thus, it is expected that Φ_1 will also be monotonic in character. Therefore, an appropriate choice of Φ_1 is given by the following correlation:

$$\Phi_1 \sim x^n$$

where

$$n \sim F_1(T,x) \sim G_1(T)$$

if T is a weakly dependent function of x. For values of $T < 1$, a Taylor series expansion of G_1 in T suggests that

$$G_1(T) = T$$

Therefore

$$n \sim T$$

For convenience taking the constant of proportionality as $\alpha/2$, we can easily rewrite the correlation for Φ_1 as follows:

$$\Phi_1 \sim x^{\alpha T/2} \qquad \ldots(3.13)$$

If Φ_1 is known, apparently the behavior of Φ_2 will be the inverse of Φ_1 and will be of the form,

$$\Phi_2 \sim x^{-\beta T/2} \qquad \ldots(3.14)$$

Using Eqns(3.13) and (3.14), Eqn.(3.12) can be rewritten as follows:

$$U_0 \sim x^{-(m + 1 + \alpha T)/2} \qquad \ldots(3.15)$$

and

$$L_0 \sim x^{(m+1+\beta T)/2} \qquad \ldots(3.16)$$

The coefficient of proportionality in Eqn.(3.13) and (3.14) can be obtained from the following boundary conditions:

when $T = 0$, Φ_1 and $\Phi_2 = 1$

Therefore, the constants of proportionality in Eqns.(3.13) and (3.14) are unity. Since the chord length of the plate ' c ' has been taken as the non-dimensional length (this is a usual practice in the area of turbomachinery) and wake origin is assumed from distance x_0/c ahead of the trailing edge, Eqns.(3.13) and (3.14) can be rewritten as follows:

$$\Phi_1 = \left(\frac{x}{c} + \frac{x_0}{c}\right)^{\alpha T/2}$$

and

$$\Phi_2 = \left(\frac{x}{c} + \frac{x_0}{c}\right)^{-\beta T/2} \qquad \ldots(3.17)$$

Equating momentum loss through coefficient of drag, it can be shown that the constant of proportionality in Eqn.(3.15) is a function (to a first order) of the coefficient of drag, ($c_d^{\frac{1}{2}}$) of the flat plate in free stream turbulence.

Therefore, the decay of the wake defect in the presence of free stream turbulence and pressure gradient in a general form may be expressed as follows:

$$1 - \frac{\bar{U}_c}{\bar{U}_e} = \frac{\bar{K} \; c_d^{\frac{1}{2}}}{\left(\frac{x}{c} + \frac{x_0}{c}\right)^{(1 + \alpha T - m)/2}} \qquad \ldots(3.18)$$

where c_d is the coefficient of drag with free stream turbulence (Eqn.6.3).

It can be shown from dimensional arguments that $\bar{K}$ in Eqn.(3.18) is a constant depending upon the turbulence parameter Φ_2 at the trailing edge of the flat plate and is of the form of

$$\bar{K} = \frac{K_{10}}{a + b \, \Phi_{2t}} \qquad \ldots(3.19)$$

The values of K_{10}, a and b were found to be 2.7, 0.76 and 1.0, respectively, from the experimental data (Chapter VI). For non-free stream turbulence case and for thick trailing edge, the value of $\bar{K}$ was found to be 1.25 (Reference 1). $\bar{K}$, x_0/c and α for the present case from the experimental data presented in Chpater(VI), were also found to be 1.534, 0.021 and 4.0, respectively.

Similarly, the growth of the length scale can be represented by the following correlation:

$$\frac{L_0 - L_{0t}}{c} = K_{11} \, c_d^{\frac{1}{2}} \left(\frac{x}{c}\right)^{(1 + \beta T + m)/2} \qquad \ldots(3.20)$$

where L_{0t} is the length scale at the trailing edge.

K_{11} and β for the present investigation were found to be 1.05 and 8.27, respectively.

It is clear from Eqns.(3.18) and (3.20), that when m is very small ($m \simeq 0$) and the free stream turbulence level is low ($T \simeq 0$), these equations correspond to the case of a flat plate and cylinder wake when placed in a uniform stream.

3.2.2 Shape of the Profile: Substituting Eqn.(3.8) in Eqn.(3.5) and neglecting the small terms, Eqn.(3.5) can be written as:

$$- K_2 \quad f + \quad K_3 \eta \, f' + \nu_T / K_1 \quad f'' = 0$$

or

$$f'' + \frac{K_1 \, K_3}{\nu_T} \eta \, f' - \frac{K_1 \, K_2}{\nu_T} f = 0 \quad \ldots(3.21)$$

Substituting the value of $\bar{U}_e$ and using Eqn.(3.12) in Eqn.(3.8), it can be shown that,

$$K_2 = - \frac{K_9 \; K_7}{K_8} \left(\frac{3 \, m + 1}{2} \right)$$

and

$$K_3 = \frac{K_7 \; K_9}{K_8} \left(\frac{- m + 1}{2} \right) \quad \ldots(3.22)$$

For $m = 0$, Eqn.(3.22) becomes,

$$- K_2 = K_3 = \frac{K_7 \; K_9}{2 \; K_8}$$

Therefore, Eqn.(3.21) becomes:

$$f'' + \frac{K_1 K_3 \eta}{\nu_T} f' + \frac{K_1 K_3}{\nu_T} f = 0$$

or
$$f'' + K_{12} (\eta f' + f) = 0 \quad \ldots(3.23)$$

where
$$K_{12} = \frac{K_1 K_3}{\nu_T} = R_T K_3 \quad \ldots(3.24)$$

and
$$R_T = U_0 L_0 \Phi_1 \Phi_2 / \nu_T \quad \ldots(3.25)$$

It is observed from the experimental data given in Chapter (VI) , that

$$K_3 R_T \sim 1 \quad \ldots(3.26)$$

The solution of the Eqn.(3.23) can be written as:

$$f = \exp(- K_3 R_T \eta^2 /2) \quad \ldots(3.27)$$

Thus, the shape of the velocity profile is given by a Gaussian function.

3.3 Turbulence Quantities:

The turbulence quantities are implicit functions of mean velocity, mean velocity gradients, shape of the velocity profile, length scale etc. Thus, similarly to the mean quantities, the behavior of the turbulence

quantities is also dependent upon the free stream turbulence level, drag coefficient, axial distance from the trailing edge of the wake producing body, turbulence parameters, turbulent Reynolds number and anisotropy of the flow.

A self-preserving solution to the plane wake problem is well described in the literature, see, for example, Ref.(2). It is shown in the self-preserving wake solution that the turbulence velocity scale (q_0) is proportional to the mean velocity scale (U_0) of the wake flow, i.e.,

$$q_0 \quad \alpha \quad U_0 \qquad \ldots(3.28)$$

and the constant of proportionality is of the order of 0.35. The actual wake is believed to satisfy the self-preservation solution in the far wake region where the wake evolves independent of the geometry of the body generating the wake. The presence of free stream turbulence is not expected to change the above situation, although it can be shown that the constant of proportionality in the above correlation will vary depending upon the free stream turbulence level. The presence of free stream turbulence also changes the mean velocity of the wake flow (U_0).

Substituting Eqn.(3.18) and (3.27) in Eqn.(3.4) and rearranging, Eqn.(3.4) can be rewritten as follows:

$$\frac{\overline{uv}}{U_e^2} = \left(\Phi_1^2 \; R_T^{-1} \eta f \right) \left[\bar{K} \, c_d^{1/2} \left(x/c + x_0/c \right)^{-(1+\alpha_T)/2} \right]^2 \qquad \ldots(3.29)$$

Since the decay of Reynolds stress is monotonic, it is expected that turbulence intensities also follow a similar trend, because Reynolds stress is responsible for turbulence production.

The average value of the correlation coefficient,

$$R_{ij} = \frac{\overline{u\,v}}{(\overline{u^2})^{\frac{1}{2}}\,(\overline{v^2})^{\frac{1}{2}}} \qquad \ldots(3.30)$$

for peak values ($\gamma \sim 1$) in the presence of free stream turbulence obtained from the experimental data is 0.44. For a weak anisotropy,

$$\overline{u^2} \sim \overline{v^2} \sim \overline{q_0^2}$$

Therefore, Eqn.(3.29) can be written as,

$$q_0 \sim (\Phi_1^2\, R_T^{-1}\, \gamma\, f/0.44)^{\frac{1}{2}}\, \bar{K}\, c_d^{\frac{1}{2}}\, (x/c + x_0/c)^{-(1+\alpha_T)/2}$$

or

$$q_0 \sim (\Phi_1^2\, R_T^{-1}\, \gamma\, f/0.44)^{\frac{1}{2}}\, U_0 \qquad \ldots(3.31)$$

In the foregoing correlation, clearly the proportionality factor is dependent upon the free stream turbulence since it is a function of Φ_1 , where

$$\Phi_1 = (x/c + x_0/c)^{\alpha_T/2}$$

Moreover, the correlation Eqn.(3.31) is valid for

values of $\eta \sim 1$, since for $\eta = 0$, $q_0 = 0$ which is contrary to the experimental evidence. On the other hand for $\eta \sim 1$, $f \sim 0.6$ achieves a maximum value. Therefore, the factors on the right hand side must be evaluated corresponding to their maximum values,

$$q_{0max} \sim \Phi_{1max} \left[R_T^{-1} \quad 1.38 \right]^{\frac{1}{2}} U_0 \qquad \ldots(3.32)$$

However, Φ_1 takes its maximum value only in the far wake region, $x/c > 0.4$, where it becomes independent of T. On the other hand,

$$\Phi_{1max}(T, \infty) \sim \frac{1}{\Phi_{2max}(T, \infty)} \sim \Phi_{2max}(T, 0) \qquad \ldots(3.33)$$

But Φ_{2max} takes its maximum value only at the trailing edge (Fig. 6.6). Since, we are interested in regions not too far from the trailing edge, an appropriate scaling for Φ_{1max} is Φ_{2max} in the present case. Keeping this in mind, $q_{0\,max}$ becomes

$$q_{0\,max} \sim \Phi_{2max} (1.38/R_T)^{\frac{1}{2}} U_0 \qquad \ldots(3.34)$$

The form of the correlation Eqns.(3.29) and (3.31) and the subsequent discussion suggest that the decay of the maximum components of turbulence intensity and Reynolds stress will be monotonic in x. Taking into account the

effect of anisotropy, the semi-empirical correlations describing this behavior may be written as follows:

$$T_{u\ max} \simeq c_1' \bar{K} c_d^{\frac{1}{2}} (x/c + x_0'/c)^{-\bar{n}_1 (1 + \alpha T)} \quad \ldots(3.35)$$

$$T_{v\ max} \simeq c_2' \bar{K} c_d^{\frac{1}{2}} (x/c + x_0'/c)^{-\bar{n}_2 (1 + \alpha T)} \quad \ldots(3.36)$$

$$T_{uv\ max} \simeq c_3' \left[\bar{K} c_d^{\frac{1}{2}} (x/c + x_0'/c)^{-\bar{n}_3 (1 + \alpha T)} \right]^2 \quad \ldots(3.37)$$

where

$$c_1'/\Phi_{2t} \sim \bar{c}_1 = (1.38/R_T)^{\frac{1}{2}} (\bar{n}_1/\bar{n}_2)_t \quad \ldots(3.38)$$

$$c_2'/\Phi_{2t} \sim \bar{c}_2 = (1.38/R_T)^{\frac{1}{2}} \quad \ldots(3.39)$$

$$c_3'/\Phi_{2t}^2 \sim \bar{c}_3 = 0.60 / R_T \quad \ldots(3.40)$$

and x_0'/c is the virtual origin. In the derivation of Eqn.(3.35) $\overline{u^2} = \overline{v^2}$ was considered, which is true only for isotropic turbulence. Thus, to account for anisotropy of the flow field investigated, the constant in Eqn.(3.35) will depend upon the trailing edge anisotropy, $(\bar{n}_1/\bar{n}_2)_t$, while in Eqns.(3.36) and (3.37), this factor cancels out.

The value of power index, $\bar{n}_1$, depends upon the level of anisotropy in the wake. For isotropic turbulence, $\bar{n}_1 = \bar{n}_2 = \bar{n}_3 = \frac{1}{2}$. Here, the value of power index $\bar{n}_1$ and

$\bar{n}_2$ was determined from the experimental data (Chapter VI). It is interesting to note that due to the monotonic nature of the turbulence parameter,

$$\Phi_{2t} = (x_0 /c)^{-\beta T/2}$$

it can be mathematically expressed as

$$\Phi_{2t} = 1 + \bar{\gamma} T + (\text{terms of lower order })$$

It has been a common practice in boundary layer study to incorporate the effect of free stream turbulence on skin friction by a parameter similar to the one, defined above (Reference 22). For the present investigations $\bar{\gamma}$ was found to be 12.4.

The experimental and scaling values of the constants given in Eqns.(3.35), (3.36) and (3.37) are compared in Table III.

The theoretical values are based on the values of $R_T = 20$, observed in Ref.(34). The value of virtual origin (x_0'/c) was found to be 0.45. Once C_1', C_2' and C_3' are determined, $T_{u\ max}$, $T_{v\ max}$ and $T_{uv\ max}$ can be determined.

TABLE III

COMPARISON OF THE CONSTANTS OBTAINED FROM THE EXPERIMENTAL DATA AND SCALING CONSIDERATIONS:

Constant	Value of Constants obtained from	
	Experimental Data	Scaling Considerations
$\bar{c}_1$	0.340	0.42
$\bar{c}_2$	0.210	0.26
$\bar{c}_3$	0.025	0.030
$\bar{n}_1$	0.320	$0.50\ (\frac{\bar{n}_2}{\bar{n}_1})_t$
$\bar{n}_2$	0.200	$0.50\ (\frac{\bar{n}_2}{\bar{n}_1})_t$
$\bar{n}_3$	0.310	$0.50\ (\frac{\bar{n}_2}{\bar{n}_1})_t$

CHAPTER IV

ANALYSIS OF WAKE - BOUNDARY LAYER INTERACTION

The main consideration in the development of theoretical approach is to understand and establish the general trends in wake - boundary layer interaction. The analysis also provides grouping of a number of variables which reduces the number of unknowns and also reduces the partial differential nature of the governing equations. The approach presented is an extension of work presented in Ref. (34).

4.1 Scaling Considerations and Similarity Analysis:

4.1.1 Governing Equations:

The governing differential equations in Cartesian and stationary frame of reference for three dimensional, turbulent and incompressible flow can be written as follows:

Momentum Equations:

$$\bar{U}\frac{\partial \bar{U}}{\partial x} + \bar{V}\frac{\partial \bar{U}}{\partial y} + \bar{W}\frac{\partial \bar{U}}{\partial z} + \frac{\partial}{\partial x}(\overline{u^2}) + \frac{\partial}{\partial y}(\overline{uv}) + \frac{\partial}{\partial z}(\overline{uw})$$

$$= -\frac{1}{\rho}\frac{\partial \bar{p}}{\partial x} + \nu\left(\frac{\partial^2 \bar{U}}{\partial x^2} + \frac{\partial^2 \bar{U}}{\partial y^2} + \frac{\partial^2 \bar{U}}{\partial z^2}\right) \quad \ldots(4.1a)$$

$$\bar{U}\frac{\partial \bar{V}}{\partial x} + \bar{V}\frac{\partial \bar{V}}{\partial y} + \bar{W}\frac{\partial \bar{V}}{\partial z} + \frac{\partial}{\partial x}(\overline{uv}) + \frac{\partial}{\partial y}(\overline{v^2}) + \frac{\partial}{\partial z}(\overline{wv})$$

$$= -\frac{1}{\rho}\frac{\partial \bar{p}}{\partial y} + \nu\left(\frac{\partial^2 \bar{V}}{\partial x^2} + \frac{\partial^2 \bar{V}}{\partial y^2} + \frac{\partial^2 \bar{V}}{\partial z^2}\right) \quad \ldots(4.1b)$$

$$\bar{U}\frac{\partial \bar{W}}{\partial x} + \bar{V}\frac{\partial \bar{W}}{\partial y} + \bar{W}\frac{\partial \bar{W}}{\partial z} + \frac{\partial}{\partial x}(\overline{uw}) + \frac{\partial}{\partial y}(\overline{vw}) + \frac{\partial}{\partial z}(\overline{w^2})$$

$$= -\frac{1}{\rho}\frac{\partial \bar{p}}{\partial z} + \nu\left(\frac{\partial^2 \bar{W}}{\partial x^2} + \frac{\partial^2 \bar{W}}{\partial y^2} + \frac{\partial^2 \bar{W}}{\partial z^2}\right) \qquad \ldots(4.1c)$$

Continuity Equation:

$$\frac{\partial \bar{U}}{\partial x} + \frac{\partial \bar{V}}{\partial y} + \frac{\partial \bar{W}}{\partial z} = 0 \qquad \ldots(4.2a)$$

$$\frac{\partial u}{\partial x} + \frac{\partial v}{\partial y} + \frac{\partial w}{\partial z} = 0 \qquad \ldots(4.2b)$$

Applying the following assumptions for the wake boundary layer interacting flow (Fig. 4.1) to the foregoing equations:

1. The boundary layer thickness and the wake width are of the same order of magnitude but both are small compared to the chord length.

2. Due to the choice of the coordinate system (Fig. 4.1), mean velocities in the normal and lateral directions are of the same order of magnitude and are very small compared to the velocity in the axial direction.

3. A high Reynolds number approximation is used, i.e. the viscous stress terms are neglected compared to the turbulent stress terms. The case considered is not too close to the wall.

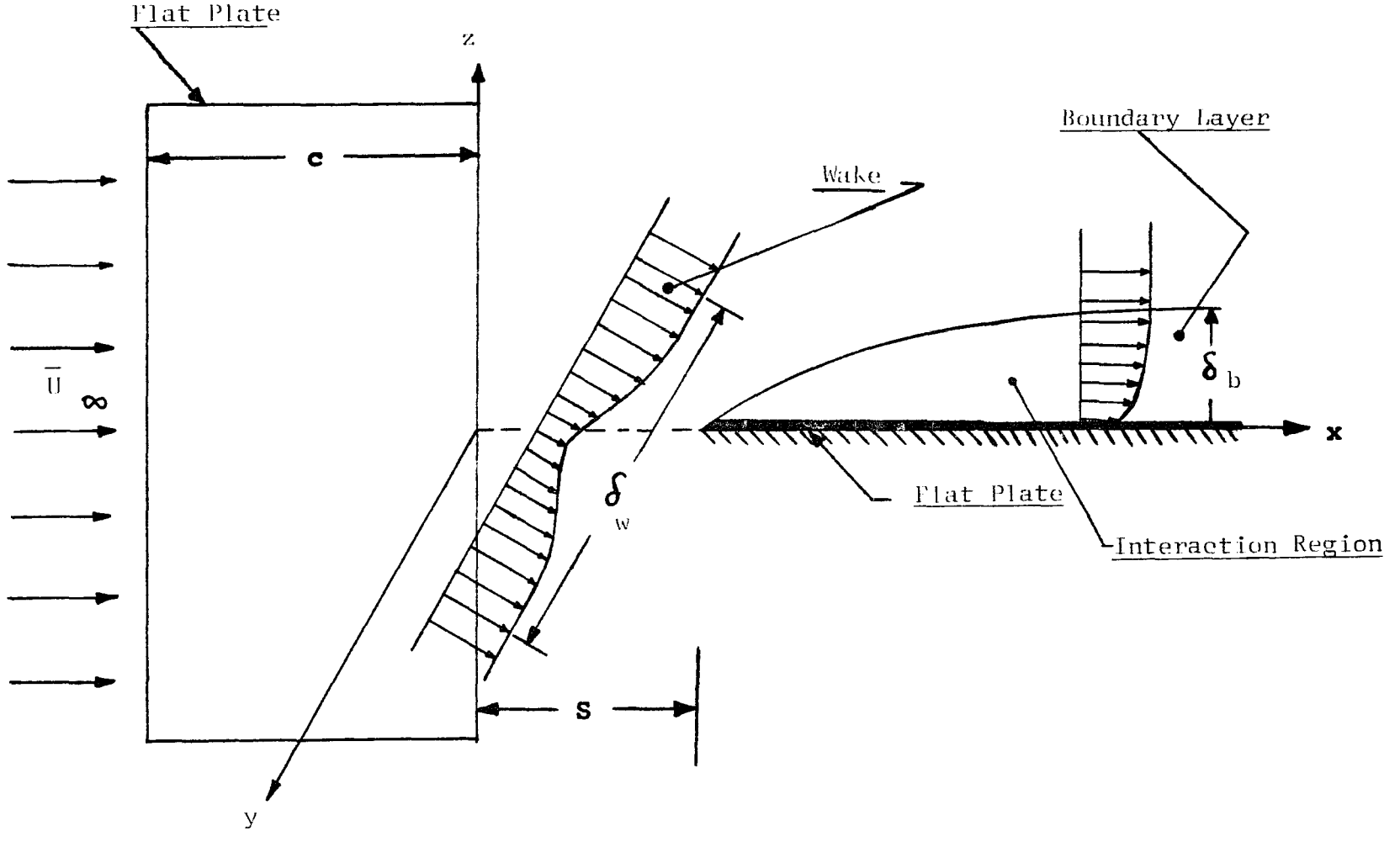

Figure 4.1 Interaction of Flat Plate Wake and Boundary Layer

4. There is no external pressure gradient in the normal, lateral and axial directions outside the wake.

5. All turbulence intensities are treated as the same order of magnitude, i.e.,

$$\overline{u^2} \sim \overline{v^2} \sim \overline{w^2}$$

and these are assumed to be nearly constant across the wake center line in the lateral direction and their variation with respect to the normal direction near the wake center line is small in the interacted outer region.

6. A turbulent diffusion model is used for replacing Reynolds stress components in terms of mean velocity gradients, i.e.,

$$\tau_{ij}/\rho = -\overline{u_i u_j} = -\nu_{T_i} \partial \bar{U}_i / \partial x_j$$

(for $i \neq j$)

We obtain,

$$\bar{U} \frac{\partial \bar{U}}{\partial x} + \bar{V} \frac{\partial \bar{U}}{\partial y} + \bar{W} \frac{\partial \bar{U}}{\partial z} - \nu_{T_1} \left(\frac{\partial^2 \bar{U}}{\partial y^2} + \frac{\partial^2 \bar{U}}{\partial z^2} \right) = - \frac{1}{\rho} \frac{\partial \bar{p}}{\partial x} \quad \ldots(4.3a)$$

$$\bar{U} \frac{\partial \bar{V}}{\partial x} + \bar{V} \frac{\partial \bar{V}}{\partial y} + \bar{W} \frac{\partial \bar{V}}{\partial z} - \nu_{T_2} \frac{\partial^2 \bar{V}}{\partial z^2} = 0 \quad \ldots(4.3b)$$

$$\bar{U} \frac{\partial \bar{W}}{\partial x} + \bar{V} \frac{\partial \bar{W}}{\partial y} + \bar{W} \frac{\partial \bar{W}}{\partial z} - \nu_{T_3} \frac{\partial^2 \bar{W}}{\partial y^2} = 0 \quad \ldots(4.3c)$$

$$\frac{\partial \bar{U}}{\partial x} + \frac{\partial \bar{V}}{\partial y} + \frac{\partial \bar{W}}{\partial z} = 0 \qquad \ldots(4.3d)$$

Writing the velocity defects:

$$\bar{U} = \bar{U}_e - U_{d_0}(x)\, f(\eta) - U_{d_1}(x,z)\, \bar{\Phi}_1(x,z)\, f_1(\eta_1)$$

$$\bar{V} = U_{d_2}(x,z)\, \bar{\Phi}_2(x,z)\, f_2(\eta_1) + \tilde{f}(\eta) \qquad \ldots(4.4)$$

$$\bar{W} = U_{d_3}(x,z)\, \bar{\Phi}_3(x,z)\, f_3(\eta_1)$$

where

U_{d_0} is the wake center line velocity defect outside the interaction region, $\tilde{f}$ is normal velocity profile outside the interaction region and U_{d_1}, U_{d_2} and U_{d_3} are the perturbations in velocity defect due to interaction in the x,y and z directions, respectively. $\bar{\Phi}_i$ (i = 1 to 3) and $\bar{\Psi}_i$ (i = 1 to 3) are the velocity and length scale parameters simulating the wake boundary layer interaction.

$$\eta = \frac{y}{L_0} \qquad \ldots(4.5a)$$

$$\eta_1 = \frac{y}{\bar{L}_0\, \bar{\Psi}_i} \qquad \ldots.(4.5b)$$

where $\bar{L}_0$ is the length scale of the wake in the interaction region and is measured in the y direction. Since the wake before interaction is two-dimensional and we are interested in the changes of $\bar{L}_0$ only in the y-direction, the parameters

$$\bar{\Psi}_1 \,, \quad \bar{\Psi}_2 \quad \text{and} \quad \bar{\Psi}_3$$

are equal.

The nature of the interacting parameters, $\bar{\Phi}_i$ and $\bar{\Psi}_i$, will be determined from the semi-empirical considerations and experimental results.

The following boundary conditions dictated the choice of Eqn.(4.4) :

(a) At the wake center line,

(i) $\eta_1 \longrightarrow 0$, $\quad \bar{U} \longrightarrow \bar{U}_c$

(ii) $\eta_1 \longrightarrow 0$, $z \longrightarrow \infty$, $\quad \bar{U}_e - \bar{U} = U_{d_0}$

This condition is also equivalent to the condition for $x \leq S$

(b) At the wake edge,

$$\eta_1 \longrightarrow \infty \quad , \quad \bar{U} \longrightarrow \bar{U}_b(z)$$

where $\bar{U}_b \longrightarrow \bar{U}_e$ for $z \longrightarrow \infty$

The wake and boundary layer thickness without the interaction can be represented as follows:

$$\delta_b = F_2(x)$$

and

$$\delta_w = F_3(x)$$

This indicates that at the start, the wake is two-dimensional. However, after the wake and boundary layer interaction, δ_b and δ_w will be functions of x, y and x, z respectively; because the boundary layer in the

y direction is interacted by the wake velocity defect in the y direction while the wake in the y direction is interacted by the boundary layer in the z direction.

Therefore,

$$\delta_b = F_2(x,y)$$
$$\delta_w = F_3(x,z) \qquad \ldots(4.6)$$

Substituting Eqns.(4.2a, 4.4 and 4.5) in Eqns.(4.3a), (4.3b) and (4.3c) and rearranging; we obtain,

4.1.1.1 $\bar{U}$ - Equation:

$$-\left[\frac{\partial}{\partial x}(\bar{U}_e U_{d_0})\right] f + \left[\frac{\bar{U}_{d_0}}{L_0}\frac{\partial}{\partial x}(\bar{U}_e L_0)\right]\eta f' + \left[U_{d_0}\frac{\partial U_{d_0}}{\partial x}\right] f^2$$

$$-\left[\frac{U_{d_0}^2 L_0'}{L_0}\right]\eta f f' + \left[\nu_{T_1}\frac{U_{d_0}}{L_0^2}\right] f'' + \left[-\bar{U}_e\frac{\partial}{\partial x}(U_{d_1}\bar{\Phi}_1)\right.$$

$$\left. + \nu_{T_1}\frac{\partial^2}{\partial z^2}(U_{d_1}\bar{\Phi}_1)\right] f_1 + \left[\frac{\bar{U}_e U_{d_1}\bar{\Phi}_1}{\bar{L}_0\bar{\Psi}_1}\frac{\partial}{\partial x}(\bar{L}_0\bar{\Psi}_i) + \right.$$

$$\frac{2\nu_{T_1}U_{d_1}\bar{\Phi}_1}{\bar{L}_0^2\bar{\Psi}_i^2}\left\{\frac{\partial}{\partial z}(\bar{L}_0\bar{\Psi}_i)\right\}^2 - \frac{2\nu_{T_1}}{\bar{L}_0\bar{\Psi}_i}\frac{\partial}{\partial z}(U_{d_1}\bar{\Phi}_1)\frac{\partial}{\partial z}(\bar{L}_0\bar{\Psi}_i)$$

$$\left. - \frac{\nu_{T_1}U_{d_1}\bar{\Phi}_1}{\bar{L}_0\bar{\Psi}_i}\frac{\partial^2}{\partial z^2}(\bar{L}_0\bar{\Psi}_i)\right]\eta_1 f_1 + \left[\frac{\partial}{\partial x}(U_{d_1}\bar{\Phi}_1 U_{d_0})\right] f f_1$$

$$-\left[\frac{U_{d_0}U_{d_1}\bar{\Phi}_1}{\bar{L}_0\,\bar{\Psi}_i}\frac{\partial}{\partial x}(\bar{L}_0\,\bar{\Psi}_i)\right]\eta_1\;\; f\,f_1' - \left[\frac{U_{d_1}\,U_{d_0}\,\bar{\Phi}_1\,\bar{L}_0'}{L_0}\right]\eta\; f_1\,f'$$

$$+\left[U_{d_1}\bar{\Phi}_1\;\frac{\partial}{\partial x}(U_{d_1}\bar{\Phi}_1)\right]f_1^{\,2} - \left[\frac{U_{d_1}^2\bar{\Phi}_1^2}{\bar{L}_0\,\bar{\Psi}_i}\;\frac{\partial}{\partial x}(\bar{L}_0\,\bar{\Psi}_i)\right]\eta_1\; f_1\; f_1'$$

$$-\left[\frac{U_{d_0}\bar{L}_0\,\bar{\Psi}_i}{L_0^2}\;\frac{\partial}{\partial x}(U_{d_0}L_0)\right]f'\int f\,d\eta - \left[\frac{U_{d_1}\bar{\Phi}_1}{L_0}\;\frac{\partial}{\partial x}(U_{d_0}L_0)\right]f_1'\int f\,d\eta$$

$$-\left[\frac{U_{d_0}}{L_0}\;\frac{\partial}{\partial x}(U_{d_1}\bar{\Phi}_1\bar{L}_0\,\bar{\Psi}i)\right]\;f'\int f_1\,d\eta_1 - \left[\frac{U_{d_1}\bar{\Phi}_1}{\bar{L}_0\,\bar{\Psi}_i}\;\frac{\partial}{\partial x}(U_{d_1}\bar{\Phi}_1\bar{L}_0\,\bar{\Psi}_i)\right]$$

$$f_1'\int f_1\,d\eta_1 - \left[\frac{U_{d_0}}{L_0}\;\frac{\partial}{\partial z}(U_{d_3}\bar{\Phi}_3\bar{L}_0\bar{\Psi}\,i)\right]\;f'\int f_3\,d\eta_1$$

$$-\left[\frac{U_{d_1}\bar{\Phi}_1}{\bar{L}_0\,\bar{\Psi}_i}\;\frac{\partial}{\partial z}(U_{d_3}\bar{\Phi}_3\bar{L}_0\,\bar{\Psi}_i)\right]f_1\int f_3 d\eta_1 - \left[U_{d_3}\bar{\Phi}_3\;\frac{\partial}{\partial z}(U_{d_1}\bar{\Phi}_1)\right]f_1 f_3$$

$$-\left[\frac{U_{d_3}\bar{\Phi}_3\;U_{d_1}\bar{\Phi}_1}{\bar{L}_0\,\bar{\Psi}_i}\;\frac{\partial}{\partial z}(\bar{L}_0\,\bar{\Psi}_i)\right]\eta_1\; f_1\; f_3 + \left[\frac{\nu_{T_1}\;U_{d_1}\bar{\Phi}_1}{(\bar{L}_0\,\bar{\Psi}_i)^2}\right]f_1''$$

$$-\;\nu_{T_1}\;\frac{U_{d_1}\bar{\Phi}_1}{(\bar{L}_0\,\bar{\Psi}_i)^2}\left[\frac{\partial}{\partial z}(\bar{L}_0\,\bar{\Psi}_i)\right]^2\eta_1^2 \qquad f_1'' = 0 \qquad \ldots(4.7a)$$

4.1.1.2 $\overline{V}$ - Equation:

$$\left[\bar{U}_e\;\frac{\partial}{\partial x}(U_{d_2}\bar{\Phi}_2) \;-\; \nu_{T_2}\frac{\partial^2}{\partial z^2}(U_{d_2}\;\bar{\Phi}_2)\right]f_2 + \left[-\frac{\bar{U}_e\;U_{d_2}\bar{\Phi}_2}{\bar{L}_0\,\bar{\Psi}_i}\;\frac{\partial}{\partial x}(\bar{L}_0\,\bar{\Psi}_i)\right.$$

$$+\frac{2\nu_{T_2}}{\bar{L}_0\,\bar{\psi}_i}\frac{\partial}{\partial z}(U_{d_2}\bar{\Phi}_2)\,\frac{\partial}{\partial z}(\bar{L}_0\,\bar{\psi}_i)\;-\;\frac{\nu_{T_2}U_{d_2}\bar{\Phi}_2}{(\bar{L}_0\,\bar{\psi}_i)^2}\left\{\frac{\partial}{\partial z}(\bar{L}_0\,\bar{\psi}_i)\right\}^2$$

$$+\;\frac{\nu_{T_2}U_{d_2}\bar{\Phi}_2}{\bar{L}_0\,\bar{\psi}_i}\frac{\partial^2}{\partial z^2}(\bar{L}_0\,\bar{\psi}_i)\Bigg]\eta_1\;f_2'-\left[\frac{\bar{U}_e L_0'}{L_0}\right]\eta f'-\left[U_{d_0}\frac{\partial}{\partial x}(U_{d_2}\bar{\Phi}_2)\right]f f_2$$

$$-\left[\frac{U_{d_0}U_{d_2}\bar{\Phi}_2}{\bar{L}_0\,\bar{\psi}_i}\frac{\partial}{\partial x}(\bar{L}_0\,\bar{\psi}_i)\right]\eta_1\,f\,f_2'-\frac{U_{d_0}L_0'}{L_0}\eta f\,\tilde{f}-\left[U_{d_1}\bar{\Phi}_1\frac{\partial}{\partial x}(U_{d_2}\bar{\Phi}_2)\right]f_1 f_2$$

$$+\left[\frac{U_{d_1}\bar{\Phi}_1U_{d_2}\bar{\Phi}_2}{\bar{L}_0\,\bar{\psi}_i}\frac{\partial}{\partial x}(\bar{L}_0\,\bar{\psi}_i)\right]\eta_1 f_1 f_2'+\left[\frac{U_{d_1}\bar{\Phi}_1L_0'}{L_0}\right]\eta f_1\,\tilde{f}$$

$$+\left[\frac{U_{d_2}\bar{\Phi}_2}{L_0}\frac{\partial}{\partial x}(U_{d_0}L_0)\right]f_2'\int f\,d\eta+\left[\frac{U_{d_2}\bar{\Phi}_2}{\bar{L}_0\,\bar{\psi}_i}\frac{\partial}{\partial x}(U_{d_1}\bar{\Phi}_1\bar{L}_0\,\bar{\psi}_i)\right]f_2'\int f_1\,d\eta_1$$

$$+\left[\frac{U_{d_2}\bar{\Phi}_2}{\bar{L}_0\,\bar{\psi}_i}\frac{\partial}{\partial z}(U_{d_3}\bar{\Phi}_3\bar{L}_0\,\bar{\psi}_i)\right]f_2'\int f_3\,d\eta_1+\left[\frac{\bar{L}_0\,\bar{\psi}_i}{L_0^2}\frac{\partial}{\partial x}(U_{d_0}L_0)\right]\tilde{f}'\int f\,d\eta$$

$$+\left[\frac{1}{L_0}\frac{\partial}{\partial x}(U_{d_1}\bar{\Phi}_1\bar{L}_0\,\bar{\psi}_i)\right]\tilde{f}'\int f_1\,d\eta_1+\left[\frac{1}{L_0}\frac{\partial}{\partial z}(U_{d_3}\bar{\Phi}_3\bar{L}_0\,\bar{\psi}_i)\right]\tilde{f}'\int f_3\,d\eta_1$$

$$+\left[U_{d_3}\bar{\Phi}_3\;\frac{\partial}{\partial z}(U_{d_2}\bar{\Phi}_2)\right]f_2f_3-\left[\frac{U_{d_2}\bar{\Phi}_2U_{d_3}\bar{\Phi}_3}{\bar{L}_0\,\bar{\psi}_i}\frac{\partial}{\partial z}(\bar{L}_0\,\bar{\psi}_i)\right]\eta_1 f_2'\,f_3$$

$$-\nu_{T_2}\frac{U_{d_2}\bar{\Phi}_2}{(\bar{L}_0\,\bar{\psi}_i)^2}\left[\frac{\partial}{\partial z}(\bar{L}_0\,\bar{\psi}_i)\right]^2\eta_1^2\;f_2''=0\qquad\ldots(4.7b)$$

4.1.1.3 $\bar{W}$ - Equation:

$$\left[\bar{U}_e \frac{\partial}{\partial x}(U_{d_3}\bar{\Phi}_3)\right] f_3 - \left[\frac{\bar{U}_e U_{d_3}\bar{\Phi}_3}{\bar{L}_0\,\bar{\Psi}_i} \frac{\partial}{\partial x}(\bar{L}_0\,\bar{\Psi}_i)\right]\eta_1 f_3'$$

$$-\left[U_{d_0}\frac{\partial}{\partial x}(U_{d_3}\bar{\Phi}_3)\right] f f_3 - \left[\frac{U_{d_0} U_{d_3}\bar{\Phi}_3}{\bar{L}_0\,\bar{\Psi}_i}\frac{\partial}{\partial x}(\bar{L}_0\,\bar{\Psi}_i)\right]\eta_1 f f_3'$$

$$-\left[U_{d_1}\bar{\Phi}_1 \frac{\partial}{\partial x}(U_{d_3}\bar{\Phi}_3)\right] f_1 f_3 - \left[\frac{U_{d_1}\bar{\Phi}_1 U_{d_3}\bar{\Phi}_3}{\bar{L}_0\,\bar{\Psi}_i}\frac{\partial}{\partial x}(\bar{L}_0\,\bar{\Psi}_i)\right]\eta_1 f_1 f_3'$$

$$+\left[\frac{U_{d_3}\bar{\Phi}_3}{L_0}\frac{\partial}{\partial x}(U_{d_0}L_0)\right] f_3' \int f\, d\eta + \left[\frac{U_{d_3}\bar{\Phi}_3}{\bar{L}_0\,\bar{\Psi}_i}\frac{\partial}{\partial x}(U_{d_1}\bar{\Phi}_1\bar{L}_0\,\bar{\Psi}_i)\right] f_3' \int f_1 d\eta_1$$

$$+\left[\frac{U_{d_3}\bar{\Phi}_3}{\bar{L}_0\,\bar{\Psi}_i}\frac{\partial}{\partial z}(U_{d_3}\bar{\Phi}_3\bar{L}_0\,\bar{\Psi}_i)\right] f_3' \int f_3 d\eta_1$$

$$+\left[U_{d_3}\bar{\Phi}_3 \frac{\partial}{\partial z}(U_{d_3}\bar{\Phi}_3)\right] f_3^2 - \left[\frac{U_{d_3}^2\bar{\Phi}_3^2}{\bar{L}_0\,\bar{\Psi}_i}\frac{\partial}{\partial z}(\bar{L}_0\,\bar{\Psi}_i)\right]\eta_1 f_3 f_3'$$

$$-\nu_{T_3}\left[\frac{U_{d_3}\bar{\Phi}_3}{(\bar{L}_0\,\bar{\Psi}_i)^2}\right] f_3'' = 0 \qquad \ldots(4.7c)$$

If the wake velocity defect outside the interaction region is small, $U_{d_0} < \bar{U}_e$, then $U_{d_0}^2 \ll \bar{U}_e^2$. Also U_{d_1}, U_{d_2} and U_{d_3} are perturbations to U_{d_0} due to the interaction effect. Therefore, these are not expected to be greater than U_{d_0}. Hence $U_{d_0} U_{d_1}$, $U_{d_0} U_{d_2}$, $U_{d_0} U_{d_3}$, $U_{d_1} U_{d_2}$ ... etc. will be smaller compared to $\bar{U}_e^2$. (This is also evident from the experimental data presented in Chapter VII). In addition, the terms associated with f and $\tilde{f}$ provide a solution of the non-interacted (2-dimensional) wake. This solution for $U_{d_0} < \bar{U}_e$ is given in Ref.(34) and hence terms representing non-interacted wake have already been taken care of. Using the foregoing considerations, Eqns.(4.7a, b and c) are simplified to:

$$\left[-\bar{U}_e \frac{\partial}{\partial x}(U_{d_1}\bar{\Phi}_1) + \nu_{T_1} \frac{\partial^2}{\partial z^2}(U_{d_1}\bar{\Phi}_1) \right] f_1 + \left[\frac{\bar{U}_e U_{d_1} \bar{\Phi}_1}{\bar{L}_0 \bar{\Psi}_i} \frac{\partial}{\partial x}(\bar{L}_0 \bar{\Psi}_i) \right.$$

$$+ \frac{2\nu_{T_1} U_{d_1} \bar{\Phi}_1}{(\bar{L}_0 \bar{\Psi}_i)^2} \left\{ \frac{\partial}{\partial z}(\bar{L}_0 \bar{\Psi}_i) \right\}^2 - \frac{2\nu_{T_1}}{\bar{L}_0 \bar{\Psi}_i} \frac{\partial}{\partial z}(U_{d_1}\bar{\Phi}_1) \frac{\partial}{\partial z}(\bar{L}_0 \bar{\Psi}_i)$$

$$\left. - \frac{\nu_{T_1} U_{d_1} \bar{\Phi}_1}{\bar{L}_0 \bar{\Psi}_i} \frac{\partial^2}{\partial z^2}(\bar{L}_0 \bar{\Psi}_i) \right] \eta_1 f_1 - \left[\frac{\nu_{T_1} U_{d_1} \bar{\Phi}_1}{(\bar{L}_0 \bar{\Psi}_i)^2} \left\{ \frac{\partial}{\partial z}(\bar{L}_0 \bar{\Psi}_i) \right\}^2 \right]$$

$$\eta_1^2 f_1'' = -\left[\nu_{T_1} U_{d_1} \bar{\Phi}_1 / (\bar{L}_0 \bar{\Psi}_i)^2 \right] f_1'' \qquad \ldots(4.8a)$$

$$\left[\bar{U}_e \frac{\partial}{\partial x}(U_{d_2}\bar{\Phi}_2) - \nu_{T_2}\frac{\partial^2}{\partial z^2}(U_{d_2}\bar{\Phi}_2)\right] f_2 +$$

$$\left[\frac{2\nu_{T_2}}{\bar{L}_0\bar{\Psi}_i}\frac{\partial}{\partial z}(U_{d_2}\bar{\Phi}_2)\frac{\partial}{\partial z}(\bar{L}_0\bar{\Psi}_i) - \frac{\bar{U}_e U_{d_2}\bar{\Phi}_2}{\bar{L}_0\bar{\Psi}_i}\frac{\partial}{\partial x}(\bar{L}_0\bar{\Psi}_i)\right.$$

$$\left. - \frac{2\nu_{T_2}U_{d_2}\bar{\Phi}_2}{(\bar{L}_0\bar{\Psi}_i)^2}\left\{\frac{\partial}{\partial z}(\bar{L}_0\bar{\Psi}_i)\right\}^2 + \frac{\nu_{T_2}U_{d_2}\bar{\Phi}_2}{\bar{L}_0\bar{\Psi}_i}\frac{\partial^2}{\partial z^2}(L_0\Psi_i)\right]\eta_1 f_2'$$

$$= \frac{\nu_{T_2}U_{d_2}\bar{\Phi}_2}{(\bar{L}_0\bar{\Psi}_i)^2}\left[\frac{\partial}{\partial z}(\bar{L}_0\bar{\Psi}_i)\right]^2 \eta_1^2 f_2'' \quad \ldots(4.8b)$$

$$\left[\bar{U}_e \frac{\partial}{\partial x}(U_{d_3}\bar{\Phi}_3)\right] f_3 - \left[\frac{\bar{U}_e U_{d_3}\bar{\Phi}_3}{\bar{L}_0\bar{\Psi}_i}\frac{\partial}{\partial x}(\bar{L}_0\bar{\Psi}_i)\right]\eta_1 f_3'$$

$$= \left[\frac{\nu_{T_3}U_{d_3}\bar{\Phi}_3}{(\bar{L}_0\bar{\Psi}_i)^2}\right] f_3'' \quad \ldots(4.8c)$$

Multiply Eqns. (4.8 a, b and c) by $\frac{\bar{L}_0\bar{\Psi}_i}{(U_{d_1}\Phi_1)^2}$, $\frac{\bar{L}_0\bar{\Psi}_i}{(U_{d_2}\bar{\Phi}_2)^2}$ and $\frac{\bar{L}_0\bar{\Psi}_i}{(U_{d_3}\bar{\Phi}_3)^2}$ respectively and obtain the equations in the non-dimensional form:

$$c_1 f_1 + c_2 \eta_1 f_1 = -\nu_{T_1}/c_3 f_1'' + \nu_{T_1} c_4/c_3 \eta_1^2 f_1'' \quad \ldots(4.9a)$$

$$c_5 \quad f_2 + c_6 \eta_1 \quad f_2' = c_4/c_7 \, \nu_{T_2} \eta_1^2 f_2'' \qquad \ldots(4.9b)$$

$$c_8 \quad f_3 - c_9 \eta_1 \quad f_3' = \nu_{T_3}/c_{10} \quad f_3'' \qquad \ldots(4.9c)$$

where

$$\frac{\bar{L}_0 \bar{\psi}_i \bar{U}_e}{(U_{d_1} \bar{\Phi}_1)^2} \left[- \frac{\partial}{\partial x}(U_{d_1} \bar{\Phi}_1) + \frac{\nu_{T_1}}{\bar{U}_e} \frac{\partial^2}{\partial z^2}(U_{d_1} \bar{\Phi}_1) \right] = c_1 \qquad \ldots(4.10)$$

$$\frac{U_e}{U_{d_1} \bar{\Phi}_1} \frac{\partial}{\partial x}(\bar{L}_0 \bar{\psi}_i) + \frac{2 \nu_{T_1}}{U_{d_1} \bar{\Phi}_1 \bar{L}_0 \bar{\psi}_i} \left[\frac{\partial}{\partial z}(\bar{L}_0 \bar{\psi}_i) \right]^2$$

$$- \frac{2 \nu_{T_1}}{(U_{d_1} \bar{\Phi}_1)^2} \frac{\partial}{\partial z}(U_{d_1} \bar{\Phi}_1) \frac{\partial}{\partial z}(\bar{L}_0 \bar{\psi}_i) - \frac{\nu_{T_1}}{U_{d_1} \bar{\Phi}_1} \frac{\partial^2}{\partial z^2}(\bar{L}_0 \bar{\psi}_i)$$

$$= c_2 \qquad \ldots(4.11)$$

$$U_{d_1} \bar{\Phi}_1 \bar{L}_0 \bar{\psi}_i = c_3 \qquad \ldots(4.12)$$

$$\left[\frac{\partial}{\partial z}(\bar{L}_0 \bar{\psi}_i) \right]^2 = c_4 \qquad \ldots(4.13)$$

$$\frac{\bar{L}_0 \bar{\psi}_i \bar{U}_e}{(U_{d_2} \bar{\Phi}_2)^2} \left[\frac{\partial}{\partial x}(U_{d_2} \bar{\Phi}_2) - \frac{\nu_{T_2}}{\bar{U}_e} \frac{\partial^2}{\partial z^2}(U_{d_2} \bar{\Phi}_2) \right]$$

$$= c_5 \qquad \ldots(4.14)$$

$$-\frac{\bar{U}_e}{U_{d_2}\bar{\Phi}_2}\frac{\partial}{\partial x}(\bar{L}_0\bar{\Psi}_i)+\frac{2\,\nu_{T_2}}{U_{d_2}^2\bar{\Phi}_2^2}\frac{\partial}{\partial z}(U_{d_2}\bar{\Phi}_2)\frac{\partial}{\partial z}(\bar{L}_0\bar{\Psi}_i)$$

$$-\frac{2\,\nu_{T_2}}{U_{d_2}\bar{\Phi}_2\,\bar{L}_0\,\bar{\Psi}_i}\left[\frac{\partial}{\partial z}(\bar{L}_0\,\bar{\Psi}_i)\right]^2+\frac{\nu_{T_2}}{U_{d_2}\bar{\Phi}_2}\frac{\partial^2}{\partial z^2}(\bar{L}_0\,\bar{\Psi}_i)$$

$$= c_6 \qquad \ldots(4.15)$$

$$U_{d_2}\,\bar{\Phi}_2\;\bar{L}_0\;\bar{\Psi}_i = c_7 \qquad \ldots(4.16)$$

$$\frac{\bar{U}_e\;\bar{L}_0\,\bar{\Psi}_i}{U_{d_3}^2\,\bar{\Phi}_3^2}\;\frac{\partial}{\partial x}(U_{d_3}\,\bar{\Phi}_3) = c_8 \qquad \ldots(4.17)$$

$$\frac{\bar{U}_e}{U_{d_3}\,\bar{\Phi}_3}\;\frac{\partial}{\partial x}(\bar{L}_0\,\bar{\Psi}_i) = c_9 \qquad \ldots(4.18)$$

$$U_{d_3}\,\bar{\Phi}_3\;\bar{L}_0\;\bar{\Psi}_i = c_{10} \qquad \ldots(4.19)$$

A similarity condition on the momentum integral of Eqns.(4.8 a, b and c) also leads to

$$U_{d_1}\;\bar{\Phi}_1\;\bar{L}_0\,\bar{\Psi}_i = \text{Constant}\;\alpha\;\nu_{T_1} \qquad \ldots(4.20)$$

$$U_{d_2}\;\bar{\Phi}_2\;\bar{L}_0\,\bar{\Psi}_i = \text{Constant}\;\alpha\;\nu_{T_2} \qquad \ldots(4.21)$$

$$U_{d_3}\;\bar{\Phi}_3\;\bar{L}_0\,\bar{\Psi}_i = \text{Constant}\;\alpha\;\nu_{T_3} \qquad \ldots(4.22)$$

and the above constants are proportional to eddy viscosity which may be different in all three directions.

The similarity condition requires that the coefficients of f_1, $\eta_1 f_1$, $\eta_1^2 f_1''$ (Eqn. 4.9a), f_2, $\eta_1 f_2'$, $\eta_1^2 f_2''$ (Eqn. 4.9b) and f_3, $-\eta_1 f_3'$ (Eqn. 4.9c) be independent of y, since the coefficients of f_1'', f_2'' and f_3'' on the right hand side of Eqns. (4.9 a, b and c) are constants due to Eqns. (4.20), (4.21) and (4.22).

Substituting constants c_3 , c_4 in c_2 and c_4, c_7 in c_6, it can be shown that

$$c_2 \propto c_1$$

and

$$c_6 \propto c_5$$

Substituting c_3 in c_8 and c_{10} in c_9 and dividing, it can again be shown that

$$\frac{U_{d_1} \bar{\Phi}_1}{U_{d_3} \bar{\Phi}_3} = \text{Constant} = c_{11} \quad \ldots(4.23)$$

Thus the problem of wake boundary layer interaction given by Eqns. (4.10), (4.14) and (4.23) may provide the solution for the perturbation velocity defects in x, y and z directions, respectively. These solutions are as follows:

4.1.2 Solution For Velocity Defects:

4.1.2.1 $\bar{U}$ - Solution: Substituting Eqn.(4.12) in Eqn.(4.10), we obtain,

$$\bar{U}_e \left[- \frac{\partial}{\partial x}(U_{d_1}\bar{\Phi}_1) + \frac{\nu_{T_1}}{\bar{U}_e} \frac{\partial^2}{\partial z^2}(U_{d_1}\bar{\Phi}_1) \right] = c_1 U_{d_1}^3 \bar{\Phi}_1^3 \quad \ldots(4.24)$$

Eqn.(4.24) is non-linear partial differential equation, the analytical solution of which is difficult if not impossible. So, the following engineering approach is offered. In the interacting region, the perturbation velocity defect ($U_{d_1}/\bar{U}_e$) at the wake center line is of small order. Therefore,

$$\left| \frac{U_{d_1}^3}{\bar{U}_e^3} \right| \ll \left| \frac{U_{d_1}}{\bar{U}_e} \right|$$

Hence for the first approximation, Eqn.(4.24) can be written as:

$$- \frac{\partial}{\partial x}\left(\frac{U_{d_1}\bar{\Phi}_1}{\bar{U}_e} \right) + \frac{\nu_{T_1}}{\bar{U}_e} \frac{\partial^2}{\partial z^2}\left(\frac{U_{d_1}\bar{\Phi}_1}{\bar{U}_e} \right) = 0 \quad \ldots(4.25)$$

Defining a similarity variable,

$$\xi = \frac{z}{2\sqrt{\nu_{T_1} x/\bar{U}_e}} \quad \ldots(4.26)$$

taking

$$\frac{U_{d_1}\bar{\Phi}_1}{\bar{U}_e} = \left(\frac{x}{c}\right)^{-\frac{1}{2}} H(\xi) \quad \ldots(4.27)$$

and substituting Eqns.(4.26 and 4.27) in Eqn.(4.25) and rearranging, we get,

$$\bar{H}'' + 2(\bar{H} + \zeta \bar{H}') = 0 \qquad \ldots(4.28)$$

The solution of Eqn.(4.28) is

$$\bar{H} = \exp(-\zeta^2)$$

Therefore,

$$\frac{U_{d_1}\,\bar{\Phi}_1}{\bar{U}_e} = \left(\frac{x}{c}\right)^{-\frac{1}{2}} e^{-\zeta^2} \qquad \ldots(4.29)$$

Since U_{d_1}, U_{d_2}, U_{d_3} are perturbations over a two-dimensional velocity defect in non-interacted wake, physical reasons suggest that their emergence in the interacted region is due only to the presence of the second flat plate. This condition can be expressed mathematically as follows.

$$x \leqslant S, \qquad U_{d_1}, U_{d_2}, U_{d_3} \longrightarrow 0$$

i.e., if the coordinate system in the solution of U_{d_1}, U_{d_2} and U_{d_3} is chosen from the trailing edge of the first flat plate, the x coordinate has to be represented by $x - S$. Therefore,

$$\frac{U_{d_1}\,\bar{\Phi}_1}{\bar{U}_e} \sim \left(\frac{x-S}{c}\right)^{-\frac{1}{2}} e^{-\zeta^2} \qquad \ldots(4.30)$$

Therefore, it follows from the momentum integral that,

$$\frac{\bar{L}_0 \bar{\Psi}_i}{c} \sim \left(\frac{x - S}{c}\right)^{\frac{1}{2}} e^{\zeta^2} \qquad \ldots(4.31)$$

However, $\bar{\Phi}_1$ and $\bar{\Psi}_1$ are not constants and represent wake boundary layer interaction. Therefore, $\bar{\Phi}_1$ and $\bar{\Psi}_1$ are functions of boundary layer parameters only. Since U_{d_1}, $\bar{L}_0$ are also functions of x and z, the only way Eqn.(4.30) can be satisfied is when both U_{d_1} and $\bar{\Phi}_1$ are of the form given on its right hand side, i.e.,

$$\bar{\Phi}_1 \sim I_{xz}^{\tilde{n}_i}$$

where I_{xz} is of the following form

$$I_{xz} \sim \left(\frac{x - S}{c}\right)^{-\frac{1}{2}} e^{-\zeta^2}$$

and $\tilde{n}_i \sim G_2(R^+, x) \sim G_3(R^+)$, where

$$R^+ = u^+ z/\nu \quad , \quad u^+ = \sqrt{\tau_{max}/\rho}$$

if R^+ does not change much with x. Physical reasoning suggests that the function $G_3(R^+)$ should go to zero when $R^+ \longrightarrow \infty$, i.e., at the outer edge of the boundary layer. A first order expansion of G_3 in R^+ suggests that,

$$\tilde{n}_i \sim \alpha_1/R^+ \quad \text{or} \quad -\alpha_1/R^+$$

where α_1 is the constant obtained from the experimental data. For physical reasons, we will represent $\bar{\Phi}_1$ as follows,

$$\bar{\Phi}_1 \sim \left[\left(\frac{x - S}{c}\right)^{-\frac{1}{2}} e^{-\xi^2} \right]^{\alpha_1/R^+} \qquad \ldots(4.32)$$

If $\bar{\Phi}_1$ is known, the behavior of $\bar{\Psi}_1$ will be the inverse of $\bar{\Phi}_1$ and will be of the form,

$$\bar{\Psi}_1 \sim \left[\left(\frac{x - S}{c}\right)^{-\frac{1}{2}} e^{-\xi^2} \right]^{-\alpha_1/R^+} \qquad \ldots(4.33)$$

Using correlations (4.32) and (4.33), correlations (4.30) and (4.31) can be rewritten as,

$$\frac{U_{d_1}}{\bar{U}_e} = \bar{K}_1 \left[\left(\frac{x - S}{c}\right)^{-\frac{1}{2}} e^{-\xi^2} \right]^{1 - \alpha_1/R^+} \qquad \ldots(4.34)$$

$$\frac{\bar{L}_0}{c} = \bar{K}_4 \left[\left(\frac{x - S}{c} \right)^{\frac{1}{2}} e^{\zeta^2} \right]^{1 - \alpha_1/R^+} \quad \ldots(4.35)$$

The coefficients of proportionality in correlations (4.32) and (4.33) can be obtained from the following boundary conditions, i.e.,

$$\text{When } R^+ \longrightarrow \infty \ , \ \bar{\Phi}_1 = 1, \quad \bar{\Psi}_1 = 1$$

i.e. wake does not interact with the boundary layer.

Therefore, correlations (4.32) and (4.33) can be rewritten as,

$$\bar{\Phi}_1 = \left[\left(\frac{x - S}{c} \right)^{-\frac{1}{2}} e^{-\zeta^2} \right]^{\alpha_{1/R^+}} \quad \ldots(4.36)$$

$$\bar{\Psi}_1 = \left[\left(\frac{x - S}{c} \right)^{-\frac{1}{2}} e^{-\zeta^2} \right]^{-\alpha_{1/R^+}} \quad \ldots(4.37)$$

Similarly the variation of length scale can be represented by:

$$\frac{\bar{L}_0 - \bar{L}_{0t}}{c} = \bar{K}_4 \left[\left(\frac{x - S}{c} \right)^{\frac{1}{2}} e^{\zeta^2} \right]^{1 - \alpha_1/R^+} \quad \ldots(4.38)$$

where $\bar{L}_{0t}$ is the length scale at the leading edge of the flat plate on which boundary layer is developed and is obtained from correlation (3.20).

4.1.2.2 $\bar{V}$ - Solution: Following a similar procedure procedure to the $\bar{U}$ - solution, using Eqns.(4.14) and (4.16), it can be shown that,

$$\frac{U_{d_2}\,\bar{\Phi}_2}{\bar{U}_e} \sim \left(\frac{x - S}{c}\right)^{-\frac{1}{2}} e^{-\eta^2} \qquad \ldots(4.39)$$

Combining correlations (4.39) with the momentum integral, (Eqn. 4.16) and following the same arguments as for $\bar{U}$ - solution, it can be shown that,

$$\frac{U_{d_2}}{\bar{U}_e} = \bar{K}_2 \left[\left(\frac{x - S}{c}\right)^{-\frac{1}{2}} e^{-\eta^2}\right]^{1 - \mathcal{L}_{2/R^+}} \qquad \ldots(4.40)$$

Since the $\bar{L}_0$ representation will remain the same as for $\bar{U}$, it suggests that $\mathcal{L}_1 = \mathcal{L}_2$, and hence $\bar{\Phi}_2$ and $\bar{\Psi}_2$ can be represented as follows,

$$\bar{\Phi}_2 = \left[\left(\frac{x - S}{c}\right)^{-\frac{1}{2}} e^{-\eta^2}\right]^{\mathcal{L}_{2/R^+}}$$

$$\bar{\Psi}_2 = \left[\left(\frac{x - S}{c}\right)^{-\frac{1}{2}} e^{-\eta^2}\right]^{-\mathcal{L}_{2/R^+}} \qquad \ldots(4.42)$$

4.1.2.3 $\bar{W}$ - Solution: The $\bar{W}$ - component solution at the wake center line (U_{d_3}) requires some explanation. Since there was no $\bar{W}$ - component in the wake before the

boundary layer interaction started, it is clear that the appearance of a $\bar{W}$ - component in the wake is due to the wake boundary layer interaction only. This interaction is characterized by the parameters $\bar{\Phi}_1$ or $\bar{\Phi}_2$ and $\bar{\Psi}_1$ and and hence an appropriate choice for U_{d_3} and $\bar{L}_0$ will be

$$U_{d_3} \quad \mathcal{L} \quad F_4(\bar{\Phi}_1)$$

and

$$\bar{L}_0 \quad \mathcal{L} \quad F_5(\bar{\Phi}_1) \qquad \ldots(4.43)$$

The nature of $\bar{\Psi}_1$ and $\bar{L}_0$ has already been established (Eqns. 4.37 and 4.38). This suggests that,

$$\bar{L}_0 \quad \mathcal{L} \quad \frac{1}{\bar{\Psi}_1} \qquad \ldots(4.44)$$

Threfore, to satisfy the momentum integral, Eqn.(4.19) and (4.23),

$$U_{d_3} \quad \mathcal{L} \quad \frac{1}{\bar{\Phi}_1} \quad \mathcal{L} \quad \frac{1}{\bar{\Phi}_3} \quad \mathcal{L} \quad U_{d_1} \qquad \ldots(4.45).$$

This solution is similar to the one reported for a three dimensional wake (References 45, 46).

Therefore,

$$\frac{U_{d_3}}{\bar{U}_e} = K_3 \left[\left(\frac{x - S}{c} \right)^{-\frac{1}{2}} e^{-\eta^2} \right]^{1 - \alpha_1/R^+} \quad \ldots(4.46)$$

$$\bar{\Phi}_3 = \left[\left(\frac{x - S}{c} \right)^{-\frac{1}{2}} e^{-\eta^2} \right]^{\alpha_{1/R^+}} \quad \ldots(4.47)$$

$$\bar{\psi}_3 = \left[\left(\frac{x - S}{c} \right)^{-\frac{1}{2}} e^{-\eta^2} \right]^{-\alpha_{1/R^+}} \quad \ldots(4.48)$$

Thus, the complete solution for the wake velocity defect for $\bar{U}$, $\bar{V}$, $\bar{W}$ components and length scale ($\bar{L}_0$) can be written as :

$$\frac{U_{d_0}}{\bar{U}_e} + \frac{U_{d_1}\bar{\Phi}_1}{\bar{U}_e} = \frac{U_{d_T}}{\bar{U}_e} = \bar{K}\, c_d^{\frac{1}{2}} \left(\frac{x + x_0}{c} \right)^{-\frac{1}{2}} + \bar{K}_1 \left[\left(\frac{x - S}{c} \right)^{-\frac{1}{2}} e^{-\eta^2} \right] \ldots(4.49)$$

$$\frac{U_{d_2}\bar{\Phi}_2}{\bar{U}_e} = \bar{K}_2 \left[\left(\frac{x - S}{c} \right)^{-\frac{1}{2}} e^{-\eta^2} \right] \quad \ldots(4.50)$$

$$\frac{U_{d_3}\bar{\Phi}_3}{\bar{U}_e} = \bar{K}_3 \left[\left(\frac{x - S}{c} \right)^{-\frac{1}{2}} e^{-\eta^2} \right] \quad \ldots(4.51)$$

$$\frac{\bar{L}_0 - \bar{L}_{0t}}{c} = \bar{K}_4 \left[\left(\frac{x - S}{c} \right)^{-\frac{1}{2}} e^{-\eta^2} \right]^{-(1 - \alpha_i/R^+)} \quad \ldots(4.52)$$

CHAPTER V

EXPERIMENTAL EQUIPMENT, METHOD, INSTRUMENTATION AND DATA PROCESSING

The objective of this experimental program is to study the characteristics of a wake due to free stream turbulence and wake boundary layer interaction. The study includes the measurements of mean quantities, turbulence intensity and Reynolds stress at various axial, lateral and normal locations. Energy spectra are also measured in the interacting region. The details on both of the above mentioned experimental programs are described in the following sections:

5.1 Free Stream Turbulence Work:

5.1.1 Equipment Used in the Experiment:

5.1.1.1 Wind Tunnel: The open circuit wind tunnel was used in the experimentation. An electric motor of 20 h.p. with a maximum speed of 1800 r.p.m. is used to drive the fan. A uniform velocity (up to 27 m/sec) of small turbulence ($\sim$ 0.4 %) is obtained at the entrance to the test section. The velocity corresponds

to the mass flow rate of 6.48 Kgm/sec. The cross - section of the test section is 45.72 x 45.72 cm^2.

5.1.1.2 Turbulence Generating Grid: Free stream turbulence was generated with the help of two grids [Fig. 5.1 (a) and (b)] . Grid I consisted of a combination of square bars placed horizontally and vertically and has the dimensions $M/\bar{b}$ = 3.25, $\bar{b}$ = 1.27 cm., where M is the spacing between two consecutive square bars and $\bar{b}$ is the dimension of each bar having square cross-section. This grid produced a free stream turbulence level of 5.23 % at the leading edge of the flat plate. Grid II, constructed of maple, has the dimensions M/d = 6.57, d = 1.11 cm., where d is the diameter of each grid cylinder. This grid produced a free stream turbulence level of 7.23 % at the leading edge of the flat plate. The horizontal distance between the grid and the leading edge of the flat plate was 27.3 cms. The main criterion for the selection of the grids was to produce two different free stream turbulence levels at the leading edge of the flat plate.

5.1.1.3 Traversing Mechanism: The traversing mechanism, holding the probe and resting on the circular rails, was capable of varying the location of the probe in the axial, lateral and transverse directions. Clamps were used to hold the mechanism firmly on the rails to damp vibrations. The probe could be traversed in the radial as

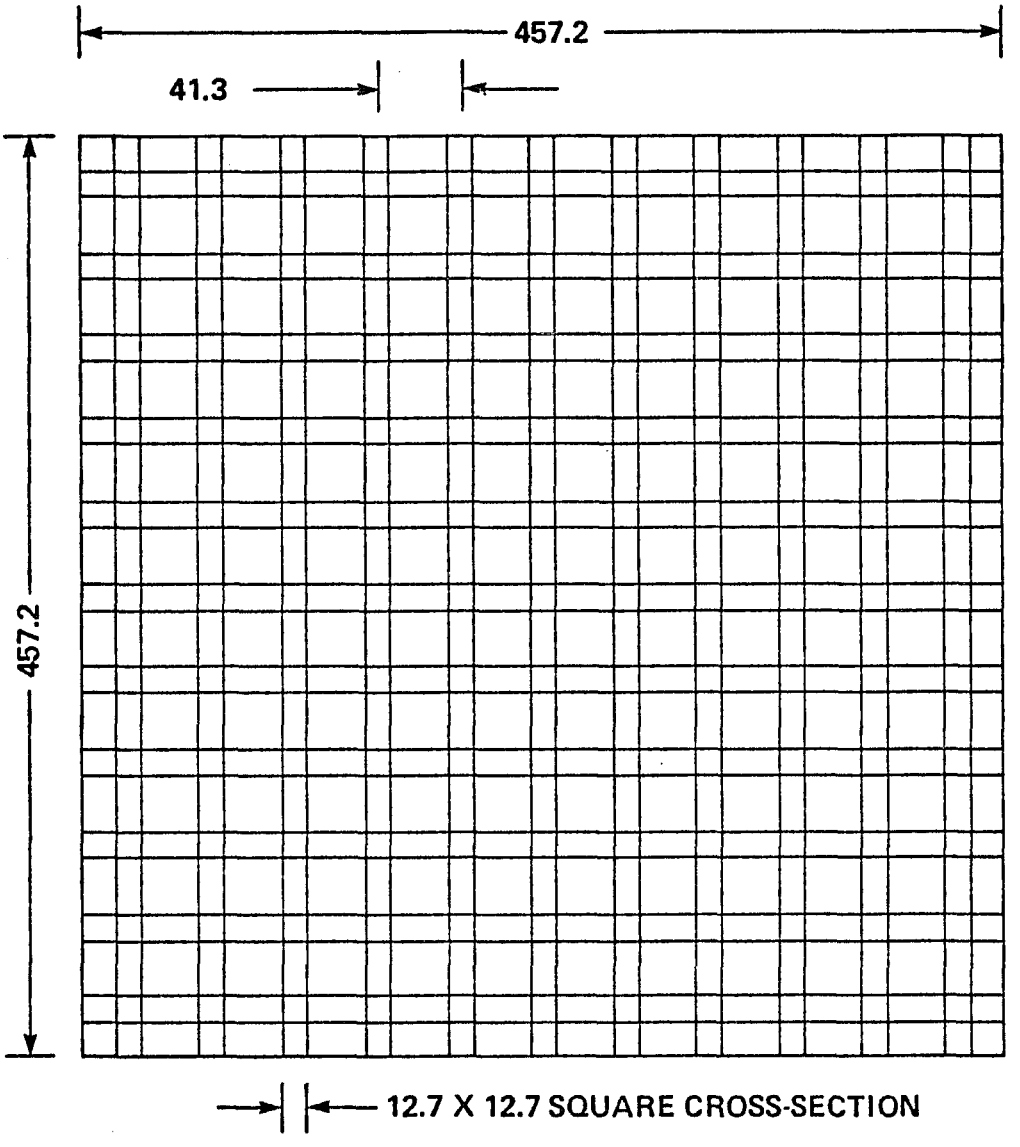

Figure 5.1(a) Schematic of the Square Bars Grid Used to Generate Turbulence

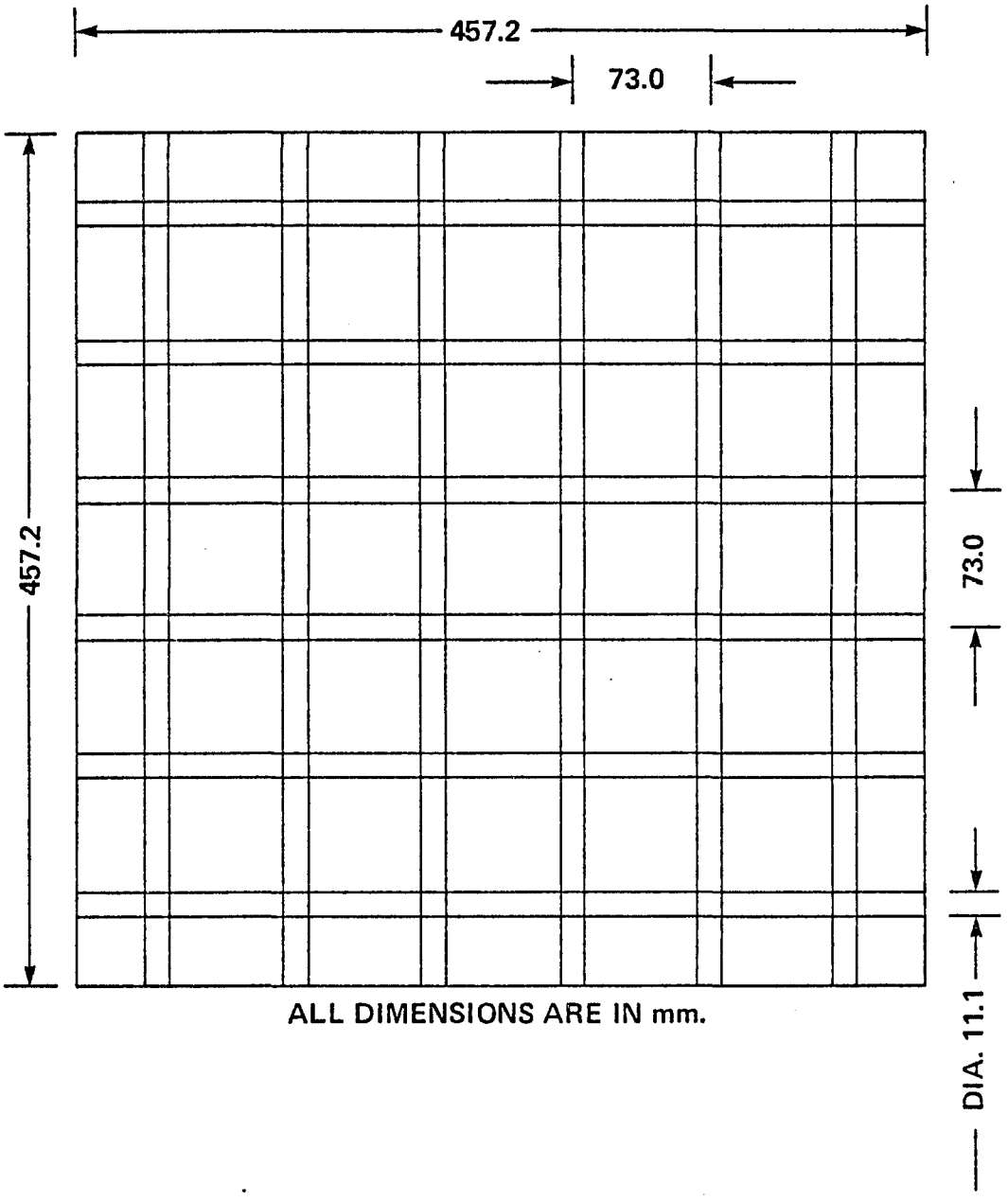

Figure 5.1(b) Schematic of the Circular Rods Grid Used to Generate Turbulence

as well as lateral directions manually, in steps of 0.03 cm. using the traverse mechanism. The axial location of the probe could also be changes manually.

5.1.1.4 Test Model: The test model consisted of a flat plate (Fig. 5.2) made of precision ground non - distorting stainless steel of the size 45.72 x 14.92 x 0.238 cm^3. Levelling of the flat plate was verified at the start of the experimentation.

The flat plate was mounted firmly in the wind tunnel in the x - z plane (Fig. 5.2) so that the wake produced from its trailing edge varied in x - y plane.

The measurements were taken downstream of the trailing edge of the flat plate, for near and far wake, with and without free stream turbulence.

The flow Reynolds number based on the inlet average velocity and chord length was 2.56 x 10^5, 2.07 x 10^5 and 2.45 x 10^5 at turbulence levels of 0.004, 0.0523 and 0.0723; respectively. The corresponding average mean velocities were 26.62, 21.52 and 25.46 m/sec.

5.1.1.5 Probes Required for the Experimentation: A three hole prism shaped measuring section probe, made of corrosion - resistant non - magnetic stainless steel, was used to measure the mean velocities in the lateral direction and at six axial locations, (Fig. 5.2), in the wake of a

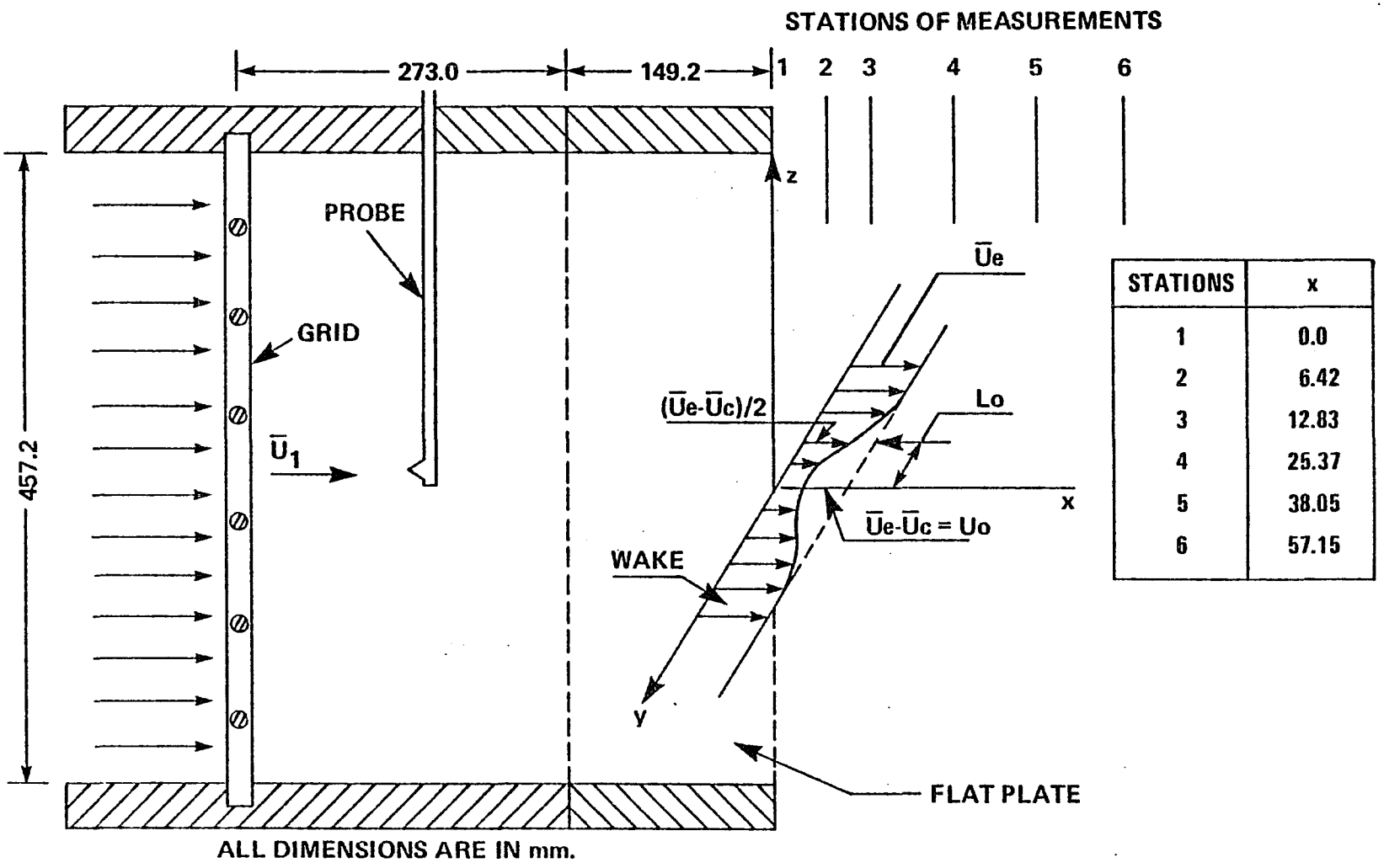

STATIONS	x
1	0.0
2	6.42
3	12.83
4	25.37
5	38.05
6	57.15

Figure 5.2 Schematic of the Experimental Set-Up

flat plate. This three hole probe was 609.6 mm. long. having 3.05 mm tip diameter and 1.52 mm take off tube diameter for the connections to the pressure transducer, etc.

A single sensor hot - wire probe $\ell / \bar{D}$ ratio of 340, was used to measure free stream turbulence. The wire diameter was 5 micron (5×10^{-6}m) and was made of tungsten. The resistance of the wire was 6.15 ohms. This wire was used to measure the turbulence level outside the wake with and without free stream turbulence.

A cross-wire probe was used to measure the wake. The sensors of the cross-wire probe were of tungsten. Each sensor was of 5 micron diameter, and had the length to diameter ratio of 300. Both wires were of approximately equal resistance (within 0.15 %). The stainless steel prongs had a diameter of 0.5 mm and taper off towards the sensor. The shortest distance between the two adjacent prong tips was 0.8 mm. Two prongs were 9.1 mm; the other two were 7.9 mm long. An overheat ratio of 1.5 was used for both wires giving good compromise between the durability and sensitivity of the wire. A high over-heat ratio increases the sensitivity but decreases the durability, i.e., there is a risk of burning the wire.

5.1.2 Method and Means of Measurement:

5.1.2.1 Measurement of Mean and Turbulence Quantities:

The mean velocity profile and turbulence quantities ($\sqrt{\overline{u^2}}$, $\sqrt{\overline{v^2}}$, $\overline{uv}$) were measured at six axial locations (Fig. 5.2) with and without free stream turbulence. All the hot-wire equipment used was DISA made. The probe was calibrated using a calibration unit, pre-calibrated pressure transducer, two anemometers, channel selector, digital voltmeter, and peripheral equipment. An auxiliary unit was used to inverse the input signal of the second channel of the anemometer. The signals were fed to a battery operated dual summing unit having a gain constant of 0.33. The output from the sum and difference unit was fed to the RMS voltmeter which was connected to the digital voltmeter through a channel selector. The output of the anemometers was also directly fed to the digital voltmeter as well as through the RMS voltmeter.

The probe was connected rigidly to the probe holder and the holder was adjusted in such a way that the plane of the cross-wire coincided with the plane of the flow. The probe was rotated in its own plane so as to adjust the angle of the flow to 45^{o} to the cross-wire.

The root mean square values of turbulence fluctuations in volts were measured and the data was processed according to the method used in Ref.(35) and the following equations were obtained using King's law:

$$\frac{\sqrt{\overline{u^2}}}{\bar{U}_e} = \frac{\sqrt{2}}{\left[1 + K_c^2/2\right]} \left\{ \frac{\sqrt{\overline{e_1^2}}}{n_1 \bar{E}_1 \left[1 - (\bar{E}_{01}/\bar{E}_1)^2\right]} \frac{\bar{U}_1}{\bar{U}_e} + \frac{\sqrt{\overline{e_2^2}}}{n_2 \bar{E}_2 \left[1 - (\bar{E}_{02}/\bar{E}_2)^2\right]} \frac{\bar{U}_2}{\bar{U}_e} \right\} \quad \ldots(5.1)$$

$$\frac{\sqrt{\overline{v^2}}}{\bar{U}_e} = \frac{\sqrt{2}}{\left[1 + K_c^2/2\right]} \left\{ \frac{\sqrt{\overline{e_2^2}}}{n_2 \bar{E}_2 \left[1 - (\bar{E}_{02}/\bar{E}_2)^2\right]} \frac{\bar{U}_2}{\bar{U}_e} - \frac{\sqrt{\overline{e_1^2}}}{n_1 \bar{E}_1 \left[1 - (\bar{E}_{01}/\bar{E}_1)^2\right]} \frac{\bar{U}_1}{\bar{U}_e} \right\} \quad \ldots(5.2)$$

$$-\frac{\overline{u\,v}}{\overline{U}_e^2} = \frac{2}{\left[G_T\,(1 + K_c^2/2)\right]^2}\left\{\frac{\overline{e_s^2}}{n_2^2\,\overline{E}_2^2\left[1 - (\overline{E}_{02}/\overline{E}_2)^2\right]^2}\right.$$

$$\left.\frac{\overline{U}_2^2}{\overline{U}_e^2} - \frac{\overline{e_d^2}}{n_1^2\,\overline{E}_1^2\left[1 - (\overline{E}_{01}/\overline{E}_1)^2\right]^2}\,\frac{\overline{U}_1^2}{\overline{U}_e^2}\right\} \quad \ldots(5.3)$$

where $\sqrt{\overline{u^2}}$ $\sqrt{\overline{v^2}}$ and $\overline{uv}$ are the turbulence intensity components in the axial and lateral directions and Reynolds stress, respectively. $\overline{U}_1$, $\overline{U}_2$ are the mean velocity components of sensors 1 and 2 respectively. $\overline{E}_{01}$, $\overline{E}_{02}$ are the voltages for zero velocity ; $\sqrt{\overline{e_1^2}}$, $\sqrt{\overline{e_2^2}}$ are the rms value of the fluctuating voltages for sensors 1 and 2, respectively . G_T is the transfer function of the summing unit. $\sqrt{\overline{u_1^2}}$ and $\sqrt{\overline{u_2}}$ are the rms value of the turbulence intensity for sensor 1 and 2, respectively. $\overline{U}_e$ is the local outer edge velocity. K_c is the correction correction factor due to $\ell/\overline{D}$ ratio of the sensor and n_1 and n_2 are the hot-wire constants.

5.2 Wake Boundary Layer Interaction Work:

5.2.1 Equipment Used in the Experiment:

5.2.1.1 Experimental Set-up and Test Model: The wind tunnel and the traversing mechanism needed for the experimental set-up are described in Section 5.1.1. A schematic of the experimental set-up and the test model is shown in Fig. 5.3.

The test model consists of two flat plates (Fig. 5.3) mounted perpendicular to each other. The flat plate producing wake is in the $x - z$ plane so as to give the wake variation in the $x - y$ plane. The flat plate on which boundary layer is developed and the flow becomes interacted, is in the $x - y$ plane so that the boundary layer varies in the $x - z$ plane and thus the interacting flow becomes three-dimensional ($x - y - z$).

The flat plates were made of precision ground, non-distorting stainless steel. Each flat plate was of $45.72 \times 14.92 \times 0.238$ cm^3. The distance between the two flat plates, S in the axial direction can be varied up to 25.4 cms. so as to establish the interaction effect of the near and the far wake. In the present study, the spacing between the two flat plates was kept as 1.0 mm, 44.7 mm and 89.4 mm. so as to obtain S/c ratios of 0.007,

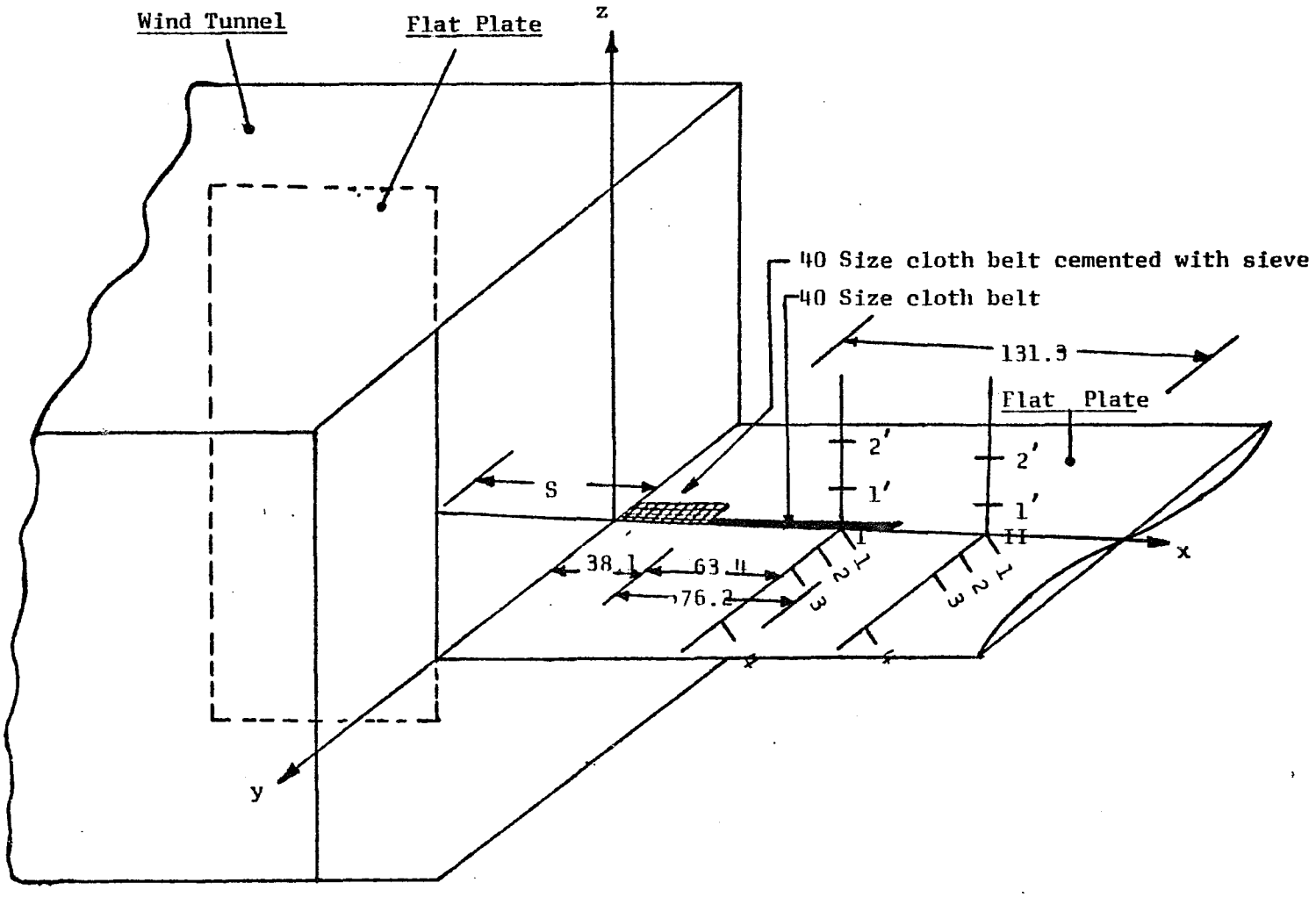

Figure 5.3 Flat Plate Interaction Set-Up in a Subsonic Wind Tunnel

0.3 and 0.6, respectively.

To obtain a thicker boundary layer a 40 XHD cloth belt, Garnet, made by Abrasive company, was pasted with rubber cement from the leading edge up to a distance of 38.1 mm axial distance, covering the complete width of the plate. The sieve passing through the Tyler standard screen mesh no. 4 having an opening of 4.7 mm but not passing through mesh no. 8 with opening of 2.362 mm, was glued over the belt with the help of Elmer's glue to increase the turbulence level as well as the boundary layer thickness. To avoid abruptness, another piece of 40 XHD cloth belt of width 76.2 mm was glued with the help of rubber cement, adjacent to the first piece giving the good boundary layer thickness as well as turbulence level for measurements. Measurements were performed at x_1/c = 0.68 and 0.88 for each spacing x_1 was measured from the leading edge of the second flat plate.

The flow Reynolds number, based on the total mean velocity (23.15 m/sec) and on the chord length of the flat plate, was 2.2×10^5. The flow Reynolds number, based on the total mean velocity at the first measuring station (x_1/c = 0.68, z/c = 0.026 and S/c = 0.007), was 3.58×10^5. The corresponding total mean velocity and the total axial distance were 22.15 m/sec and 251.7mm, respectively, where axial distance was measured from the leading edge of the first flat plate.

5.2.1.2 Calibration Tunnel: The three dimensional hot-wire probe was calibrated in an air jet. The calibration tunnel included a variable speed blower, a diffuser fitted with axial vanes so as to reduce secondary circulation, a plenum chamber and a bell mouth nozzle terminating in a short cylinder through which air was discharged to the atmosphere. The jet produced in the tunnel is parallel to the axis of the cylinder and of constant magnitude over a cross-section perpendicular to the cylinder axis at the exit of the cylinder. The appropriate adjustment of the blower and the variac could provide the steady air jet velocities ($\sim$ 110 m/sec), having negligible turbulence intensity.

5.2.1.3 Probes Used in the Experiment: The preliminary measurements of the interacting region were taken using a single wire probe, described in Section 5.1.1.5, to measure the approximate values of the total mean velocity and the total turbulence intensity.

A triple sensor hot-wire probe (Fig. 5.4) was used for the detailed measurements of the interacting region. This probe has three orthogonal cylindrical hot-wire sensors; each supported by two prongs. Each sensor is made of tungsten wire, with $\bar{D}$ = 0.000381 mm (0.00015") and ℓ = 1.27 mm (0.05"). This provided an $\ell/\bar{D}$ ratio of 333.33. All the three sensors were of nearly equal resistance (within 0.65 %).

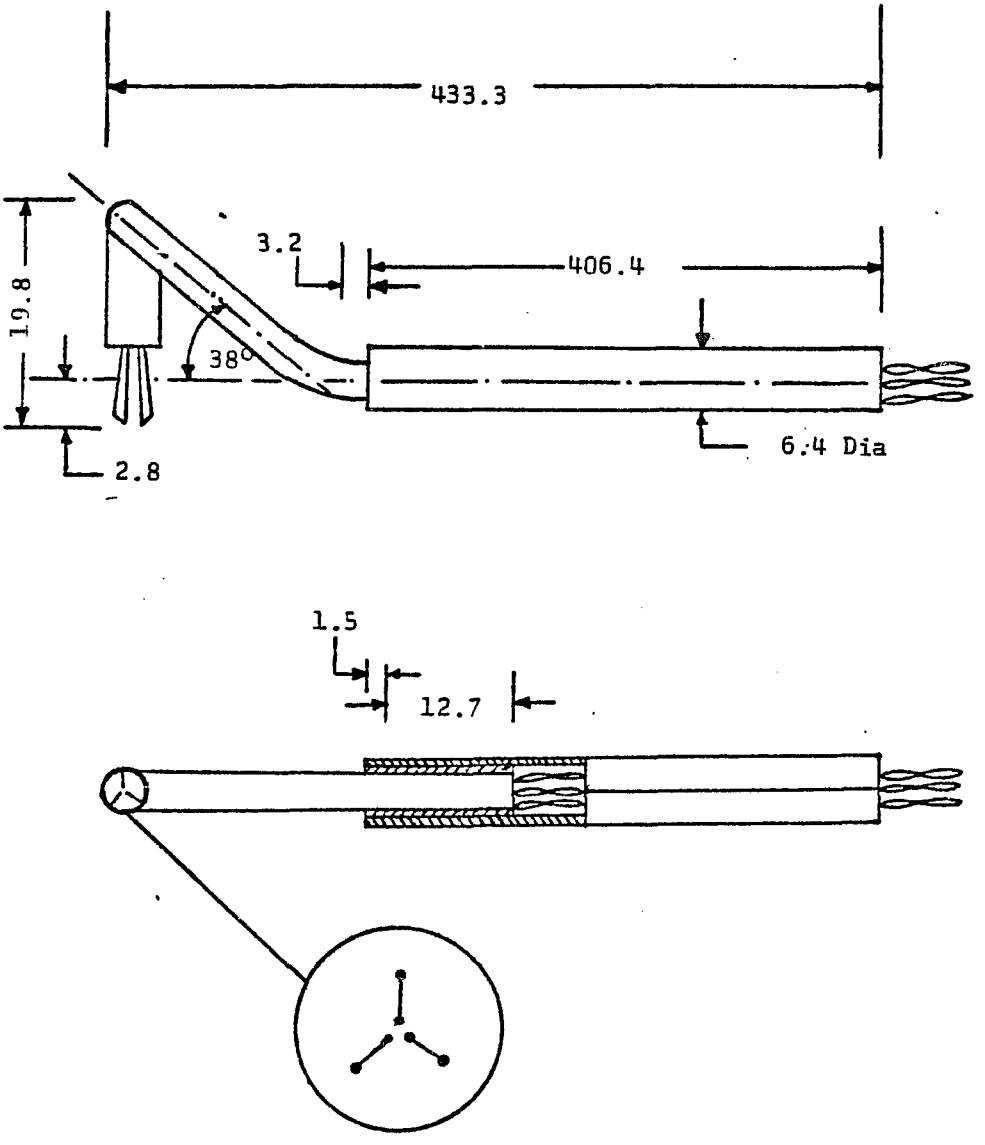

All Dimensions are in mm.

Figure 5.4 Schematic of a Three-Dimensional Hot - Wire Probe (1294 CT-T-1.5)

5.2.1.4 Spectrum Analyzer: Energy spectra, in a frequency domain were measured, with the help of Panoramic spectrum analyzer, in the wake boundary layer interacting flow for the near and the far wake interaction.

Following the preliminary adjustments, the abscissa of the frequency spectra was calibrated by giving the known frequency signal (up to 20 KHZ) through the wave analyzer, with the appropriate adjustment of the sweep width dial (0 to 200 KC) and other necessary controls. The ordinate scale was calibrated using the appropriate controls for DB scale (0 to 60 DB).

5.2.2 Calibration of Three-Dimensional Hot-Wire Probe:

The three-dimensional hot-wire probe was calibrated in the core of an air jet apparatus, using pre - calibrated pressure transducer, three anemometers, digital voltmeter, RMS voltmeter and oscilloscope. The velocity in the tunnel was varied from zero to 80.0 metres/sec; covering the full range of measurements.
The readings of the pressure transducer and the three anemometers through the digital voltmeter were noted and the calibration curve for each of the sensors was obtained using King's law.

5.2.3 Method and Means of Measurements:

5.2.3.1 Measurement of Mean Velocity Profile: Two wake profiles were measured at each axial location and for

each spacing. Two axial locations were chosen for measurements for each spacing. The stations of measurements for the interacting region are shown in Table IV and Fig. 5.3.

The preliminary measurements were taken with a single wire probe. These measurements helped in choosing the probe intervals in the critical regions of measurements.

The detailed measurements of mean and turbulence quantities were taken with a three sensor hot-wire probe. The approximate mean velocity and turbulence intensity obtained from the single wire data were compared with the corresponding values obtained from the three sensor probe and were found to be in good agreement. The mean velocity components obtained by three sensor probe were plotted for further discussion (Fig. 5.5).

5.2.3.2 Measurement of Turbulence Intensity and Reynolds Stress: Three components of turbulence intensity ($\overline{u^2}$, $\overline{v^2}$, $\overline{w^2}$) and three components of $-\rho\overline{u_i u_j}$ ($-\rho\overline{uv}$, $-\rho\overline{vw}$, $-\rho\overline{wu}$) were measured with three sensor hot - wire probe and its associated anemometry. The output signals from three anemometers were connected to the integrating digital voltmeter to obtain the components of turbulence intensity. The output signal from the anemometers were inverted using an auxiliary unit. The sum and difference of the signals

TABLE IV

LOCATION OF STATIONS FOR WAKE-BOUNDARY LAYER INTERACTION (FIG. 5.3)

x_1/c	Stations	z/c	Profile	S/c
0.68	1	0.010		0.007
			Wake	0.300
I	2	0.026		0.600
0.88	1	0.010		0.007
			Wake	0.300
II	2	0.026		0.600

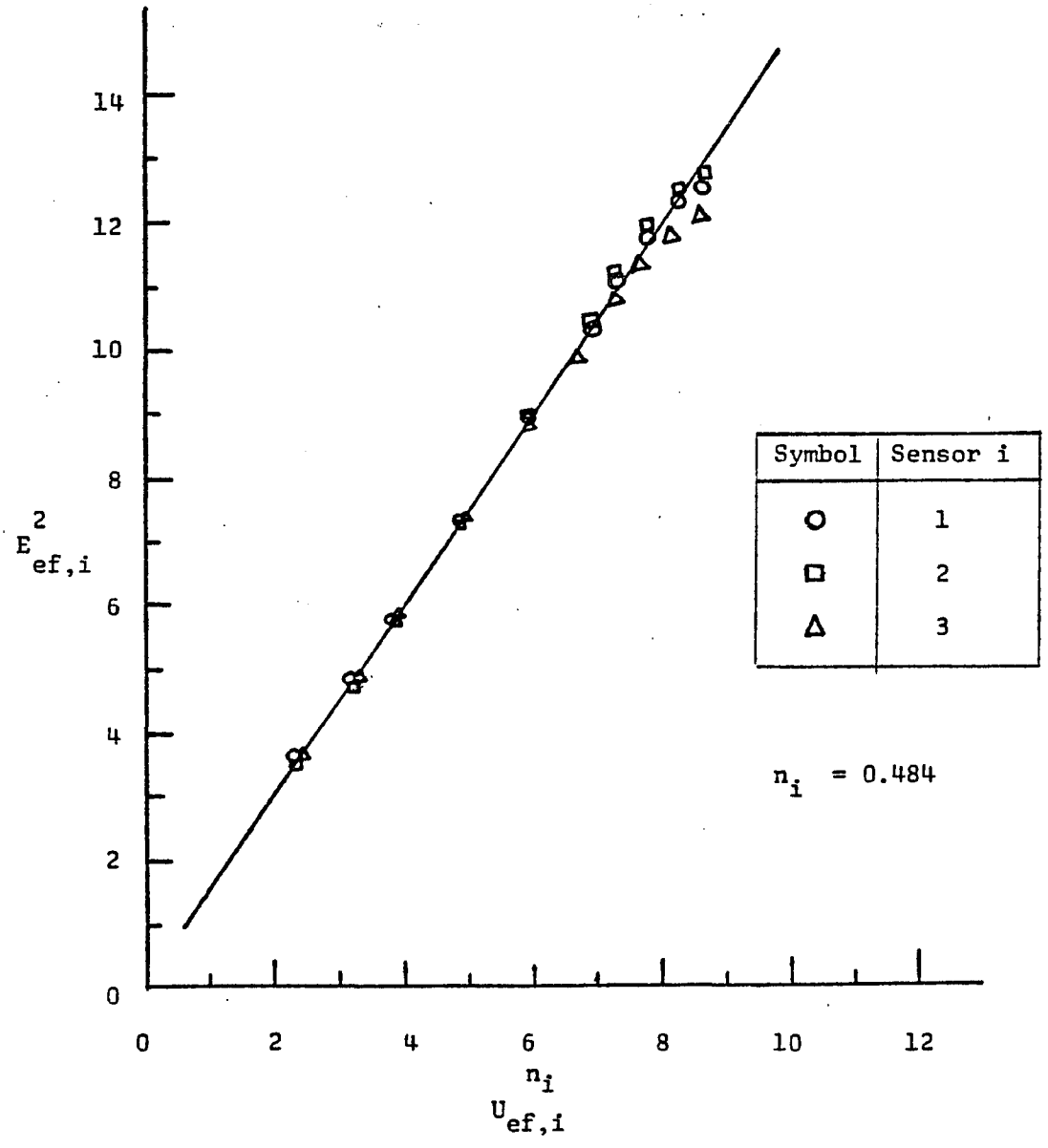

Figure 5.5 Calibration Curve of a Three Sensor Hot-Wire Probe

were obtained with the help of dual summing unit. The output from the dual summing unit was fed to the integrating digital voltmeter through the RMS meter so as to obtain the r.m.s. value of the sum and difference of the outputs of the anemometers. The initial oscillations of the anemometers was kept to zero with the help of the oscilloscope with the appropriate adjustment of the Q and L screws.

5.2.3.3 Spectral Measurement: The energy spactra at six axial locations and at the wake center line, 1 mm up from the wall were measured with the help of a spectrum analyzer, using a single wire probe. A wave analyzer was used for the appropriate frequency setting. Photographs were taken with the help of oscilloscope camera. The camera uses the Polaroid film roll of Type C-42. The image to the object ratio is close to unity. Scaling in the picture area is very accurate and the magnification is constant. Each print was coated with the print coater immediately after the print was removed from the camera to increase the durability of the photograph.

5.2.4 Data Processing:

5.2.4.1 For Three Sensor Probe: The general method of data processing from equations of triple sensor hot-wire anemometry is given in Refs.(45,46). The same steps are followed here, Accordingly,

$$U_{ef,i} = \left[\left(E_i^2 - E_{0i}^2 \right) / D_i \right]^{n_i} \quad \ldots(5.4)$$

$i = 1,2$ and 3.

where $U_{ef,i}$ and E_i are the effective cooling velocity and instantaneous voltage for sensor i, respectively.

The hot-wire constants E_{0i} , D_i , n_i were obtained from the calibration curve (Fig. 5.5). The value of n_i obtained from the calibration curve was 0.484.

The relation between the actual mean velocity vector , $\underline{\bar{U}}$, and the effective cooling velocity, $U_{ef,i}$, can be expressed as:

$$U_{ef,i}^2 = \underline{\bar{U}}^2 \left[\cos^2 \gamma_i + K_{c,i} \sin^2 \gamma_i \right] \quad \ldots(5.5)$$

where γ_i is the angle between the mean velocity vector and normal to the sensor i, in the plane constituted by the sensor i, and the mean velocity vector. $K_{c,i}$ is the correction due to cosine law depending upon the length to diameter ratio of the sensor i, material of the sensor i, and the velocity range.

Since all three sensors have the same length to diameter ratio and are of the same material

$$K_{c,1} = K_{c,2} = K_{c,3} = K_c$$

Thus, Eqn.(5.5) can be simplified as:

$$\underline{\bar{U}}^2 = \sum_{i=1}^{3} \left[\frac{U_{ef,i}^2}{2 + K_c^2} \right]^{\frac{1}{2}} \quad \ldots(5.6)$$

The value of $K_{c,i}$ can be obtained from the following equation, (Reference 47),

$$K_{c,i} = \cot \gamma_i \left[\left(D_i + \frac{1 - D_i}{\cos^{\frac{1}{2}} \gamma_i} \right)^4 - 1 \right] \quad \ldots(5.7)$$

For low incompressible speed and the length to diameter ratio of the order of 340, the average value of $K_{c,i}$ obtained from Eqn.(5.7) and Ref.(48) was 0.195.

Angles of the sensors to the probe can be determined as:

$$\gamma_i = \sin^{-1} \left[\frac{1 - U_{ef,i}^2 / \bar{U}^2}{1 - K_c^2} \right]^{\frac{1}{2}} \quad \ldots(5.8)$$

Thus, the components of the absolute velocity vector along the three sensors of the probe can be written as,

$$U_i = \bar{U} \sin \gamma_i \,, \quad i = 1 \text{ to } 3 \quad \ldots(5.9)$$

However, in the present case, to obtain the mean and turbulence quantities in the required form,

1. The plane containing sensors 2 and 3 (y-z plane) is rotated by an angle θ_1 , so that sensor 1 is in the axial direction. The magnitude of angle θ_1 obtained from the probe configuration was 35.264^{o}, (Fig. 5.6).

2. The plane containing sensors 2 and 3 is next rotated by an angle θ_2 about the x - axis, so that sensor

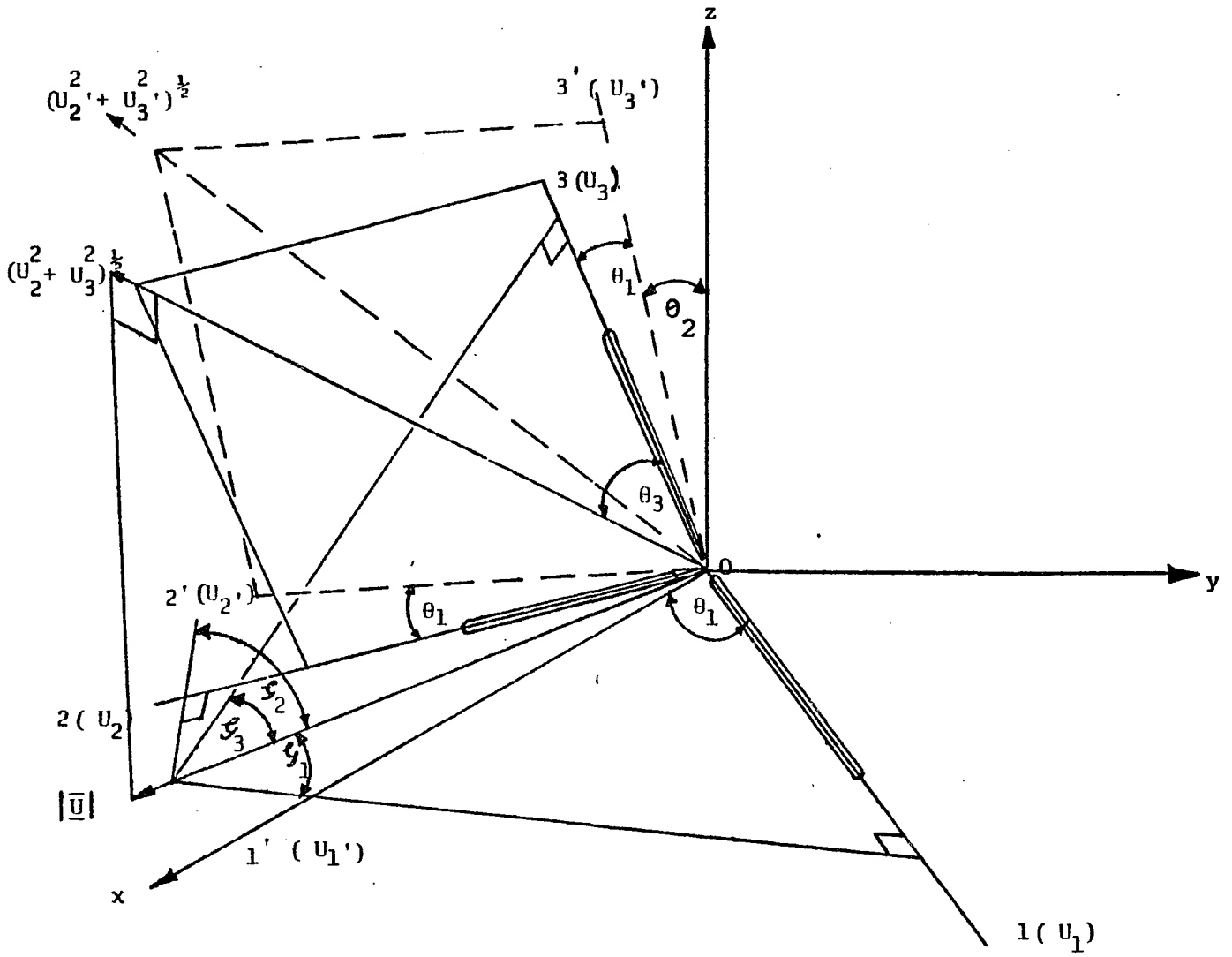

Figure 5.6 Coordinate Transformation and Symbols Used in Hot-Wire (3 D) Date Processing

3 points in the z-direction and sensor 2 in the y - direction. The transformations are similar to those in Refs.(45, 46).

If 1, 2 and 3 are the directions of the sensors forming an orthogonal system, $1'$, $2'$ and $3'$ are the directions of the sensors after first transformation forming an orthogonal system and x , y and z are the orthogonal Cartesian system (set-up axes), then

$$U_1' = (U_2^2 + U_3^2)^{\frac{1}{2}} \sin \theta_1 + U_1 \cos \theta_1 \quad ...(5.10)$$

$$(U_2'^2 + U_3'^2)^{\frac{1}{2}} = (U_2^2 + U_3^2)^{\frac{1}{2}} \cos \theta_1 - U_1 \sin \theta_1 \quad ..(5.11)$$

where,

$$(U_2^2 + U_3^2)^{\frac{1}{2}} = \overline{U} \cos \gamma_1 \quad ...(5.12)$$

Let θ_3 be the angle, the velocity vector $\overline{U} \cos \gamma_1$ makes with sensor 3, then,

$$\cos \theta_3 = \sin \gamma_3 / \cos \gamma_1 \quad ...(5.13)$$

$$\sin \theta_3 = \sin \gamma_2 / \cos \gamma_1 \quad ...(5.14)$$

i.e.

$$U_2' = (U_2'^2 + U_3'^2)^{\frac{1}{2}} \sin \theta_3 \quad ...(5.15)$$

$$U_3' = (U_2'^2 + U_3'^2)^{\frac{1}{2}} \cos \theta_3 \quad ...(5.16)$$

where U_2 and U_3 are the velocity components along the

intermediate axes, making an angle of $\theta_2 = 45^o$ to the y and z axes, respectively. Therefore,

$$U_x = U_1' \qquad \ldots(5.17)$$

$$U_y = \cos\theta_2 \; (U_2' + U_3') \qquad \ldots(5.18)$$

$$U_z = \cos\theta_2 \; (U_3' - U_2') \qquad \ldots(5.19)$$

Combining all the earlier transformations, the mean velocity components along the set-up axes, can be written as,

$$U_x = (U_2^2 + U_3^2)^{\frac{1}{2}} \sin\theta_1 + U_1 \cos\theta_1 \qquad \ldots(5.20)$$

$$U_y = 0.707(\sin\theta_3 + \cos\theta_3) \left[(U_2^2 + U_3^2)^{\frac{1}{2}} \cos\theta_1 - U_1 \sin\theta_1 \right] \qquad \ldots(5.21)$$

$$U_z = 0.707(\cos\theta_3 - \sin\theta_3) \left[(U_2^2 + U_3^2)^{\frac{1}{2}} \cos\theta_1 - U_1 \sin\theta_1 \right] \qquad \ldots(5.22)$$

U_1 , U_2 , U_3 , θ_1 and θ_3 are known; therefore therefore, the mean velocity components along the set-up axes are known.

To obtain the turbulence quantities from the measured data, the following equations, as explained in the Appendix A are obtained. The listing of the computer program for the data processing of the interacting flow is given in Appendix B.

$$\sqrt{\overline{u_x^2}} = \left[\overline{u_1^2} \cos^2\theta_1 + \frac{\overline{U_3^2}\,\overline{u_3^2} + \overline{U_2^2}\,\overline{u_2^2} + 2\,\overline{U}_3\,\overline{U}_2\overline{u_2u_3}}{\overline{U_2^2} + \overline{U_3^2}} \sin^2\theta_1 \right.$$

$$\left. + \frac{\overline{U}_3\,\overline{u_1\,u_3} + \overline{U}_2\,\overline{u_1\,u_2}}{(\overline{U_2^2} + \overline{U_3^2})^{\frac{1}{2}}} \sin 2\theta_1 \right]^{\frac{1}{2}} \qquad \ldots(5.23)$$

$$\sqrt{\overline{u_y^2}} = a\left[\overline{u_1^2} \sin^2\theta_1 + \frac{\overline{U_2^2}\,\overline{u^2}_2 + \overline{U_3^2}\,\overline{u_3^2} + 2\,\overline{U}_2\overline{U}_3\overline{u_2u_3}}{\overline{U_2^2} + \overline{U_3^2}} \cos^2\theta_1 \right.$$

$$\left. - \frac{\overline{U}_2\,\overline{u_1\,u_2} + \overline{U}_3\,\overline{u_1\,u_3}}{(\overline{U_2^2} + \overline{U_3^2})^{\frac{1}{2}}} \sin 2\theta_1 \right]^{\frac{1}{2}} \qquad \ldots(5.24)$$

$$\sqrt{\overline{u_z^2}} = b\left[\overline{u_1^2}\sin^2\theta_1 + \frac{\overline{U_2^2}\,\overline{u_2^2} + \overline{U_3^2}\,\overline{u_3^2} + 2\,\overline{U}_2\overline{U}_3\overline{u_2u_3}}{\overline{U_2^2} + \overline{U_3^2}} \cos^2\theta_1 \right.$$

$$\left. - \frac{\overline{U}_2\,\overline{u_1\,u_2} + \overline{U}_3\,\overline{u_1\,u_3}}{(\overline{U_2^2} + \overline{U_2^2})^{\frac{1}{2}}} \sin 2\theta_1 \right]^{\frac{1}{2}} \qquad \ldots(5.25)$$

$$\overline{u_x u_y} = a\left[\tfrac{1}{2}\left(-\overline{u_1^2} + \frac{\overline{U_3^2}\,\overline{u_3^2} + \overline{U_2^2}\,\overline{u_2^2} + 2\,\overline{U}_2\overline{U}_3\,\overline{u_2 u_3}}{\overline{U_2^2} + \overline{U_3^2}}\right)\sin 2\theta_1 + \frac{\overline{U}_2\,\overline{u_1 u_2} + \overline{U}_3\,\overline{u_1 u_3}}{\left(\overline{U_2^2} + \overline{U_3^2}\right)^{\frac{1}{2}}}\cos 2\theta_1\right] \quad \ldots(5.26)$$

$$\overline{u_y u_z} = a\,b\left[\overline{u_1^2}\sin^2\theta_1 - \frac{\overline{U}_2\,\overline{u_1 u_2} + \overline{U}_3\,\overline{u_1 u_3}}{\left(\overline{U_2^2} + \overline{U_3^2}\right)^{\frac{1}{2}}}\sin 2\theta_1 + \frac{\overline{U_2^2}\,\overline{u_2^2} + \overline{U_3^2}\,\overline{u_3^2} + 2\,\overline{U}_2\,\overline{U}_3\,\overline{u_2 u_3}}{\overline{U_2^2} + \overline{U_3^2}}\cos^2\theta_1\right] \quad \ldots(5.27)$$

and

$$\overline{u_z u_x} = b\left[\tfrac{1}{2}\left(-\overline{u_1^2} + \frac{\overline{U_3^2}\,\overline{u_3^2} + \overline{U_3^2}\,\overline{u_3^2} + 2\,\overline{U}_2\overline{U}_3\overline{u_2 u_3}}{\overline{U_2^2} + \overline{U_3^2}}\right)\sin 2\theta_1 + \frac{\overline{U}_2\,\overline{u_1 u_2} + \overline{U}_3\,\overline{u_1 u_3}}{\left(\overline{U_2^2} + \overline{U_3^2}\right)^{\frac{1}{2}}}\cos 2\theta_1\right] \quad \ldots(5.28)$$

where,

$$a = \cos\theta_2\,(\sin\theta_3 + \cos\theta_3) \quad \ldots(5.29)$$

$$b = \cos\theta_2\,(\cos\theta_3 - \sin\theta_3) \quad \ldots(5.30)$$

Thus, from Eqns.(5.23) to (5.28), $\sqrt{\overline{u_x^2}}$, $\sqrt{\overline{u_y^2}}$, $\sqrt{\overline{u_z^2}}$, $\overline{u_x u_y}$, $\overline{u_y u_z}$, $\overline{u_z u_x}$ can be calculated as the right hand side of these equations is known; giving the three components of turbulence intensity and Reynolds stress along the set-up axes, respectively.

5.2.4.2 For Frequency Spectra: Energy frequency spectra were measured with the help of a spectrum analyzer. However, a wave number representation of the spectra is needed to the understanding of turbulence structure from theoretical considerations. One-dimensional wave number spectra are defined as (References 4, 49),

$$\int_0^{\infty} \frac{F(k)}{\overline{u^2}}\, dk \simeq 1 \qquad (5.31)$$

where $F(k)$ is the spectral energy at wave number k.

Writing Eqn. (A-6) for a single sensor, i.e, $i = 1$ and removing subscript i,

$$\frac{\sqrt{\overline{u^2}}}{\overline{U}} = \frac{2}{n\left[1 - (\overline{E}_0/\overline{E})^2\right]} \frac{\sqrt{\overline{e^2}}}{\overline{E}} \qquad \ldots(5.32)$$

The spectra distributions obtained from the spectrum analyzer in the frequency domain are transferred to the wave number domain and are obtained in the average sense from the actual spectra in frequency domain.

The approach followed to transfer the frequency dependence ($\bar{f}$) to wave number dependence (k) is as follows:

$$k = \frac{2\pi\bar{f}}{\bar{U}} \qquad \ldots(5.33)$$

By definition,

$$Db = 20\ Log_{10}\left(\sqrt{\overline{e^2}}\ /\sqrt{\overline{e_0^2}}\right) \qquad \ldots(5.34)$$

Also

$$\frac{F(k)}{\overline{u^2}} \simeq \frac{\sqrt{\overline{u^2}}}{2\pi\bar{f}} \qquad \ldots(5.35)$$

where $\bar{f}$ and Db are the frequency and magnitude, respectively of the spectrum at any location. $\sqrt{\overline{e_0^2}}$ is the reference voltage taken as unity in the present case.

Substituting $\sqrt{\overline{u^2}}$ and $\sqrt{\overline{e^2}}$ from Eqns.(5.32) and (5.34) respectively, and rearranging:

$$\frac{F(k)}{\overline{u^2}} \simeq \frac{2}{n\left[1 - (\bar{E}_0/\bar{E})^2\right]} \frac{10^{Db/20}}{\bar{E}} \left[\frac{\overline{E^2} - \overline{E_0^2}}{D}\right]^{1/n} \frac{1}{2\pi\bar{f}} \qquad \ldots(5.36)$$

Thus, at any frequency, f , $F(k)/\overline{u^2}$ and k can be calculated from Eqns.(5.36) and (5.33), respectively.

CHAPTER VI

EXPERIMENTAL RESULTS AND COMPARISON WITH PREDICTIONS OF FREE STREAM TURBULENCE WORK

The trends in the mean and turbulence characteristics of a wake in the presence of free stream turbulence environment are presented in Chapter (III). The experimental data presented in this section is used to establish the semi-empirical correlations to predict the decay of wake velocity defect, wake width, wake profile, maximum component of turbulence intensities and Reynolds stress. Using the experimental data, the concept of self-preservation is also examined. The various unknown constants appearing in Chapter(III) are also determined.

6.1 Inlet Mean Velocity Profile:

Mean velocity profiles are measured across the wind tunnel test section in x, y, and z directions without the test model to establish the uniformity in the inlet flow. The data is presented in Figures 6.1(a), (b) and (c). At location ($\bar{x}/c = 2.83$, where $\bar{x}$ is the axial distance from the grid), the deviation from the mean velocity is below 6.5 %. However, at the location where the wake profiles are measured, the maximum variation in velocity profile from the mean value is less than 1.5 %, [Fig. 6.1 (b), (c) and Table V] .

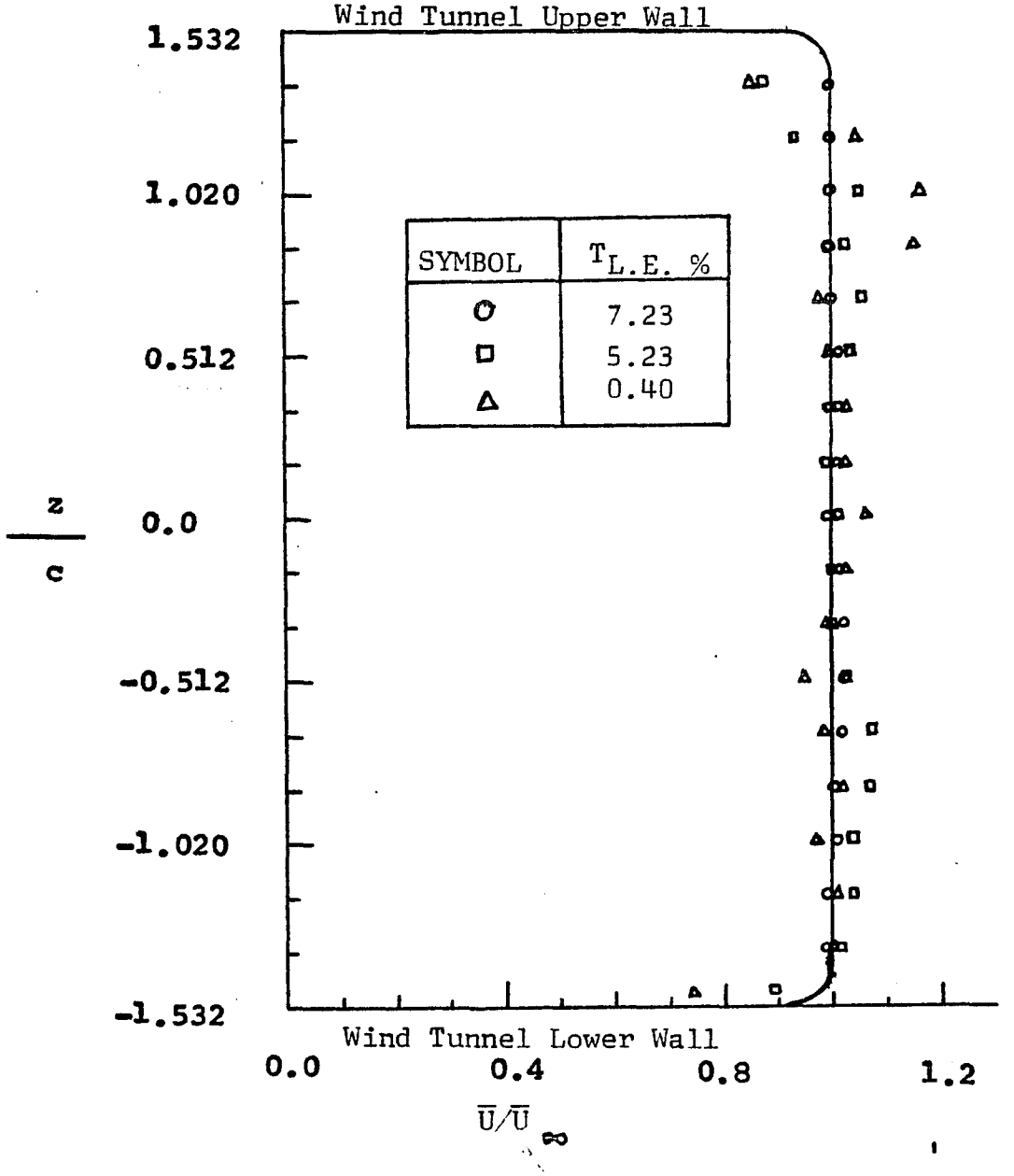

Figure 6.1(a) Variation of the Inlet Mean Velocity Profile in Normal Direction With and Without Free Stream Turbulence ($\overline{x}/c = 1.56$)

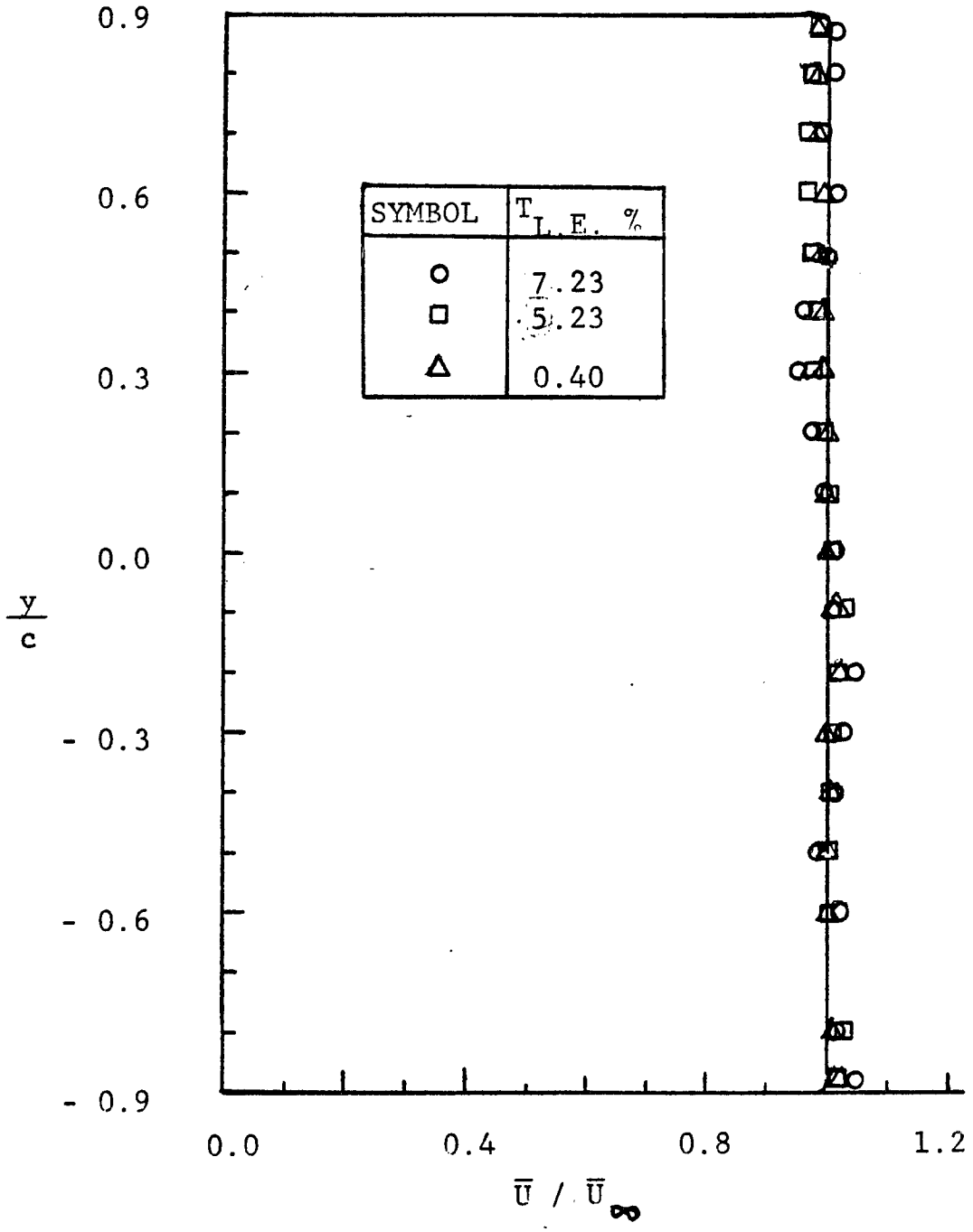

Figure 6.1(b) Variation of the Inlet Mean Velocity Profile in Lateral Direction With and Without Free Stream Turbulence (x/c = 2.83)

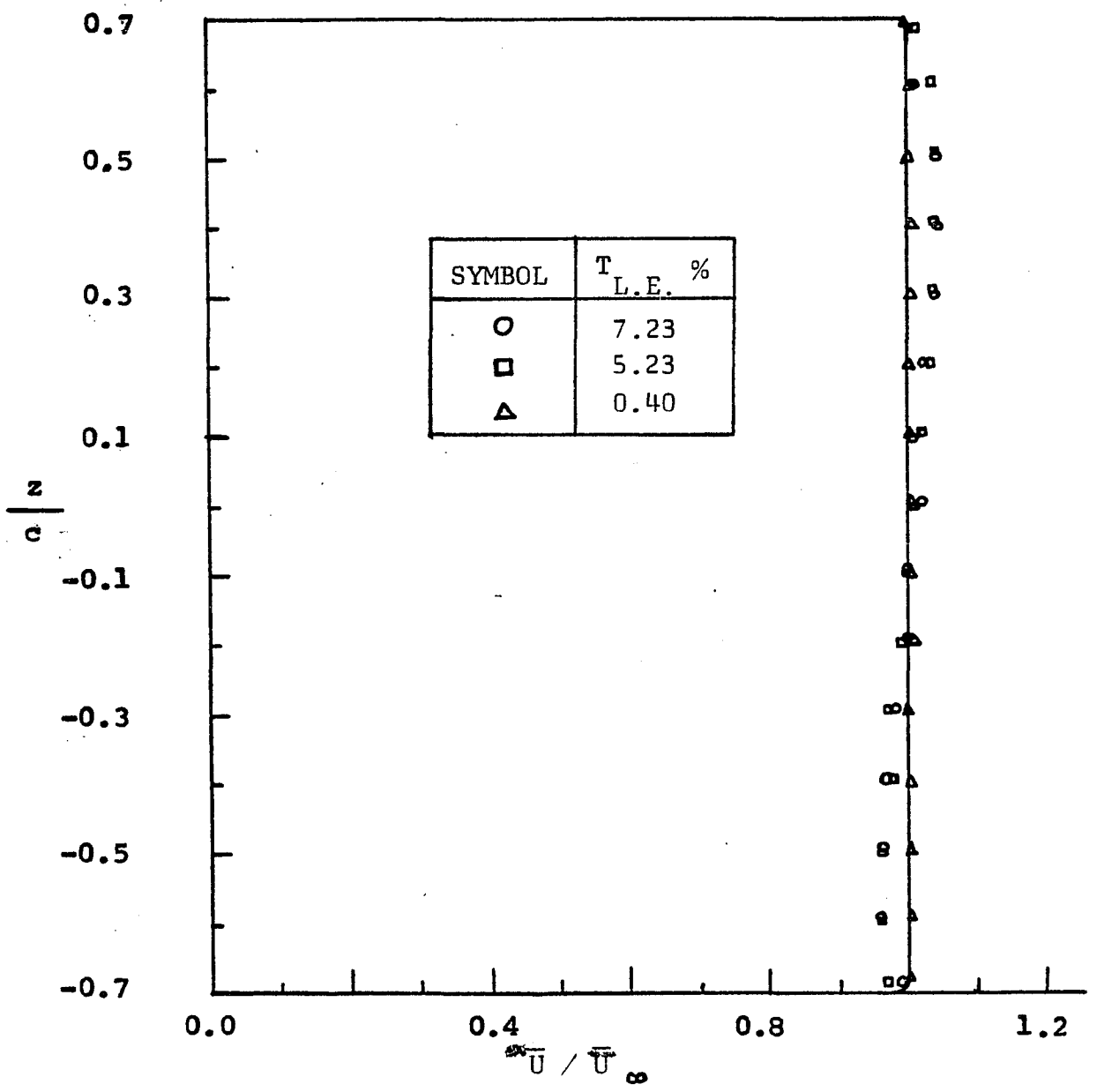

Figure 6.1(c) Variation of the Inlet Mean Velocity Profile in Normal Direction With and Without Free Stream Turbulence ($\bar{x}/c = 2.83$)

TABLE V

VARIATION IN THE MEAN VELOCITY PROFILE IN X, Y AND Z DIRECTIONS WITH AND WITHOUT FREE STREAM TURBULENCE

Grid Cross Section	Turbulence level at the L.E.	Maximum Variation in $\bar{U}/\bar{U}_\infty$ at $\bar{x}/c = 2.83$ y/c	$\bar{x}/c = 2.83$ z/c	$\bar{x}/c = 1.56$ y/c	Symbol	Maximum Variation in $\bar{U}/\bar{U}_\infty$ in Working Range at $\bar{x}/c = 2.83$ in y/c	z/c
No Grid	0.0040	± 0.5%	± 0.5%	± 1.7 %	△	± 0.2 %	± 0.2 %
Square Grid	0.0523	± 3.0%	± 3.5%	± 4.9 %	□	± 1.2 %	± 1.2 %
Circular Grid	0.0723	± 4.8%	± 4.6%	± 6.1 %	○	± 1.4 %	± 1.4 %

6.2 Free Stream Turbulence Level:

The variation of the free stream turbulence level (T) with downstream distance beginning with the leading edge of the flat plate is shown in Figure 6.2. It is clear from Figure 6.2 that T is a weakly dependent function of x/c behind the trailing edge of the flat plate. This is one of the assumptions made in the development of the analytical model. The free stream turbulence level at the leading edge was found to be 0.4 % for no grid, 5.23 % with square bars grid and 7.23 % with circular rods grid. However, at the trailing of the flat plate, the point of beginning of the wake, the free stream turbulence level was found to be 0.4 % for no grid, 2.56 % with square bars grid and 4.0 % with circular rods grid.

6.3 Mean Quantities:

The data is presented in the dimensionless form using 'c' and $\bar{U}_e$ as dimensional parameters; c being the chord length of the flat plate and $\bar{U}_e$ is the local mean velocity at the outer edge of the wake. The experimental behavior of the mean velocity, wake width, similarity, turbulence parameters, displacement thickness, momentum thickness, shape factor and energy thickness of the wake in the presence of free stream turbulence will be presented in the following sections.

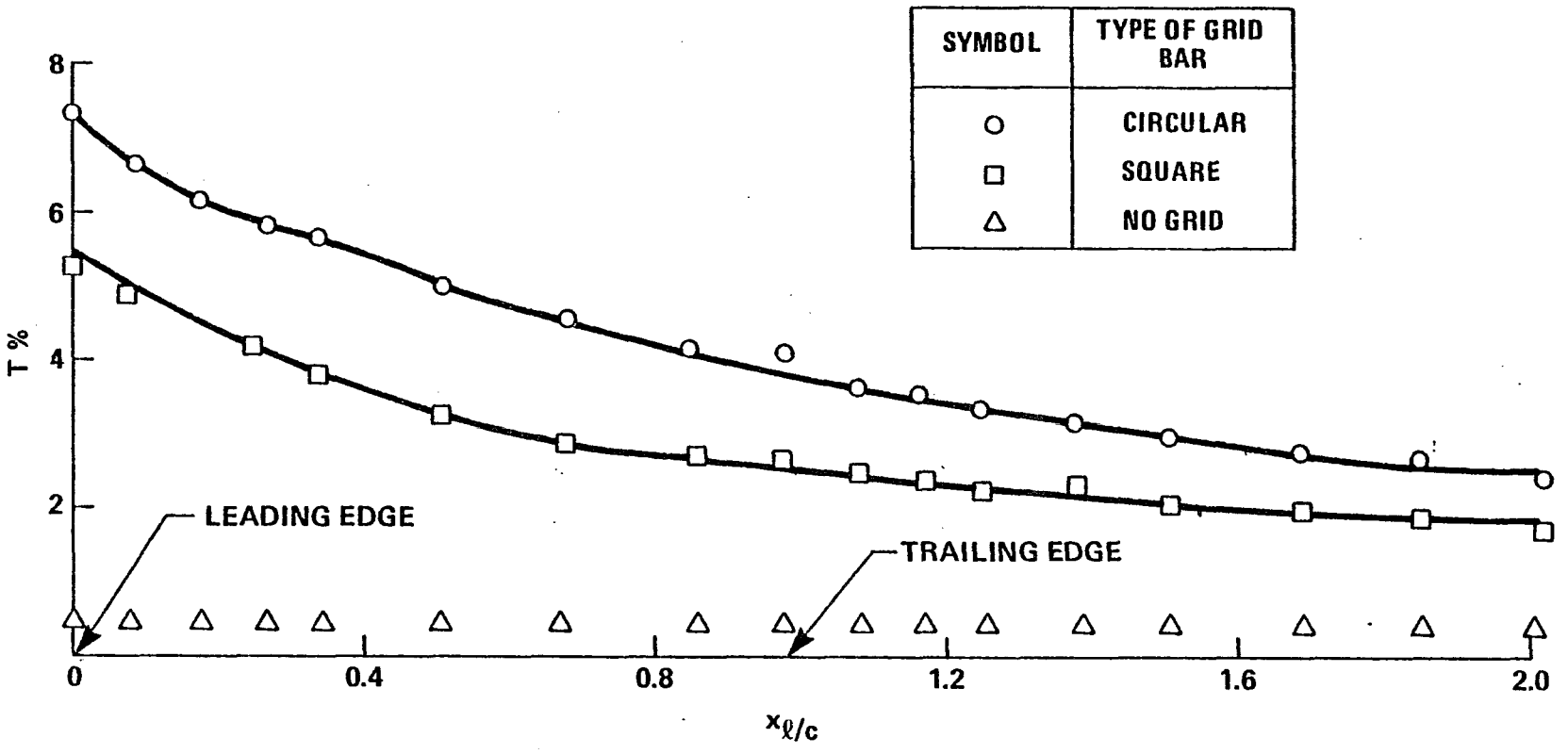

Figure 6.2 Variation of the Free Stream Turbulence Intensity with Downstream Distance

6.3.1 Mean Velocity Profile:

Mean velocity profiles at six axial stations and for three inlet free stream turbulence levels are plotted in Figures 6.3(a), (b) and (c). It is clear from these figures that the presence of free stream turbulence did not disturb the symmetry of the profiles. An observation was made that the instrument readout was more stable near the wake edges for the cases of data presented in Figures 6.3 (b) and (c) than the case of data presented in Figure 6.3 (a). This probably was due to the fact that the presence of free stream turbulence reduces intermittency at the wake edges.

6.3.2 Wake Recovery Rate:

Variation of the wake center line velocity with downstream distance for three free stream turbulence levels is presented in Figure 6.4 (a). It is clear from this plot that an increase in the free stream turbulence level increases the wake recovery rate. A logarithmic plot of data presented in Figure 6.4 (a) is shown in Figure 6.4 (b). The change in the slope of lines in Figure 6.4(b) represents the change in velocity power law. For a change in free stream turbulence level from 0 to 4 percent, the velocity power index changed from - 0.50 to -0.58. Based on this change in velocity power index, the value of $\mathcal{L}$ in Eqn.(3.18) suggests a value of 4.0. For a free stream turbulence level of the order of 15.0 %, which is the case

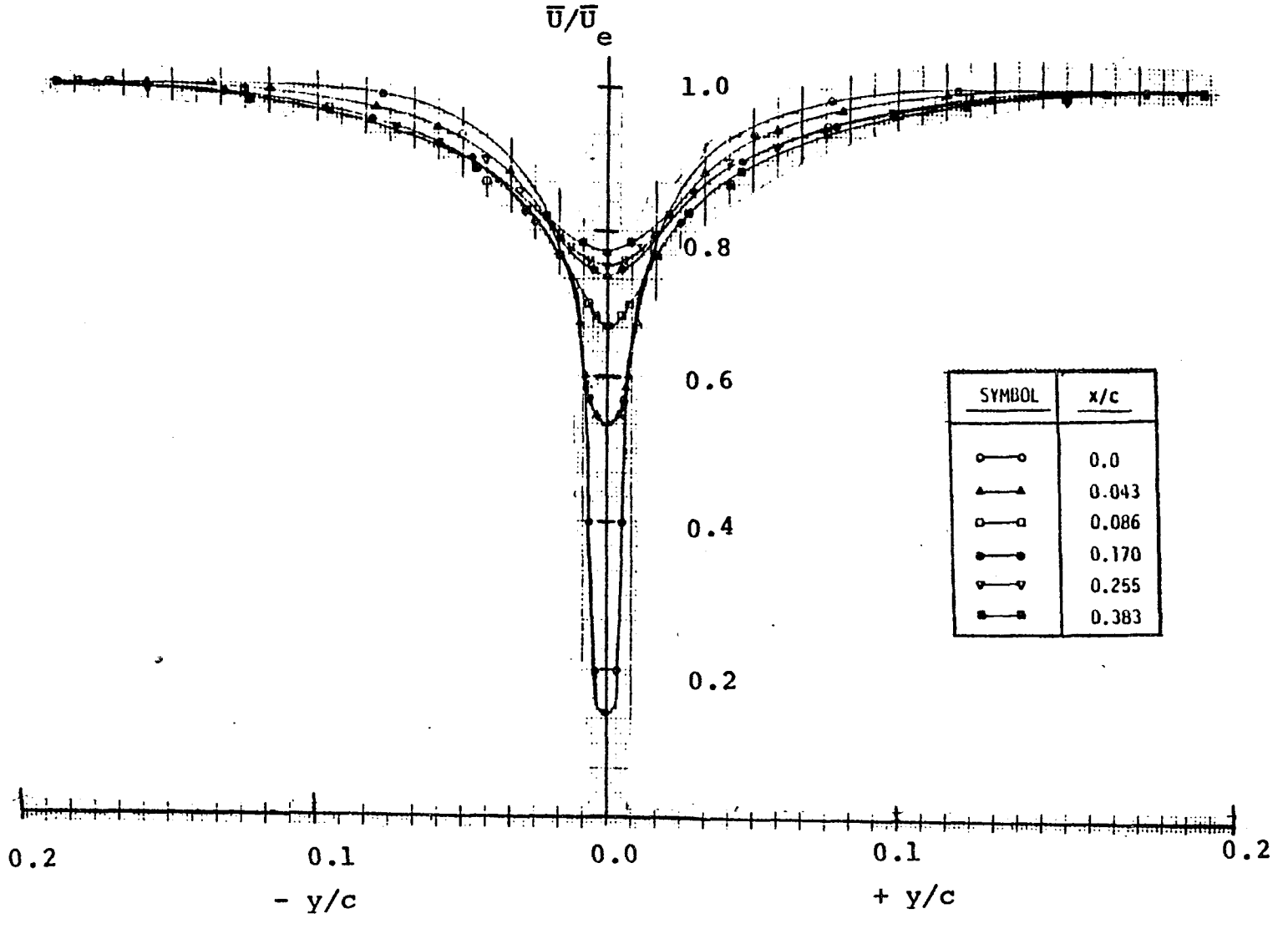

Figure 6.3(a) Mean Velocity Profile With Downstream Distance ($T_{L.E.}$ = 0.004)

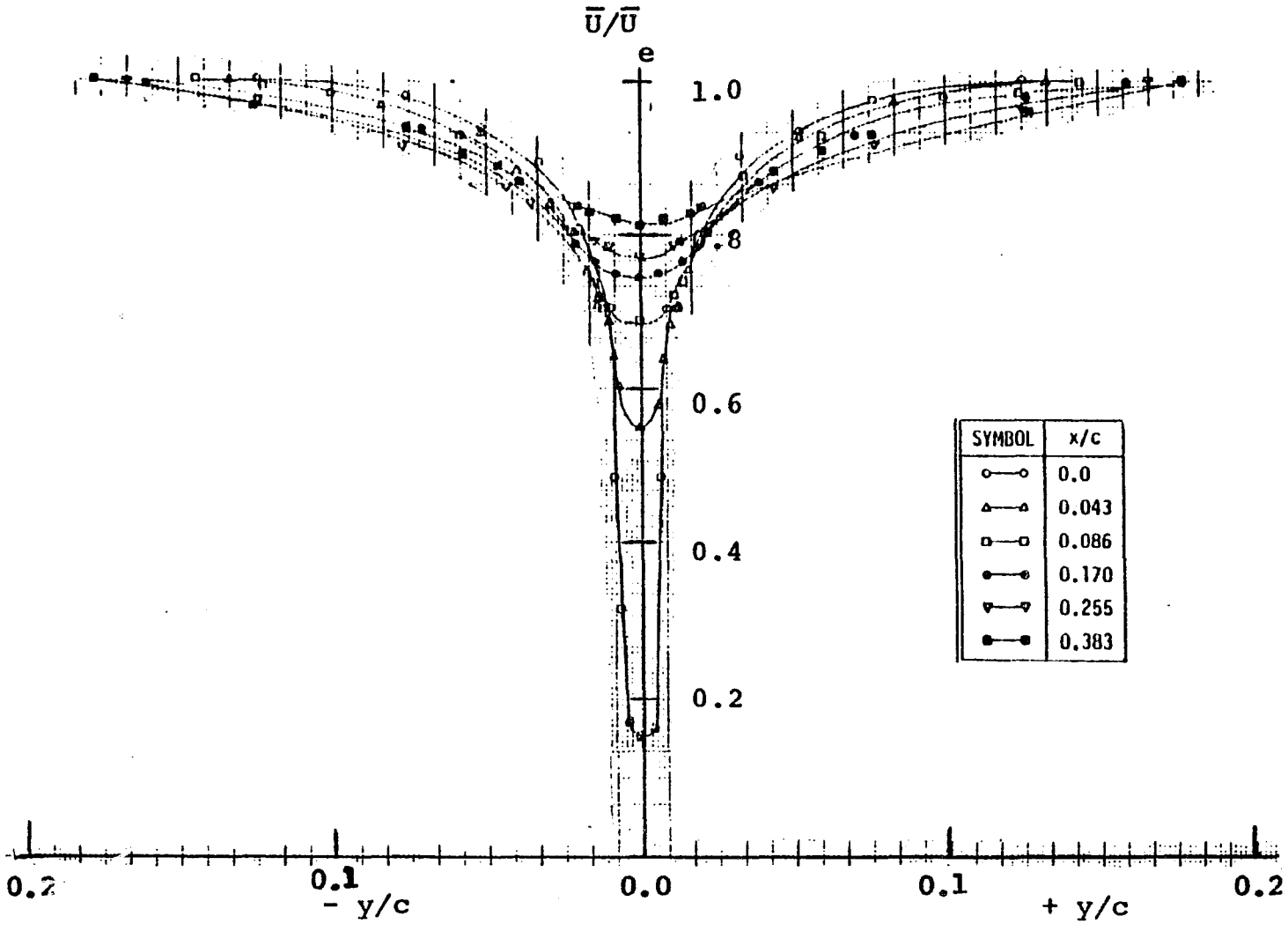

Figure 6.3(b) Mean Velocity Profile With Downstream Distance Distance ($T_{L.E.}$ = 0.0523)

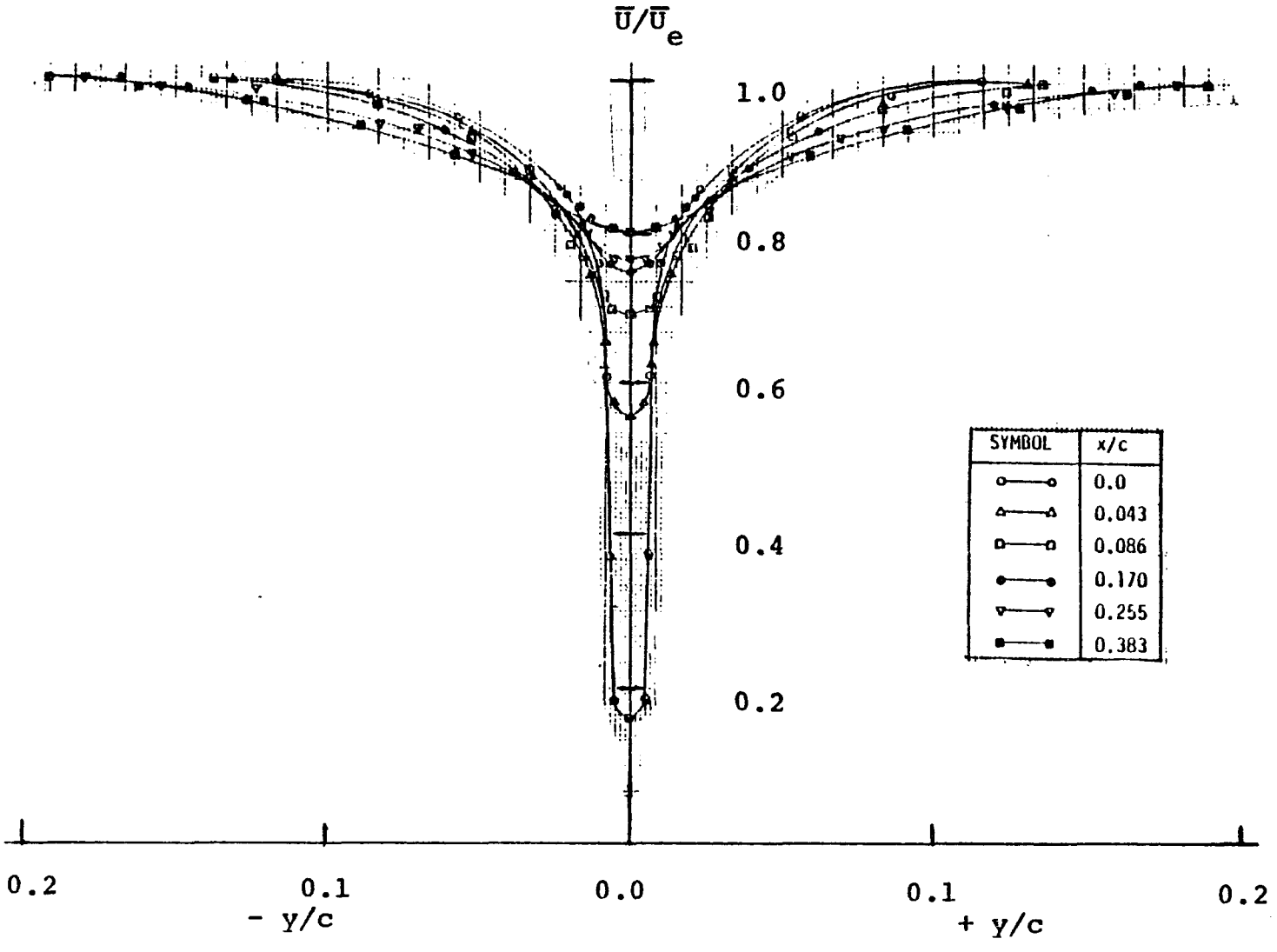

Figure 6.3(c) Mean Velocity Profile With Downstream Distance ($T_{L.E.}$ = 0.0723)

in multi-stage turbomachines, the velocity power index will be of the order of - 0.8 for the no pressure gradient case and is significantly larger than the ordinary power law of - 0.5 for no free stream and no pressure gradient.case. Note, therefore, that the above change in velocity power index is purely due to the effect of free stream turbulence. Earlier observation by Eagleson et. al. (30) on the flat plate wake data indicates that a presence of free stream turbulence of the order of 10 % changes the velocity power index to the order of - 1.00 and is consistent with the trends predicted by the present correlation (Eqn.3.18):

$$1 - \frac{\bar{U}_c}{\bar{U}_e} = \bar{K} \; c_d^{\frac{1}{2}} \left(\frac{x}{c} + \frac{x_0}{c}\right)^{-(1+\alpha_T)/2} \qquad \ldots(6.1)$$

The constant $\bar{K}$ in Eqn.(6.1) was found to depend upon the value of Φ_2 at the trailing edge and is given by the following correlation:

$$\bar{K} = \frac{2.70}{\Phi_{2t} + 0.76} \qquad \ldots(6.2)$$

For zero free stream turbulence case $\Phi_{2t} = 1.0$

and $\bar{K}$ becomes equal to 1.534, which is of the oder of magnitude of 1.25 reported in Ref.(1). The discrepancy in the value of $\bar{K}$ is due to the fact that the correlations developed in the present investigation are based on the flat plate data while the correlations given in Ref.(1) are based on isolated airfoil data. The

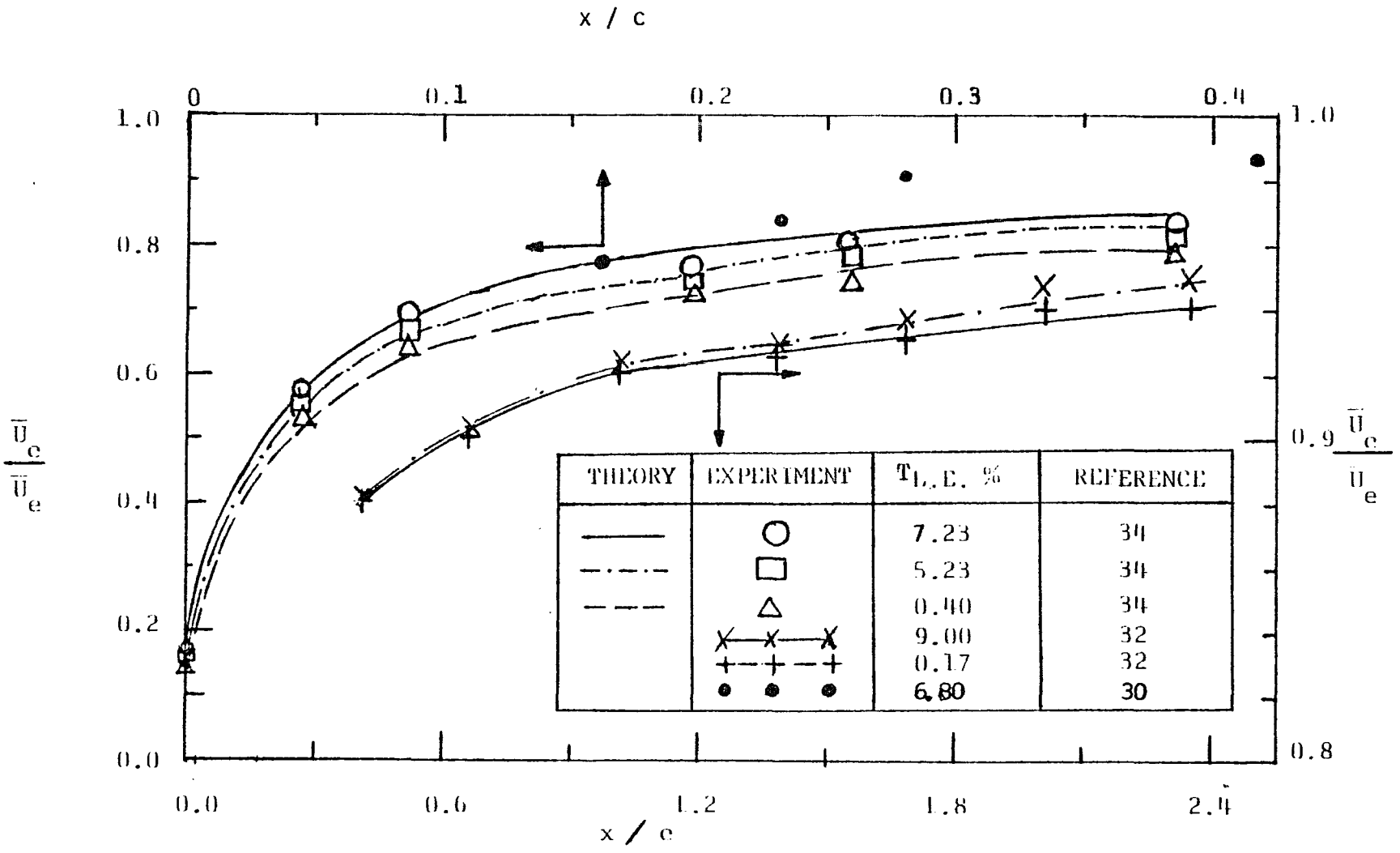

Figure 6.4(a) Variation of Wake Centerline Velocity With Downstream Distance

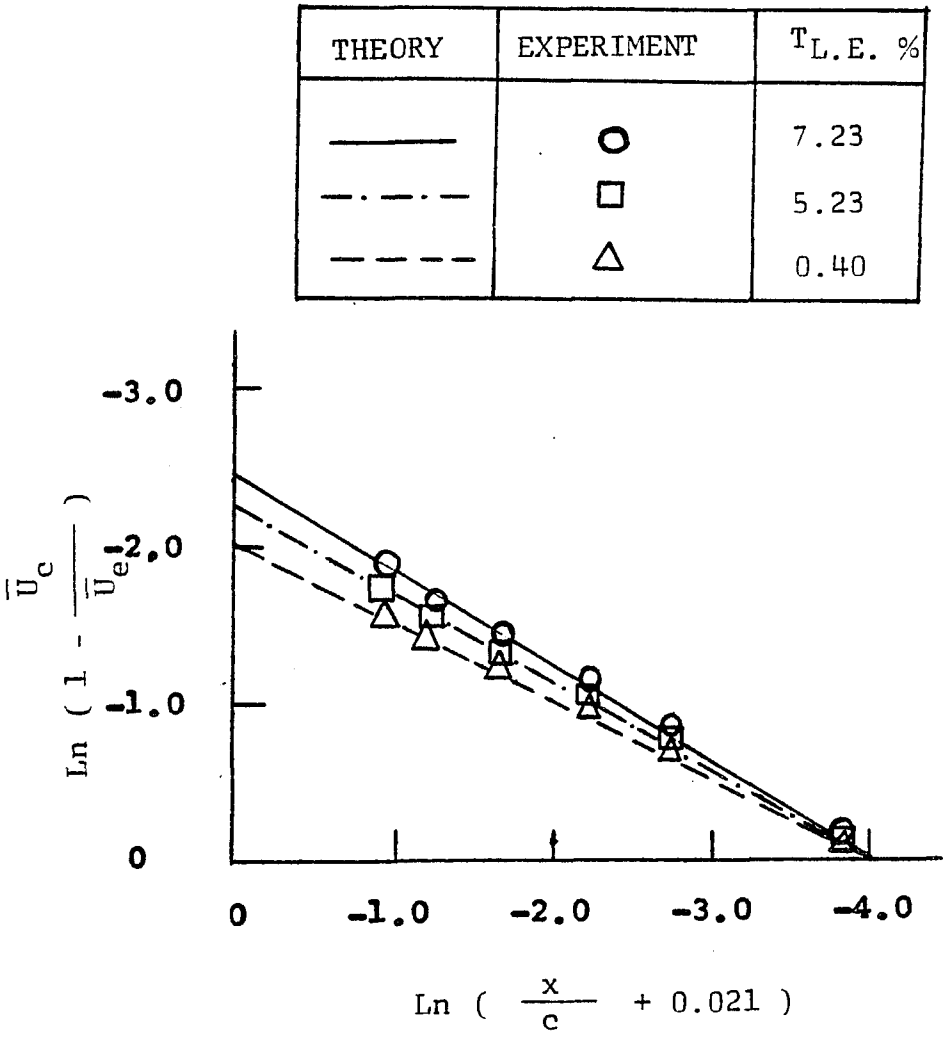

Figure 6.4(b) **Logarithmic Variation of the Center line Velocity With Downstream Distance**

trailing edge thickness in each case is different. The value of x_0/c in the present investigation was found to be 0.021. The coefficient of drag in the absence of free stream turbulence was found to be 0.0064. The coefficient of drag in the presence of free stream turbulence was obtained from the modified correlation given in Ref.(22) and is as follows:

$$C_d = C_{d0} (1 + 4.8 T) \qquad \ldots(6.3)$$

A few important observations can be made from Figure(6.4) about the wake center line velocity:

a. The effect of free stream turbulence on wake center line is predominant only in the near wake region, $x/c < 0.3$

b. The wake center line velocity recovers to about 65 % for $x/c < 0.1$.

c. The wake velocity power index is strongly dependent upon the free stream turbulence level.

d. The constant of proportionality in Eqn.(6.1) is dependent upon the trailing edge conditions.

The available data on the effect of free stream turbulence on the cylinder wake is beyond the range of our experimental data. Therefore, it is not possible to compare the two data. However, the trends indicated are similar to the one obtained in the present investigation.

The data of Ref.(30) is also shown in this figure. This data is for a turbulence level of the order of 6.8 %.

6.3.3 Length Scale (Half Wake Width) :

The effect of free stream turbulence on the variation of wake length scale in the downstream direction is shown in Figure 6.5. It is clear that free stream turbulence increases the length scale in the downstream direction. The increase in length scale of the wake is adequately given by the following correlation :

$$\frac{L_0 - L_{0t}}{c\, c_d^{\frac{1}{2}}} = 1.05 \left(x/c \right)^{(1 + \beta T)/2} \qquad \ldots(6.4)$$

where L_{0t} is the value of the length scale at the trailing edge of the flat plate. The value of β obtained from the experimental data is 8.27. The predictions of the growth law for the length scale of the wake with downstream distance in the presence of free stream turbulence are in good agreement with the data obtained experimentally (Fig. 6.5). It is interesting to note that the increase in exponent of the length scale is nearly twice the value of the exponent of the recovery of the wake center line velocity. This is due to the fact that free stream turbulence acts more strongly at the wake edges than at the wake center line.

The available data on the effect of free stream

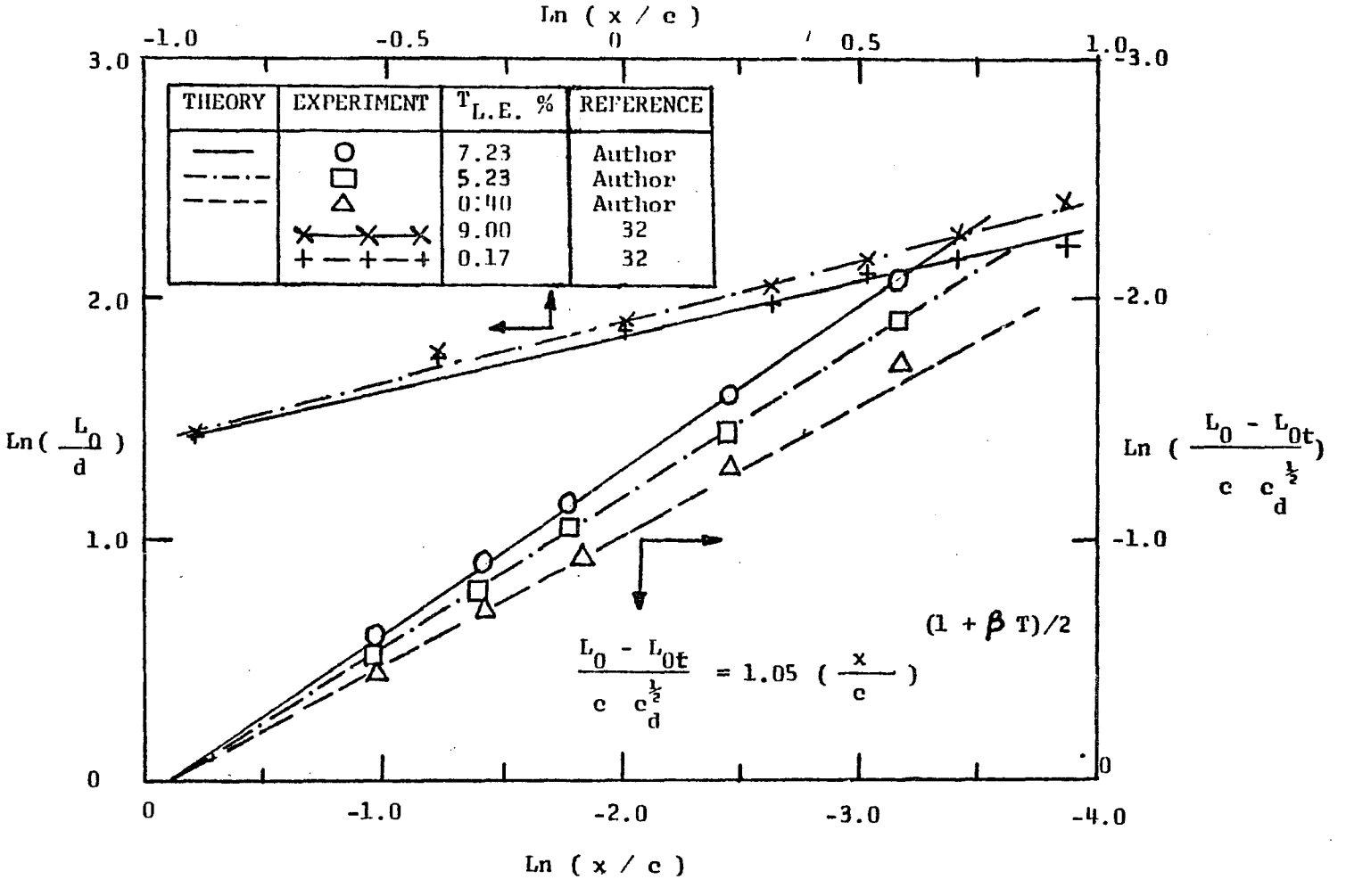

Figure 6.5 Logarithmic Variation of Length Scale With Downstream Distance

turbulence on the cylinder wake (Reference 32) is beyond the range of our experimental data. Therefore, it is not possible to compare the two data. But for far wake, an increase in length scale is observed and is consistent with the present investigation. It can be concluded that the higher is the free stream turbulence, the quicker is the growth of the wake.

6.3.4 Turbulence Parameters:

The parameters Φ_1 and Φ_2 are known as turbulence parameters. They are given by the following equations derived earlier in Chapter(III):

$$\Phi_1 = \left(\frac{x}{c} + \frac{x_0}{c} \right)^{\mathcal{L}_{T/2}} \qquad \ldots(6.5)$$

$$\Phi_2 = \left(\frac{x}{c} + \frac{x_0}{c} \right)^{-\beta_{T/2}} \qquad \ldots(6.6)$$

It is observed in earlier Sections 6.3.2 and 6.3.3 that $\mathcal{L}$ was found to be 4, β was found to be 8.27 and x_0/c was found to be 0.021 from the present investigation. The plots of Φ_1 and Φ_2 are shown in Figure 6.6. As mentioned in Chapter (III), these parameters represent the effect of free stream turbulence on velocity and length scales, respectively. The behavior of Φ_1 and Φ_2 is inverse to each other. While Φ_1 reduces the velocity scale, Φ_2 increases the length scale

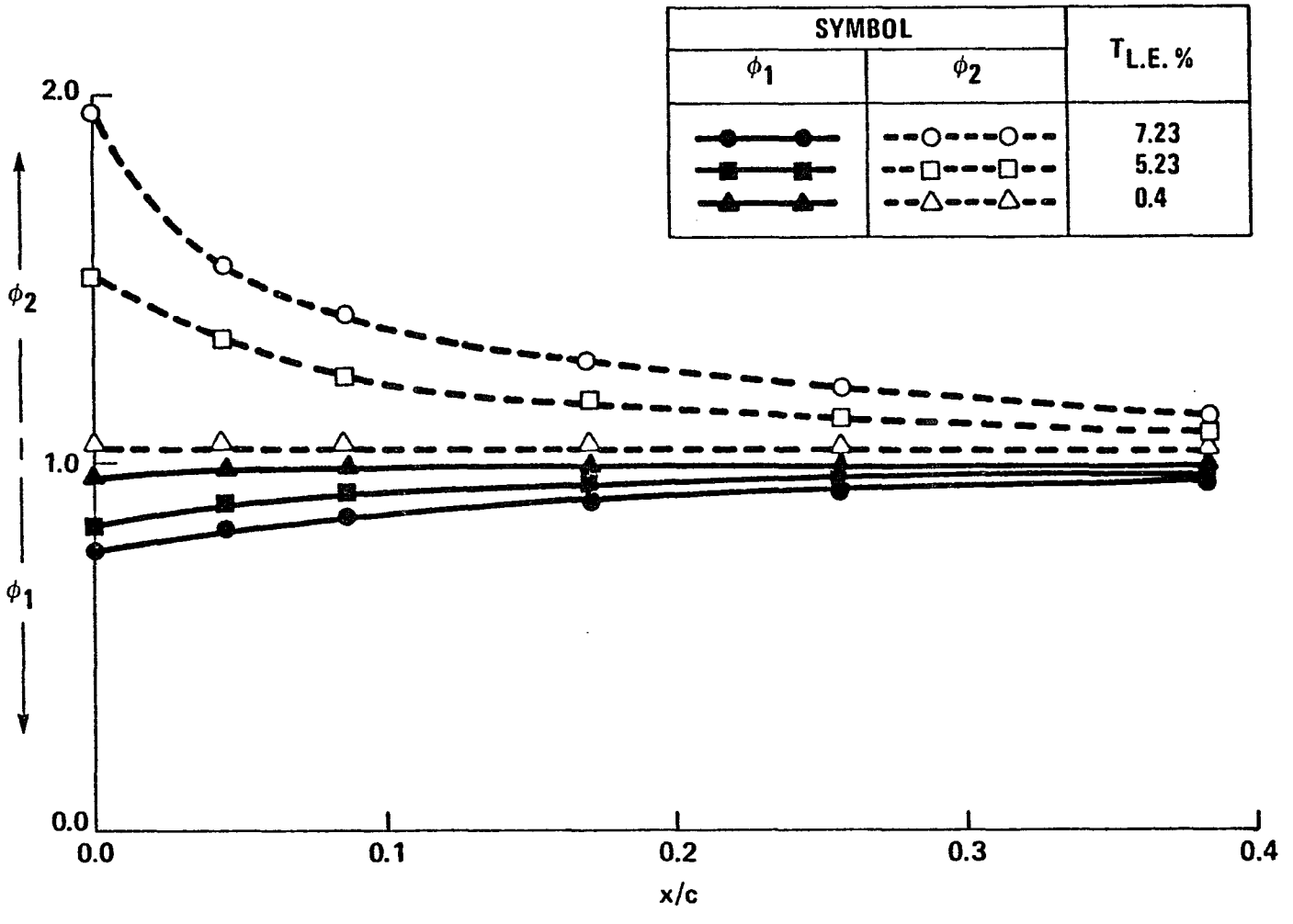

Figure 6.6 Variation of Turbulence Parameters with Distance Downstream of the Trailing Edge of a Flat Plate

with increase in free stream turbulence. However, both the parameters approach unity for zero free stream turbulence level or for far downstream distances where the free stream turbulence is substantially dissipated. The plots of these parameters also indicate that the maximum effect of free stream turbulence is felt only up to $x/c < 0.2$ and and this effect is negligible beyond $x/c > 1$.

6.3.5 Similarity:

In Figures 6.7(a), (b) and (c) an effort is made to reduce the velocity profiles given in Figures 6.3(a), (b) and (c) to a single curve. For this purpose, $L_0\ \Phi_2$ is used as the length scale while $U_0\ \Phi_1$ is used as the velocity scale. L_0 is the distance from the wake centerline to a point in the lateral direction where the velocity defect is 50 % and the velocity scale $U_0 = \bar{U}_e - \bar{U}_c$. It is clear from Figures 6.7(a), (b) and (c) that the similarity is maintained to a good extent and the similarity profiles are well described and lie between the functions $\left[1 - (\eta/2)^{1.5}\right]^2$ and $\exp(-\eta^2/2)$ wher $\eta = y/L_0\ \Phi_2$.

The ratio $\dfrac{U_0\ L_0\ \Phi_1\ \Phi_2}{\bar{U}_e\ c}$ is found to be nearly constant at all the axial locations beyond $x/c > 0.05$ (Fig. 6.8). This confirms the similarity assumptions

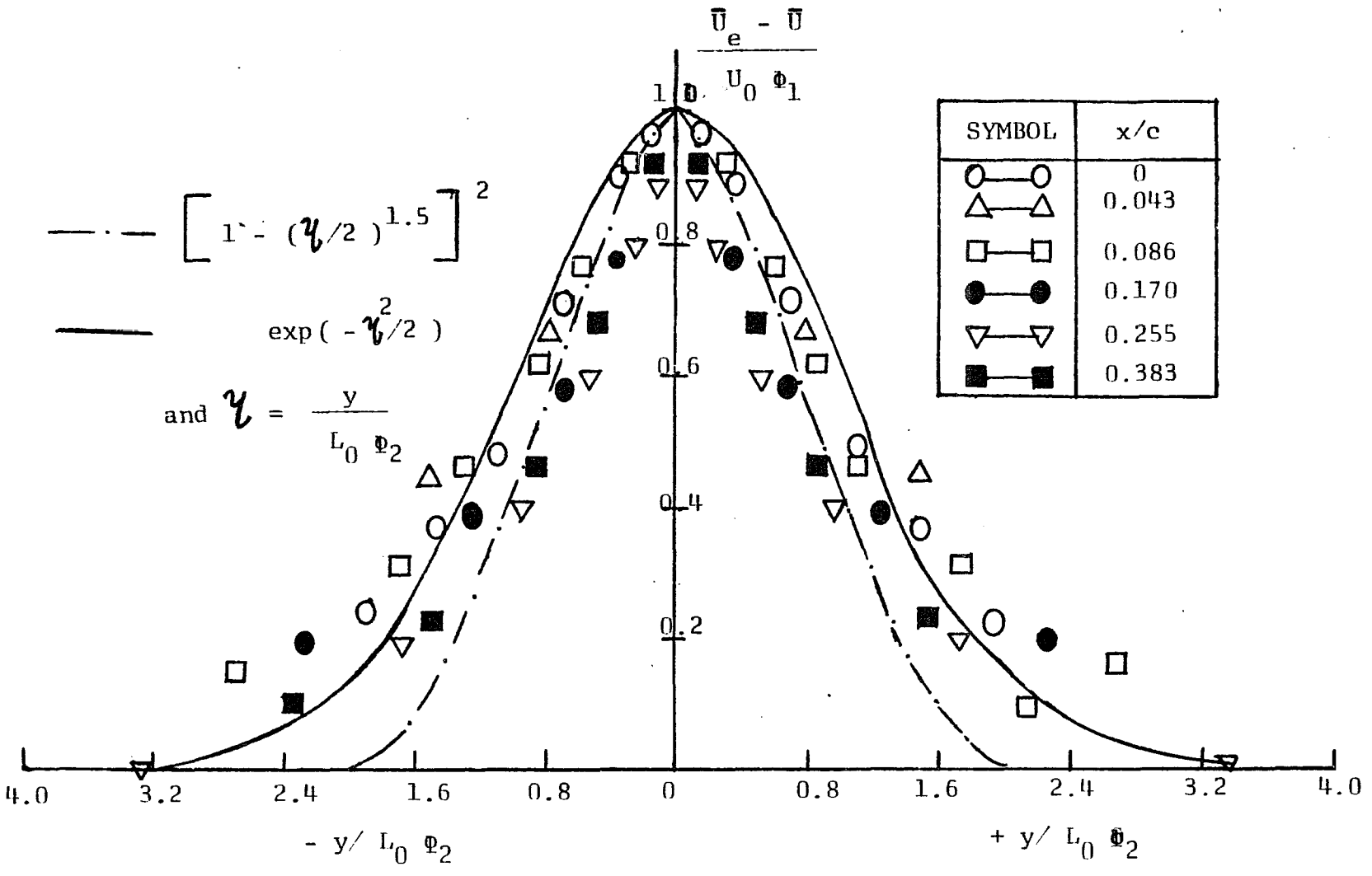

Figure 6.7(a) Similarity of Mean Velocity Profile ($T_{L.E.} = 0.004$)

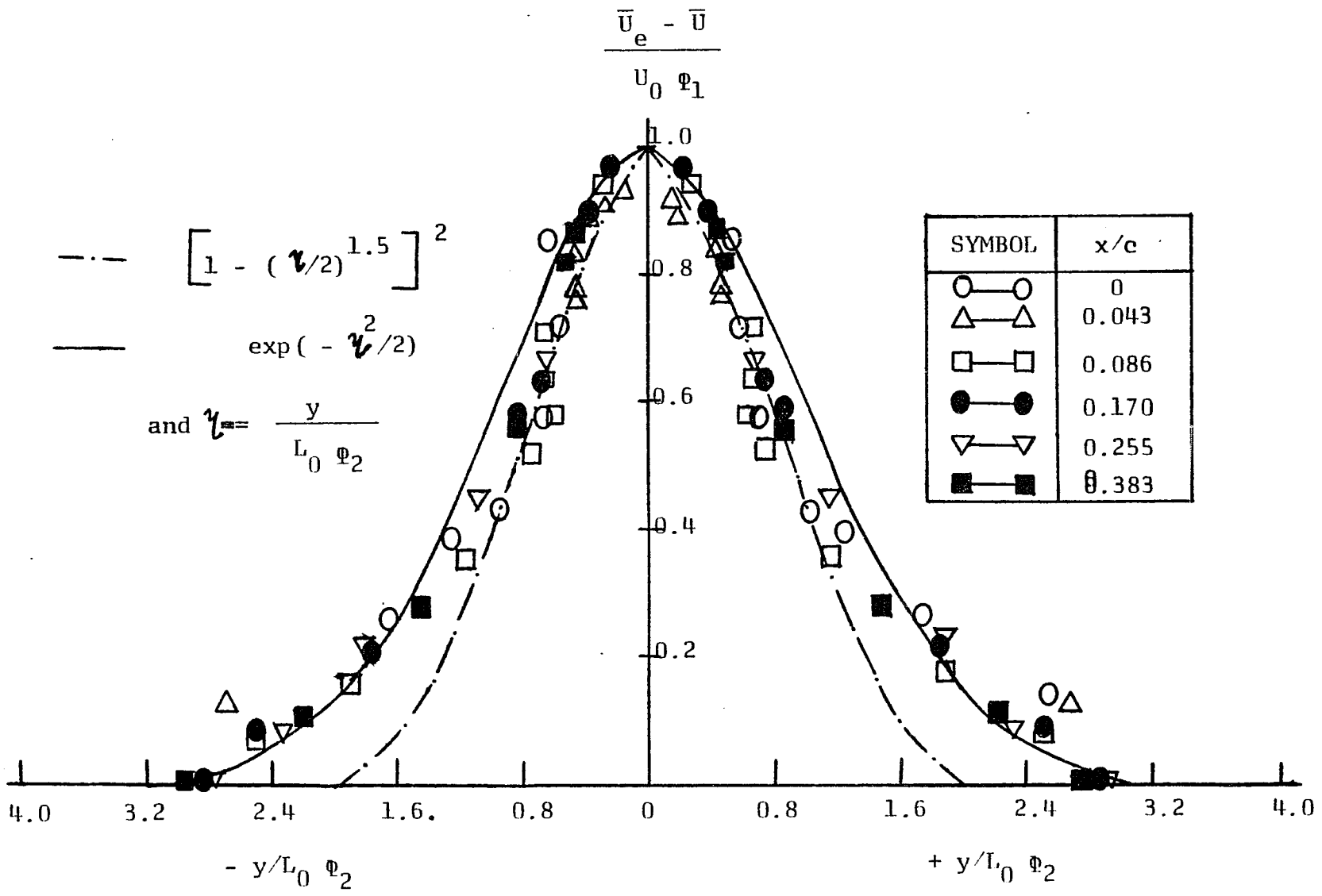

Figure 6.7 (b) Similarity of Mean Velocity Profile ($T_{L.E.} = 0.0523$)

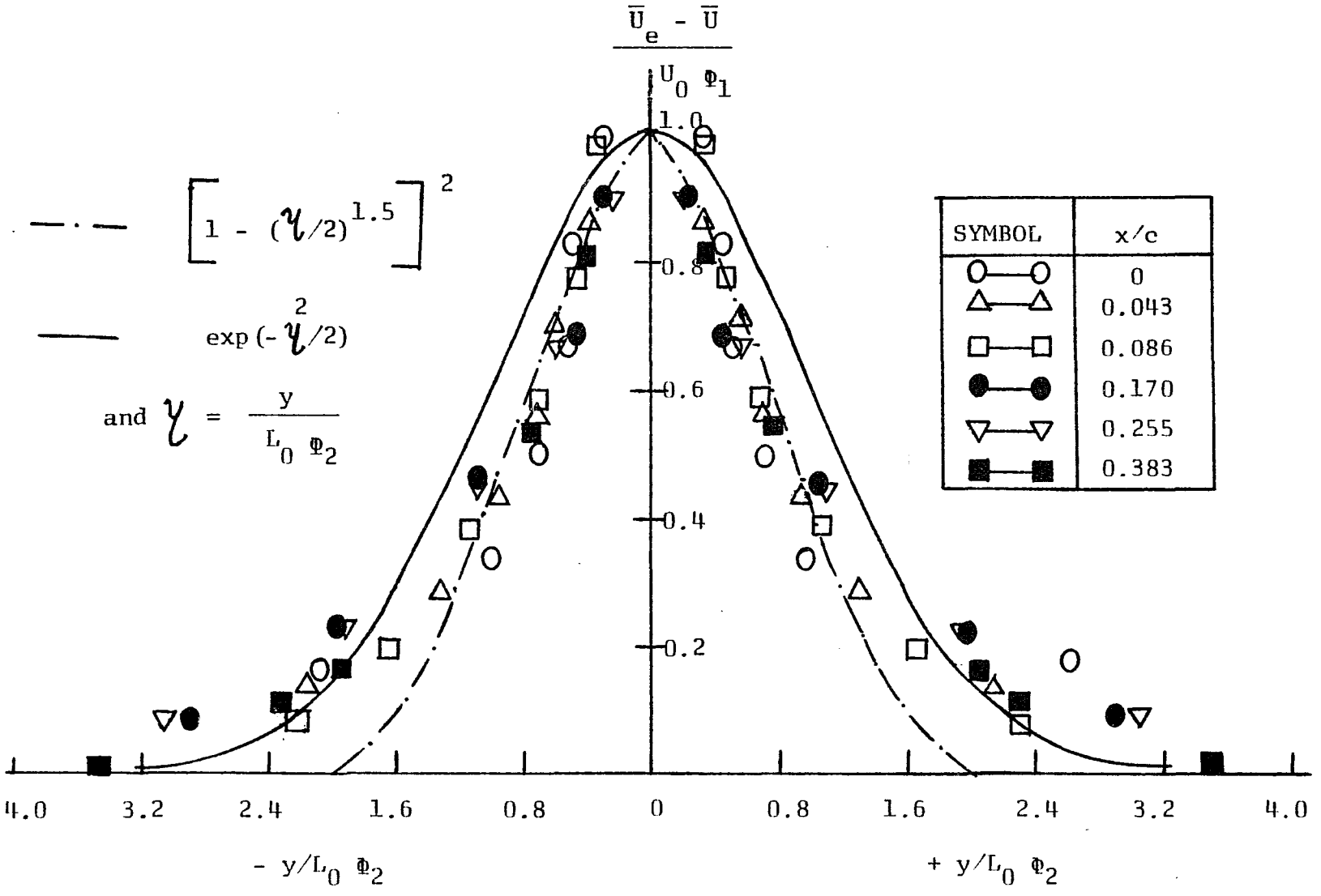

Figure 6.7 (c) Similarity of Mean Velocity Profile ($T_{L.E.} = 0.0723$)

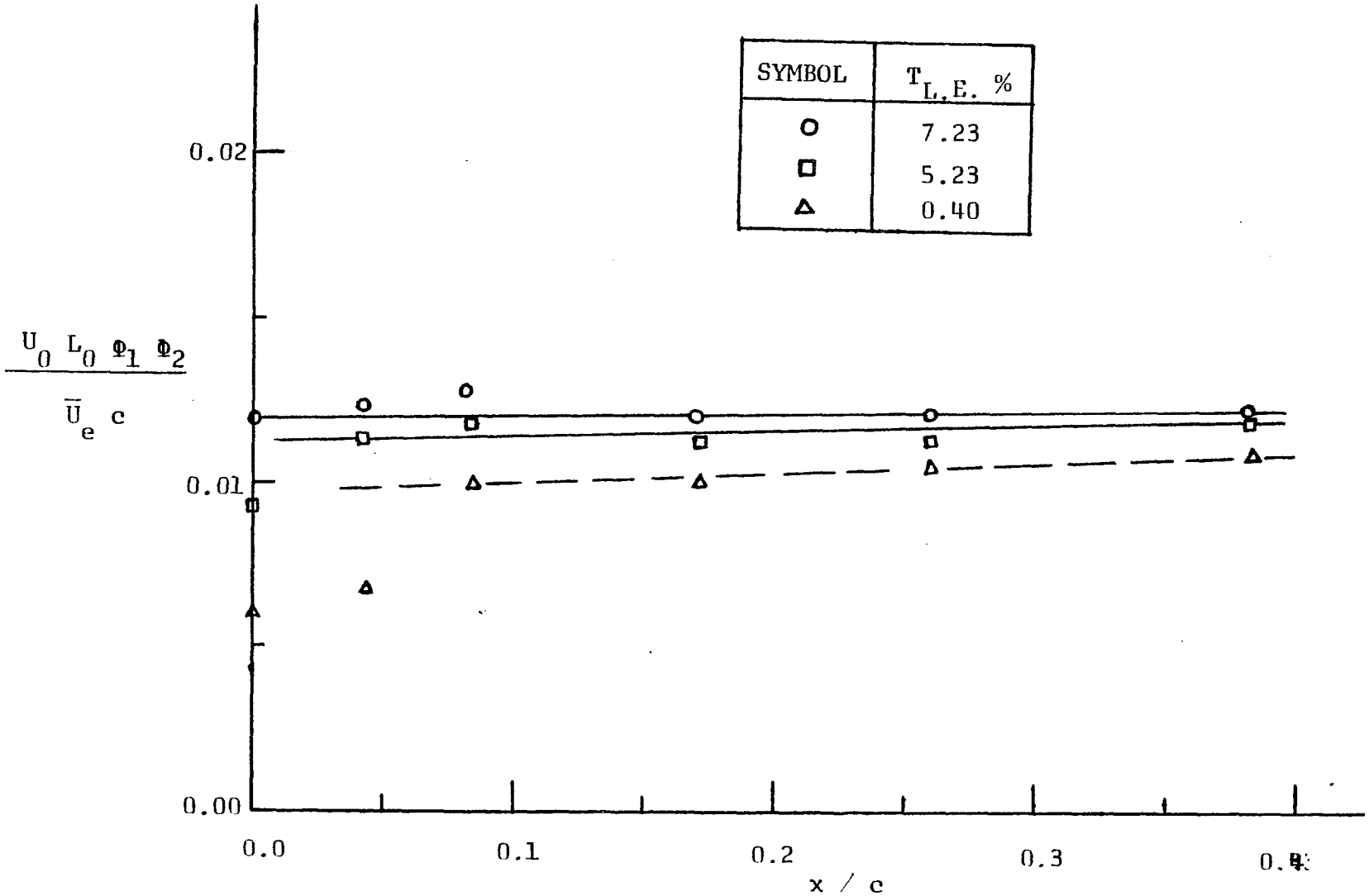

Figure 6.8 Variation of $\frac{U_0 L_0 \Phi_1 \Phi_2}{\bar{U}_e c}$ With Downstream Distance

made in Chapter (III). However, for $x/c < 0.05$, a slight scatter in the value $\frac{U_0 L_0 \Phi_1 \Phi_2}{\bar{U}_e c}$ is observed.

6.3.6 Displacement Thickness, Momentum Thickness, Shape Factor and Energy Thickness:

The variation of displacement thickness (δ_1), momentum thickness (θ), shape factor (H) and energy thickness (δ_2) with downstream distance from the trailing edge of a flat plate is shown in Figures 6.9(a), (b), (c), and (d), respectively. It is clear from Figure 6.9(a) that the displacement thickness is very slowly decreasing, i.e., nearly constant with downstream distance. This is also predicted from theory, since

$$\delta_1 = \int_{-\infty}^{\infty} \left(1 - \frac{\bar{U}}{\bar{U}_e} \right) dy$$

after substitution of Eqn.(3.3), can be rewritten as:

$$\frac{\delta_1}{c} = \frac{U_0 L_0 \Phi_1 \Phi_2}{\bar{U}_e c} \int_{-\infty}^{\infty} f \, d\eta \qquad \ldots(6.7)$$

It is also shown in Sections 3.2.2 and 6.3.5 that the similarity profile 'f' , can be well described by the function:

$$f = \exp(- \eta^2/2)$$

Therefore Eqn.(6.7) becomes:

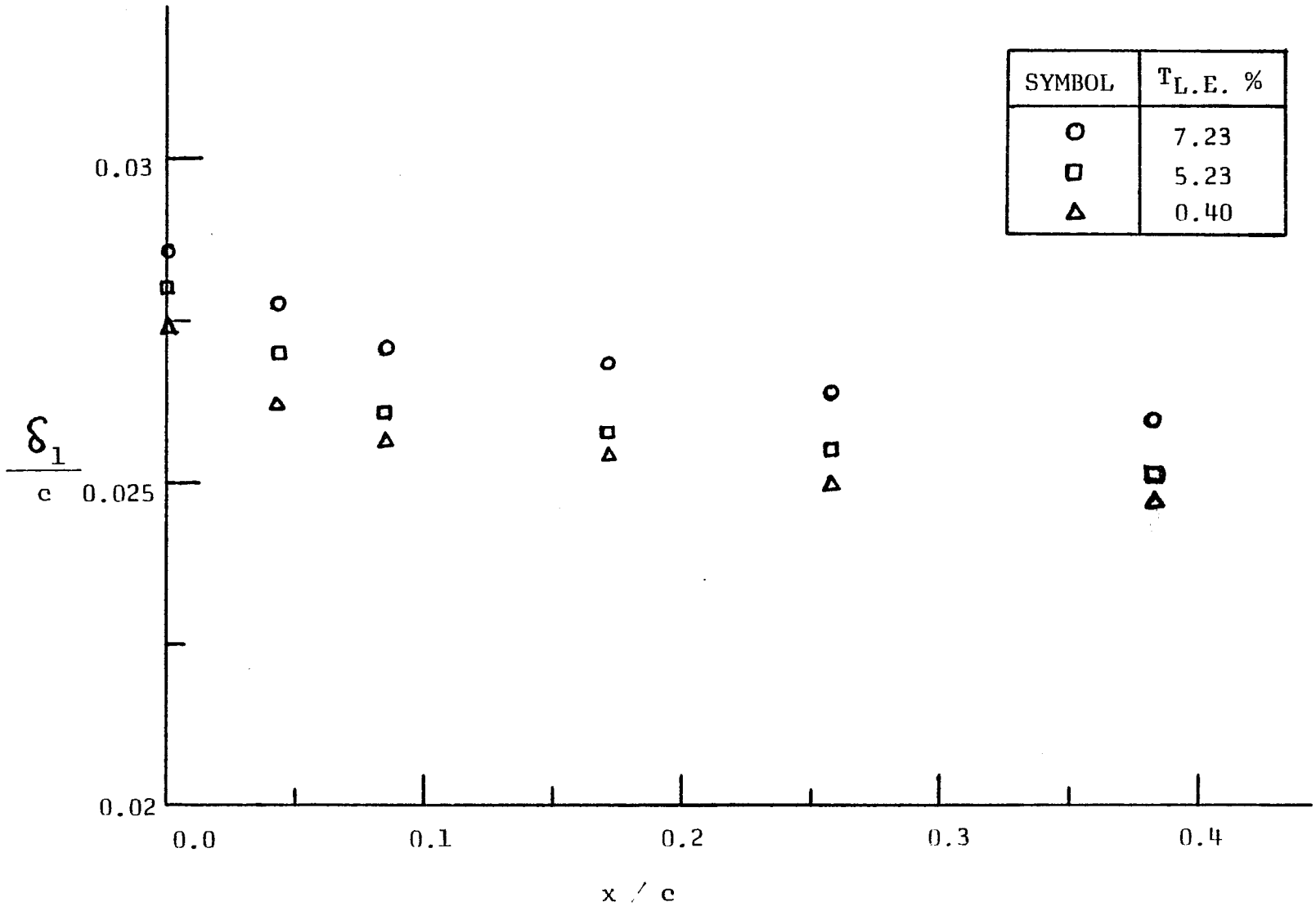

Figure 6.9(a) Variation of Displacement Thickness With Downstream Distance

$$\frac{\delta_1}{c} = \frac{U_0 \; L_0 \; \Phi_1 \; \Phi_2}{\bar{U}_e \; c} \left(2\pi \right)^{\frac{1}{2}} \qquad \ldots(6.8)$$

Since $U_0 \; L_0 \; \Phi_1 \; \Phi_2 = K_1$ from Eqn.(3.7).

Therefore, δ_1 is constant for a given level of free stream turbulence. A plot of $U_0 \; L_0 \; \Phi_1 \; \Phi_2 / \bar{U}_e \; c$ (Fig.6.8) when multiplied by $\left(2\pi \right)^{\frac{1}{2}}$ gives the results presented in Figure 6.9 (a). However, note that the larger is the free stream turbulence, the higher is the value of δ_1, as is evident from Figures 6.8 and 6.9(a).

The momentum thickness, Figure 6.9(b), on the other hand, increases slightly near the trailing edge and further downstream ($x/c \simeq 0.075$) becomes constant. This trend is also predicted by theory, since

$$\theta = \int_{-\infty}^{\infty} \frac{\bar{U}}{U_e} \left(1 - \frac{\bar{U}}{\bar{U}_e} \right) dy$$

after substitution of Eqn.(3.3), becomes,

$$\theta = \frac{U_0 \; L_0 \; \Phi_1 \; \Phi_2}{\bar{U}_e} \left(I_1 - \frac{U_0 \Phi_1}{\bar{U}_e} I_2 \right) \qquad \ldots(6.9)$$

where $I_1 = \int_{-\infty}^{\infty} f \, d\eta$ and $I_2 = \int_{-\infty}^{\infty} f^2 \, d\eta$

Rearranging Eqn.(6.9)

$$\frac{\theta}{c} = \frac{K_1}{\bar{U}_e \; c} \left[I_1 - \frac{U_0 \; \Phi_1}{\bar{U}_e} I_2 \right] \qquad \ldots(6.10)$$

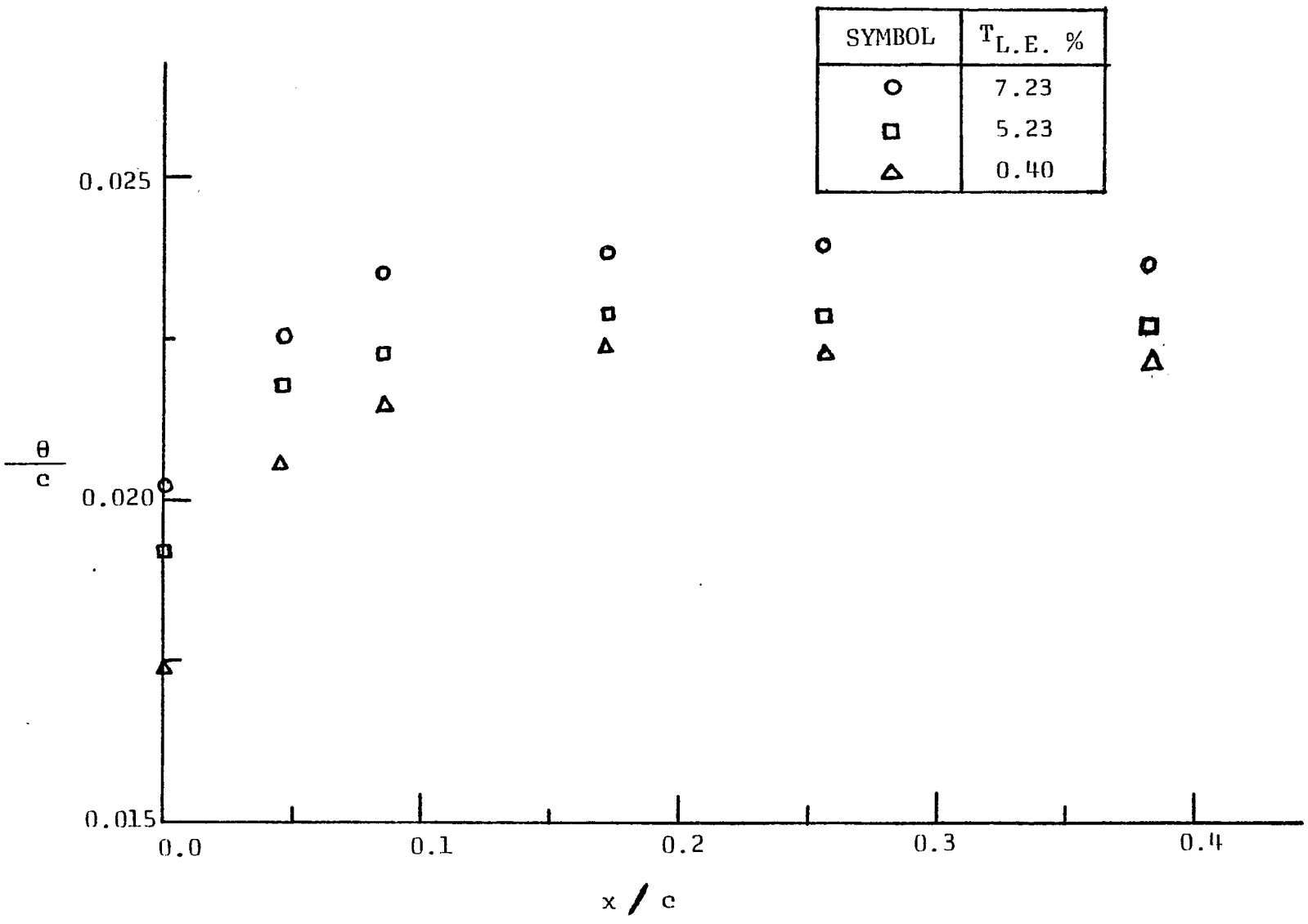

Figure 5.9(b) Variation of Momentum Thickness With Downstream Distance

Since for a given similarity profile, f, I_1 and I_2 are constant and $U_0 \Phi_1$ decreases with downstream distance. However, further downstream ($x/c > 0.38$), the term $U_0 \Phi_1/\bar{U}_e << 1$, therefore,

$$\frac{\theta}{c} \simeq \frac{K_1}{\bar{U}_e c} \simeq \frac{\delta_1}{c}$$

Note here also that the larger the free stream turbulence, the larger is the increase in momentum thickness. At the trailing edge, free stream turbulence levels of 2.56 and 4.00 percent increase the momentum thickness by 9.56 and 15.92 percent respectively, compared to the free stream turbulence level of 0.4 %.

The shape factor, (H), is obtained from Eqns. Eqns.(6.8) and (6.10), $H = \delta_1/\theta$ and can be rewritten by the following equation:

$$\frac{1 - \frac{1}{H}}{1 - \frac{1}{H_t}} = \frac{\Phi_1}{\Phi_{1t}} \left(1 + \frac{x/c}{x_0/c} \right)^{-(1 + \mathcal{C}_T)/2} \qquad \ldots(6.11)$$

where Φ_{1t} and H_t are values of Φ_1 and H at the trailing edge. The theoretical curve (Equation 6.11) is plotted together with the experimentally obtained results, Figure 6.9(c), and is found to be quite satisfactory. It is clear from the data and Eqn.(6.11) that free stream

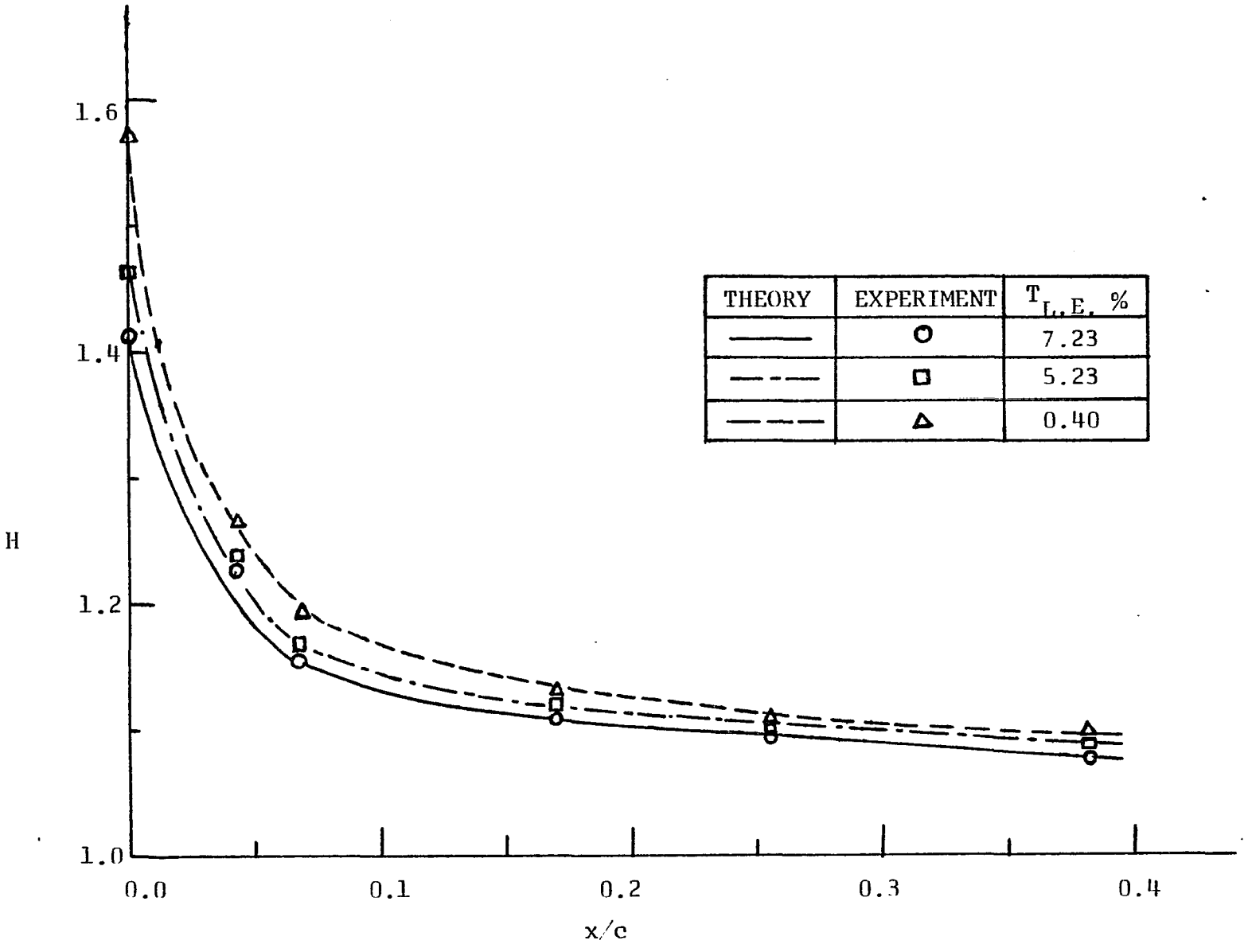

Figure 6.9(c) Variation of Shape Factor With Downstream Distance

turbulence reduces the value of shape factor.

Energy thickness, δ_2, Figure 6.9(d) increases slowly with downstream distance up to $x/c = 0.25$ and then starts decreasing with downstream distance. This is also predicted from theory, since

$$\delta_2 = \int_{-\infty}^{\infty} \frac{\bar{U}}{\bar{U}_e} \left(1 - \frac{\bar{U}^2}{\bar{U}_e^2} \right) dy$$

after substitution of Eqn.(3.3), can be rewritten as:

$$\delta_2 = \frac{U_0 L_0 \Phi_1 \Phi_2}{\bar{U}_e} \left[2 I_1 - 3 \frac{U_0 \Phi_1}{\bar{U}_e} I_2 + \frac{U_0^2 \Phi_1^2}{\bar{U}_e^2} I_3 \right] \quad \ldots(6.12)$$

where $I_3 = \int_{-\infty}^{\infty} f^3 \, d\eta$

Rearranging Eqn.(6.12),

$$\frac{\delta_2}{c} = \frac{K_1}{\bar{U}_e \; c} \left[2 I_1 - 3 \frac{U_0 \Phi_1}{\bar{U}_e} I_2 + \frac{U_0^2 \Phi_1^2}{\bar{U}_e^2} I_3 \right] \quad \ldots.(6.13)$$

Since for a given similarity profile, f, I_1 , I_2 and I_3 are constant and $U_0 \Phi_1$ decreases with downstream distance, therefore, δ_2/c , increases with downstream distance. However, further, downstream ($x/c > 0.38$), the term $U_0 \Phi_1 / \bar{U}_e << 1.0$, therefore,

$$\frac{\delta_2}{c} \sim \frac{2 K_1}{\bar{U}_e \; c} \sim \frac{2 \delta_1}{c}$$

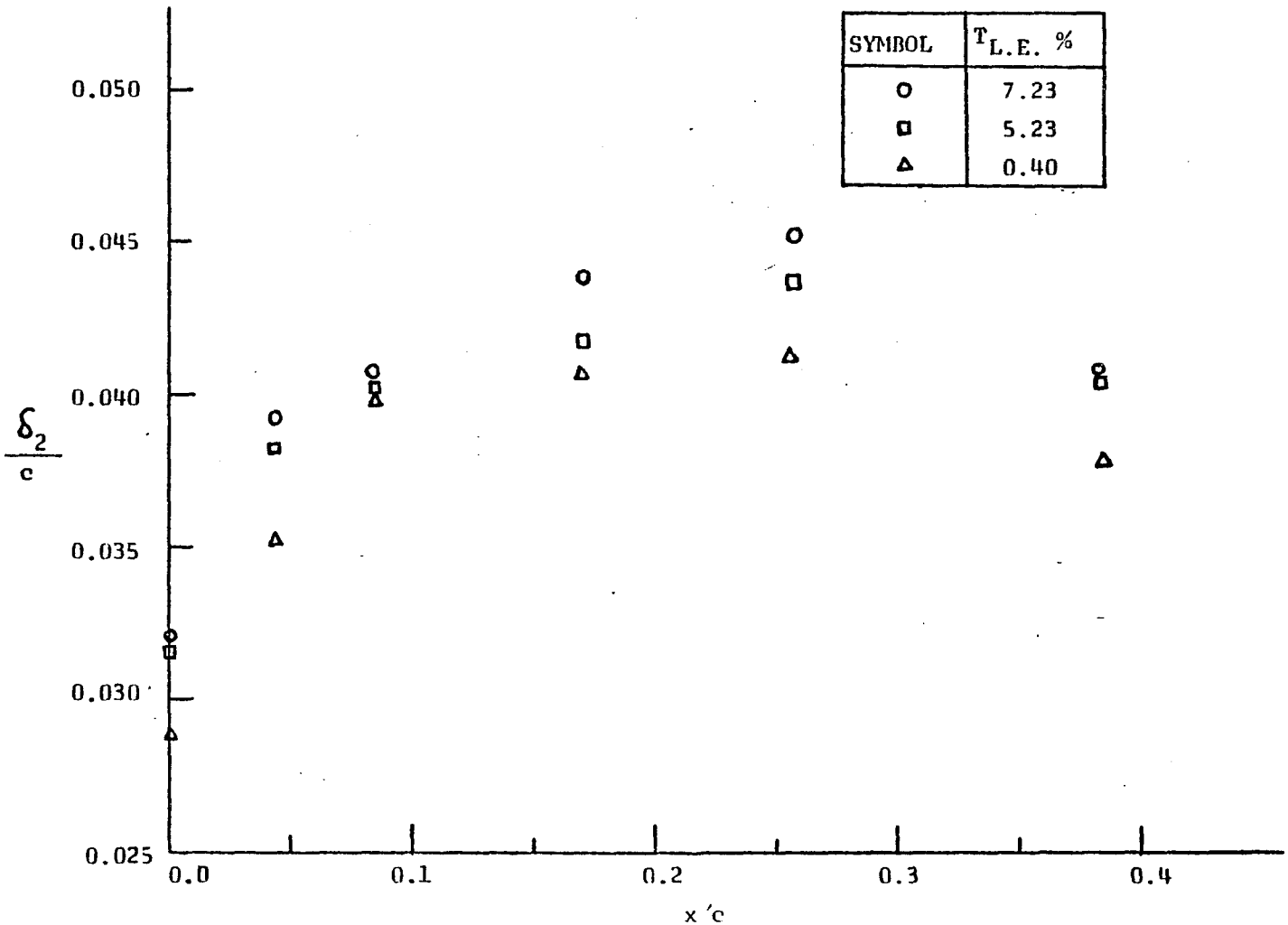

Figure 6.9(d) Variation of Energy Thickness With Downstream Distance

It is also observed that the increase of free stream turbulence increases the energy thickness.

6.4 Turbulence Quantities:

The data on turbulence quantities ($\sqrt{\overline{u^2}}$, $\sqrt{\overline{v^2}}$, $\overline{uv}$) are presented in the dimensionless form using 'c' and $\overline{U}_e$ as the dimensional parameters for the axial distance and the turbulence intensity, respectively. Decay behavior of maximum values of turbulence intensity and Reynolds stress is presented. Correlation coefficient and self - preservation parameters are obtained.

6.4.1 Turbulence Intensity:

Longitudinal and lateral components of turbulence intensity for three levels of free stream turbulence and at six axial locations (Fig. 5.2) are shown in Figures 6.10(a) to 6.10(f) and Figures 6.11(a) to (f), respectively. Longitudinal and lateral components of turbulence intensity were found to be nearly symmetrical about the wake center line. Peak values of the components of turbulence intensity occur away from the wake center line. It is observed that the distance in the lateral direction from the wake center line to a point where the maximum value of turbulence intensity occurs, increases due to free stream turbulence and to the distance downstream of the flat plate trailing edge. It is also observed that the turbulence intensities increase with increase in free stream

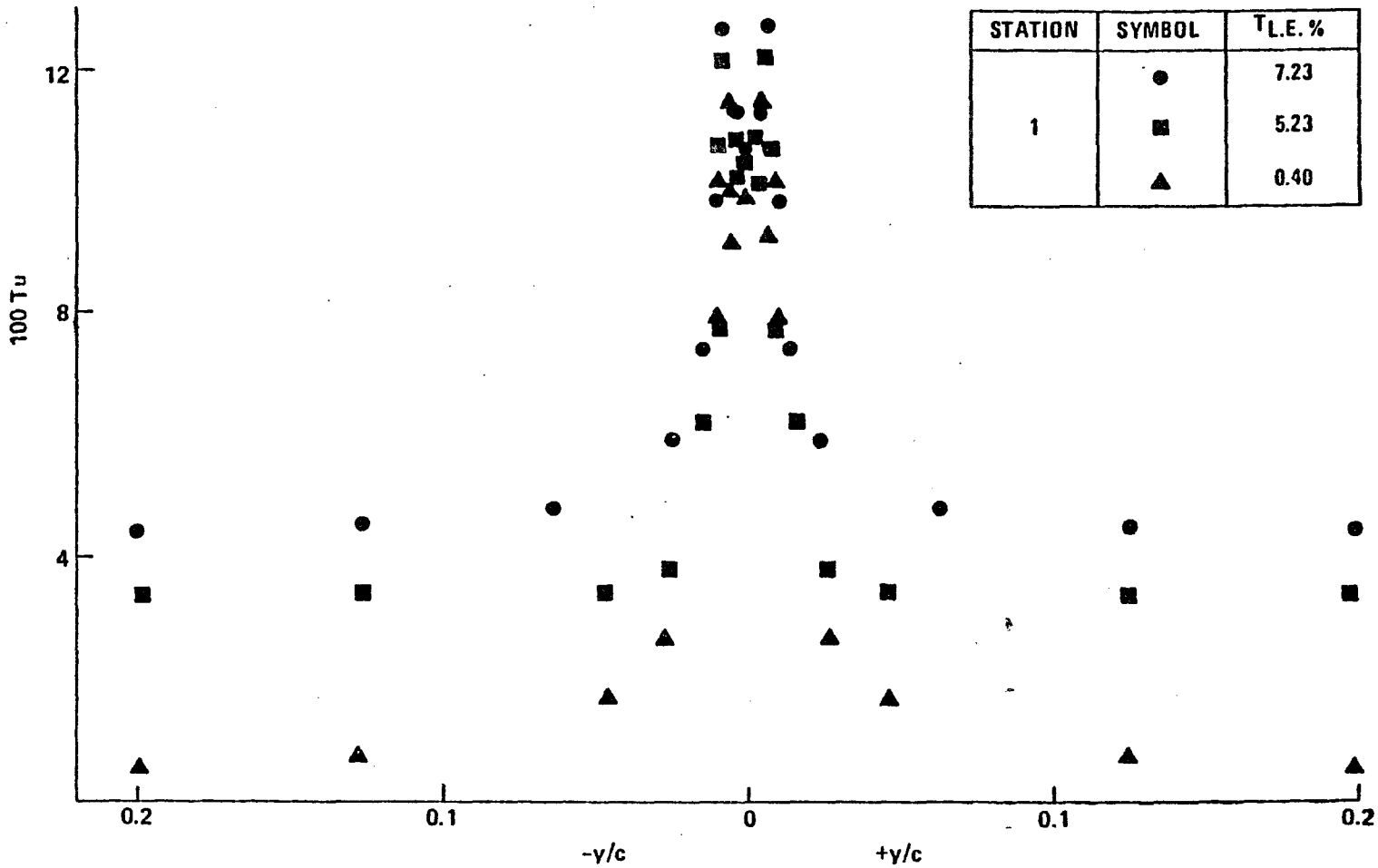

Figure 6.10(a) Variation of Longitudinal Component of Turbulence Intensity Across the Wake (x/c = 0.0)

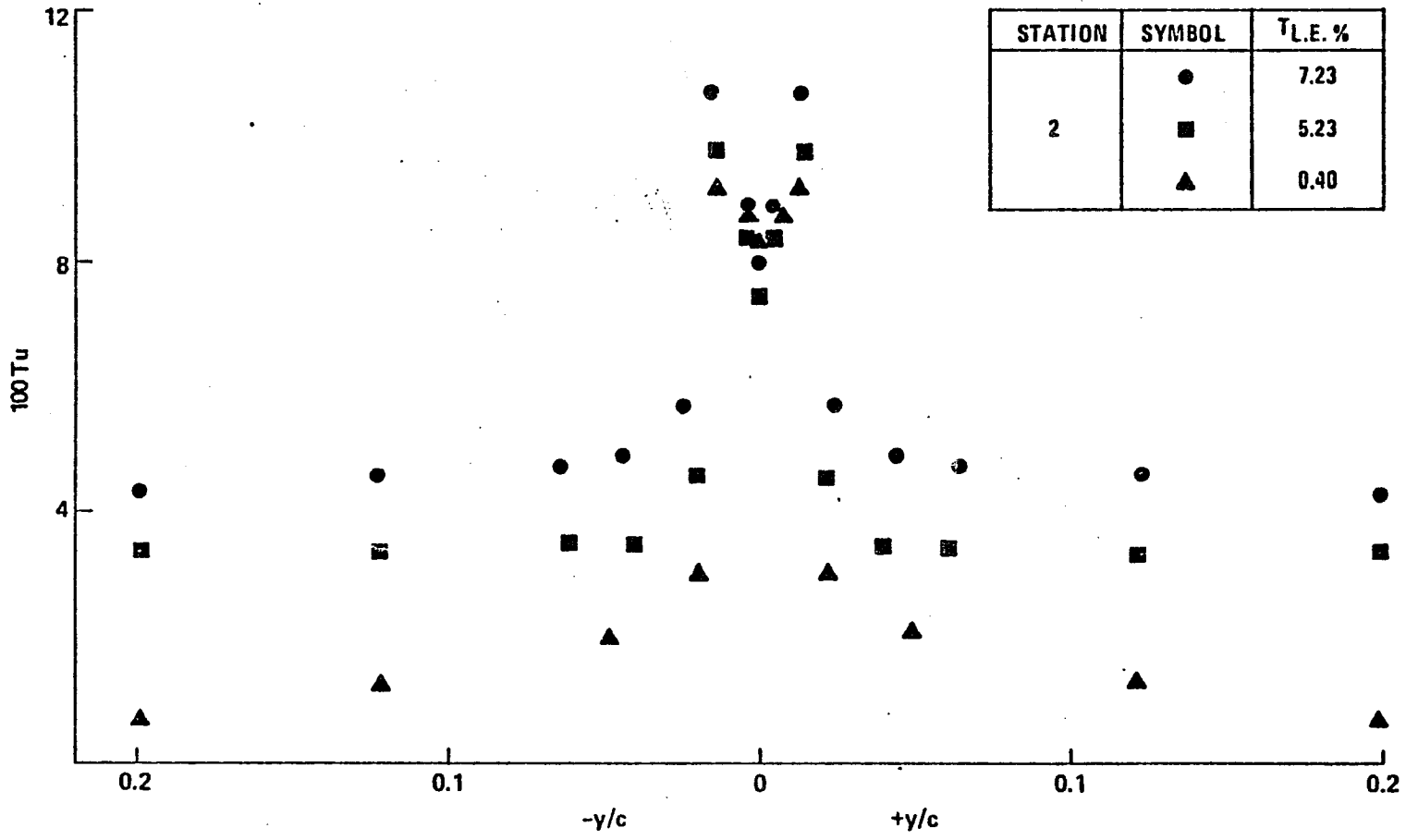

Figure 6.10(b) Variation of Longitudinal Component of Turbulence Intensity Across the Wake (x/c = 0.043)

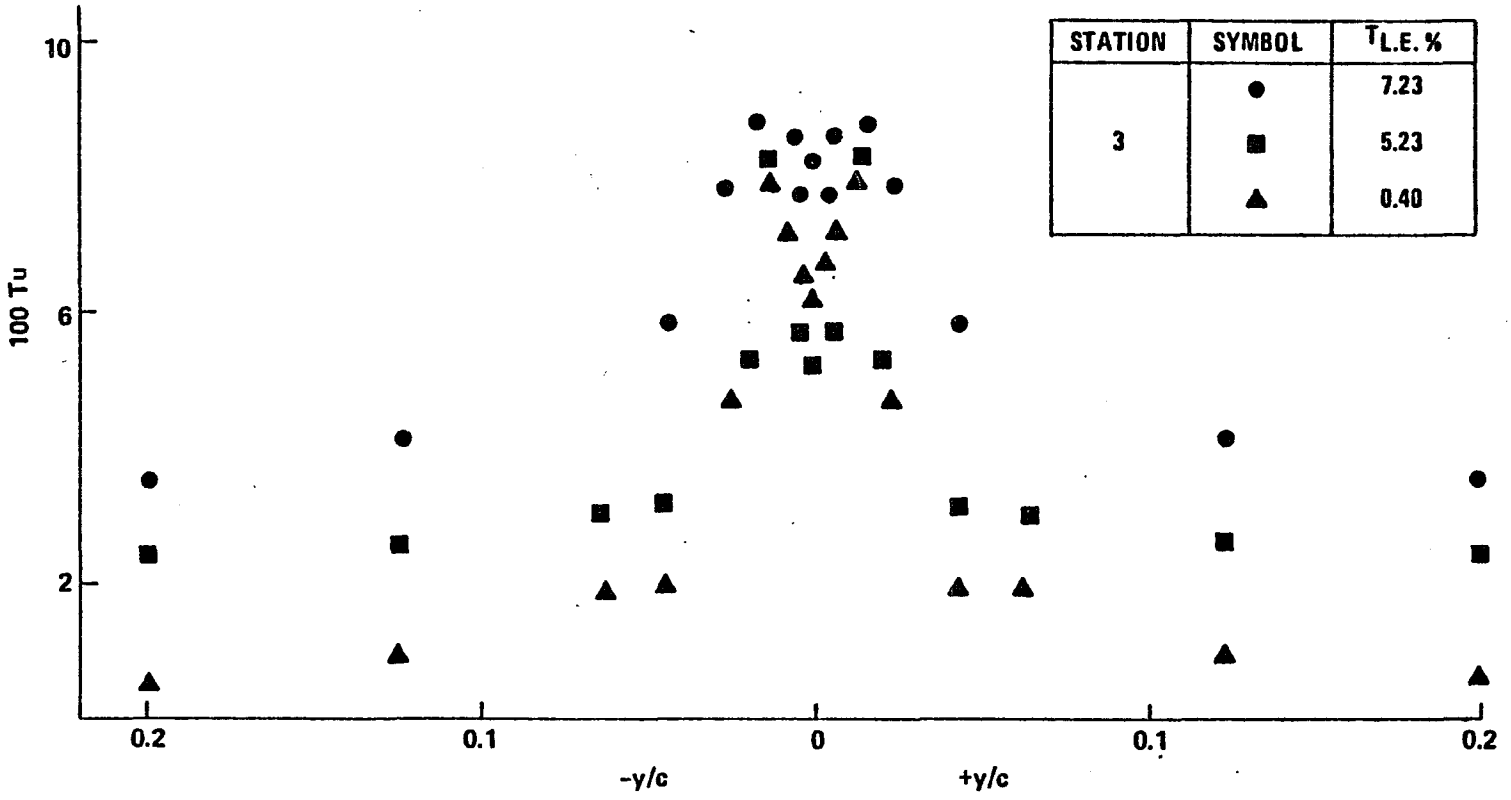

Figure 6.10(c) Variation of Longitudinal Component of Turbulence Intensity Across the Wake (x/c = 0.086)

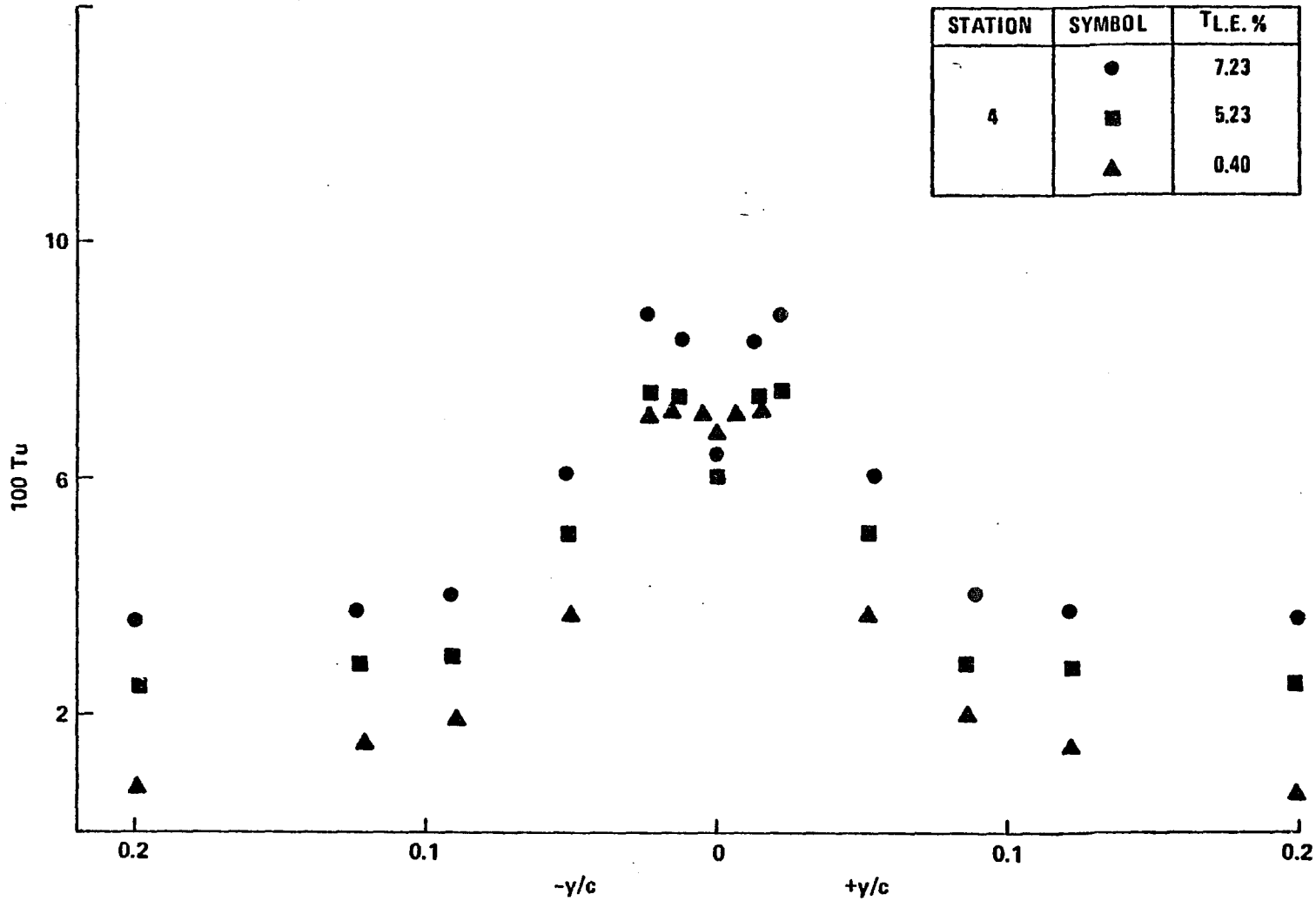

Figure 6.10(d) Variation of Longitudinal Component of Turbulence Intensity Across the Wake (x/c = 0.170)

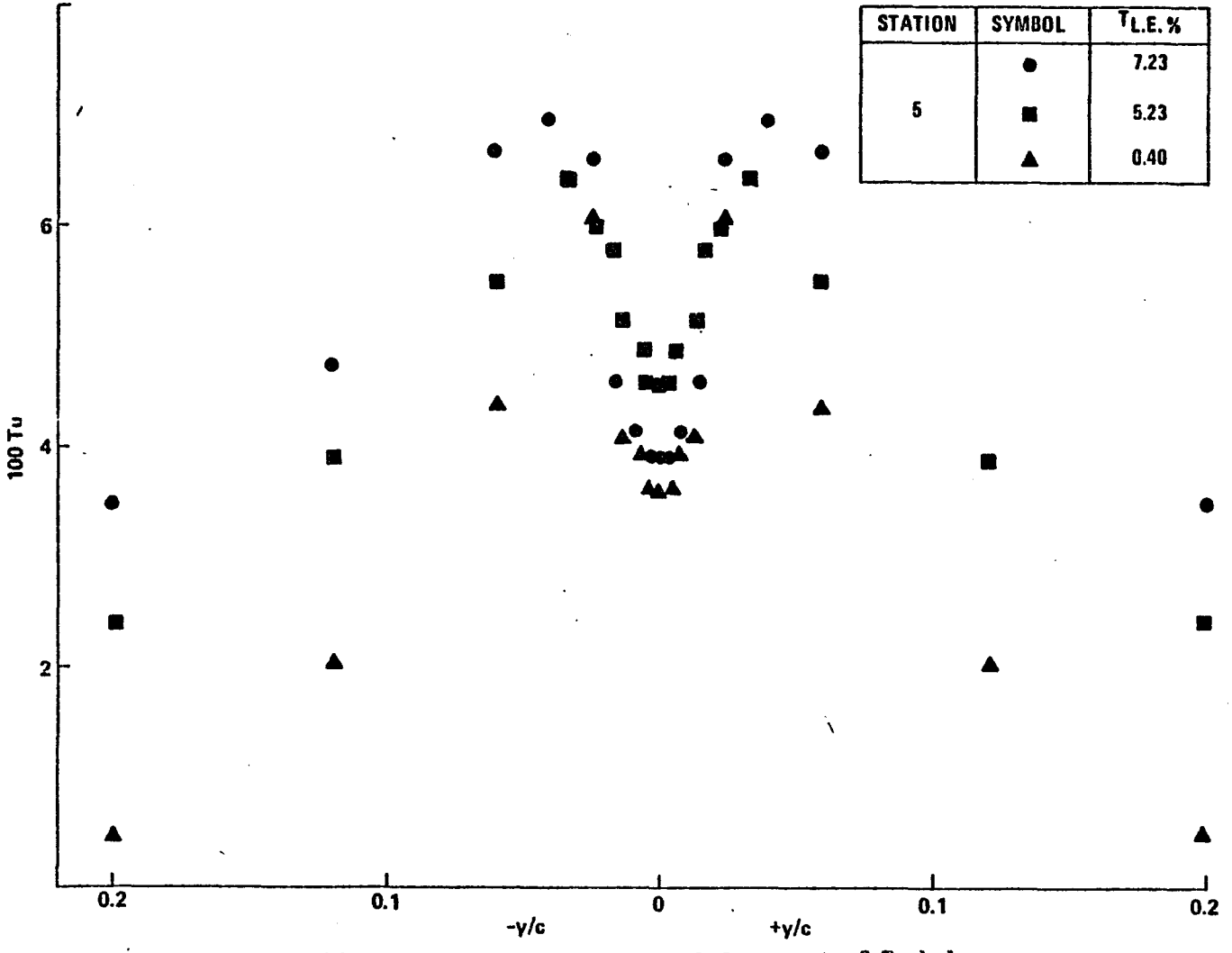

Figure 6.10(e) Variation of Longitudinal Component of Turbulence Intensity Across the Wake (x/c = 0.255)

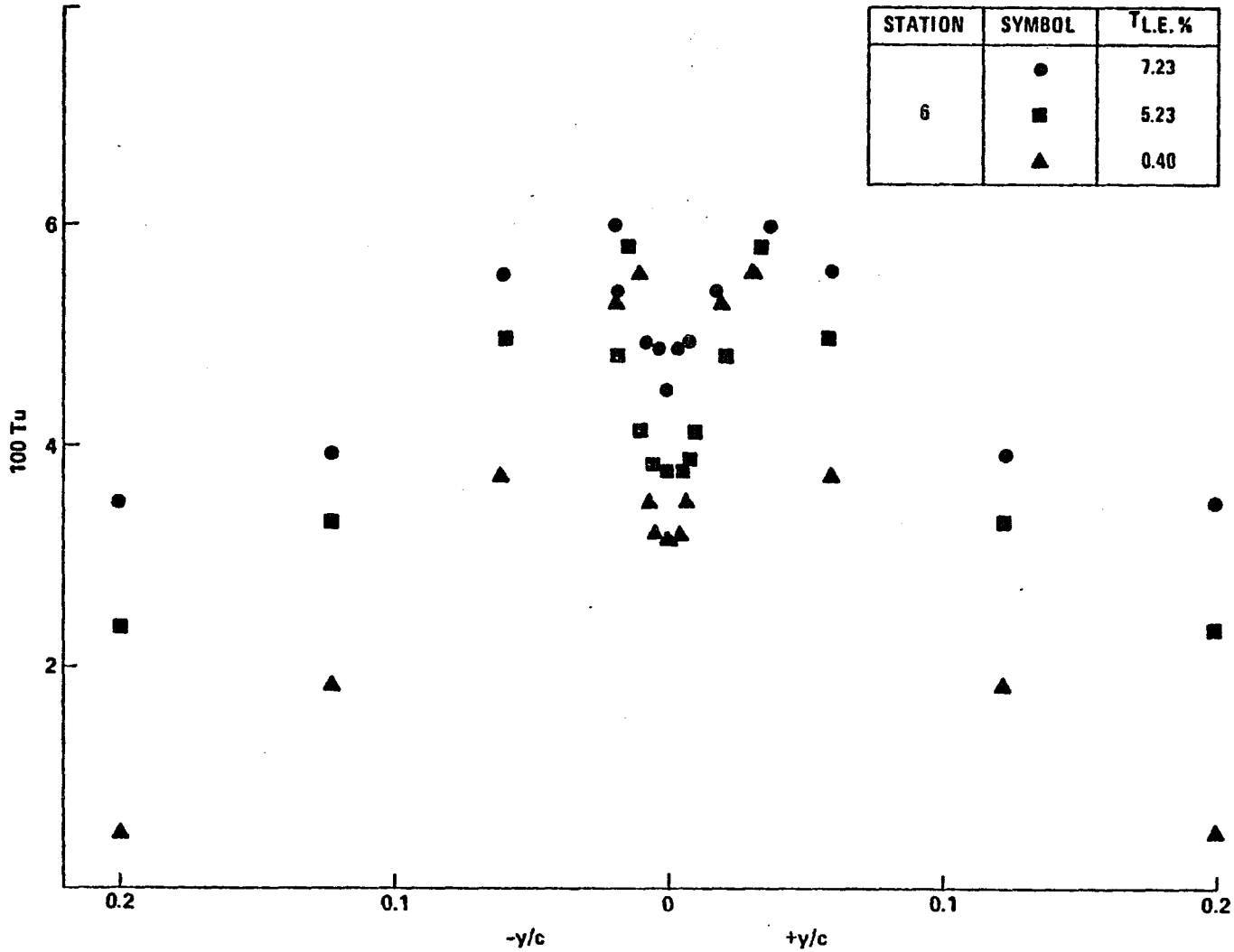

Figure 6.10(f) Variation of Longitudinal Component of Turbulence Intensity Across the Wake (x/c = 0.383)

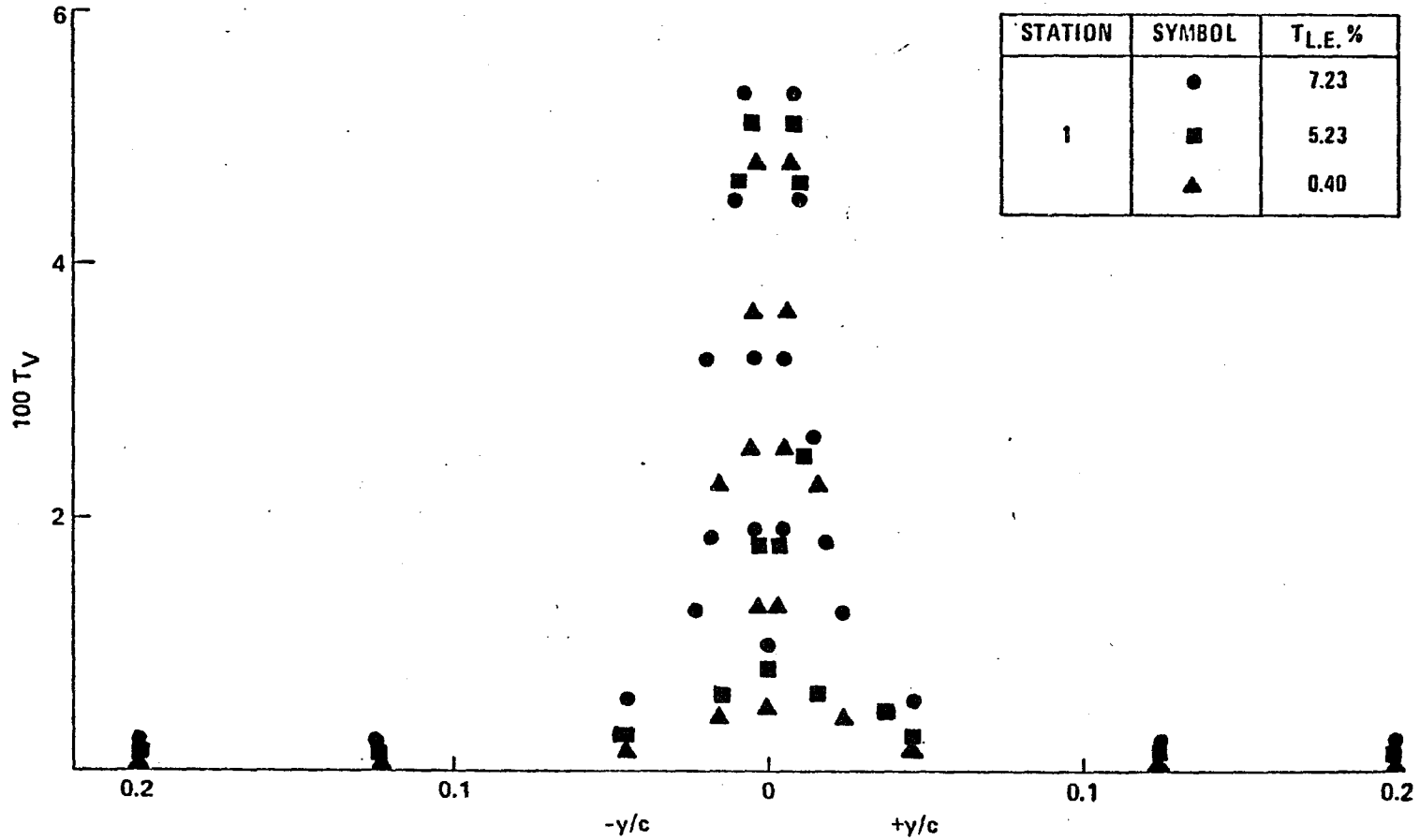

Figure 6.11 (a) Variation of Lateral Component of Turbulence Intensity Across the Wake (x/c = 0.0)

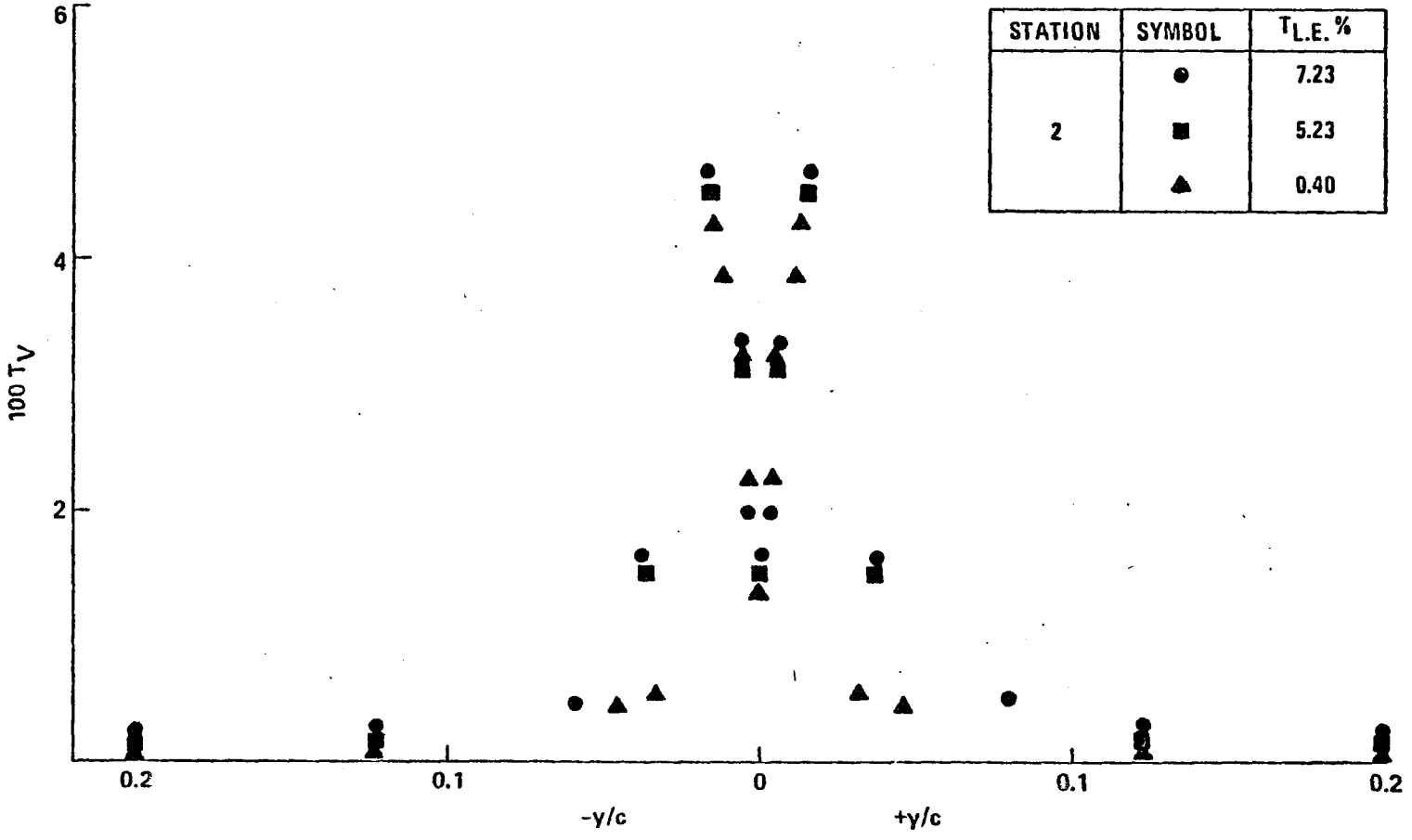

Figure 6.11(b) Variation of Lateral Component of Turbulence Intensity Across the Wake (x/c = 0.043)

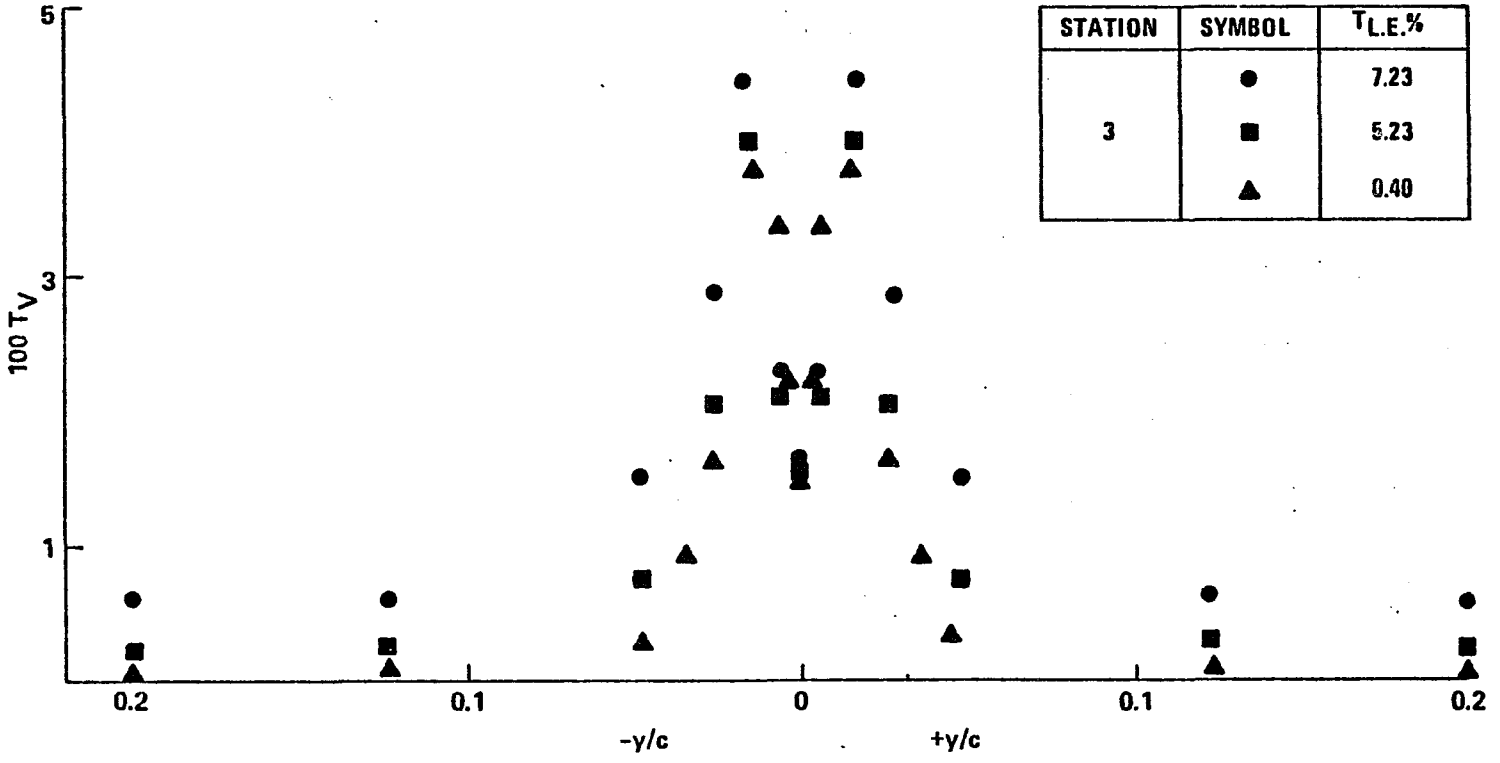

Figure 6.11(c) Variation of Lateral Component of Turbulence Intensity Across the Wake (x/c = 0.086)

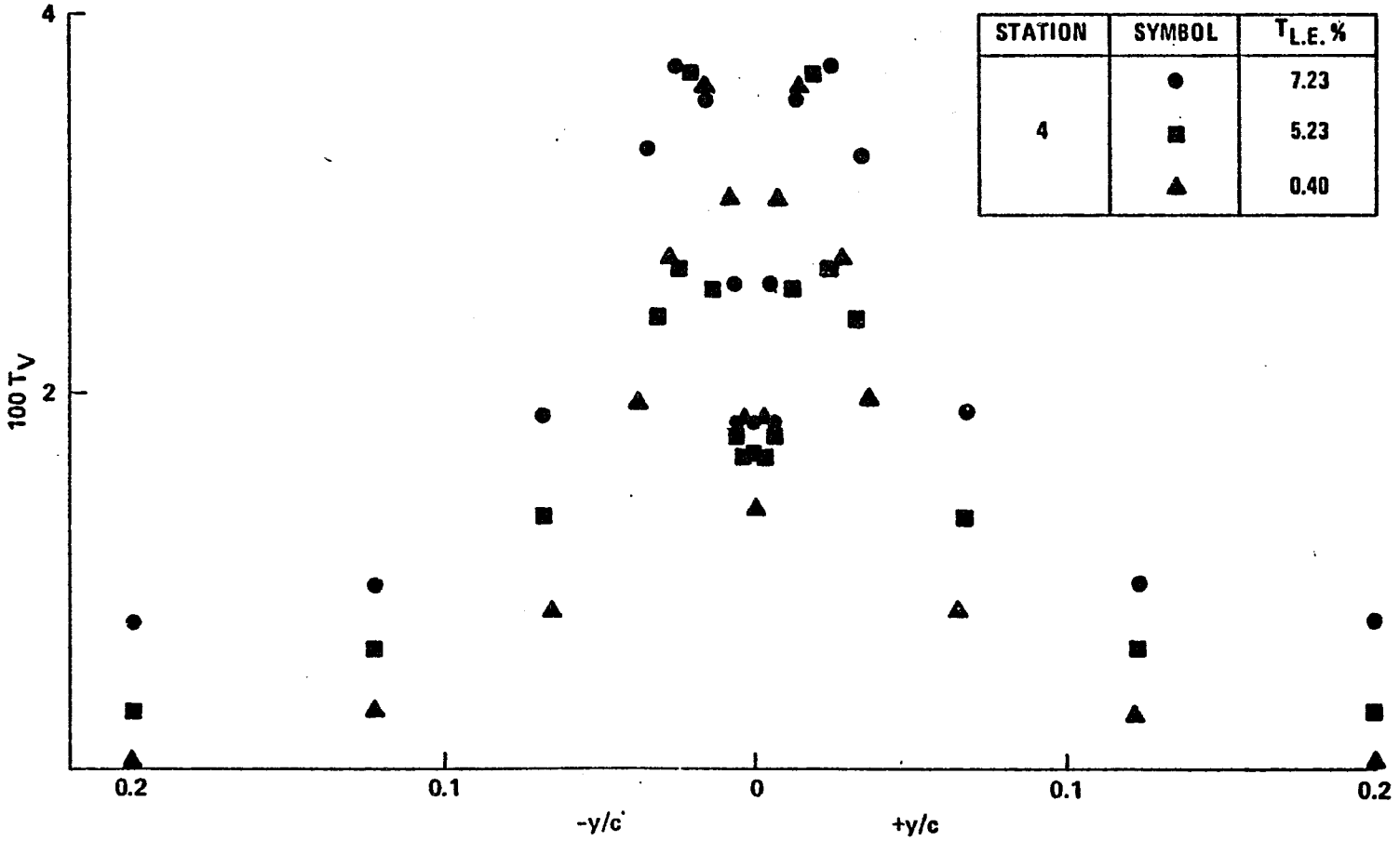

Figure 6.11 (d) Variation of Lateral Component of Turbulence Intensity Across the Wake (x/c = 0.170)

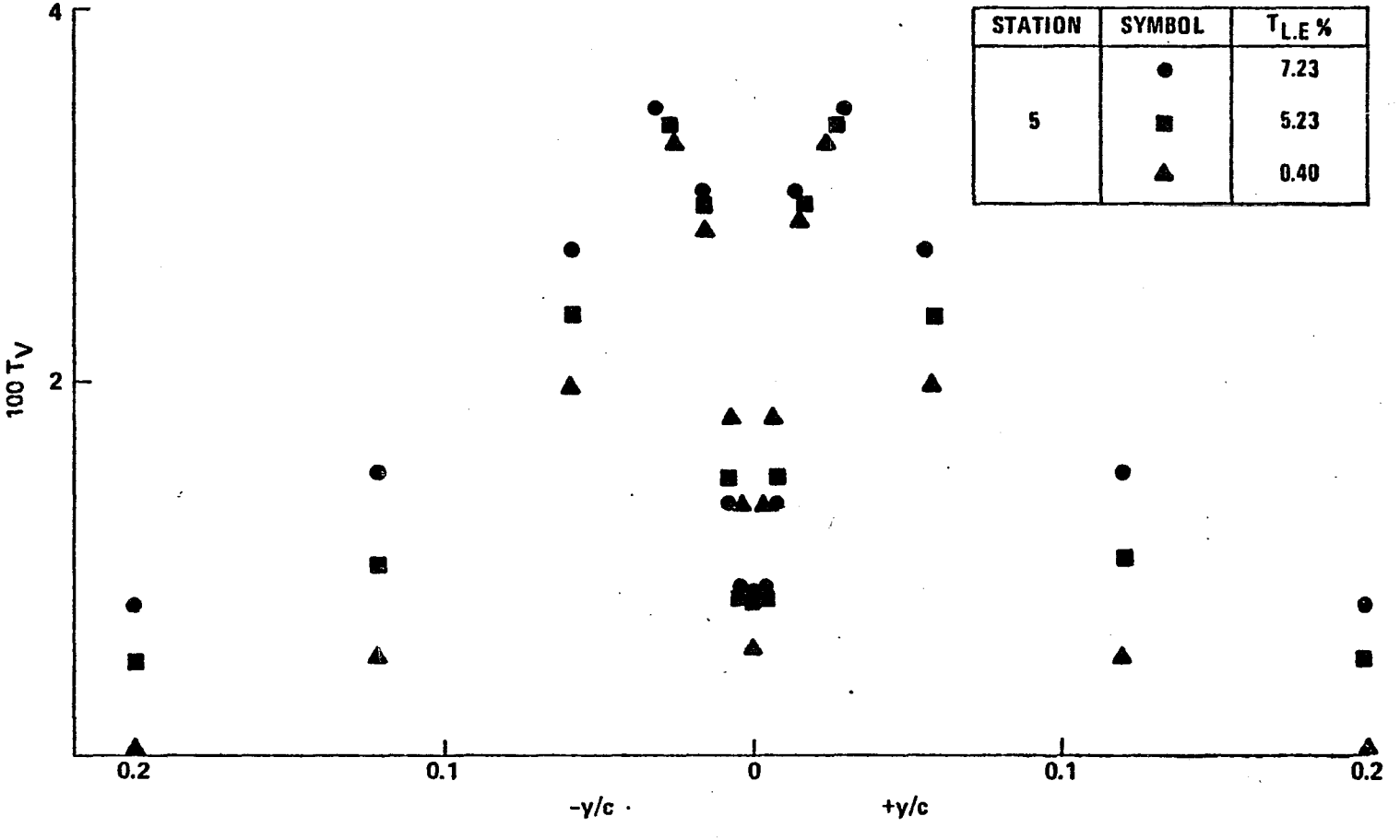

Figure 6.11(e) Variation of Lateral Component of Turbulence Intensity Across the Wake (x/c = 0.255)

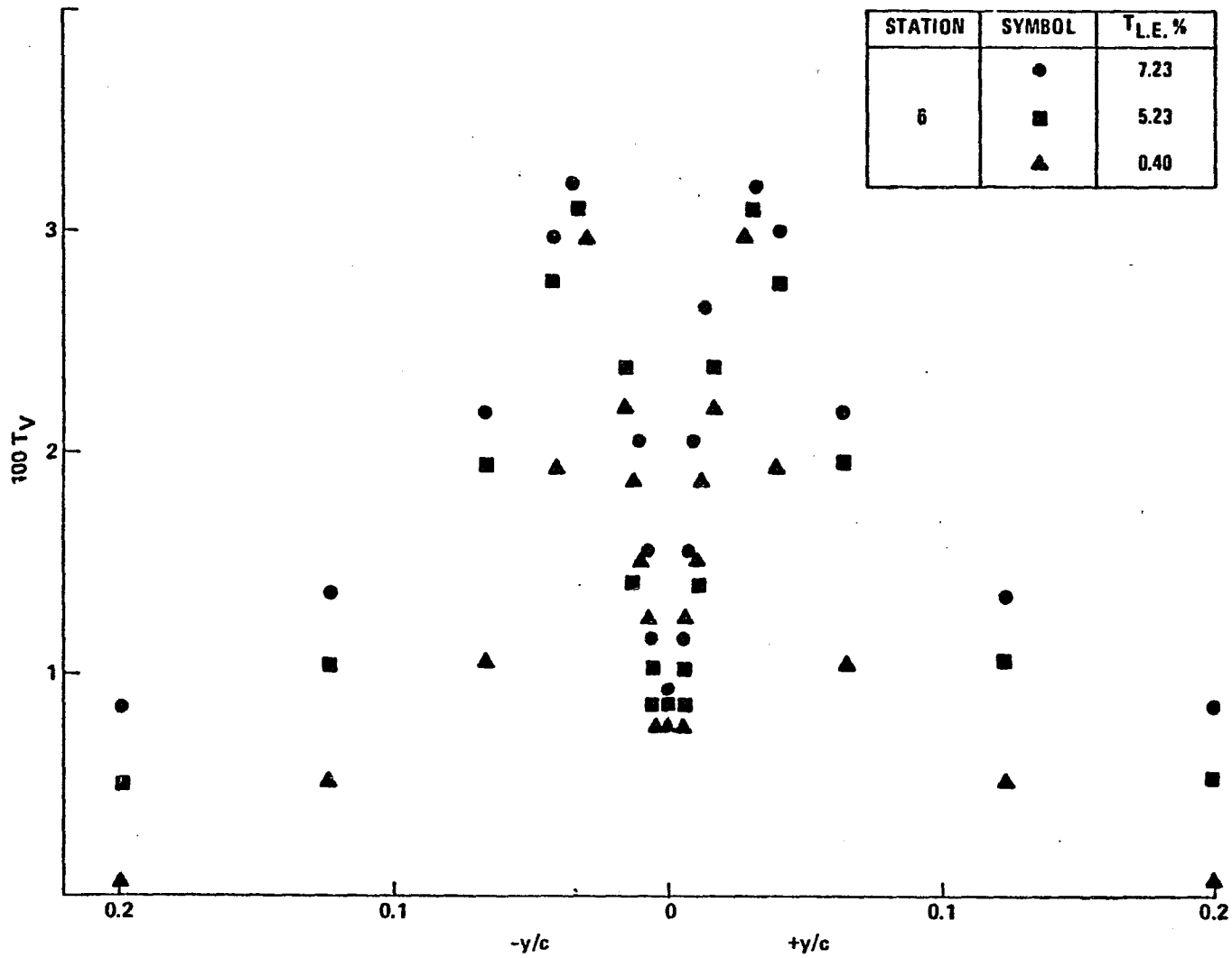

Figure 6.11(f) Variation of Lateral Component of Turbulence Intensity Across the Wake (x/c = 0.383)

turbulence level.

The foregoing observations can be easily explained. Due to mixing from both sides of the wake at the center line, the turbulence dissipation is nearly constant, while the turbulence production is zero at the wake center line and increases until it reaches the maximum value near $\eta = 1$. Near $\eta = 0$, the production of turbulence is equal to zero hence a dip in turbulence intensities is observed at the wake center line. The shift in maximum of turbulence intensities with downstream distance is associated with the wake spreading (growth) while the shift in maximum of turbulence intensities with increase in free stream turbulence is associated with the variation in the mean velocity gradient due to free stream turbulence effect. The increase in the wake turbulence intensities due to the increase in free stream turbulence level is associated with the increase in drag coefficient and other related para - meters given in Eqns.(3.35) and (3.36). Another interesting observation is that the point at which the peak values of turbulence intensities occur, lies in the neighborhood of the point where the velocity defect is equal to the defect required for half wake width.

The components of turbulence intensity tend to approach values nearly equal to the free stream turbulence values at the wake edge because near the wake edges the production of turbulence is negligible as compared to the

free stream turbulence. Thus, at the wake edges, free stream turbulence predominates. The longitudinal component of turbulence intensity is observed to be nearly twice the values of the lateral component with and without free stream turbulence, especially at the location of the occurrence of the maximum values.

6.4.2 Reynolds Stress:

Reynolds stress for three levels of free stream turbulence at six axial locations is shown in Figures 6.12 (a) to 6.12 (f). Reynolds stress distribution about the wake center line is anti-symmetric. The maximum value of the Reynolds stress occurs in the vicinity of the occurrence of the maximum values of the turbulence intensity because the velocity gradients are usually maximum near that location. Reynolds stress decreases sharply after the occurrence of the maximum value. At any fixed location in the wake, the Reynolds stress increases with increase in free stream turbulence level. This trend is predicted by Eqn. (3.37).

Reynolds stress tends towards a finite value in the presence of free stream turbulence at the outer edge instead of tending towards zero as is the case of no free stream turbulence.

6.4.3 Correlation Coefficient:

Figure 6.13 shows the variation of the correlation

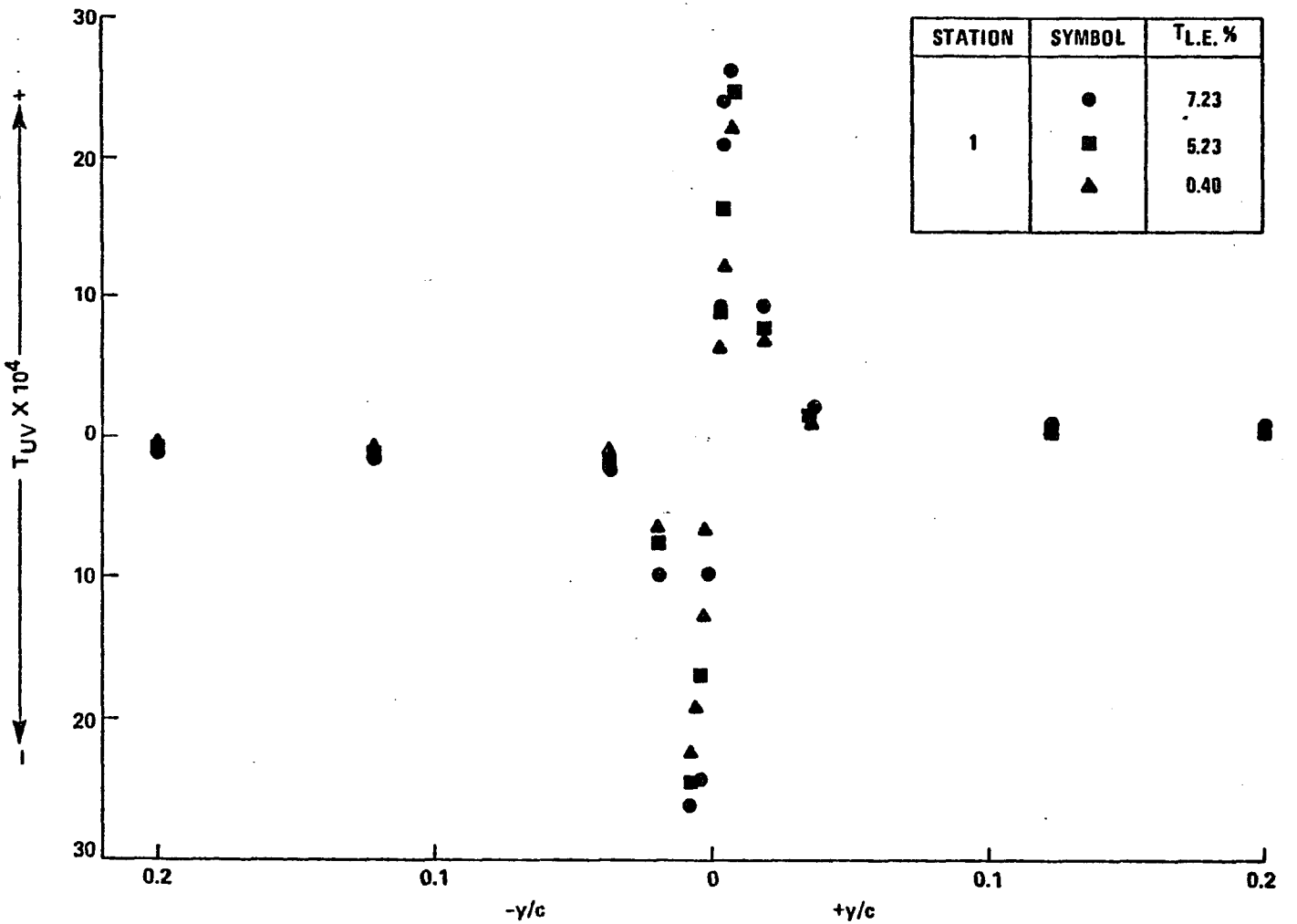

Figure 6.12(a) Variation of Reynolds Stress Across the Wake (x/c = 0.0)

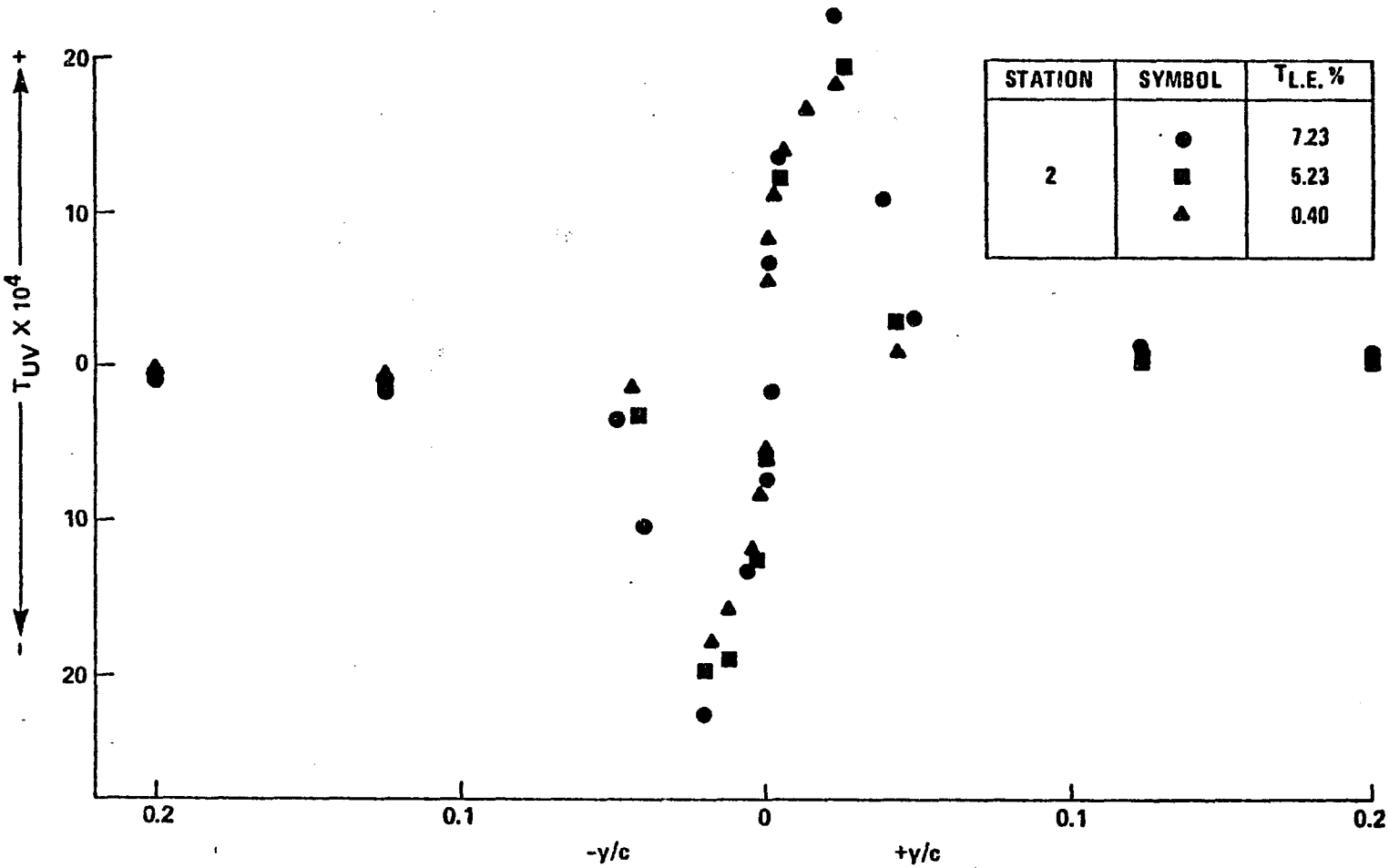

Figure 6.12 (b) Variation of Reynolds Stress Across the Wake (x/c = 0.043)

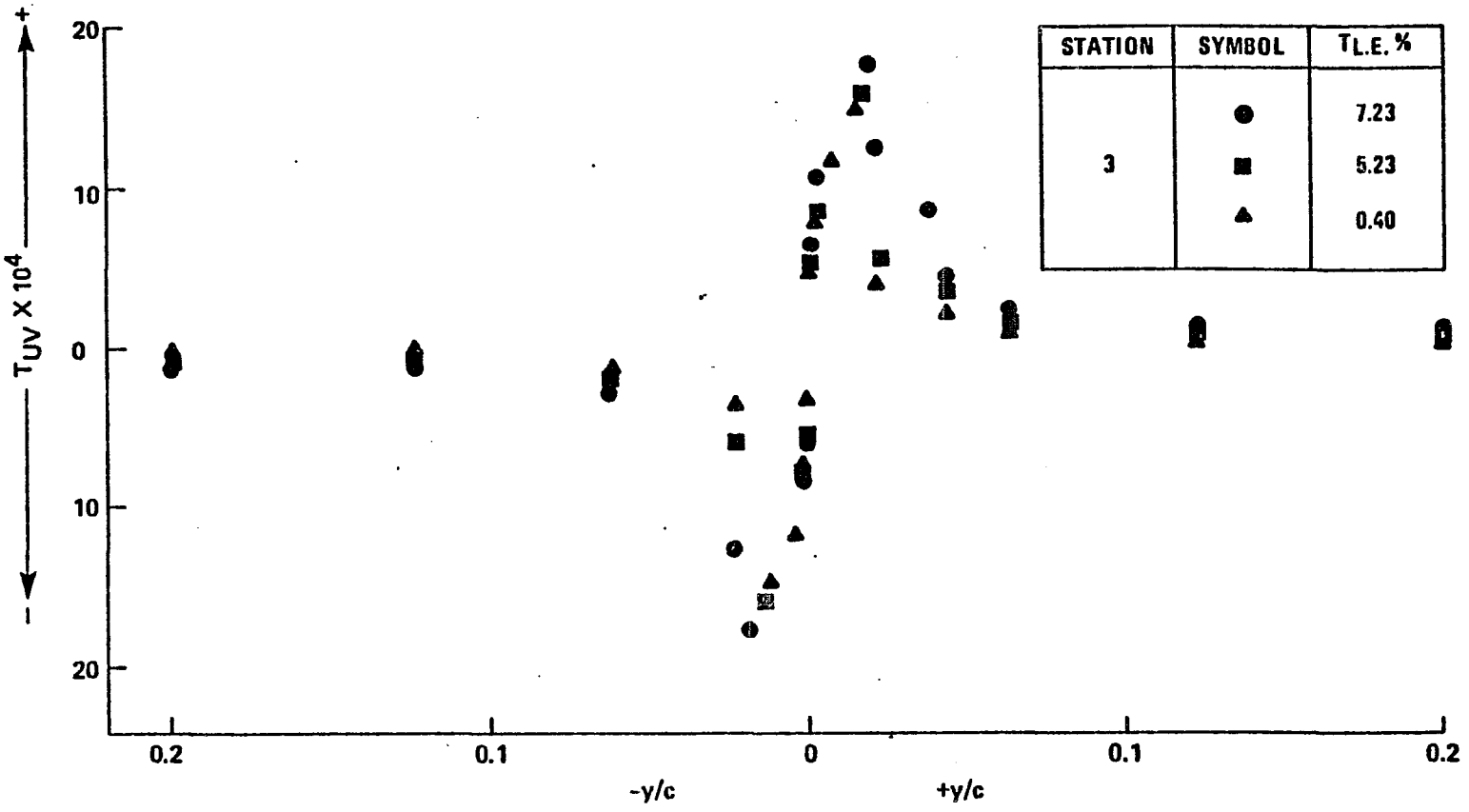

Figure 6.12 (c) Variation of Reynolds Stress Across the Wake (x/c = 0.086)

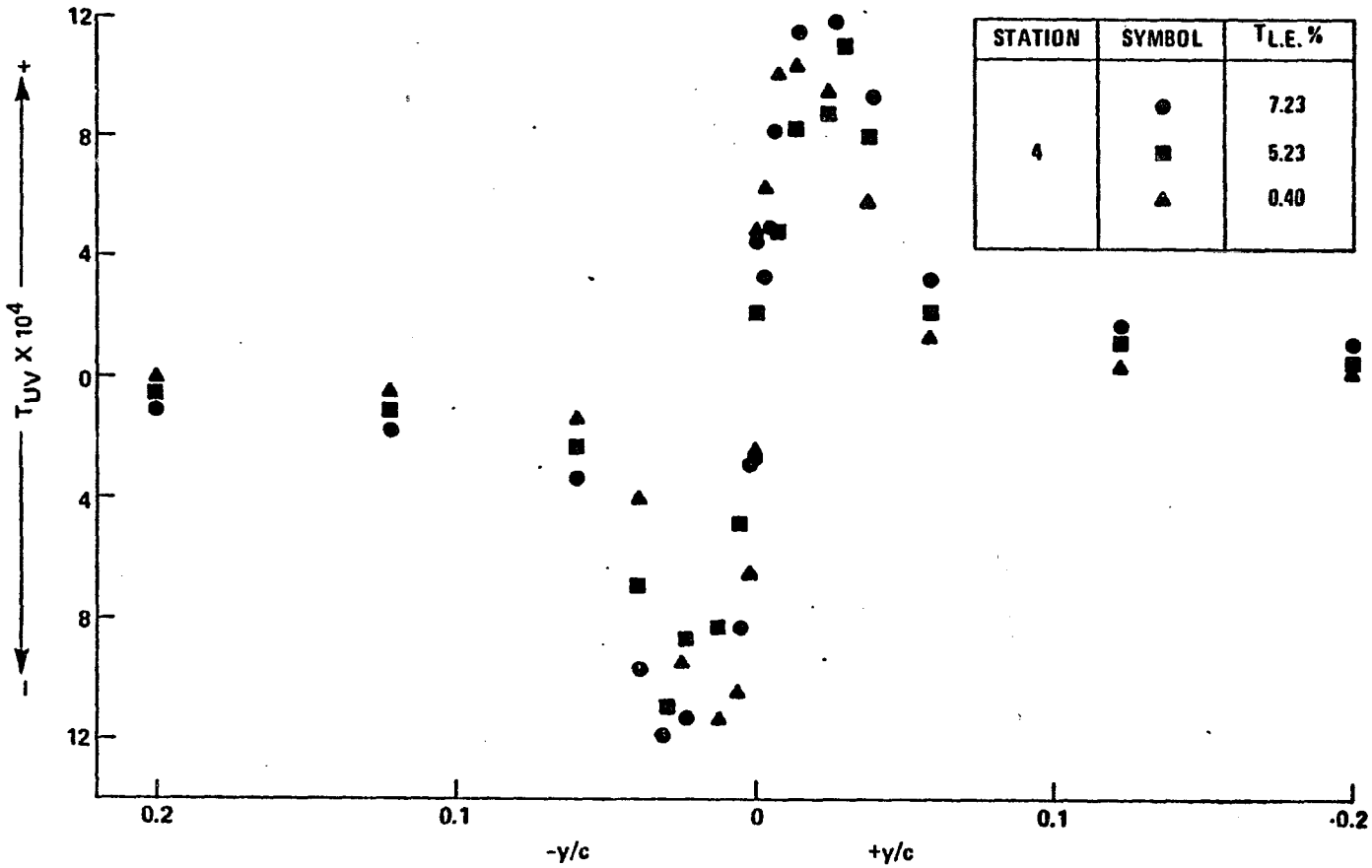

Figure 6.12 (d) Variation of Reynolds Stress Across the Wake (x/c = 0.170)

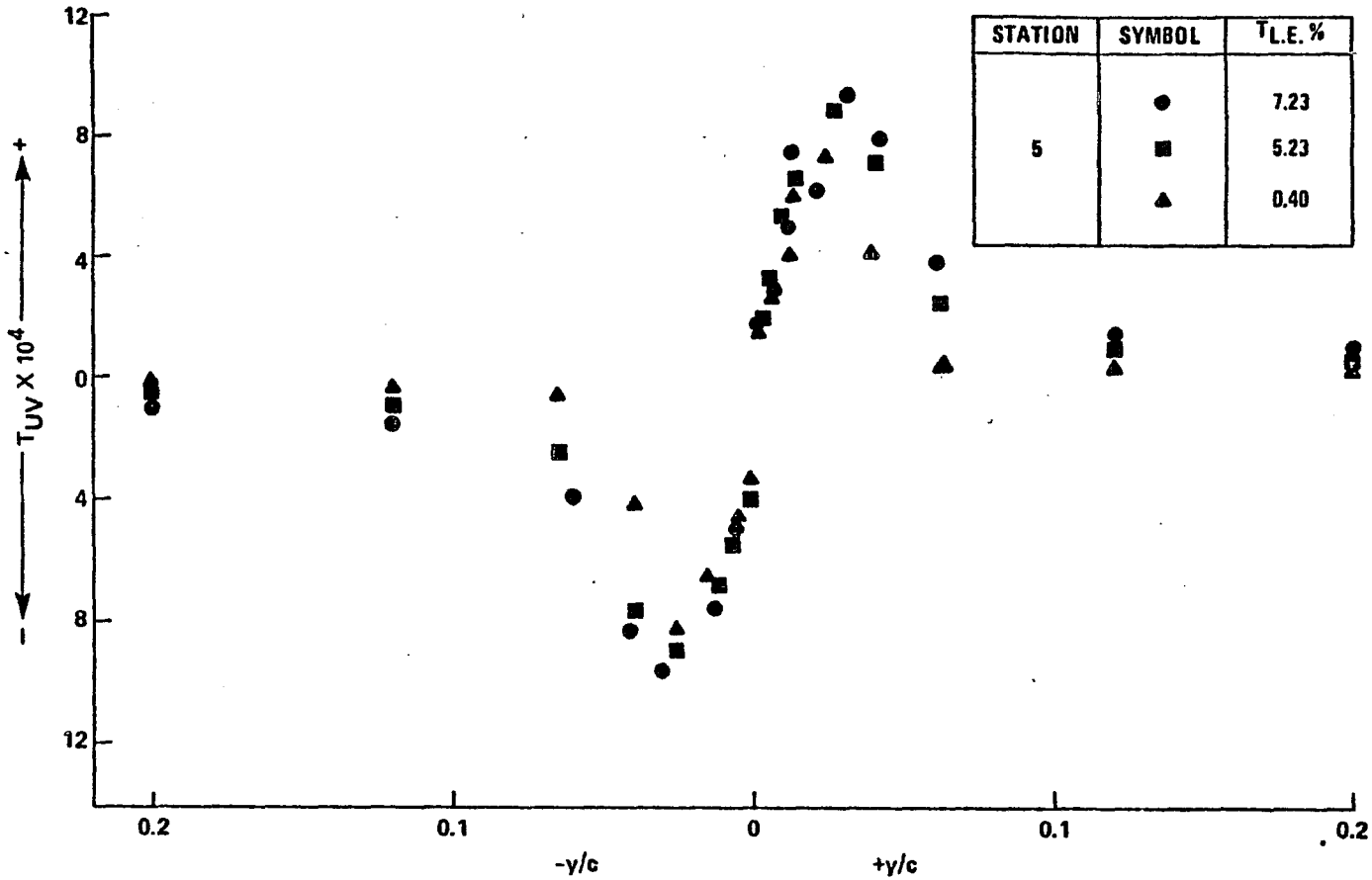

Figure 6.12(e) Variation of Reynolds Stress Across the Wake (x/c = 0.255)

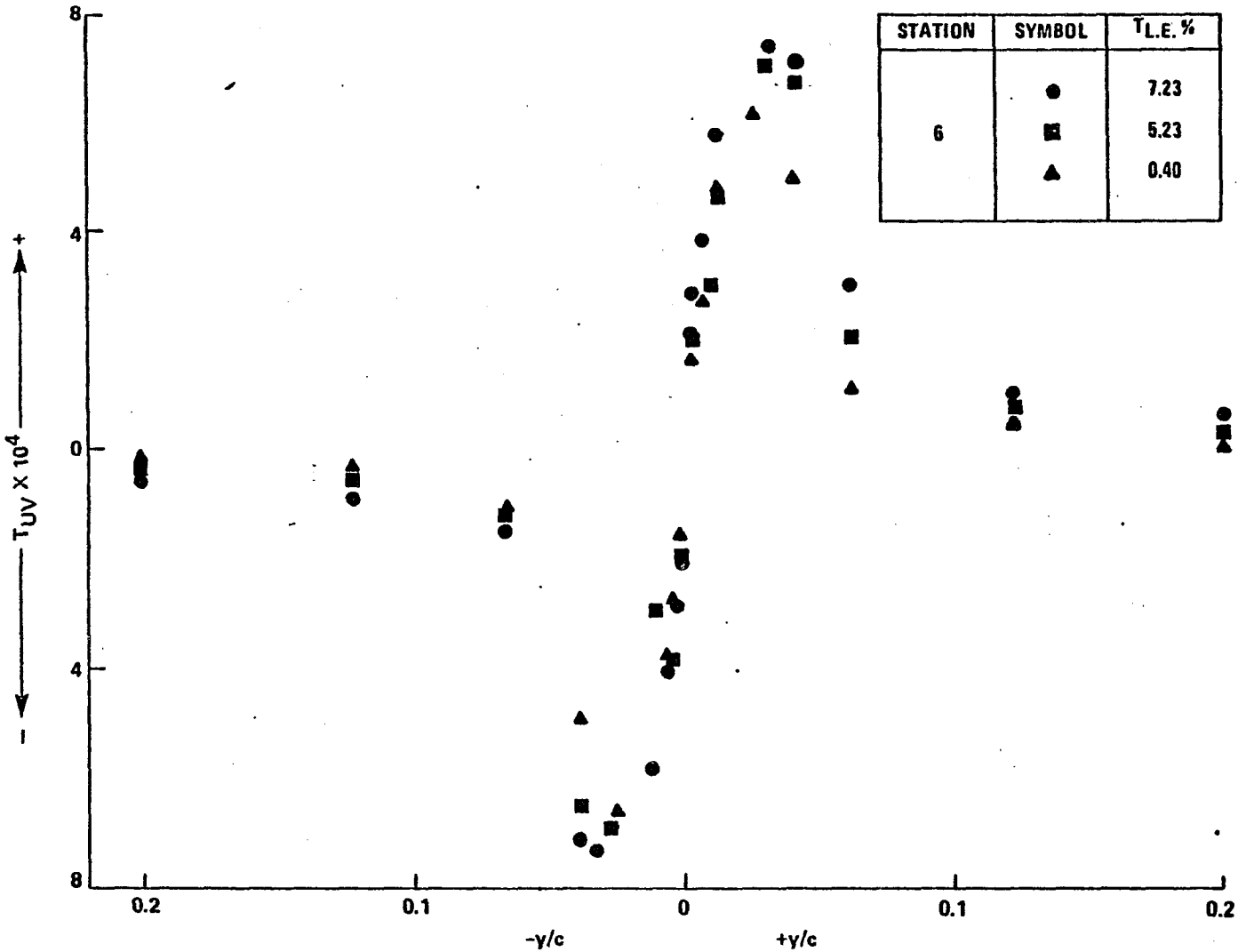

Figure 6.12(f) Variation of Reynolds Stress Across the Wake (x/c = 0.383)

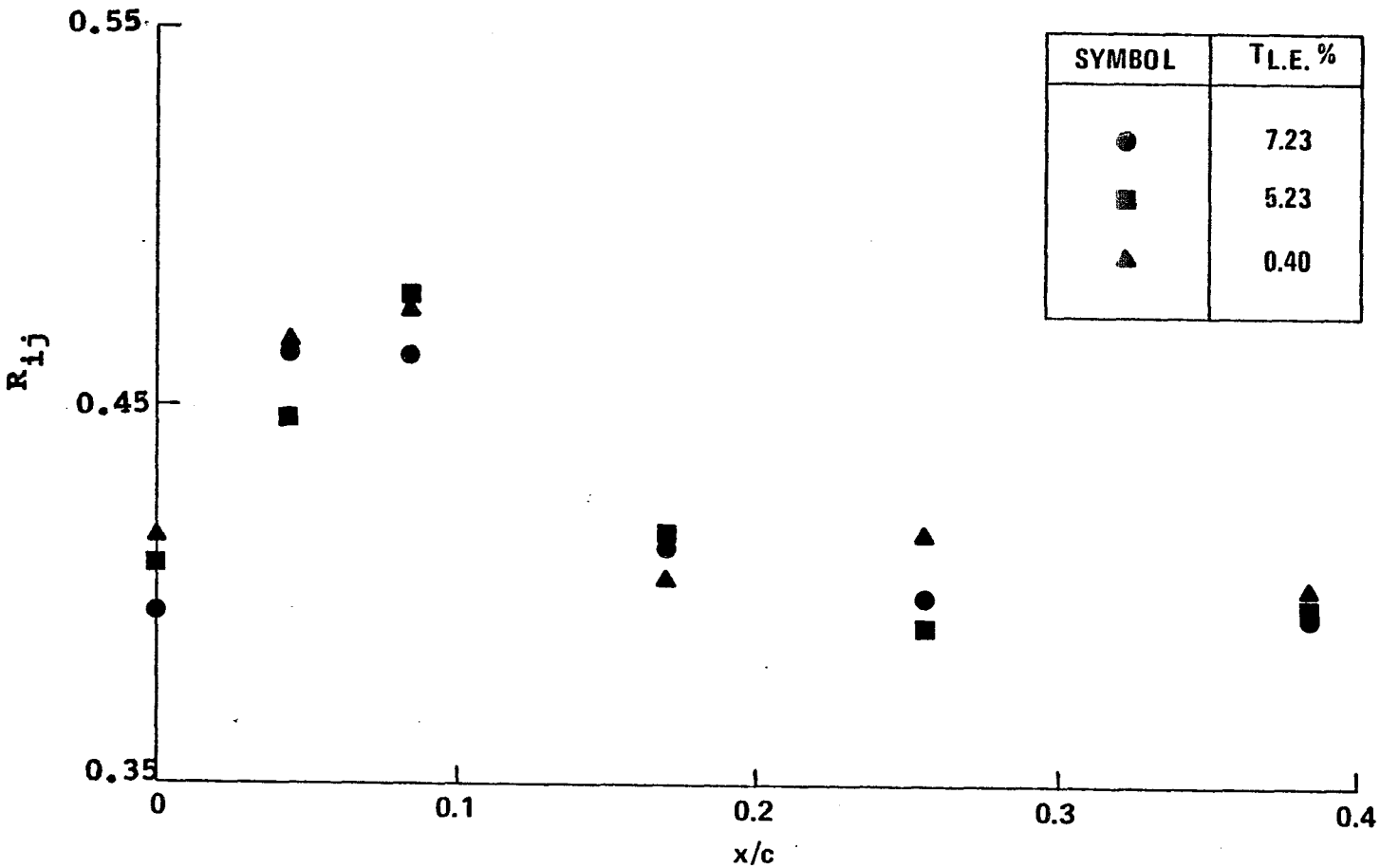

Figure 6.13 Variation of Correlation Coefficient (R_{ij}) With Downstream Distance

coefficient (R_{ij}) between the maximum values of the turbulence stress and turbulence intensities, defined as,

$$R_{ij} = \frac{\overline{u\,v}}{\sqrt{\overline{u^2}}\ \sqrt{\overline{v^2}}} \quad \ldots(6.14)$$

for three levels of free stream turbulence as the distance downstream of the trailing edge of the flat plate varies. It is clear from Figure 6.13, that the correlation coefficient varies between 0.39 to 0.48. For a nearly homogeneous turbulence, the value of correlation coefficient is nearly 0.45. Clearly, the value of the correlation coefficient for the maximum turbulence quantities for all the free stream turbulence levels, is far from this value in the present investigation. Therefore, turbulence cannot be considered homogeneous in the region of occurrence of maximum values.

6.4.4 Self-Preservation:

The self-preservation of wake in the presence of free stream turbulence can be examined by considering the following two turbulence production terms in the turbulence energy equation for a two-dimensional mean flow,

$$\left(\overline{u^2} - \overline{v^2}\right)\frac{\partial \overline{U}}{\partial x} \quad \text{and} \quad -\overline{u\,v}\,\frac{\partial \overline{U}}{\partial Y}$$

The first term represents production of turbulence due to anisotropy in the flow while the second

is due to non-homogeneity. Clearly, the first term is responsible for the creation of non self-preservation in the wake flow. Near the trailing edge, the two production terms are of comparable magnitude. Farther downstream, however, the first term becomes smaller than the second term. The distance beyond which the first term becomes small depends upon geometry of the body and external flow conditions, i.e., it will be smaller for streamlined bodies than for the bluff bodies. Therefore, a parameter 'P',

$$P = \left[\frac{-\overline{u\,v}\,\dfrac{\partial \bar{U}}{\partial y}}{(\overline{u^2} - \overline{v^2})\,\dfrac{\partial \bar{U}}{\partial x}} \right]_{y = L_0} \qquad \ldots(6.15)$$

where L_0 is the length scale, should be able to describe the self-preservation of flow. In shear dominated flow, for $P > 1$, the flow approaches self-preservation, while for complete self-preservation P must be greater than 10 (Reference 48). Figure 6.14 represents the variation of P with distance downstream of the trailing edge of the flat plate for three levels of free stream turbulence. It is observed that the higher the free stream turbulence level, the greater is the tendency of wake flow towards self-preservation. The increase in P with the increase of free stream turbulence is mainly due to the increase in turbulence stress which implictly depends upon turbulence

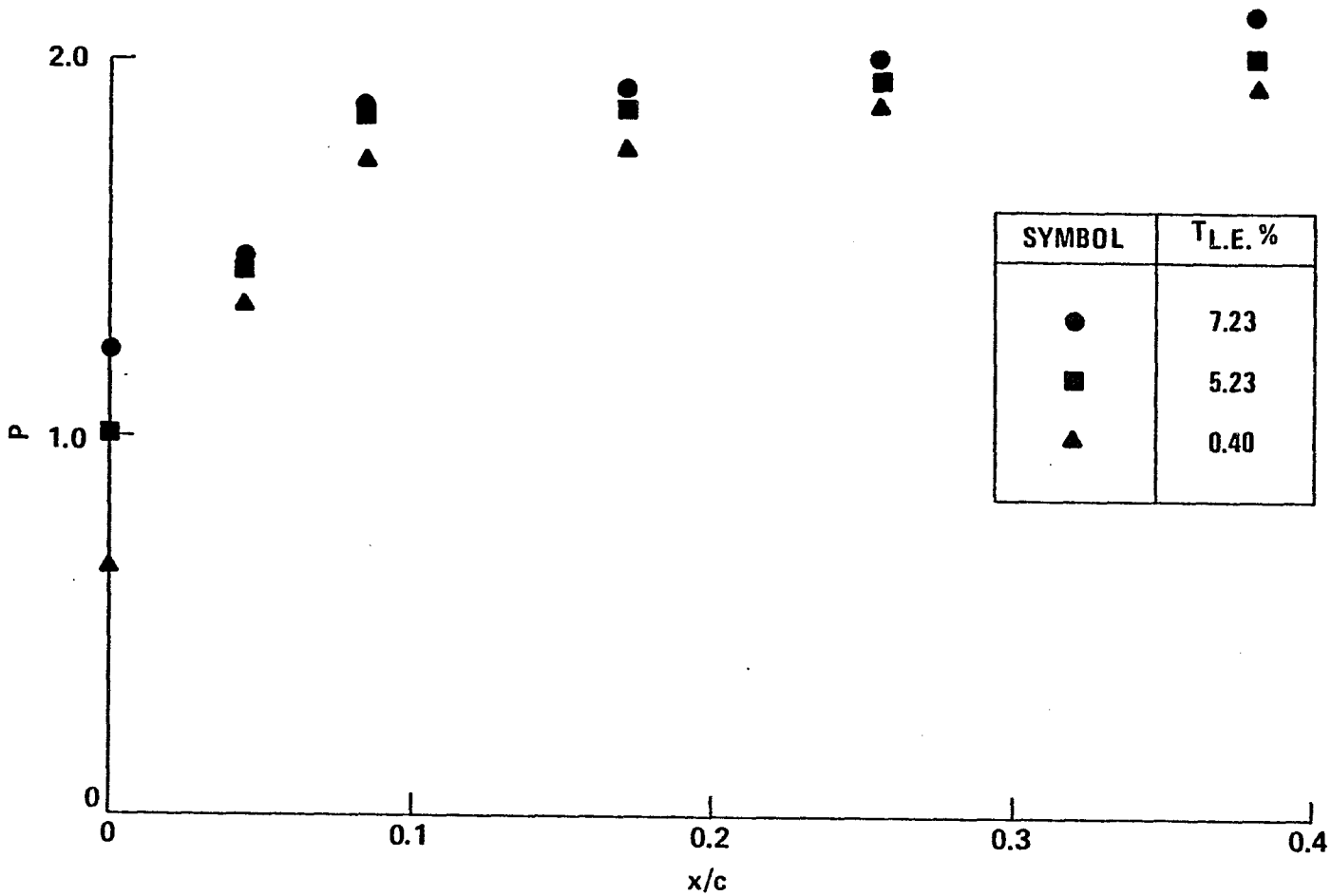

Figure 6.14 Variation of Self-Preservation Parameter (P) with Distance Downstream of the Trailing Edge of a Flat Plate

parameters, axial distance in the downstream direction, free free stream turbulence level, etc. For $x/c > 0.1$, the flow is nearly self-preserving. It is also interesting to note that 'P' increases sharply with the increase of free stream turbulence for $x/c < 0.1$, because of the large production of the turbulence energy near the trailing edge. However, energy production is comparatively reduced for a distant wake region and hence for $x/c > 0.1$, P varies slowly with distance downstream of the trailing edge.

6.4.5 Decay of Turbulence Quantities:

Maximum value of the longitudinal component of turbulence intensity, from the self-preservation consideration, was obtained in Chapter (III). The value of x_0'/c obtained as 0.45 from the experimental data. Figure 6.15 (a) shows decay of the maximum value of the longitudinal component of turbulence intensity, for three levels of free stream turbulence, varying with distance downstream of the trailing edge of the flat plate. The following correlation equation is also plotted:

$$T_{u\ max} \simeq 0.34\,(\,1 + \bar{\gamma}\,T\,)\left[\bar{K}\,c_d^{\frac{1}{2}}\,(\,x/c + x_0'/c\,)\right]^{-0.32\,(1+\bar{\gamma}T)} \qquad \ldots(6.16)$$

The data is found to be in good agreement with the correlation Eqn.(6.16). As is clear from the comparison (Fig. 6.15 a), the higher the free stream turbulence, the higher the value of the longitudinal component of the

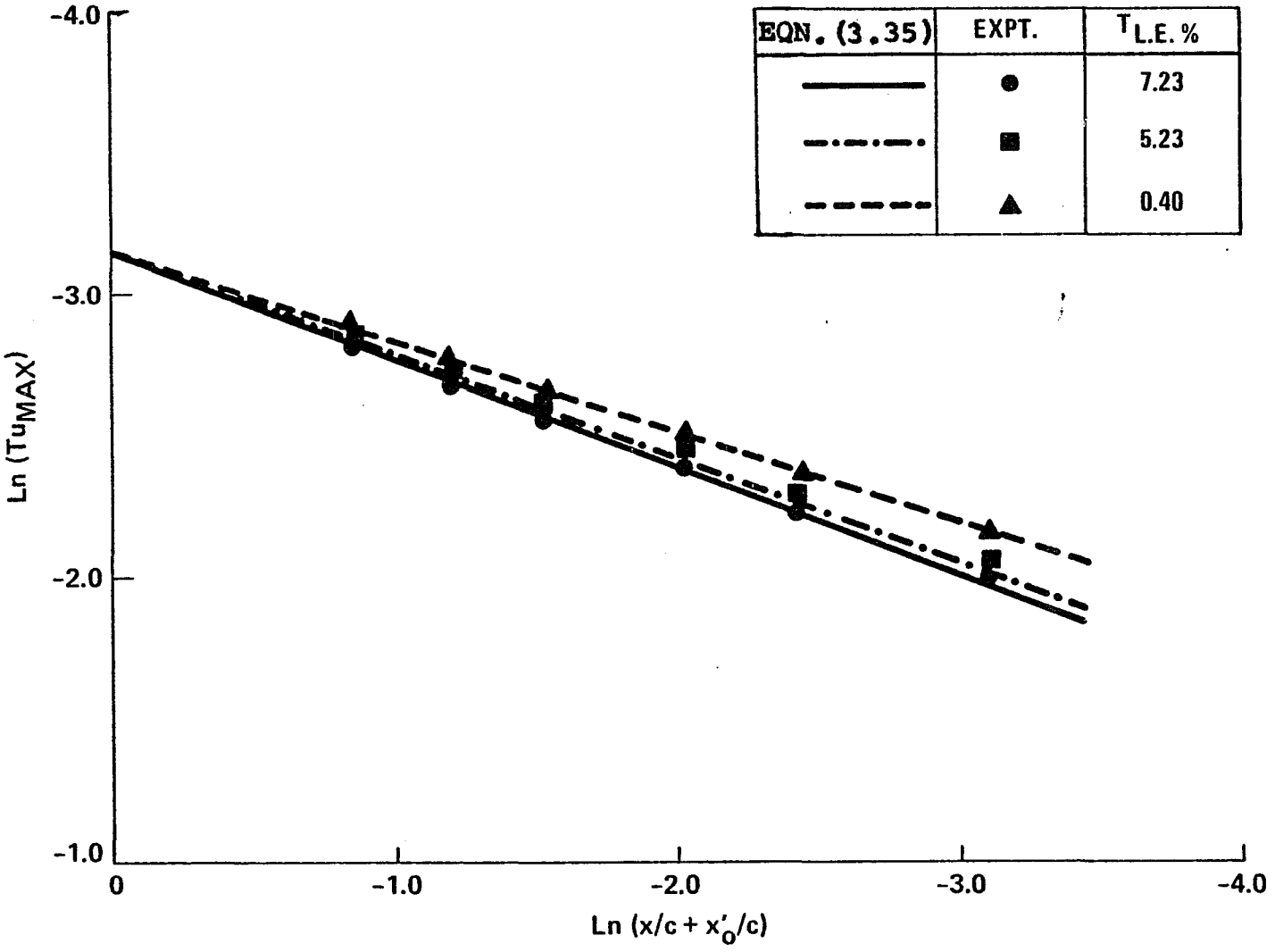

Figure 6.15(a) Decay Characteristics of Maximum Longitudinal Component of Turbulence Intensity With Distance Downstream from the Trailing Edge of a Flat Plate

turbulence intensity. Turbulence intensity decays in the downstream direction with and without free stream turbulence because of the decreased effect of turbulence production in the downstream direction. This trend is consistent with the earlier results (Reference 32).

Figure 6.15 (b) represents the decay behavior of the maximum values of lateral component of turbulence intensity for three levels of free stream turbulence with distance downstream of the trailing edge of the flat plate. The comparison with both the experimental data and the following correlation equation,

$$T_{v\ max} \simeq 0.21\left(1 + \bar{\gamma}\, T\right)\left[\bar{K}\, c_d^{\frac{1}{2}}\left(x/c + x_0'/c\right)\right]^{-0.20(1+\bar{\gamma}T)} \qquad \ldots(6.17)$$

is found to be good. The general behavior is similar to that of the longitudinal component of turbulence intensity.

The decay of the maximum values of the turbulent shear stress, obtained from the experimental data and the following correlation equation,

$$T_{uv\ max} \simeq 0.025\ (1 + \bar{\gamma}T)^2\left[\bar{K}\, c_d^{\frac{1}{2}}\left(x/c + x_0'/c\right)^{-0.31(1+\bar{\gamma}T)}\right] \qquad \ldots(6.18)$$

is shown in Figure 6.15(c), for three levels of free stream turbulence. It is observed that with the increase of free

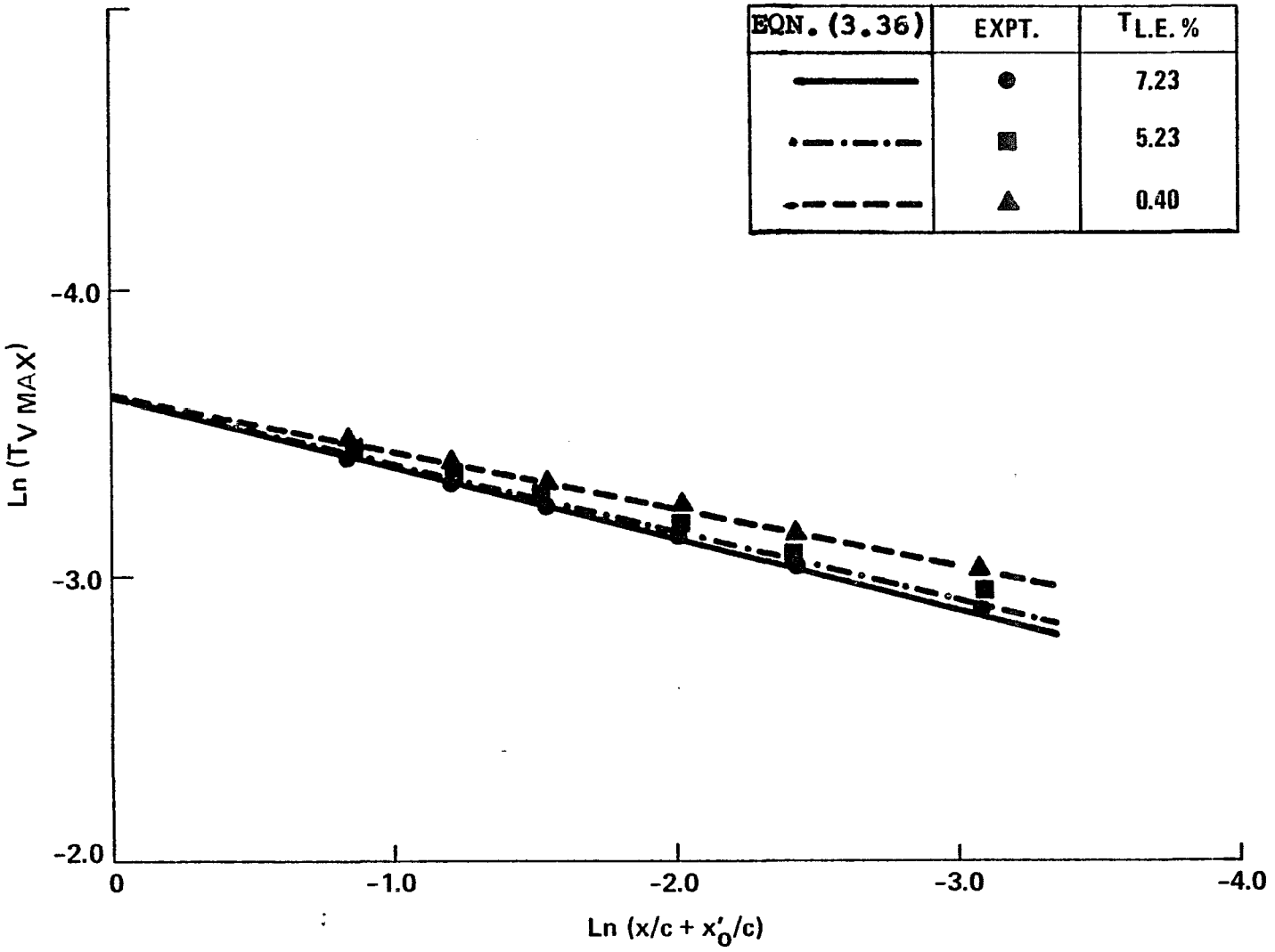

Figure 6.15(b) Decay Characteristics of Maximum Lateral Component of Turbulence Intensity With Distance Downstream from the Trailing Edge of a Flat Plate

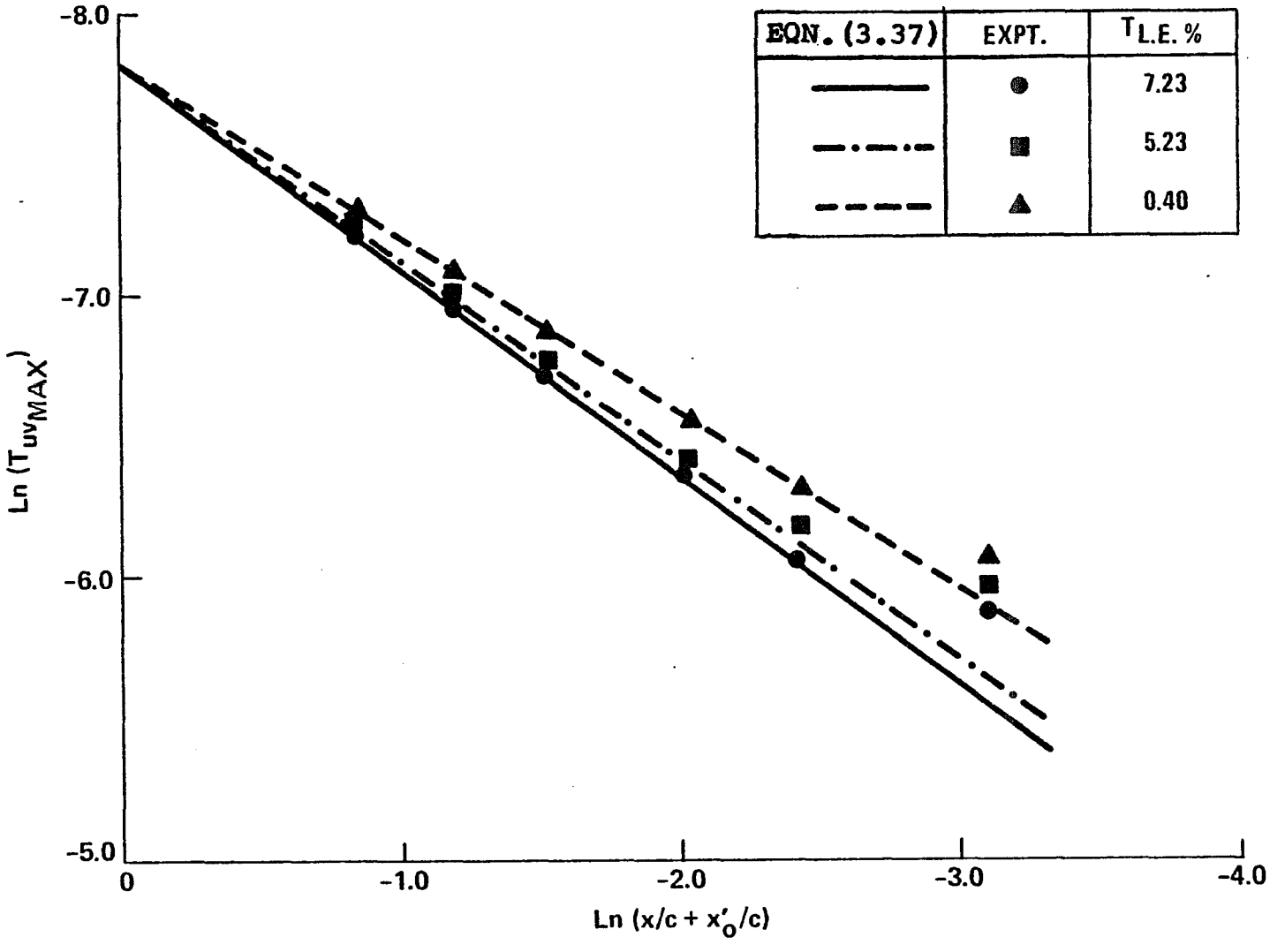

Figure 6.15(c) Decay Characteristics of Maximum of Reynolds Stress With Distance Downstream from the Trailing Edge of a Flat Plate

stream turbulence, the maximum value of the turbulent shear stress increases. Maximum value of shear stress occurs in the vicinity of the occurrence of maximum values of the components of turbulence intensity. The increase in free stream turbulence increases the lateral distance from the wake center line to the occurrence of the maximum value of the shear stress.

The correlation Eqn.(6.18) and the experimental data are in good agreement, except at the trailing edge, where the correlation Eqn.(6.18) over-predicts the values. Turbulent shear stress decreases in the downstream direction with and without free stream turbulence because of the decrease in velocity gradient.

The power indices for decay rates are very close to those found in Ref.(1).

CHAPTER VII

EXPERIMENTAL RESULTS AND COMPARISON WITH PREDICTIONS OF WAKE BOUNDARY LAYER INTERACTION

The experimental data and semi-empirical correlations for wake boundary layer interaction effect on mean and turbulence quantities are presented in this chapter. Semi-empirical correlations for the wake velocity defect and wake width are shown to be a function of axial distance, normal distance, spacing, chord length of the flat plate and turbulence interaction parameters. Turbulence interaction parameters describing the effect of wake interaction with the boundary layer on length and velocity scale are also established. Experimentally, the decay of the maximum values of the three components of turbulence intensity and Reynolds stress are established. Observations on the variation of the spacing and interaction effect are made. The correlation coefficient of the peak values of the turbulence intensities and Reynolds stresses is also discussed.

Wake profiles were measured at two axial locations and two normal locations for three values of spacings (Fig. 5.3 Table IV) giving the far wake interaction with the inner and outer regions of the boundary layer.

7.1 Mean Quantities:

Mean velocity is normalized with respect to the axial component of the local outer edge velocity, while the axial and normal distance are non-dimensional with respect to the chord length and $2\sqrt{x\ \nu_{T_i}/\overline{U}_e}$, respectively.

7.1.1 Mean Velocity Profile:

The axial component of mean velocity profile of a wake for two axial stations and two normal locations at each axial station for different values of spacing ratio is presented in Figures 7.1(a) to (d). The profiles of lateral and normal components of the mean velocity are given in Figures 7.2(a) to (d) and 7.3(a) to (d), respectively.

Both sides of the wake about the wake center line were measured. The number points of measurements on both sides, however, were not equidistant from the wake center line. A slight asymmetry about the wake center line in the axial, normal and lateral components of the mean velocity profile is observed. This asymmetry is due to non-uniformity in surface roughness layer in the y-direction. The axial component of wake center line velocity increases with the increase in spacing and is due to the wake mixing and recovery. The velocity defect decreases in the inner region of the interacted boundary

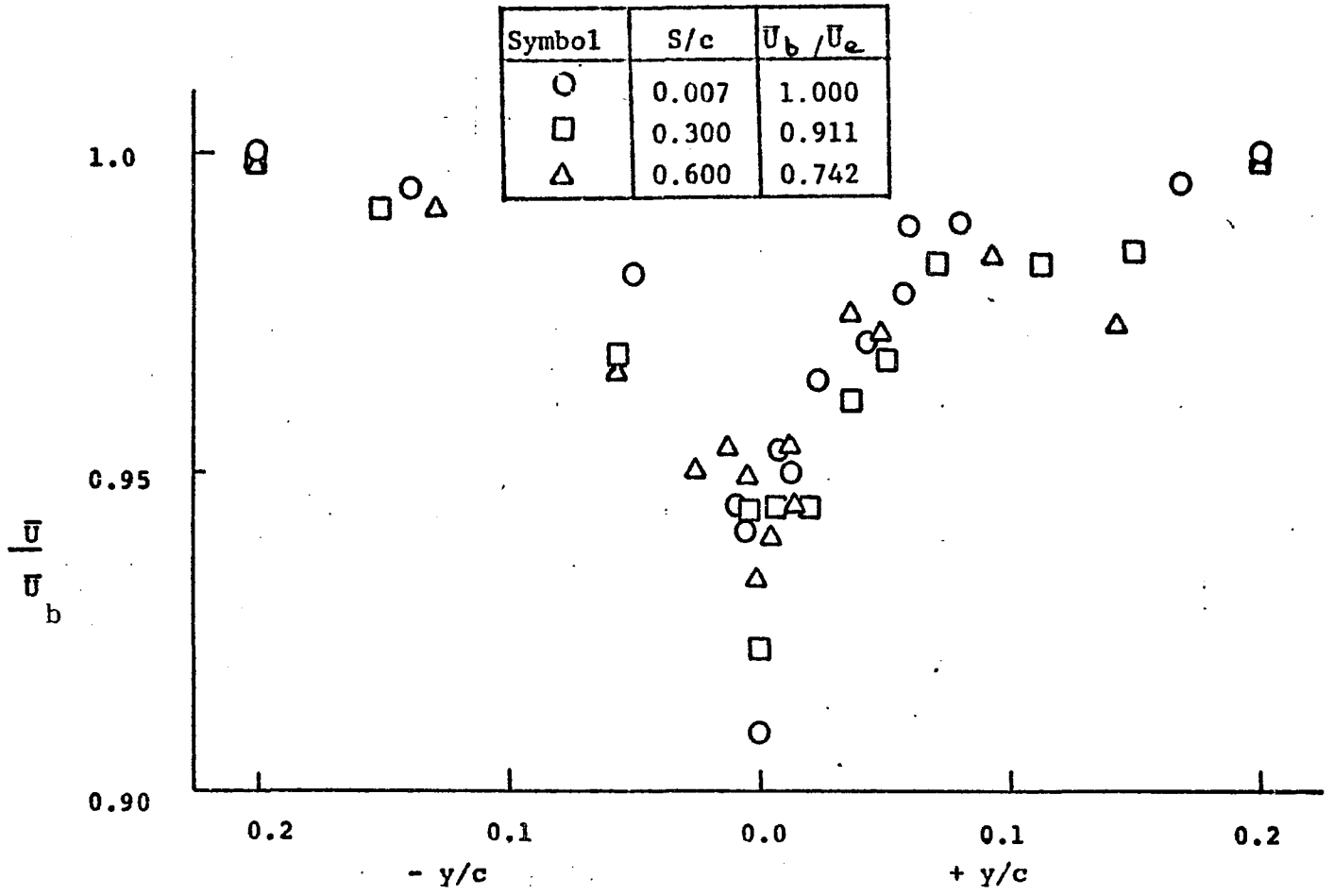

Figure 7.1(a) Variation of Axial Component of Mean Velocity Profile Across the Wake (x /c = 0.68, z/c = 0.026).

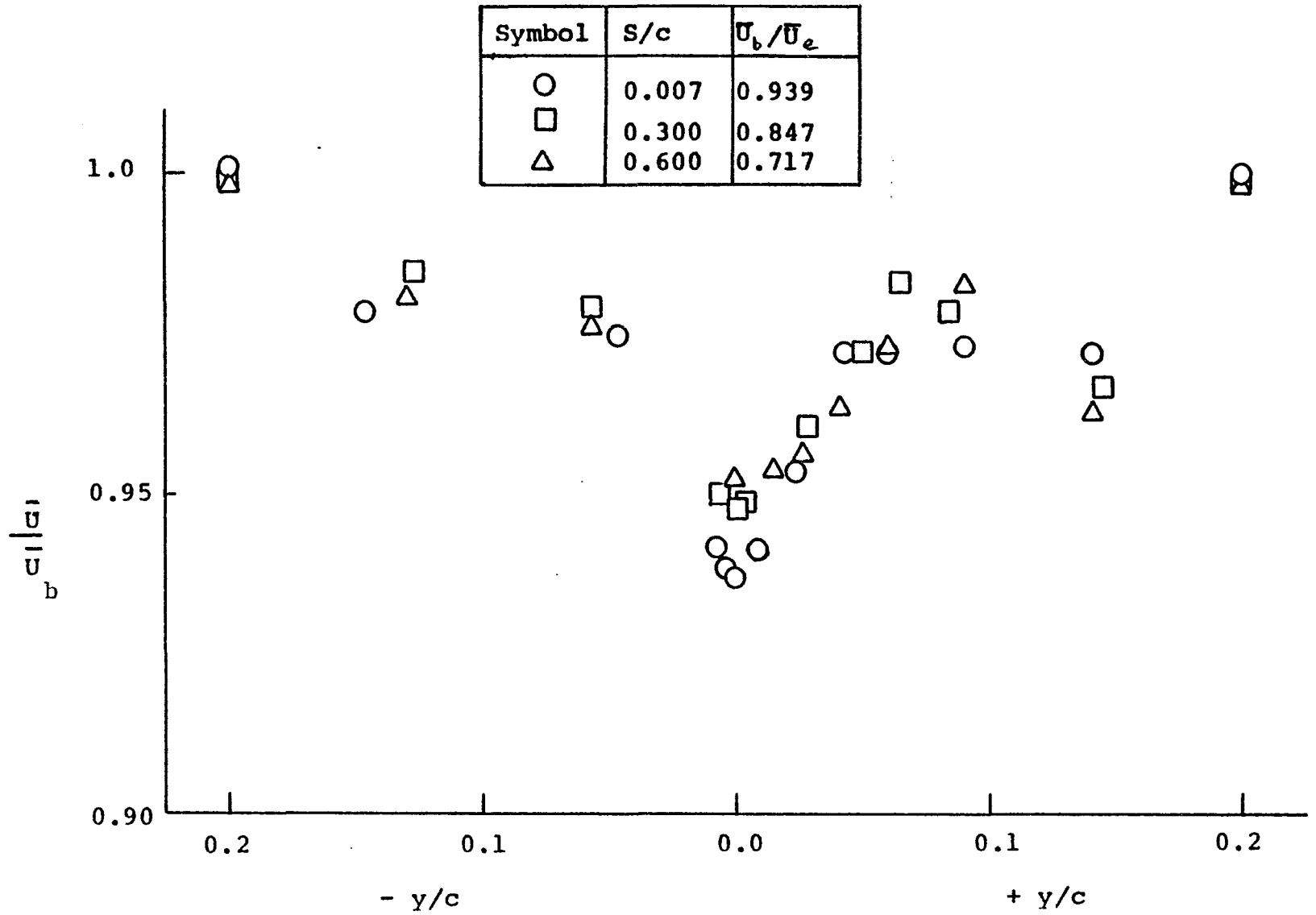

Figure 7.1 (b) Variation of Axial Component of Mean velocity Profile Across the Wake ($x_1/c = 0.68$, $z/c = 0.01$)

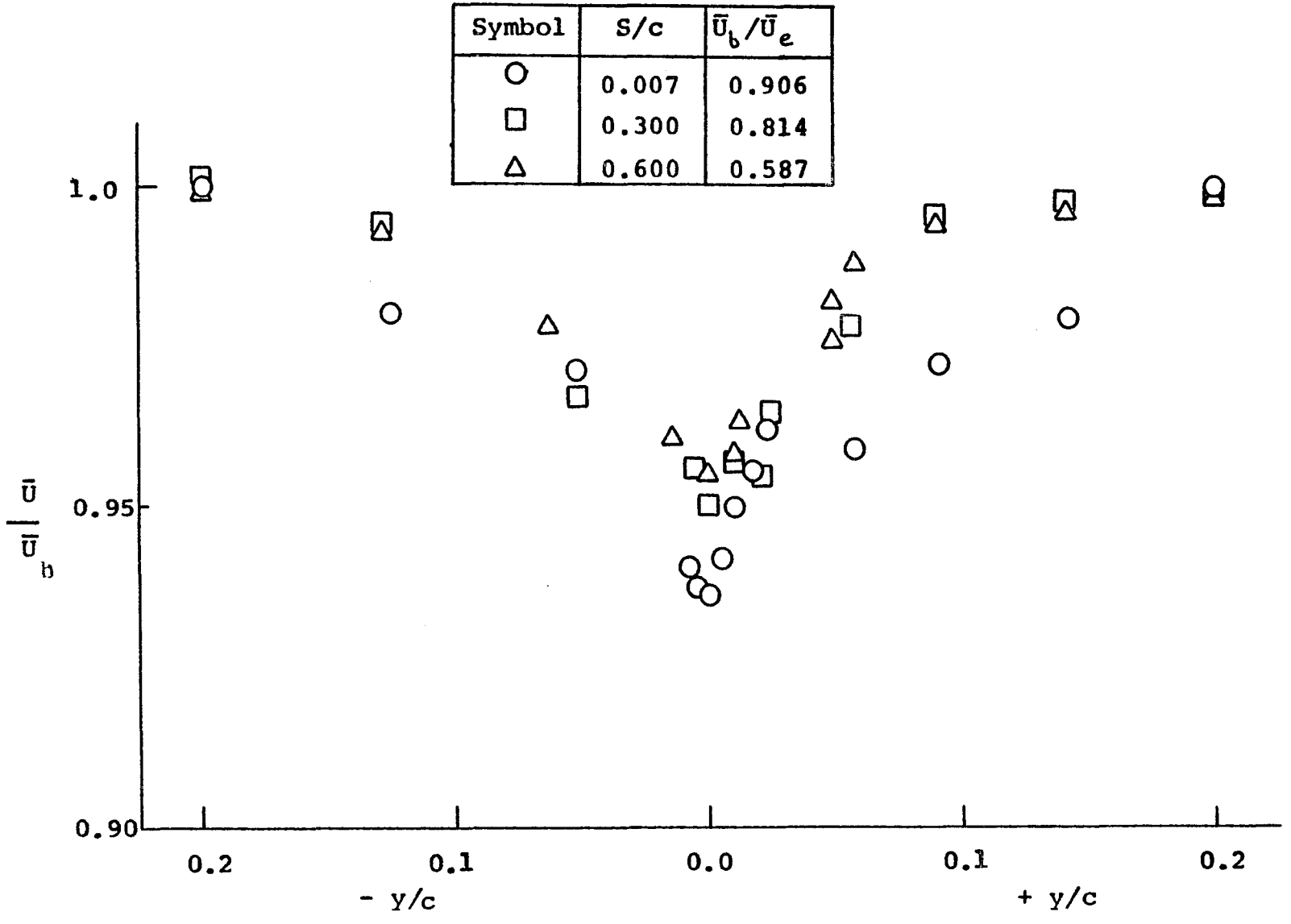

Figure 7.1(c) Variation of Axial Component of Mean Velocity Profile Across the Wake ($x_1/c = 0.88$, $z/c = 0.026$)

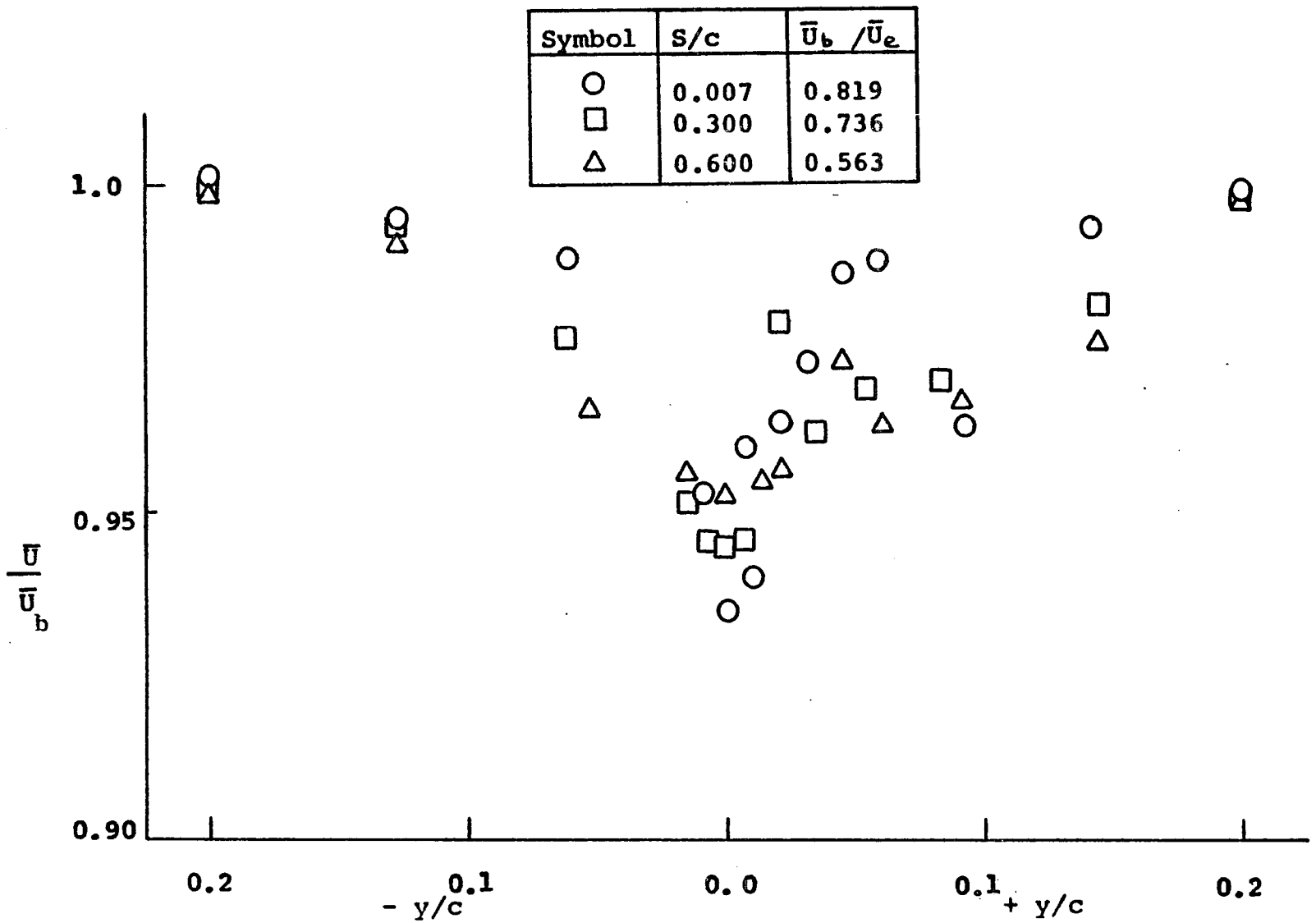

Figure 7.1(d) Variation of Axial Component of Mean Velocity Profile Across the Wake ($x_1/c = 0.88$, $z/c = 0.01$)

layer as compared to the outer region. This is due to the stronger interaction of the boundary layer on the wake.

The lateral component of the mean velocity is slightly larger towards the outer region of the boundary layer. The velocity defect in the lateral component of mean velocity at the wake center line decreases with the increase in downstream distance. Lateral component of the wake center line velocity is about 15 % of the axial component for $S/c \sim 0.007$, while it decreases to about 7 % for $S/c \gtrsim 0.03$.

Normal component of the mean velocity is about 6.3 % of the axial component at the wake center line for $S/c \sim 0.007$, while it decreases to about 2 % for $S/c \gtrsim 0.3$ because of the least effect of interaction felt with the increase downstream distance. There is a dip in the normal component of mean velocity at the wake center line and the maximum of values occur away from the wake center line. The values of the normal components of mean velocity at the outer edge of the wake are higher for $S/c \sim 0.007$ as compared to $S/c \sim 0.6$ in the outer region of the interacted boundary layer because of the stronger influence of wake. For $S/c = 0.6$, the values of normal component of mean velocity at the outer edge are higher in the inner region of the interacted boundary layer as compared to the outer region, because of the strong influence of the boundary layer. Even the wake center line

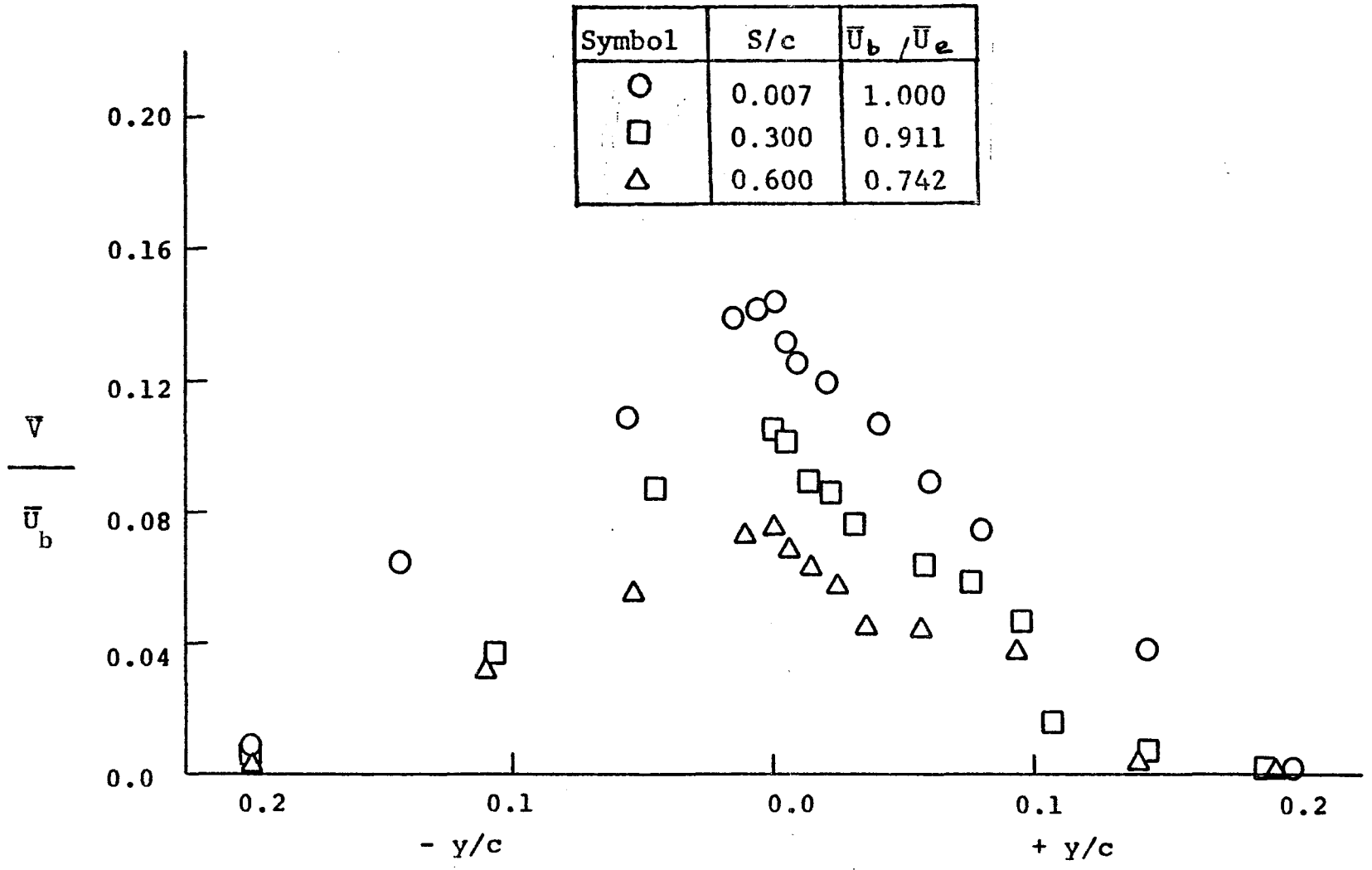

Figure 7.2(a) Variation of Lateral Component of Mean Velocity Profile Across the Wake ($x_1/c = 0.68$, $z/c = 0.026$)

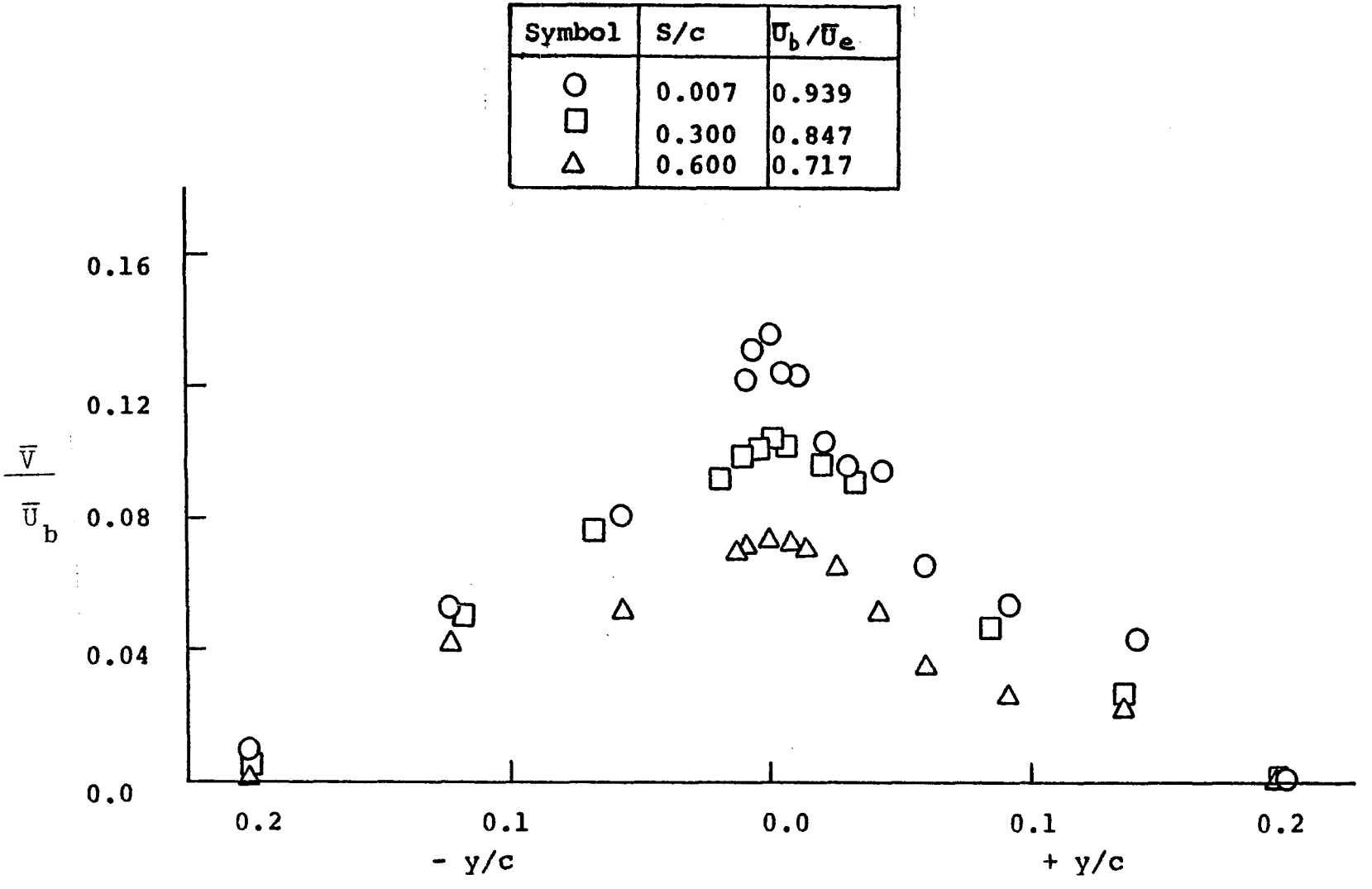

Figure 7.2(b) Variation of Lateral Component of Mean Velocity Profile Across the Wake ($x_1/c = 0.68$, $z/c = 0.01$)

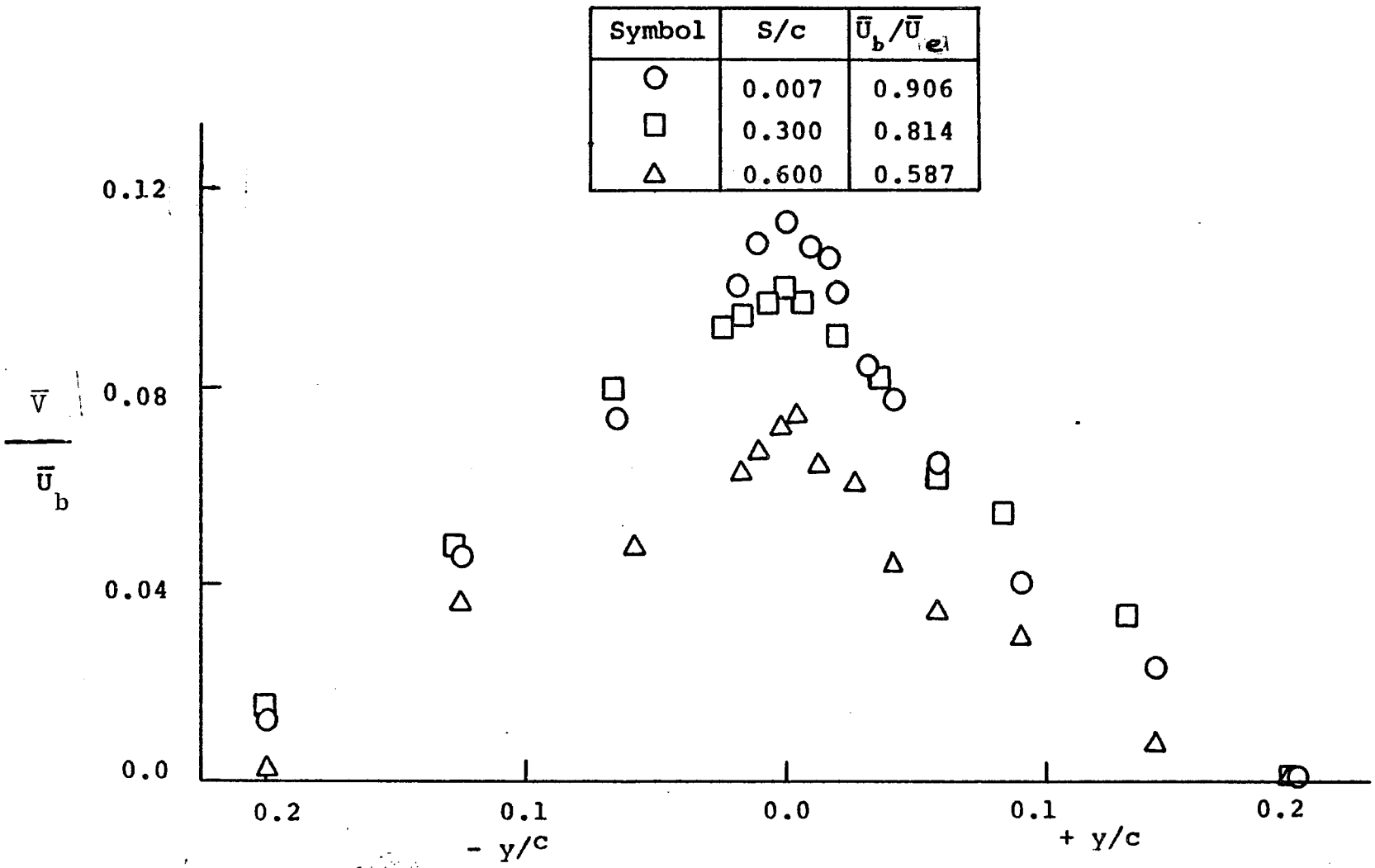

Figure 7.2(c) Variation of Lateral Component of Mean Velocity Profile Across the Wake ($x_1/c = 0.88$, $z/c = 0.026$)

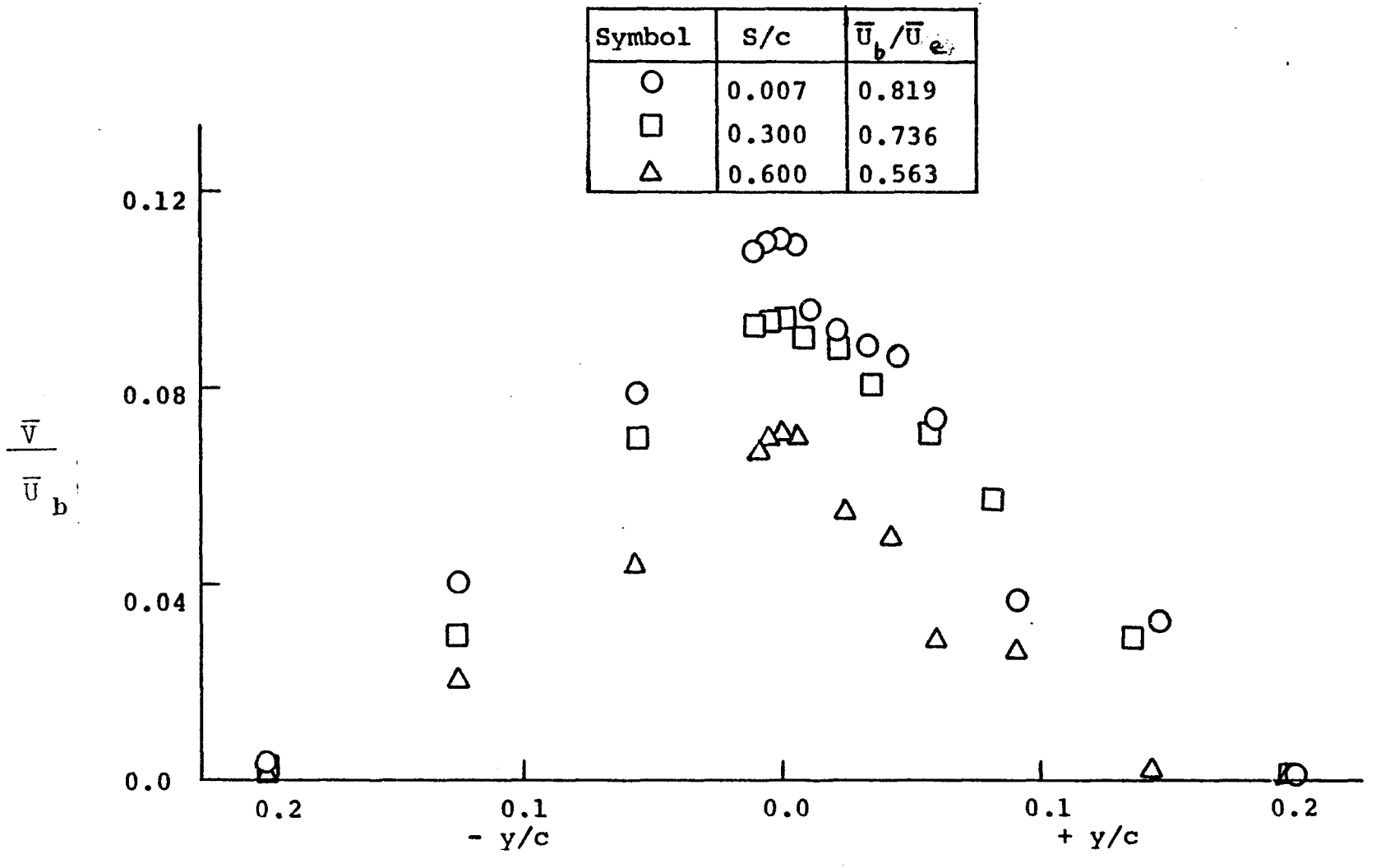

Figure 7.2(d) Variation of Lateral Component of Mean Velocity Profile Across the Wake ($x_1/c = 0.88$, $z/c = 0.01$)

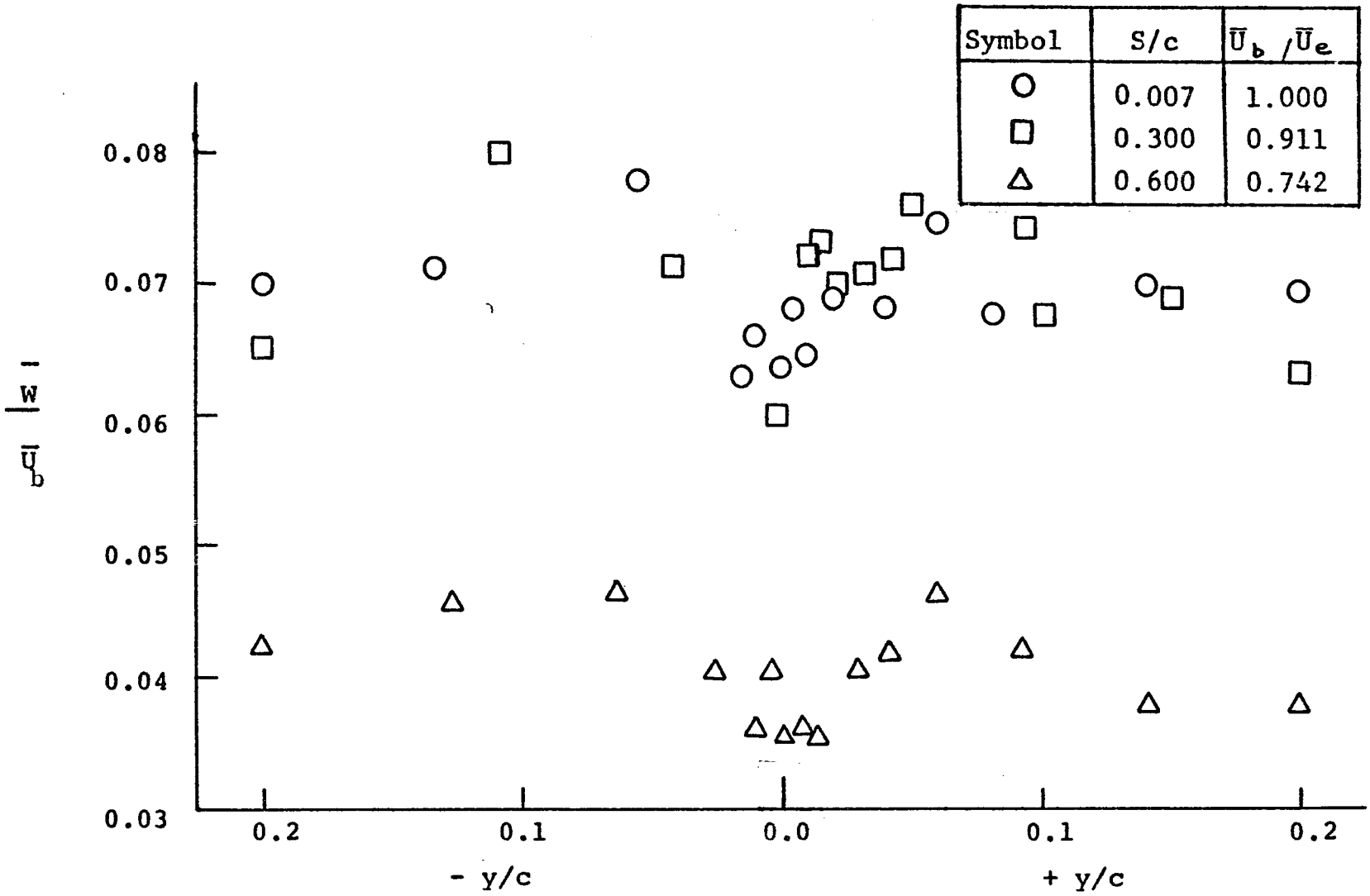

Figure 7.3(a) Variation of Normal Component of Mean Velocity Profile Across the Wake ($x_1/c = 0.68$, $z/c = 0.026$)

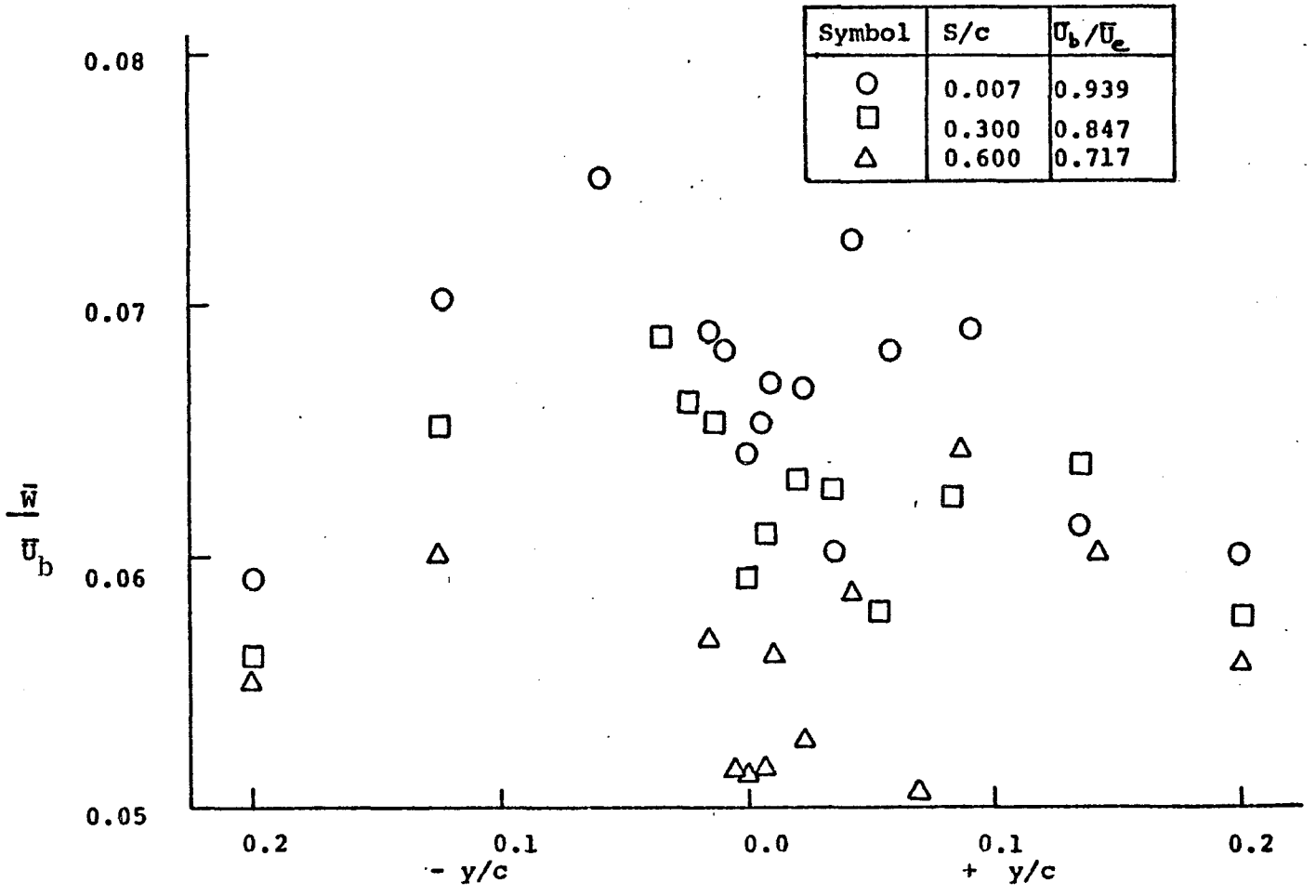

Figure 7.3(b) Variation of Normal Component of Mean Velocity Profile Across the Wake ($x_1/c = 0.68$, $z/c = 0.01$)

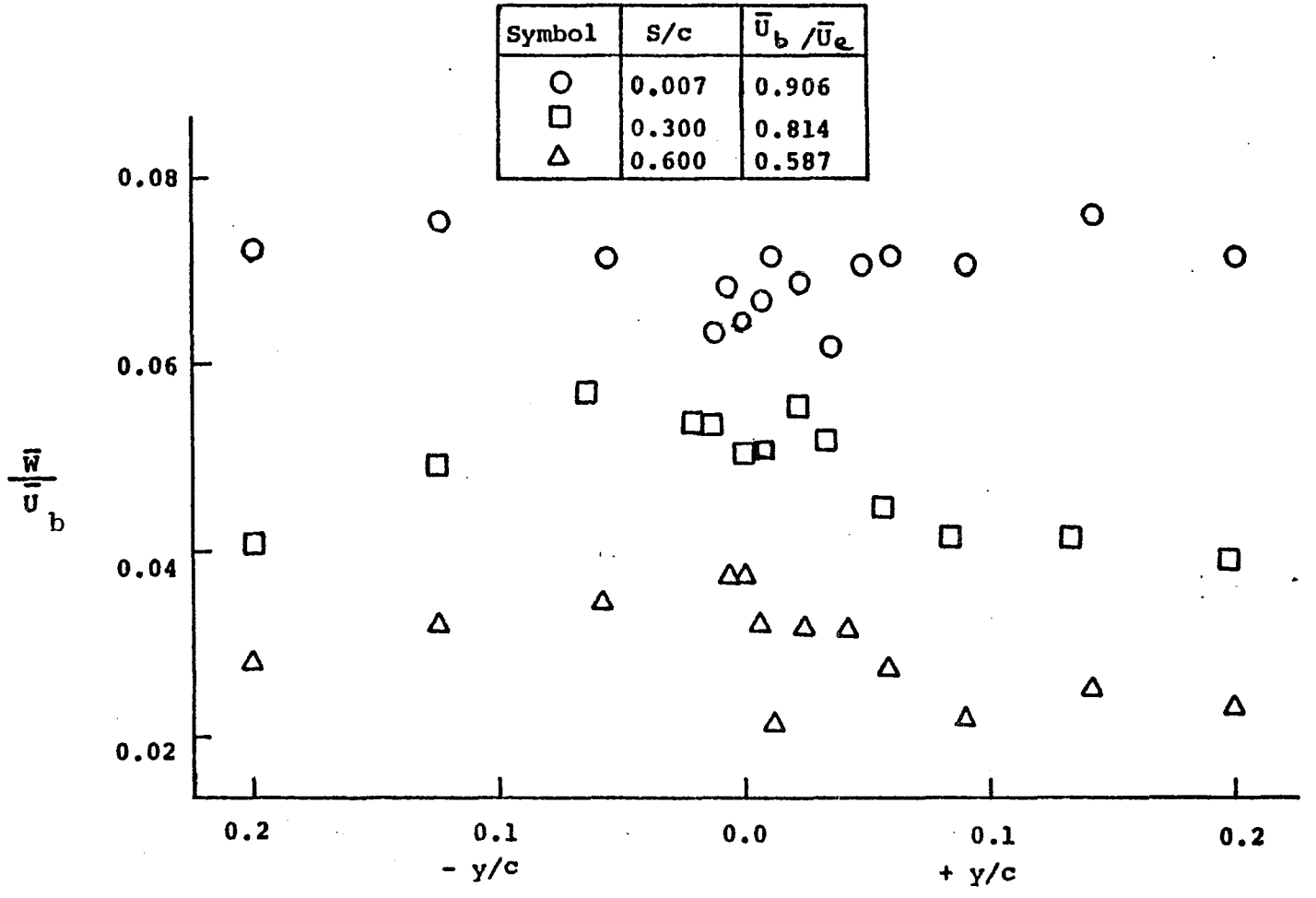

Figure 7.3(c) Variation of Normal Component of Mean Velocity Profile Across the Wake ($x_1/c = 0.88$, $z/c = 0.026$)

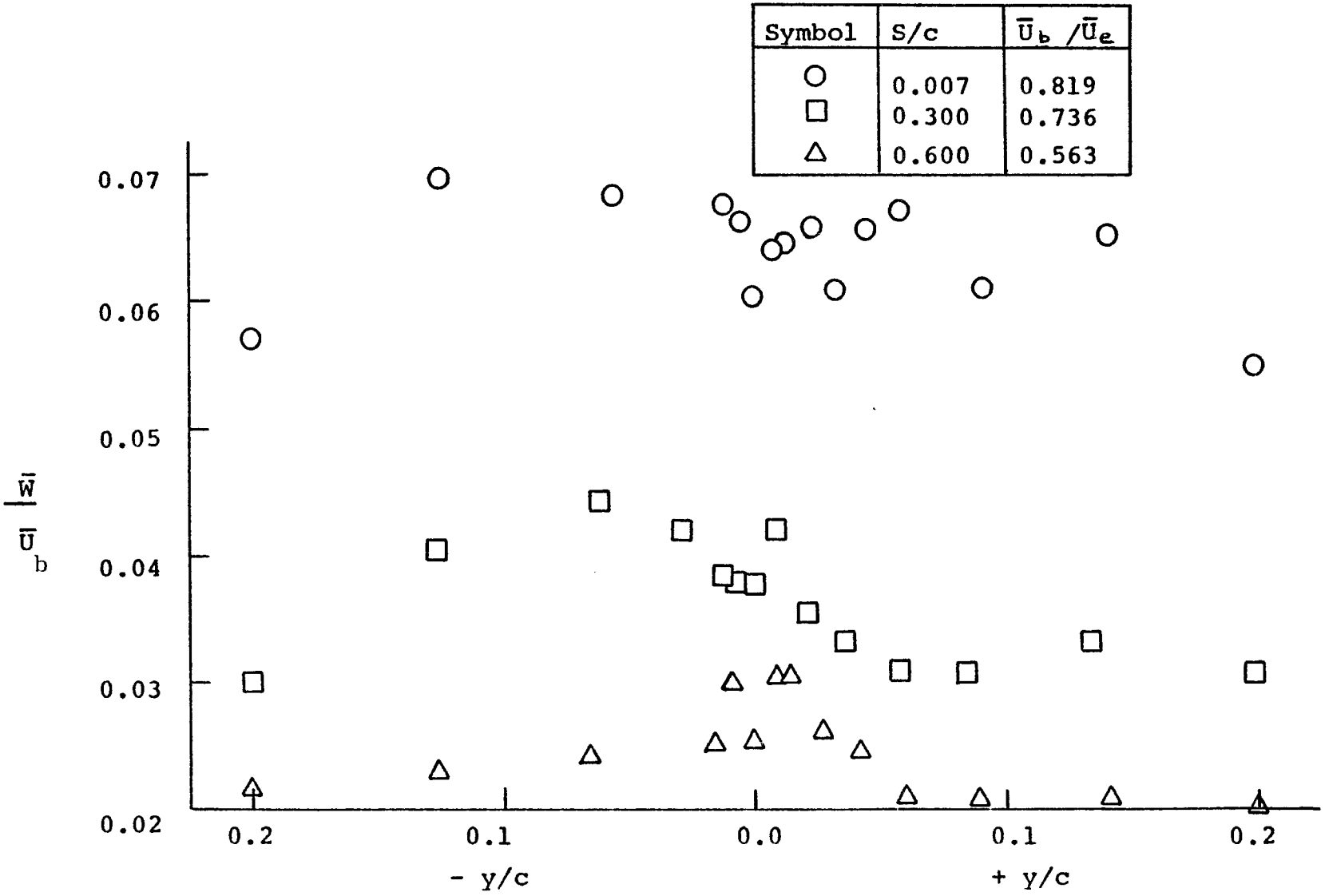

Figure 7.3(d) Variation of Normal Component of Mean Velocity Profile Across the Wake ($x_1/c = 0.88$, $z/c = 0.01$)

value of the normal mean velocity component is higher in the inner region of the boundary layer as compared to the outer region of the boundary layer. The opposite is true for the wake interaction ($S/c \sim 0.007$) because of the stronger effect of wake due to minimum spacing ratio.

7.1.2 Wake Recovery Rate:

Figure 7.4(a) shows the logarithmic variation of the wake velocity defect in the axial component of the mean velocity with downstream distance. The experimental results of the axial component of mean velocity are compared with the values obtained from the following semi-empirical correlation,

$$\frac{U_{d_1}}{\overline{U}_e} = \overline{K}_1 \left[\left(\frac{x - S}{c} \right)^{-\frac{1}{2}} e^{-\eta^2} \right]^{1 - \alpha_1/R^+} \quad \ldots(7.1)$$

The value of the constant $\overline{K}_1$ obtained from the experimental data is 0.263. A slight scatter in the data is observed. But the semi-empirical correlation represents reasonably good average value of the corresponding experimental data. The value of the power constant, α_1, obtained from the experimental data is unity.

The axial component of the mean velocity defect decreases towards the inner region as well as decreases with the increase in spacing as is clear from

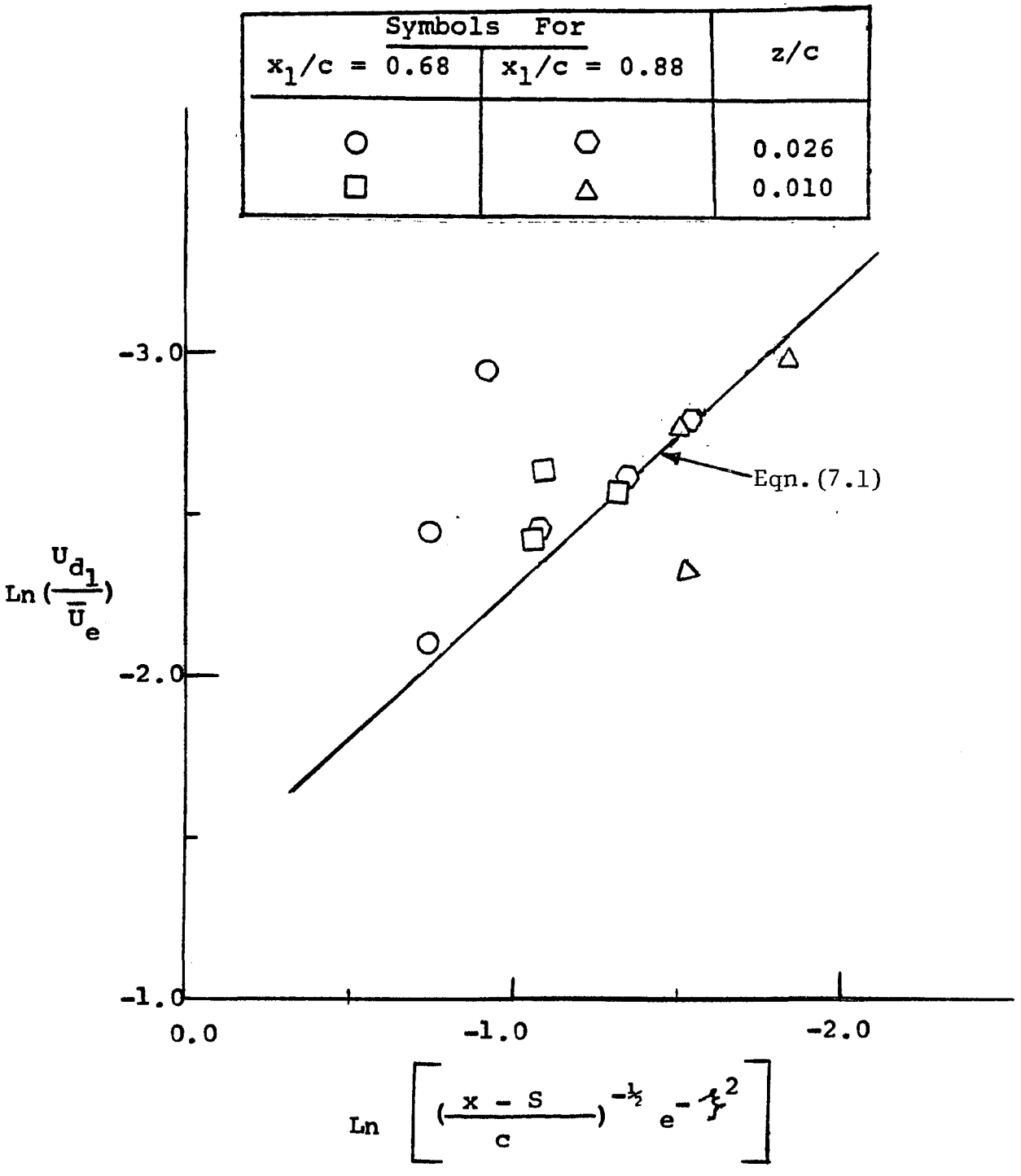

Figure 7.4(a) Logarithmic Variation of Axial Component of Mean Velocity Defect With Downstream Distance

Figure 7.4(a).

It is observed that U_{d_1} should first increase and then decrease, since at $x \leq S$ there is no interaction. Further, U_{d_T} must also decrease because finally the wake will disappear. This increase in U_{d_1} is not predicted because the first measuring station, due to the experimental nature of the set-up is very far from the leading edge of the second flat plate. Therefore, the region where the perturbation components reach maximum values could not be established. The theory presented in Chapter (IV) could also not predict the increase which is due to non-linear interaction. The non-linear interaction term was assumed to be small in Eqn.(4.24) to obtain the solution. We believe that U_{d_1} first increases sharply, then stays constant and finally decreases again. However, we do not know at this point precisely where to separate the above regions; this will require additional investigation.

The similarity variable is defined as

$$\eta = \frac{z}{2\sqrt{\nu_{T_1} x/\bar{U}_e}}$$

where ν_{T_1} is obtained from

$$\nu_{T_1} = \frac{\left| -(\overline{uv})_{max} \right|}{\partial \bar{U}/\partial y}$$

The velocity gradients were taken at the occurrence of the maximum value of the Reynolds stress component $\left[-\rho(\overline{u\,v})_{max}\right]$.

The value of the power constant, α_1, obtained from the experimental data is unity. R^+ is obtained from

$$R^+ = \frac{z\ u^+}{\nu}$$

where

$$u^+ = \sqrt{\tau_{max}/\rho}$$

τ_{max} is the maximum value of τ across the boundary layer at any axial station. R^+ decreases towards the wall. The decrease towards the wall is associated with the decrease in the coordinate z, resulting in the decrease in R^+. The value of R^+ ranges from 20 to 100.

Figure 7.4(b) shows the logarithmic variation of the mean velocity defect of the lateral component of mean velocity with downstream distance. A comparison of the experimental results with the values obtained from the following correlation,

$$\frac{U_{d_2}}{\overline{U}_e} = \overline{K}_2 \left[\left(\frac{x - S}{c} \right)^{-\frac{1}{2}} e^{-\zeta^2} \right]^{1 - \alpha_2/R^+} \qquad \ldots(7.2)$$

is made.

The value of the constant $\overline{K}_2$, obtained from the experimental data is 0.161. The agreement between

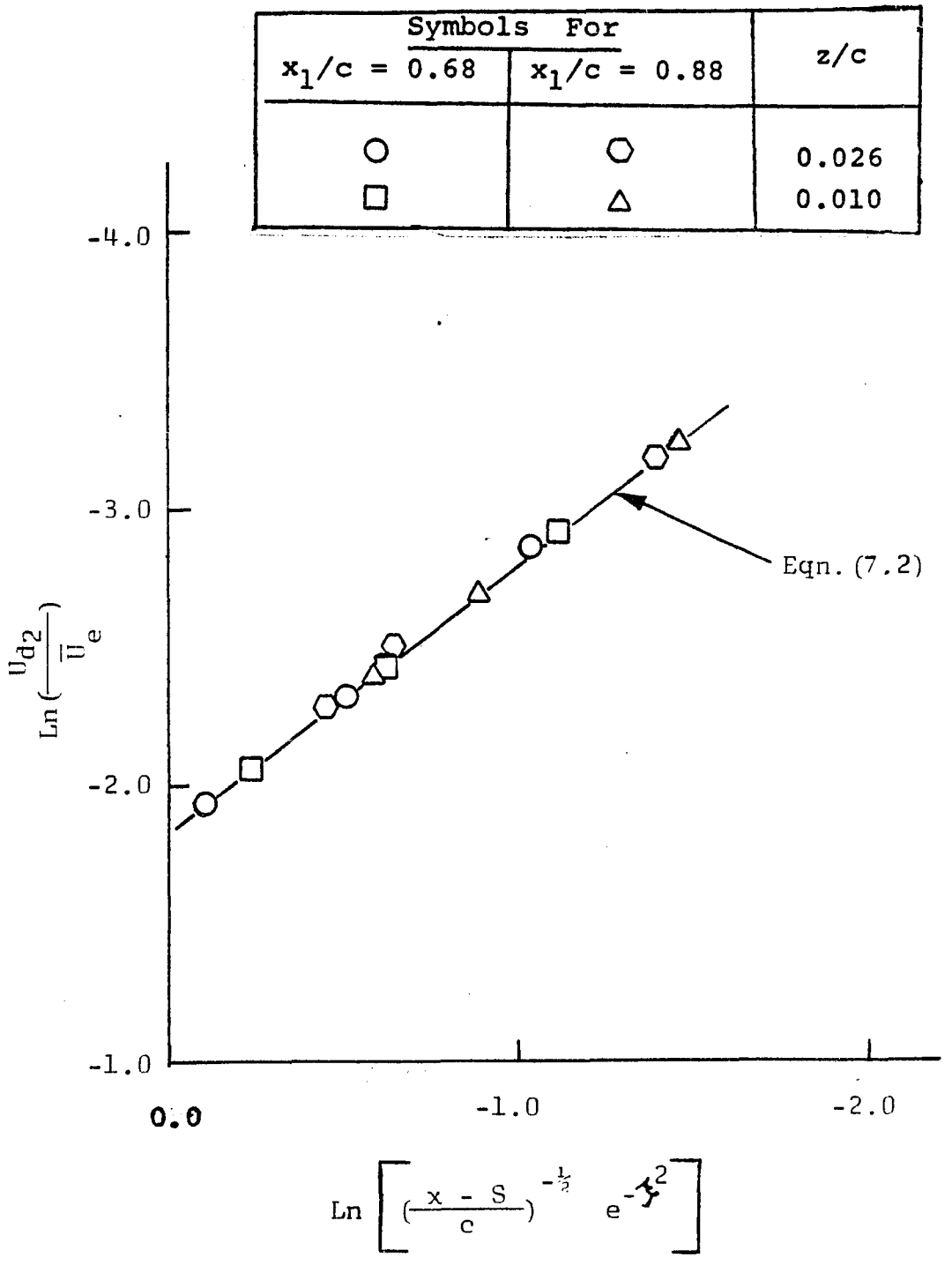

Figure 7.4(b) Logarithmic Variation of Lateral Component of Mean Velocity Defect With Downstream Distance

the semi-empirical correlation and the experimental data is quite favorable.

Here, to calculate ζ, ν_{T_2}, was obtained from

$$\nu_{T_2} = \frac{\left| -(\overline{vw})_{max} \right|}{\partial \bar{v}/\partial z}$$

The velocity gradients were taken at the occurrence of the maximum value of the Reynolds stress component $\left[-\rho(\overline{v\,w})_{max} \right]$. The value of the power constant, α_2, obtained from the experimental data is unity.

The variation of the mean velocity defect of the lateral component decreases towards the inner region as well as with increase in spacing.

Figure 7.4(c) shows the logarithmic variation of the normal component of mean velocity defect ($U_{d_3} = \bar{W}_{max} - \bar{W}_c$) at the wake center line with downstream distance. The normal component of the mean velocity defect decreases towards the inner region and with the increase in spacing. This indicates that the interaction of the wake with the boundary layer becomes weaker with increase in downstream distance as well as with the increase in spacing. The comparison of the experimental results with the values obtained from the following correlation,

$$\frac{U_{d_3}}{\bar{U}_e} = \bar{K}_3 \left[\left(\frac{x - S}{c} \right)^{-\frac{1}{2}} e^{-\zeta^2} \right]^{1 - \alpha_1/R^+} \quad \ldots(7.3)$$

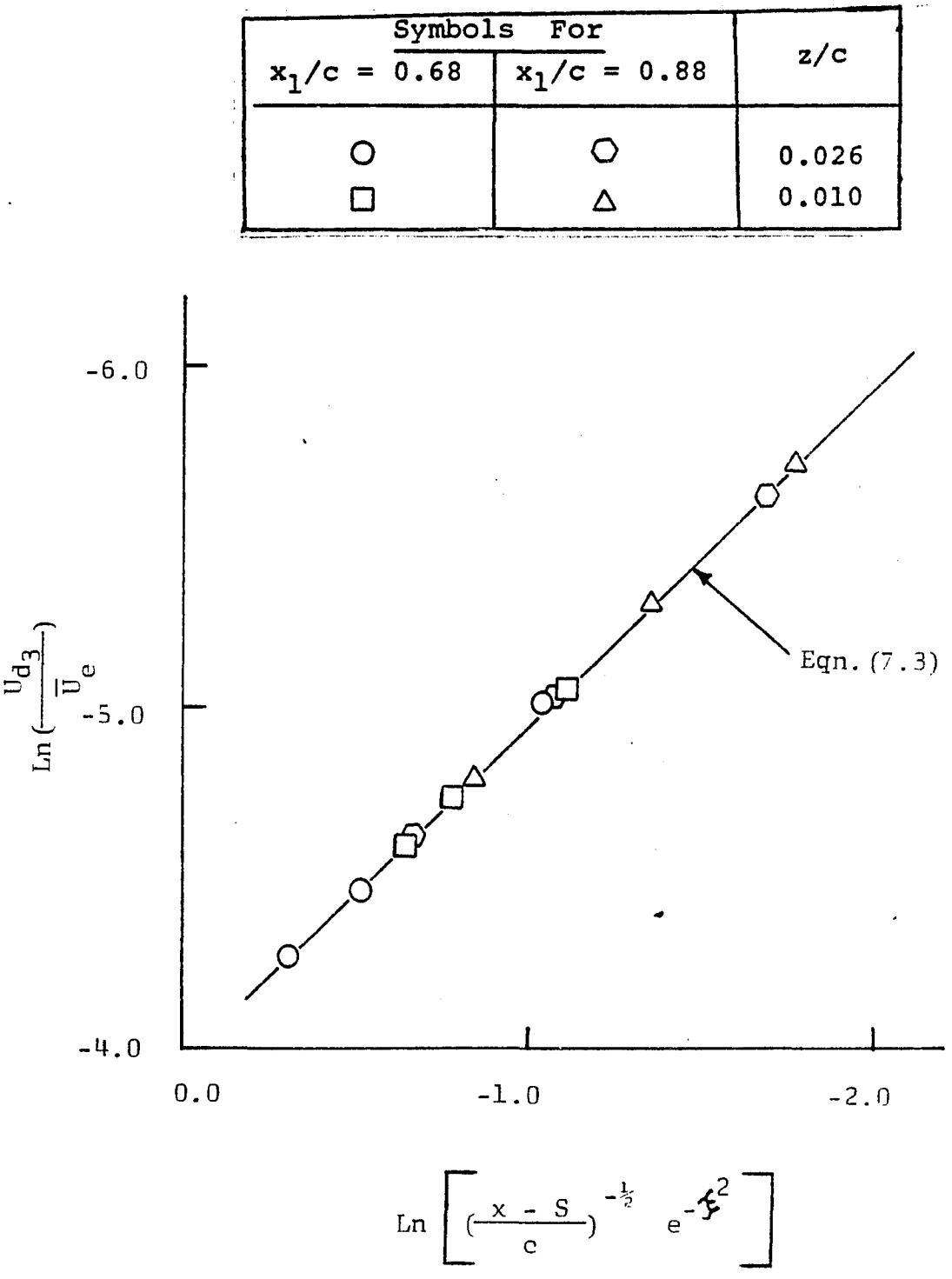

Figure 7.4(c) Logarithmic Variation of Normal Component of Mean Velocity Defect With Downstream Distance

is made.

The value of the constant, $\bar{K}_3$, obtained from the experimental data, is 0.019. Here, to calculate ξ , ν_{T_3} was obtained from,

$$\nu_{T_3} = \frac{\left| -(\overline{wu})_{max} \right|}{\partial \bar{w} / \partial x}$$

The velocity gradients were taken at the occurrence of the peak values of the Reynolds stress component $\left[-\rho \left(\overline{wu} \right)_{max} \right]$. The agreement between the experimental data and the semi-empirical correlation is quite good.

The value of the wake center line velocity defect in the axial, lateral and normal directions for three spacings at stations I and II is shown in Figures 7.5(a) and (b), respectively. It is observed that axial, lateral and normal velocity defects at the wake center line decrease with the increase in spacing because of the weaker interaction of the wake with the boundary layer. The lateral and normal velocity defects are higher in the outer region of the boundary layer as compared to the inner region at any spacing. This means that the strong interaction decays the velocity defect faster.

7.1.3 Length Scale:

Figure 7.6 shows the logarithmic variation of the length scale with the downstream distance. It is clear

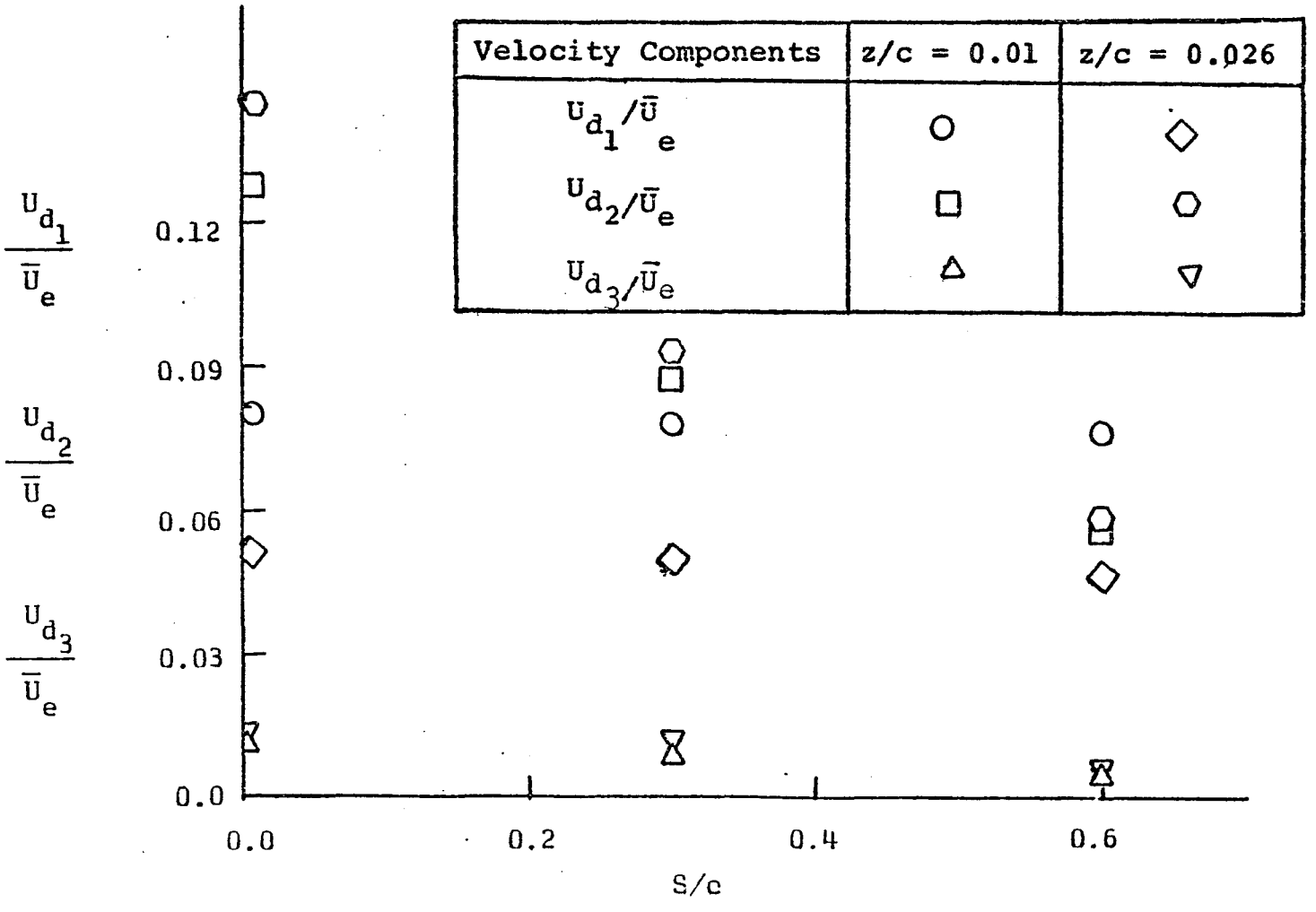

Figure 7.5(a) Variation of Axial Component of Mean Velocity Defect, Lateral Component of Mean Velocity Defect and Normal Component of Mean Velocity Defect at the Wake Center Line With S/c Ratio ($x_1/c = 0.68$)

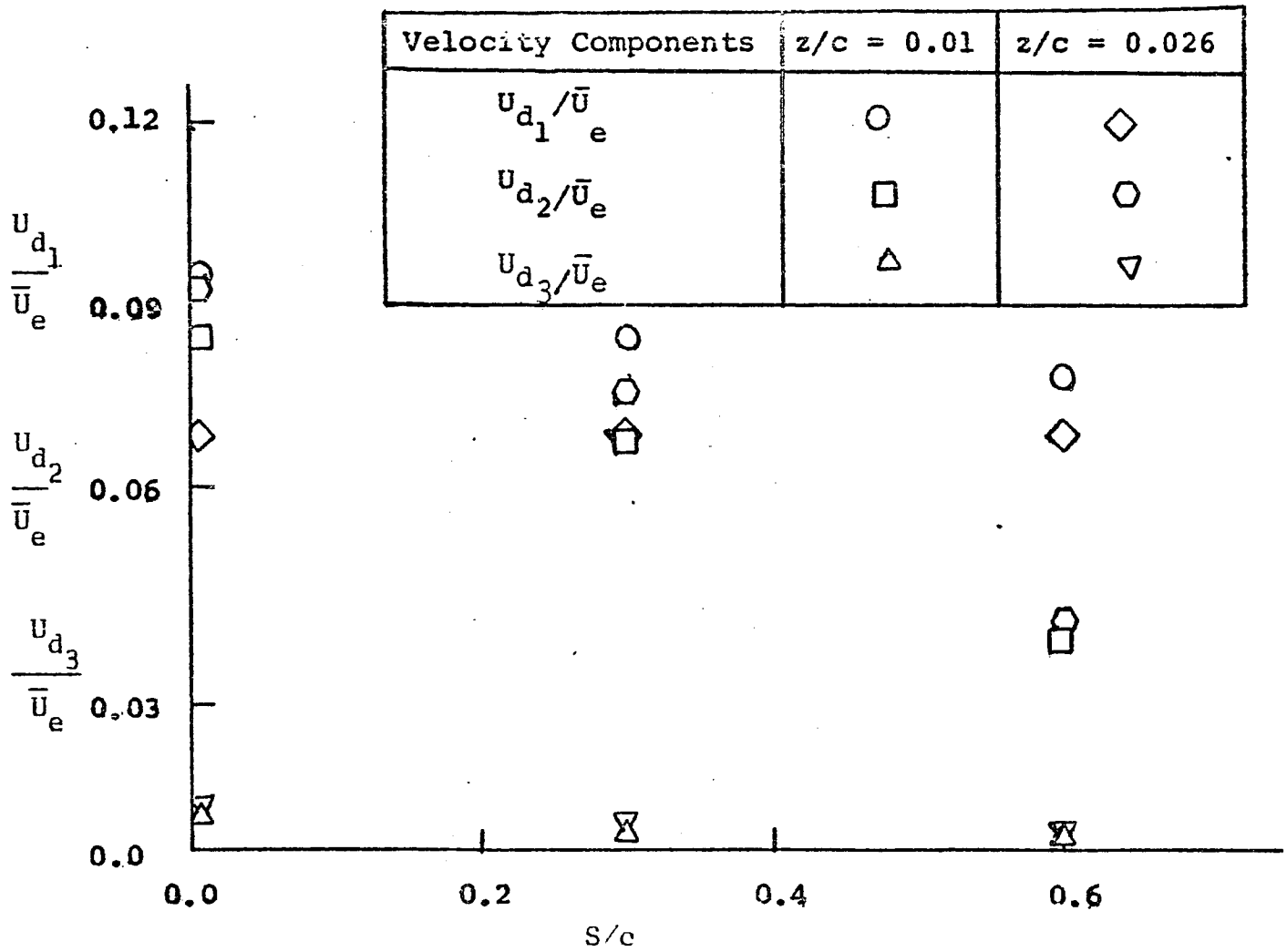

Figure 7.5(b) Variation of Axial Component of Mean Velocity Defect, Lateral Component of Mean Velocity Defect and Normal Component of Mean Velocity Defect at the Wake Center Line With S/c Ratio (x_1/c = 0.88)

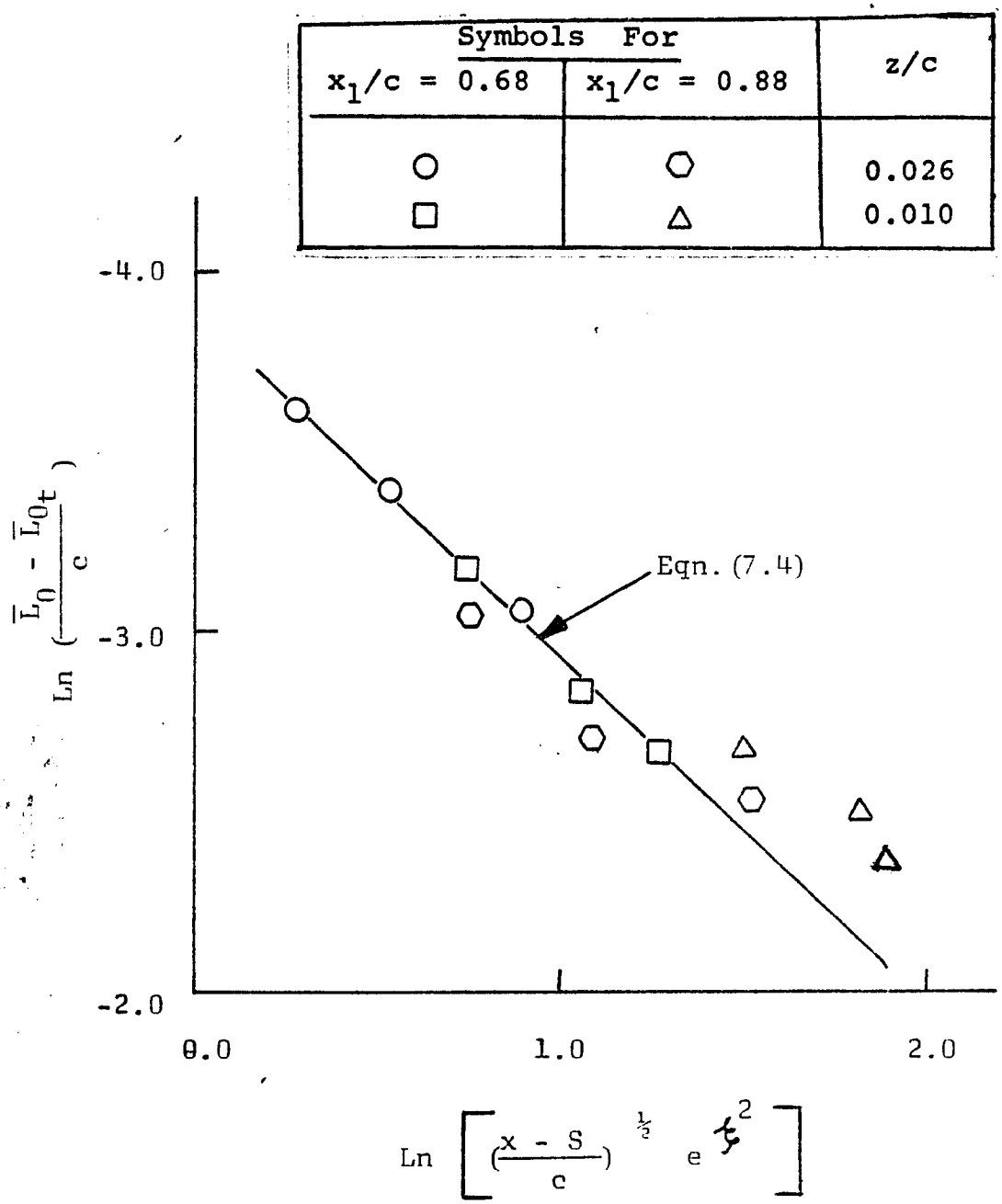

Figure 7.6 Logarithmic Variation of Length Scale With Downstream Distance

from the theoretical considerations that the interaction increases the length scale with the increase in downstream distance and is given by the following correlation

$$\frac{\bar{L}_0 - \bar{L}_{0t}}{c} = \bar{K}_4 \left[\left(\frac{x - S}{c} \right)^{\frac{1}{2}} e^{\eta^2} \right]^{1 - \mathcal{L}_i/R^+} \quad \ldots(7.4)$$

where $\bar{L}_{0_t}$ is the value of the wake length scale at the beginning of the boundary layer interaction and is obtained from the two-dimensional correlations, (Eqn. 3.20). The value of the constant $\bar{K}_4$, obtained from the experimental data is 0.020. Half wake width increases towards the wall as well as with downstream distance because of the decrease in velocity defect.

7.1.4 Turbulence Interaction Parameters:

The non-dimensional parameters $\bar{\Phi}_i$ and $\bar{\Psi}_i$ have been named as the turbulence interaction parameters in the present investigation. They are given by the following equations, derived in Chapter (IV),

$$\bar{\Phi}_1 = \left[\left(\frac{x - S}{c} \right)^{-\frac{1}{2}} e^{-\eta^2} \right]^{\mathcal{L}_{1/R^+}} \quad \ldots(7.5)$$

$$\bar{\Phi}_2 = \left[\left(\frac{x - S}{c} \right)^{-\frac{1}{2}} e^{-\eta^2} \right]^{\mathcal{L}_{2/R^+}} \quad \ldots(7.6)$$

$$\bar{\Phi}_3 = \left[\left(\frac{x - S}{c} \right)^{-\frac{1}{2}} e^{-\eta^2} \right]^{\mathcal{L}_{3/R^+}} \quad \ldots(7.7)$$

$$\bar{\Psi}_1 = \left[\left(\frac{x - S}{c} \right)^{-\frac{1}{2}} e^{-\eta^2} \right]^{\bar{\mathcal{L}}_{1/R^+}} \quad \ldots(7.8)$$

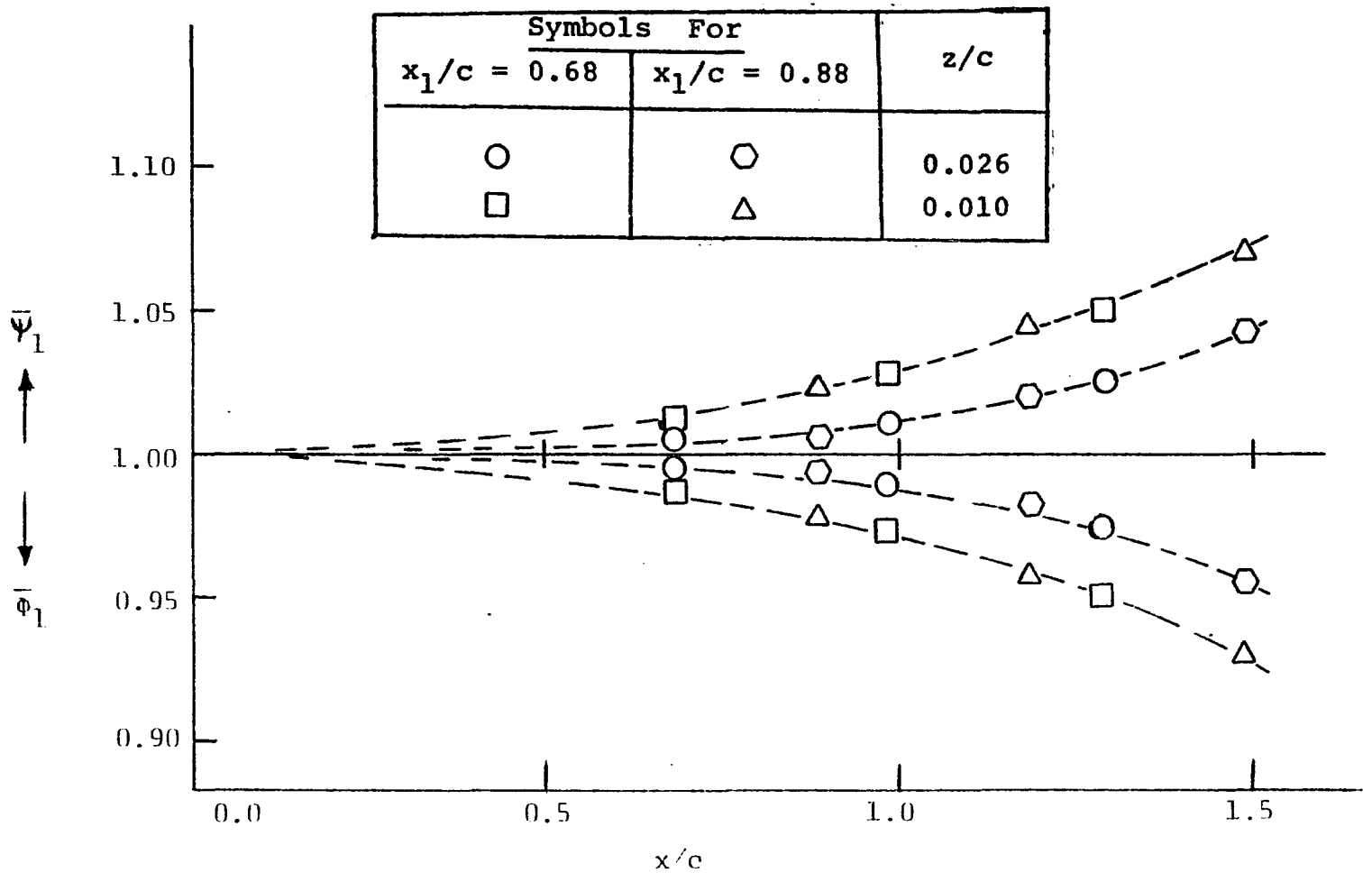

Figure 7.7(a) Variation of Turbulence Interaction Parameters ($\bar{\Phi}_1$, $\bar{\Psi}_1$) With Downstream Distance

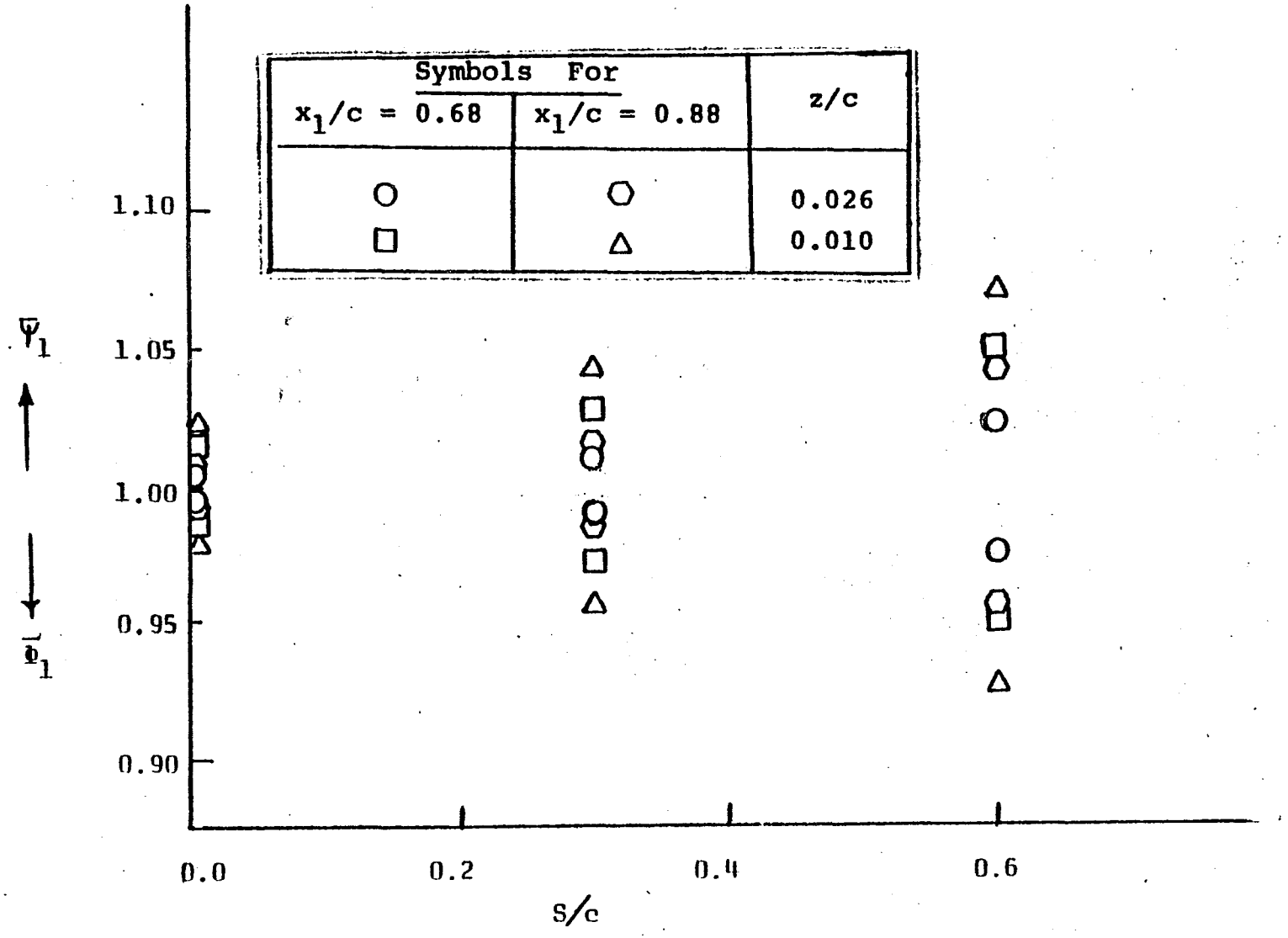

Figure 7.7(b) Variation of Turbulence Interaction Parameters ($\bar{\Phi}_1$, $\bar{\Psi}_1$) With S/c Ratio

$$\overline{\Psi}_2 = \overline{\Psi}_3 = \overline{\Psi}_1 \qquad \ldots(7.9)$$

These parameters ($\overline{\Phi}_i$, $\overline{\Psi}_i$) are shown in Figures 7.7(a) and (b) and represent the wake boundary layer interaction effect due to turbulence. $\overline{\Phi}_i$ tends to decrease the velocity defect while $\overline{\Psi}_i$ tends to increase the length scale. Their behavior is inverse to each other. At the start of the wake boundary layer interaction, both of these parameters are unity. $\overline{\Phi}_i$ decreases while $\overline{\Psi}_i$ increases in the inner region of the interacted boundary layer as compared to the outer region. With the increase in in downstream distance, $\overline{\Phi}_i$ goes on decreasing, while $\overline{\Psi}_i$ goes on increasing as the velocity defect decreases and length scale increases with the spreading of the wake. The variation of $\overline{\Phi}_i$ and $\overline{\Psi}_i$ with the increase in spacing is shown in Figure 7.7(b). $\overline{\Phi}_i$ decreases while $\overline{\Psi}_i$ increases with the increase in spacing. The same behavior is true toward the wall for any spacing ratio. The value of α_3, obtained from the experimental data is unity.

7.1.5 Similarity:

In Figures 7.8(a), (b) and (c) an attempt is made to reduce the axial mean velocity profiles given in Figures 7.1(a), (b), (c) and (d) to a single curve. For this purpose, $\overline{L}_0\,\overline{\Psi}_i$ is used as the length scale while U_{d_T} (total axial component of mean velocity defect at the wake center line) is used as the velocity scale.

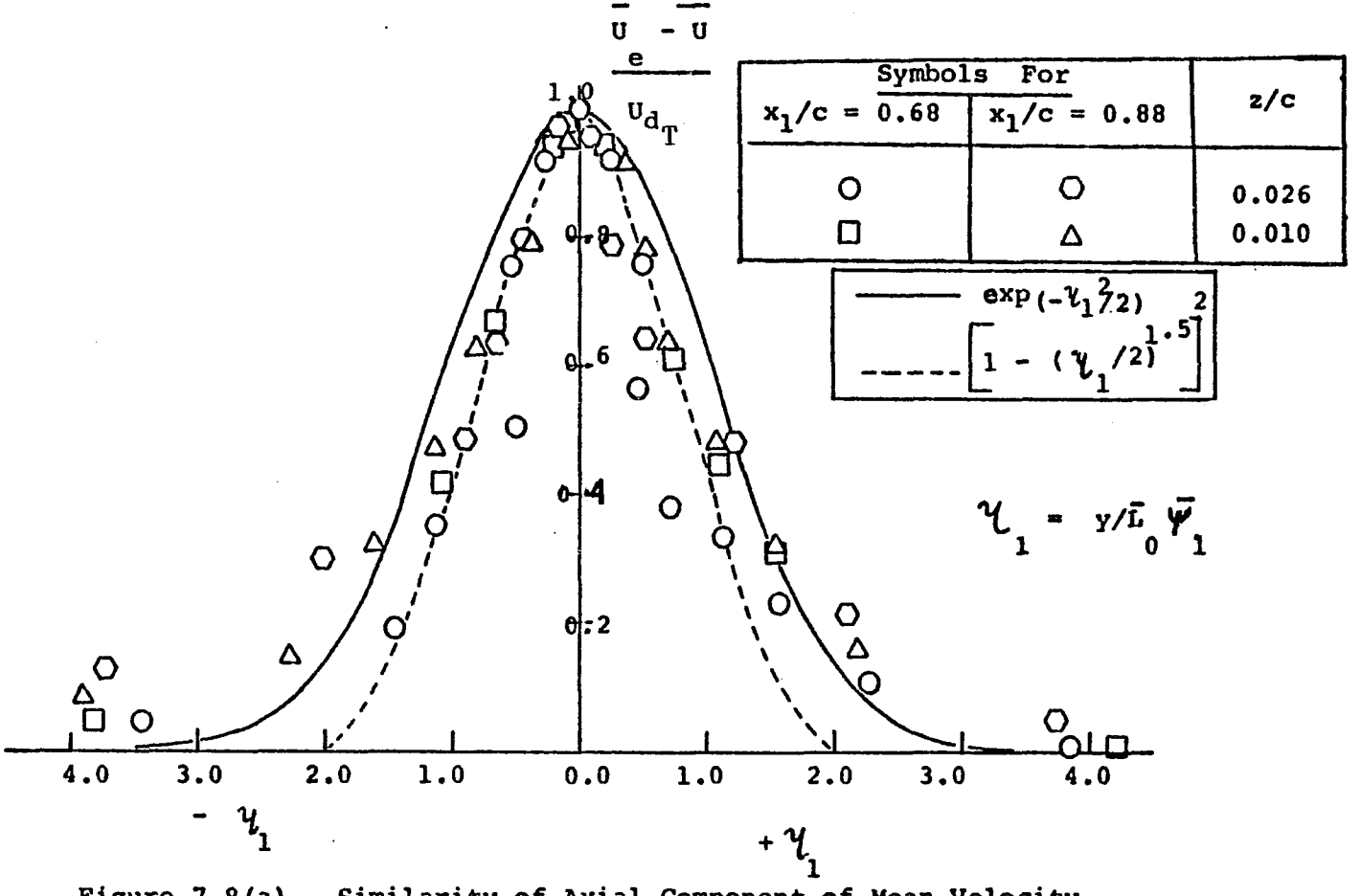

Figure 7.8(a) Similarity of Axial Component of Mean Velocity Profile (S/c = 0.007)

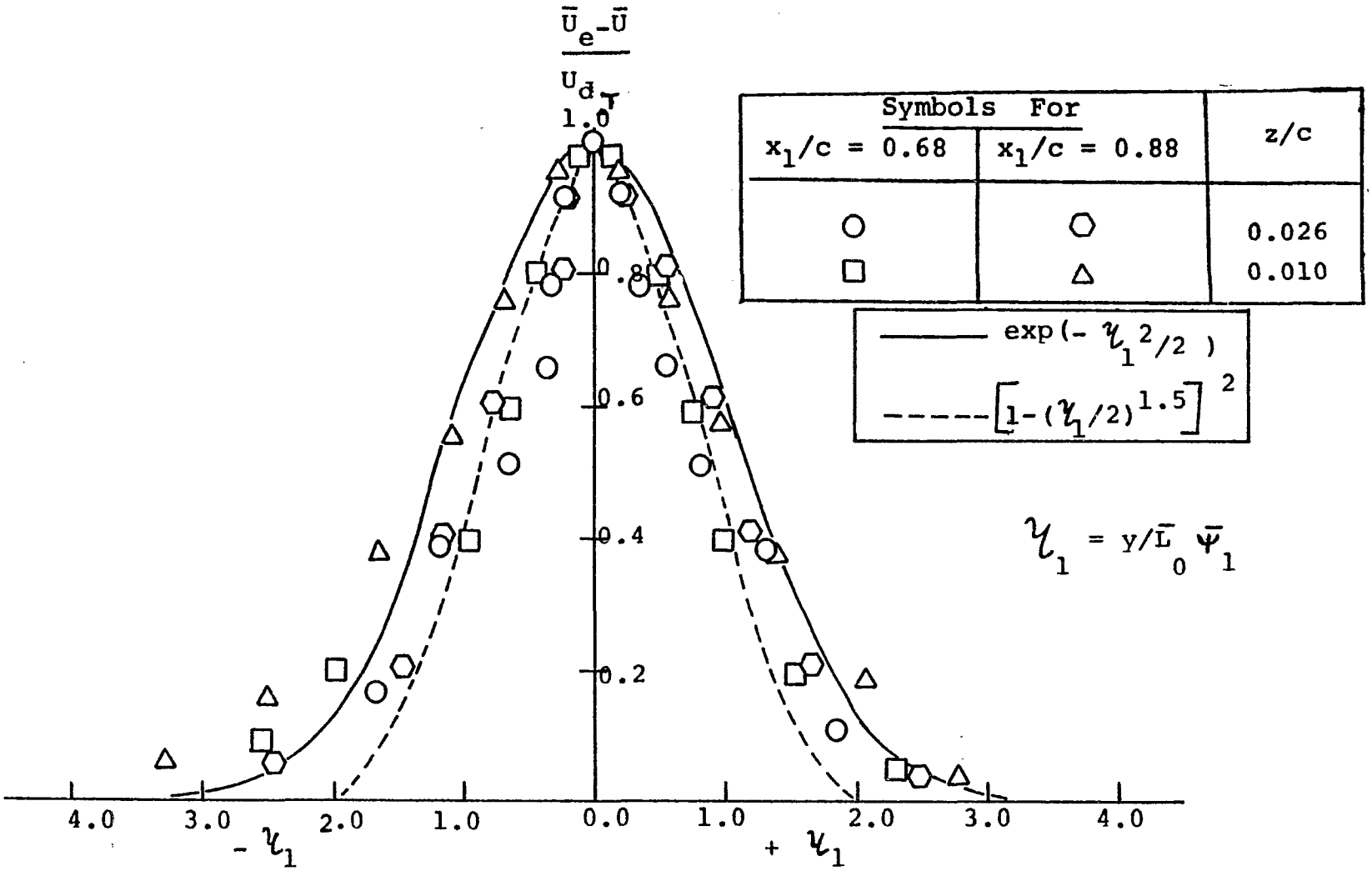

Figure 7.8(b) Similarity of Axial Component of Mean Velocity Profile (S/c = 0.3)

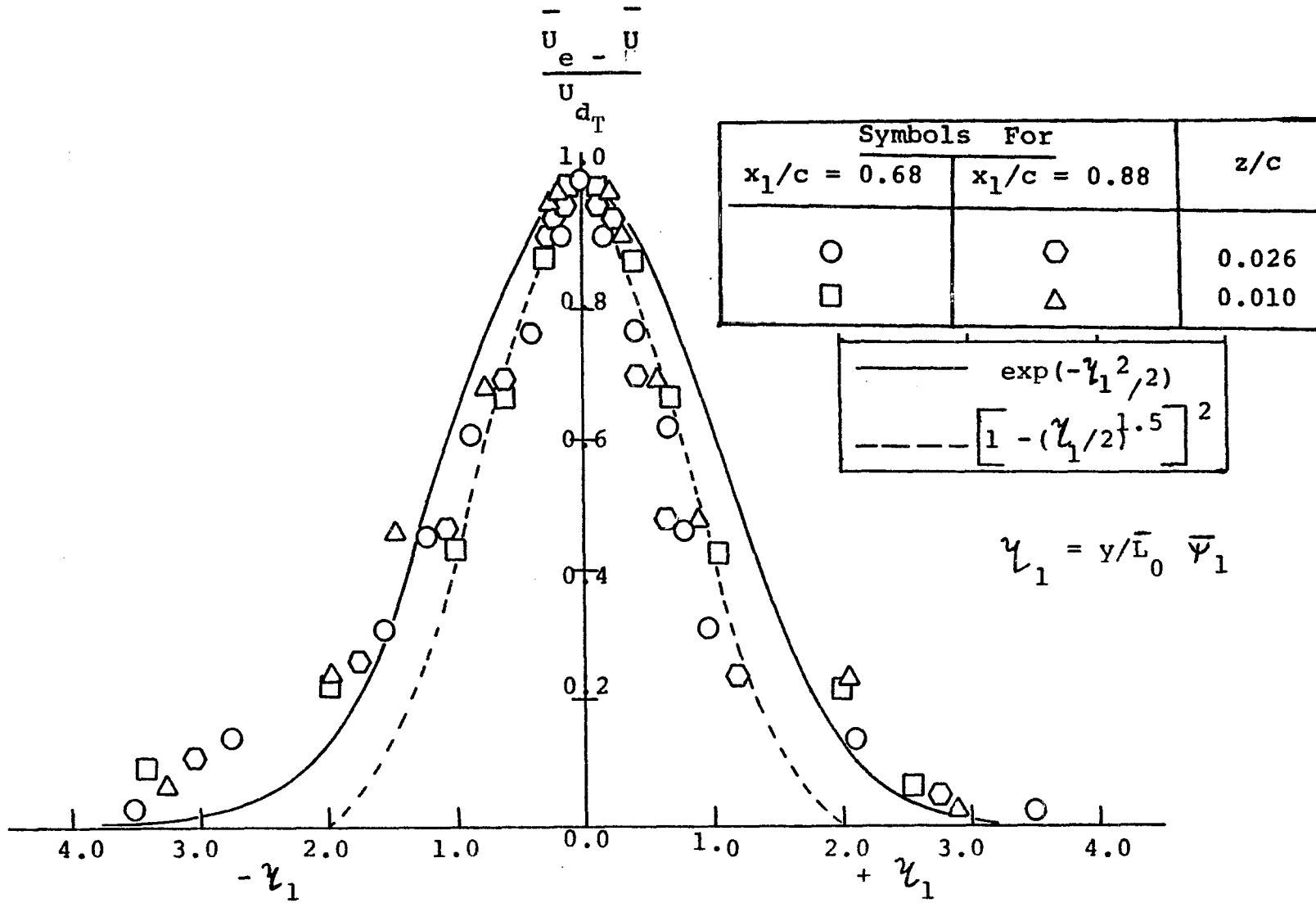

Figure 7.8(c) Similarity of Axial Component of Mean Velocity Profile (S/c = 0.6)

$\bar{L}_0$ is the distance from the wake center line to a point in the lateral direction where the velocity defect is 50 % and the velocity scale $U_{d_T} = \bar{U}_e - \bar{U}_c$. It is clear from Figures 7.8(a), (b) and (c) that the similarity in the axial component of the mean velocity profile is maintained to a good extent and the similarity profiles are well described and lie between the functions $\left[1 - (\eta_1/2)^{1.5}\right]^2$ and $\exp(-\eta_1^2/2)$, where $\eta_1 = y/\bar{L}_0 \bar{\Psi}_1$. In the case of smaller S/c, slight scatter in data in the inner region of interaction, is observed. This may be due to the stronger boundary layer effect and is an indication that if the interaction is strong, the concept of similarity is partially violated.

7.2 Turbulence Quantities:

7.2.1 Turbulence Intensity Profiles:

The axial component of the turbulence intensity for two axial locations and two normal locations corresponding to each of the axial location is presented in Figures 7.10(a) to (d) and 7.11(a) to (d), respectively.

The axial component of turbulence intensity is found to be slightly asymmetrical about the wake center line. This asymmetry may be due to the non-uniform distribution of surface roughness in the y-direction. Peak values of the axial component of turbulence intensity

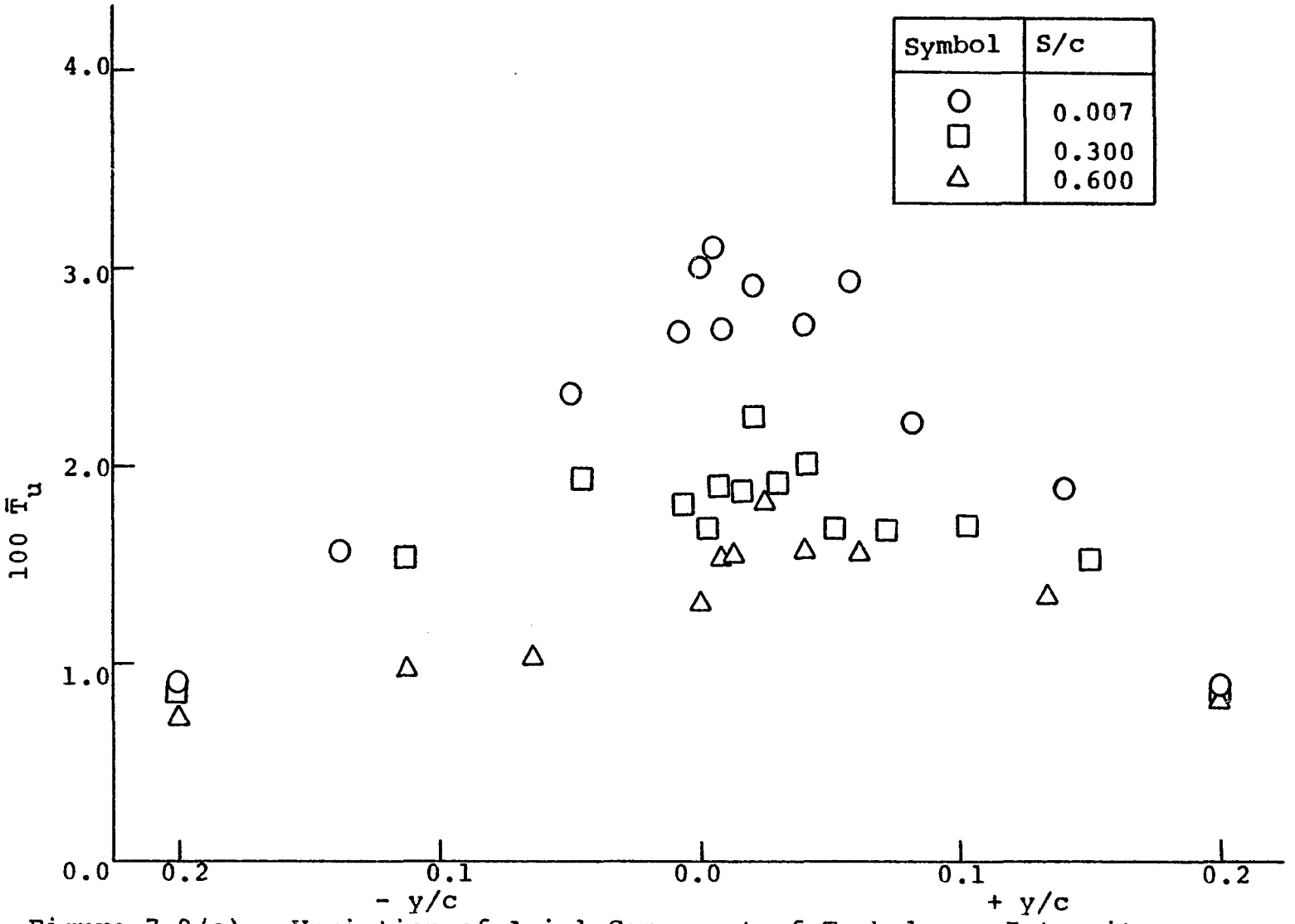

Figure 7.9(a) Variation of Axial Component of Turbulence Intensity Across the Wake ($x_1/c = 0.68$, $z/c = 0.026$)

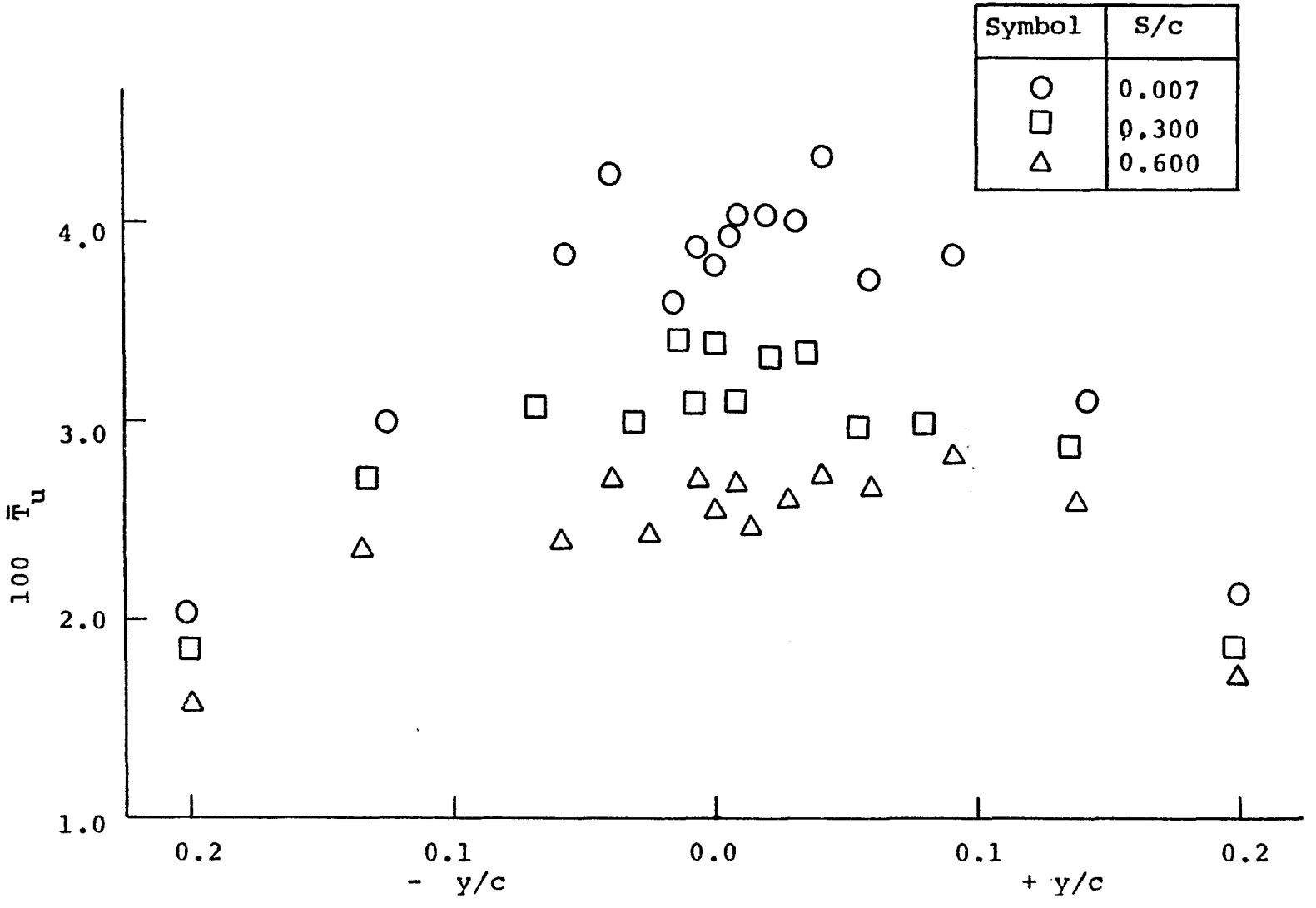

Figure 7.9(b) Variation of Axial Component of Turbulence Intensity Across the Wake ($x_1/c = 0.68$, $z/c = 0.01$)

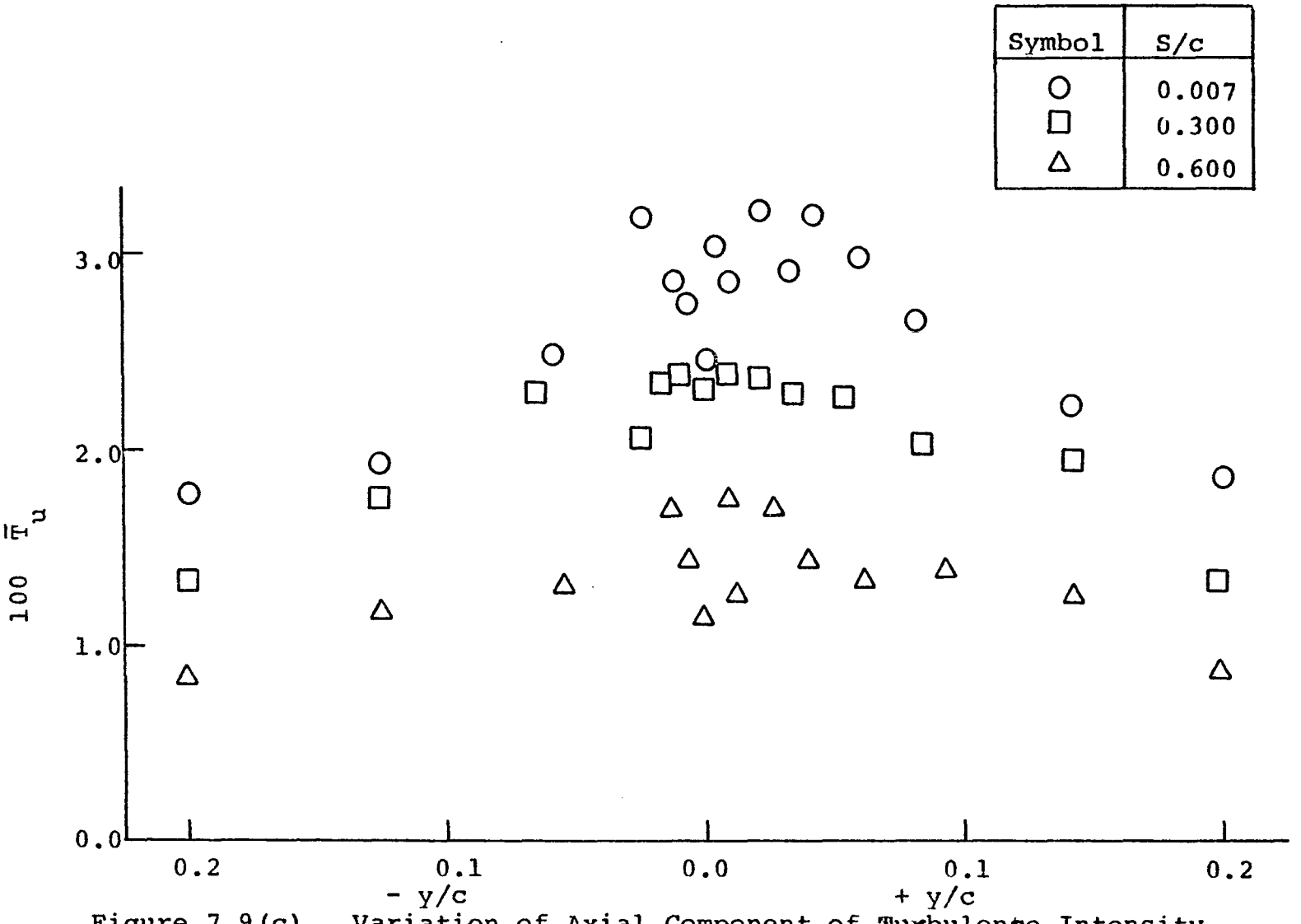

Figure 7.9(c) Variation of Axial Component of Turbulence Intensity Across the Wake ($x_1/c = 0.88$, $z/c = 0.026$)

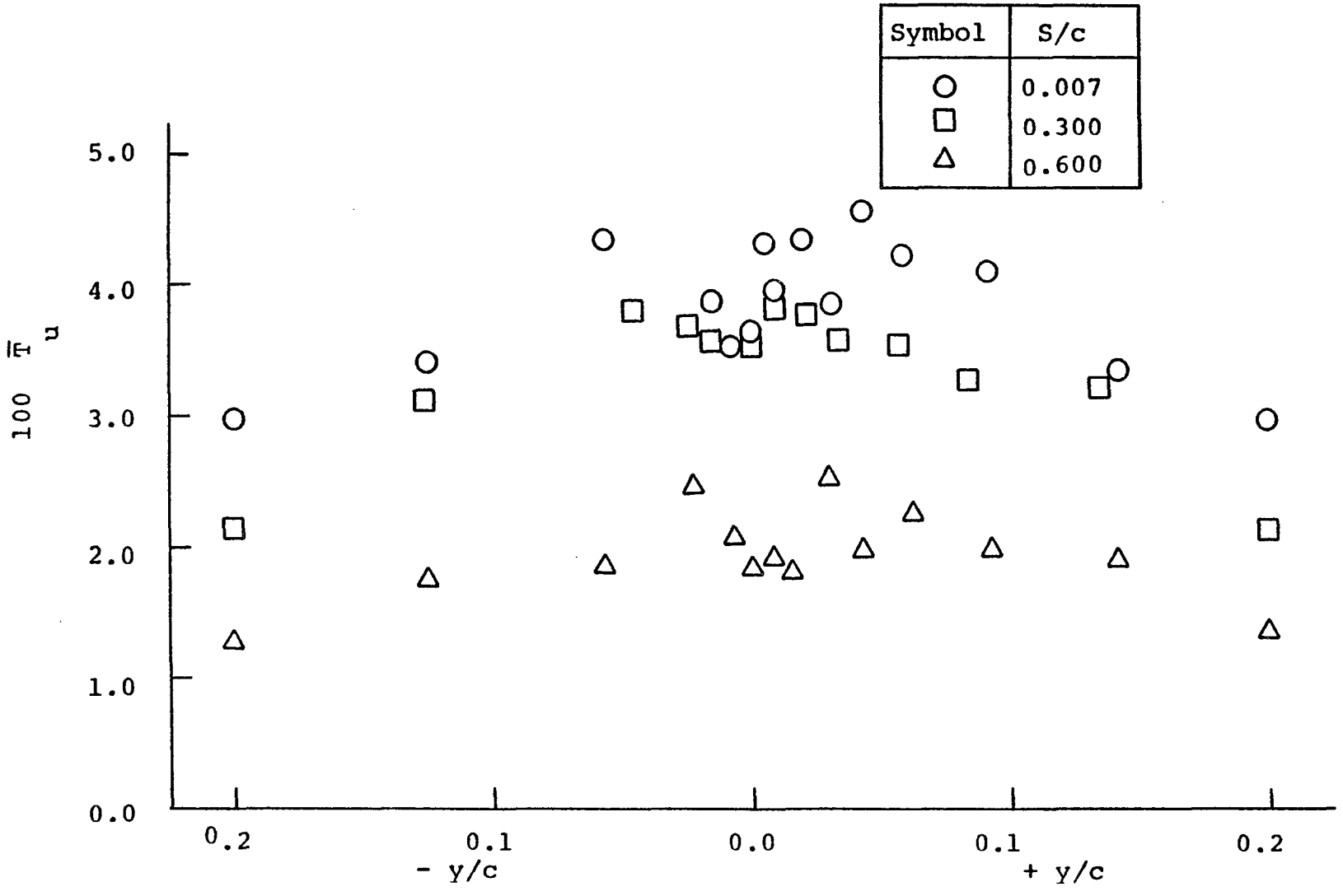

Figure 7.9(d) Variation of Axial Component of Turbulence Intensity Across the Wake (x_1/c = 0.88, z/c = 0.01)

occur away from the wake center line. The occurrence of peak values of the axial component of turbulence intensity shifts away from the wake center line with the increase in spacing. This is due to wake spread.

The axial component of turbulence intensity decreases with the increase in normal distance, i.e. the axial component of turbulence intensity increases towards the wall and decreases away from the wall, giving the usual boundary layer behavior.

In the lateral direction, the axial component of turbulence intensity tends to approach the values nearly equal to the boundary layer values at the wake edges because at the wake edges production of turbulence due to boundary layer interaction is negligible as compared to the wake center line. The axial component of turbulence intensity increases due to interaction of wake with the boundary layer as compared to that in the absence of wake.

The axial component of turbulence intensity increases slightly with the downstream distance while decreasing with the increase in spacing at the same axial station. The slight increase is due to the strong wake boundary layer interaction. The decrease in axial component of turbulence intensity , due to the increase in spacing, is associated with weak wake boundary layer interaction.

The general profile for the lateral [Figure 7.10 (a) to (d)] and normal [Figure 7.11(a) to (d)] components of turbulence intensity is similar to the axial component of turbulence intensity. However, both lateral and normal components of turbulence intensity decrease with the increase in spacing as well as with downstream distance.

7.2.2 Reynolds Stress:

The $\overline{T}_{uv}$ component of Reynolds stress for two axial locations and two normal locations corresponding to each of the axial location, is presented in Figures 7.12(a) to (d). The value of $\overline{T}_{vw}$ and $\overline{T}_{wu}$ components is presented in Figures 7.13(a) to (d) and Figures 7.14(a) to (d), respectively.

The Reynolds stress distribution of the $\overline{T}_{uv}$ component changes sign about the wake center line, is unequal at the occurrence of peak values and antisymmetric about the wake center line. The $\overline{T}_{uv}$ component increases towards the wall because of the increase in mean velocity gradients. Its value decreases with the downstream distance and with the increase in spacing. Its value tends to that of boundary layer towards the outer edge of the wake. The values in the inner region at the outer edge of the wake increase with the decrease in the normal distance due to the stronger velocity gradients towards the wall. The outer edge values decrease with the

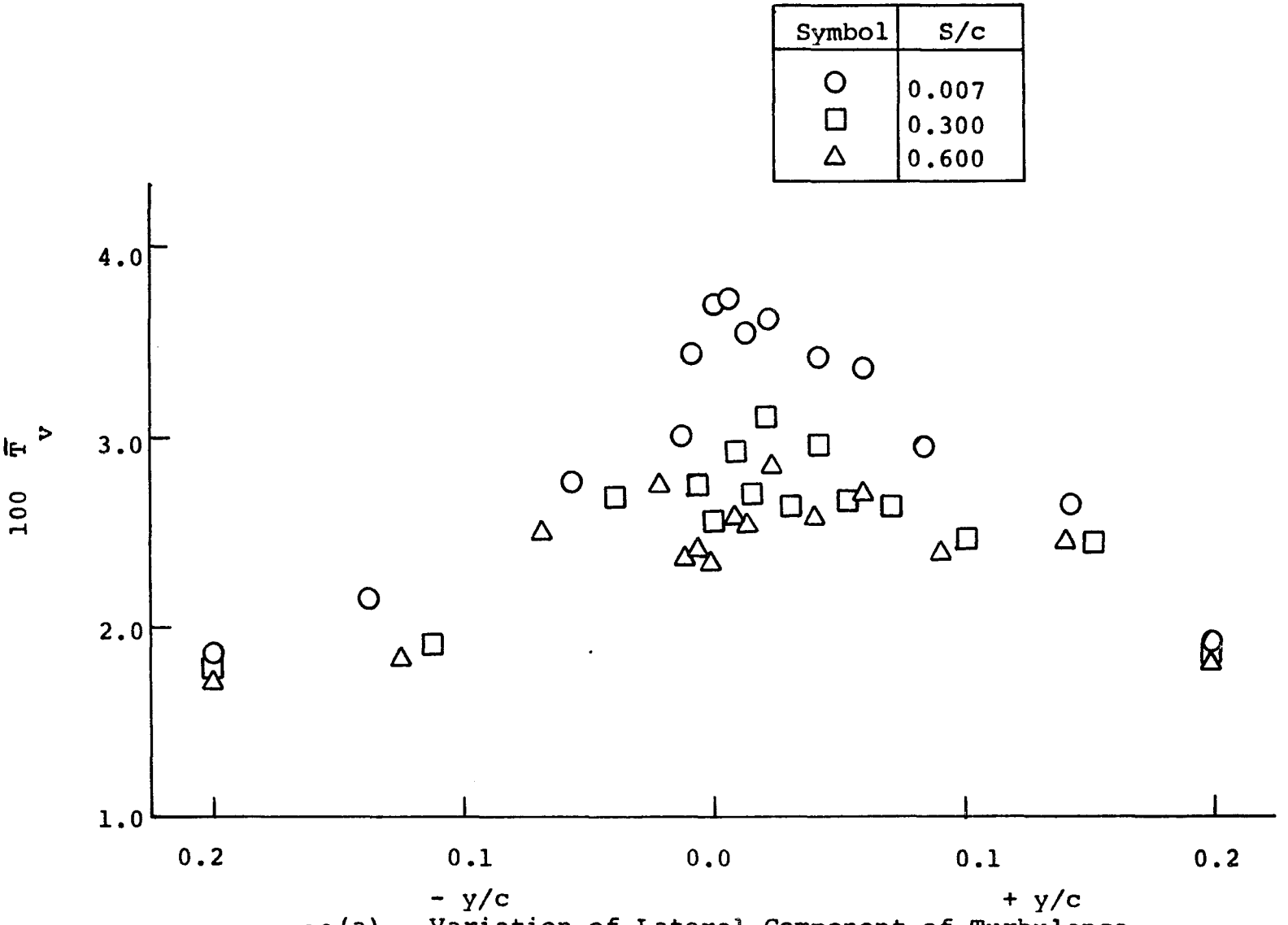

Figure 7.10(a) Variation of Lateral Component of Turbulence Intensity Across the Wake ($x_1/c = 0.68$, $z/c = 0.026$)

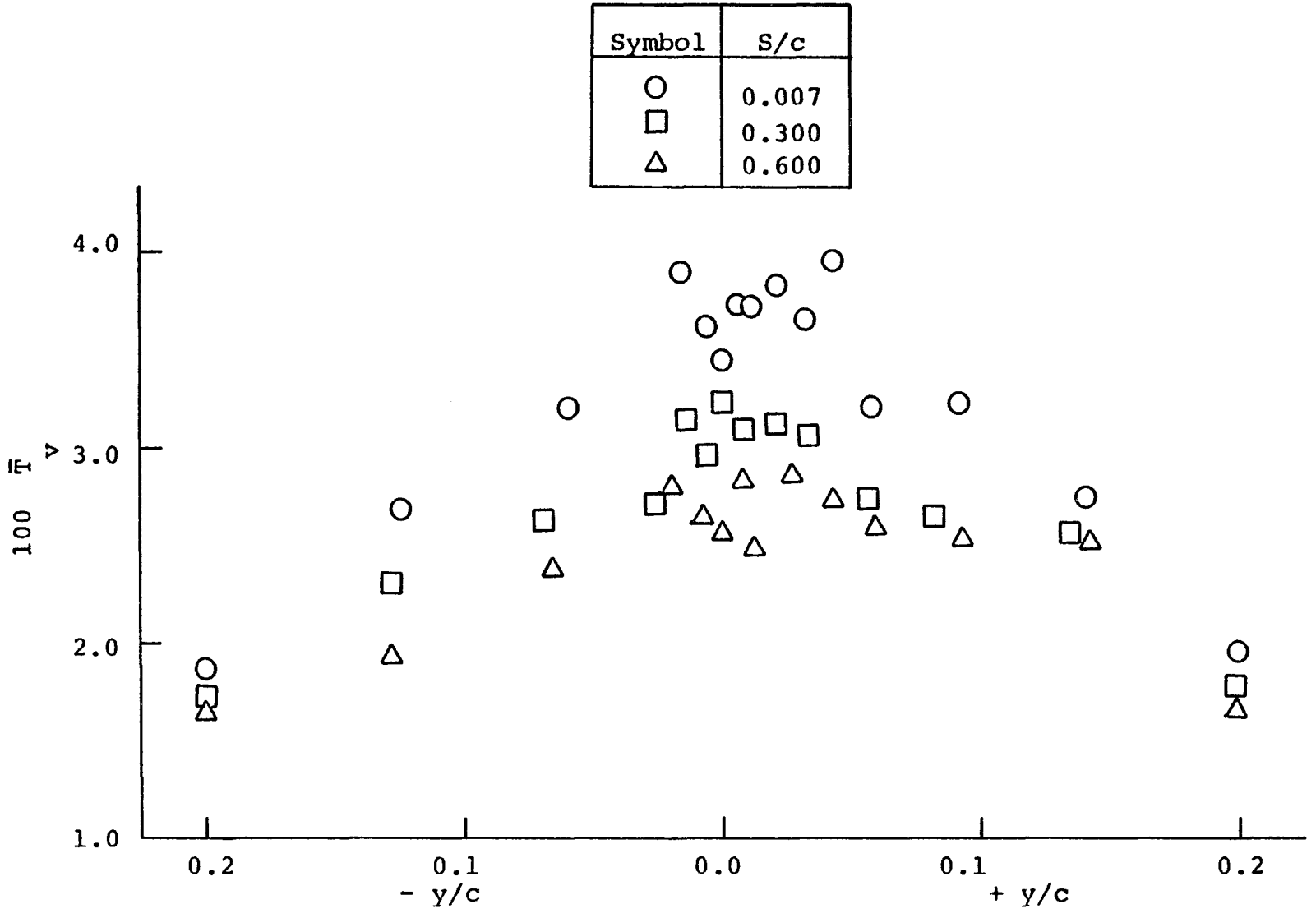

Figure 7.10(b) Variation of Lateral Component of Turbulence Intensity Across the Wake (x /c = 0.68, z/c = 0.01)

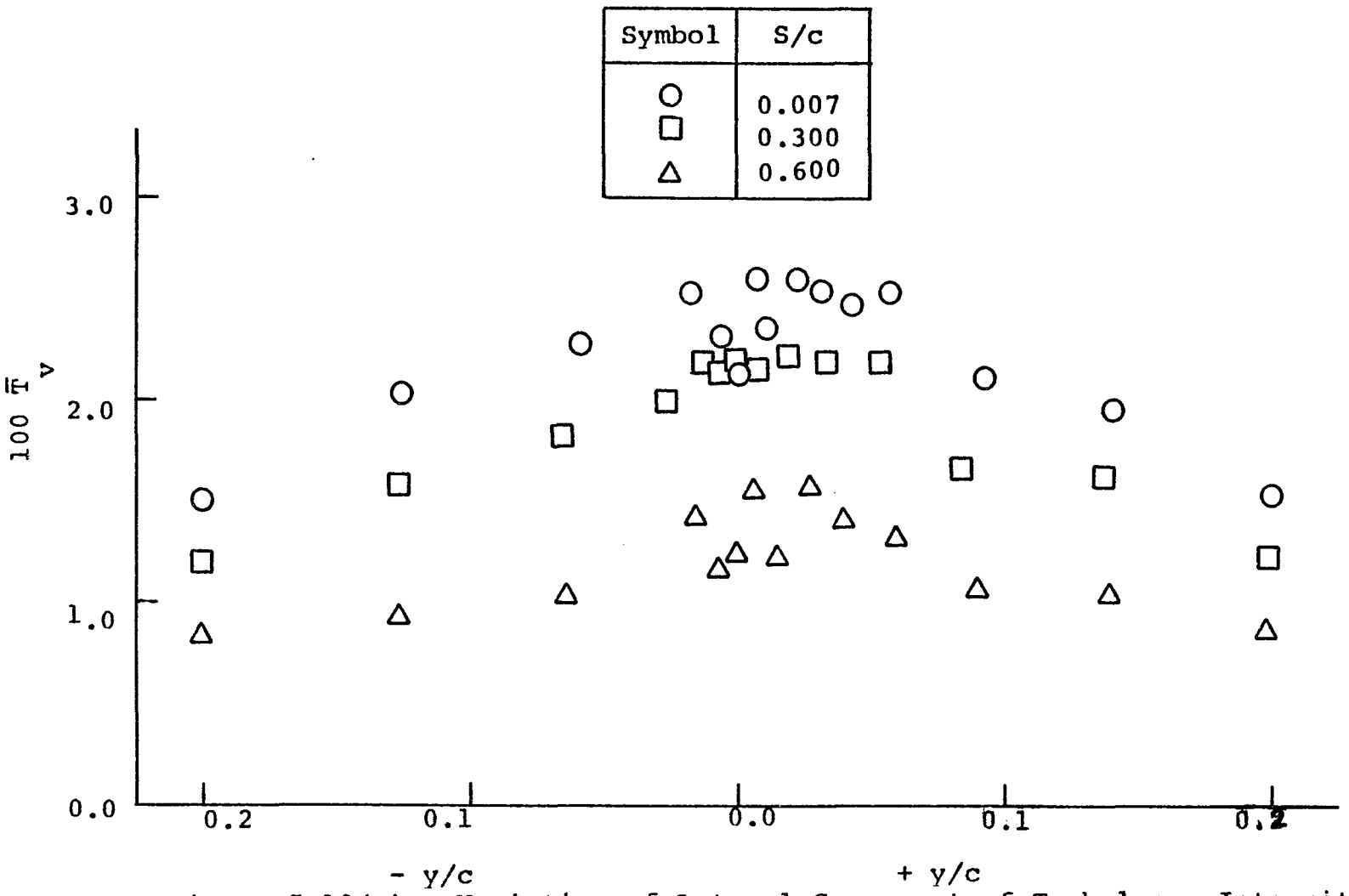

Figure 7.10(c) Variation of Lateral Component of Turbulence Intensity Across the Wake ($x_1/c = 0.88$, $z/c = 0.026$)

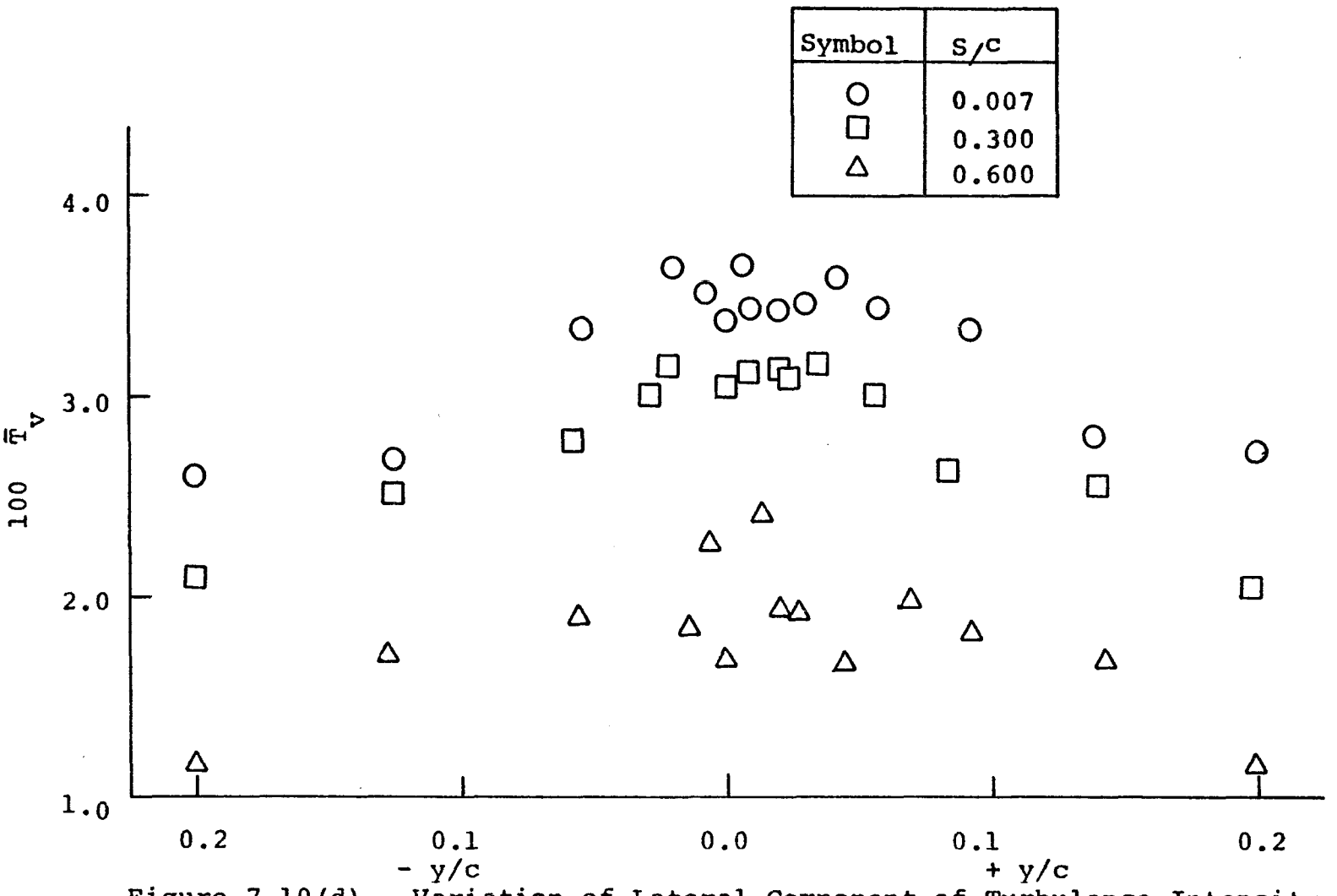

Figure 7.10(d) Variation of Lateral Component of Turbulence Intensity Across the Wake ($x_1/c = 0.88$, $z/c = 0.01$)

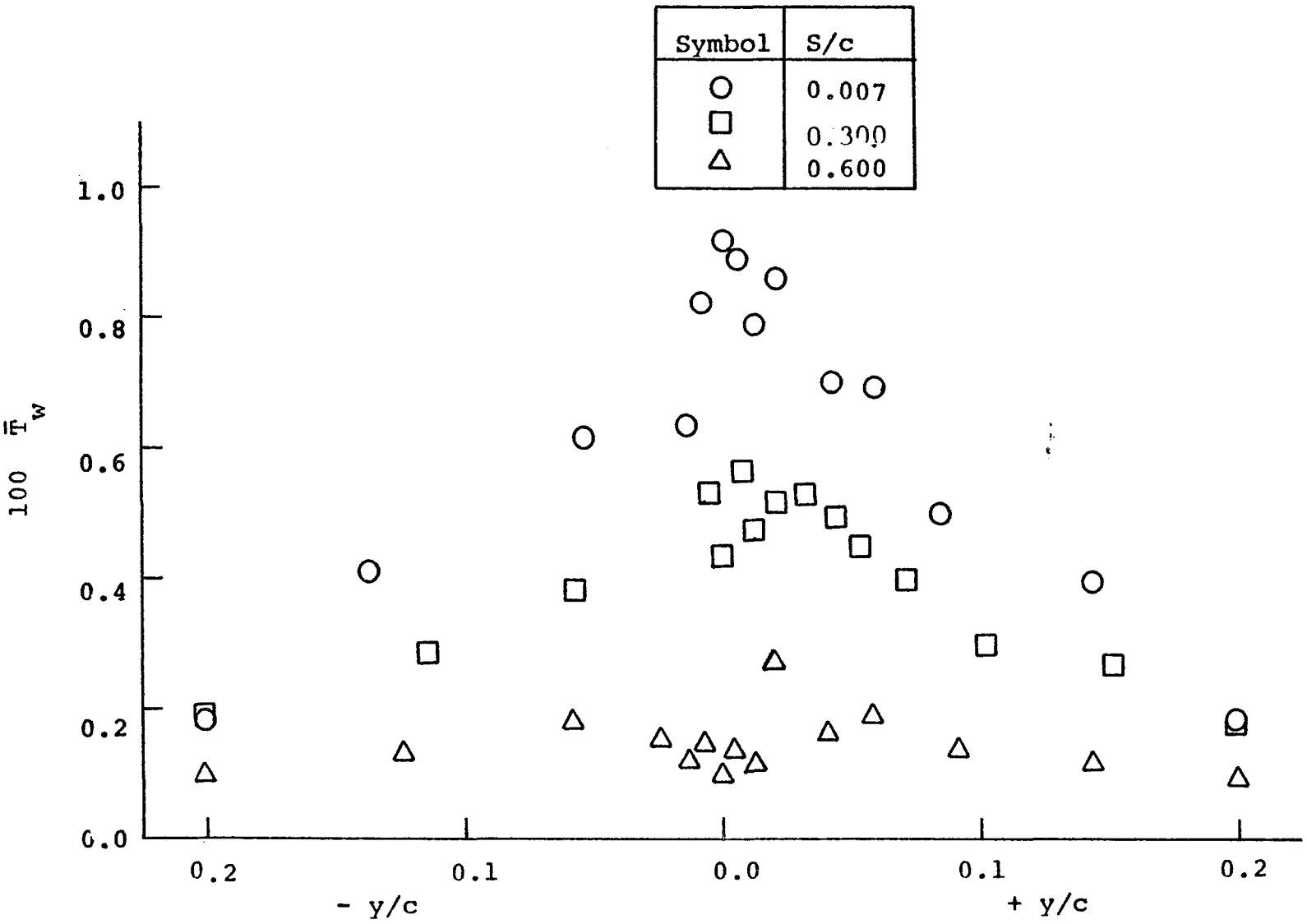

Figure 7.11(a) Variation of Normal Component of Turbulence Intensity Across the Wake ($x_1/c = 0.68$, $z/c = 0.026$)

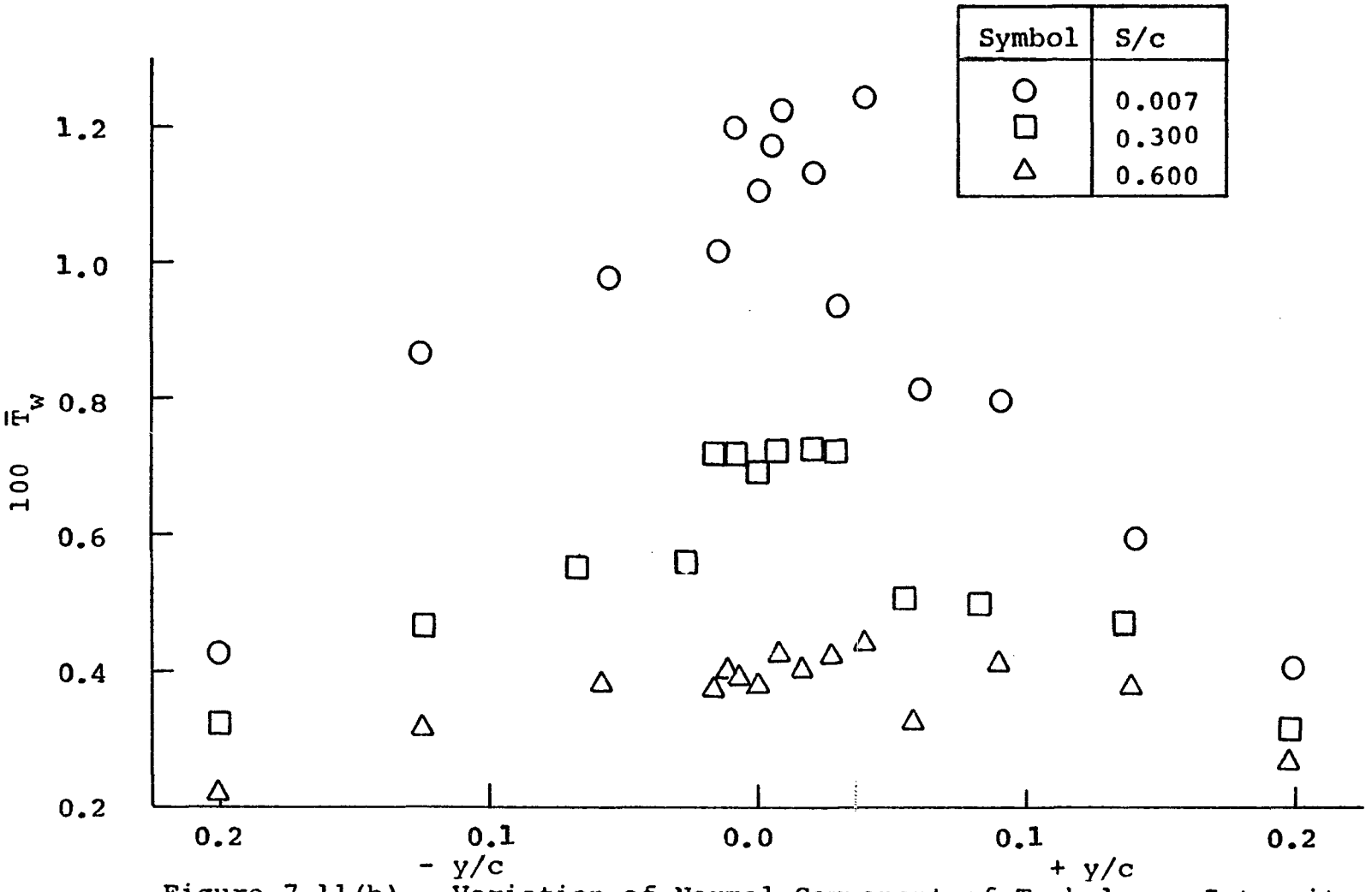

Figure 7.11(b) Variation of Normal Component of Turbulence Intensity Across the Wake ($x_1/c = 0.68$, $z/c = 0.01$)

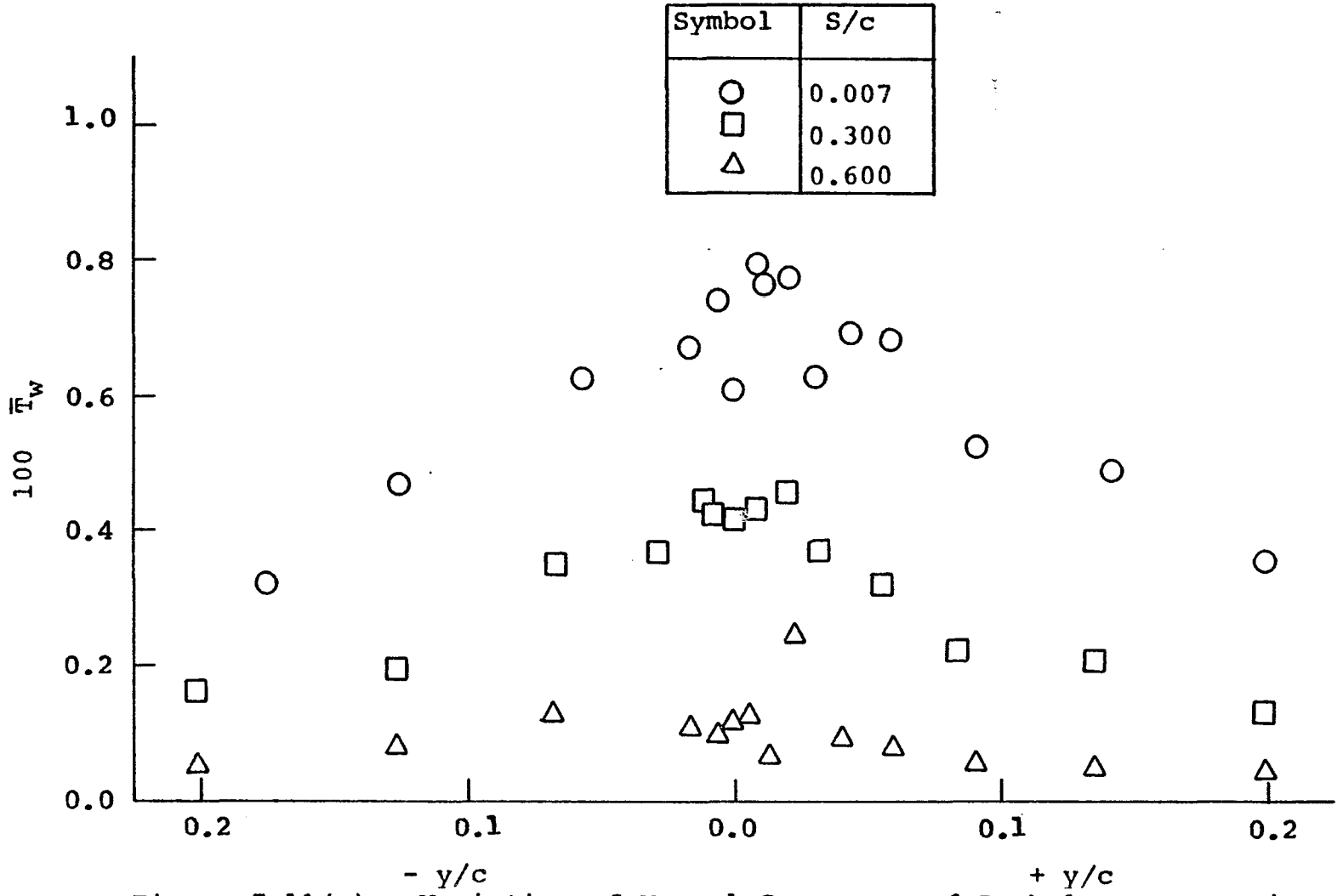

Figure 7.11(c) Variation of Normal Component of Turbulence Intensity Across the Wake ($x_1/c = 0.88$, $z/c = 0.026$)

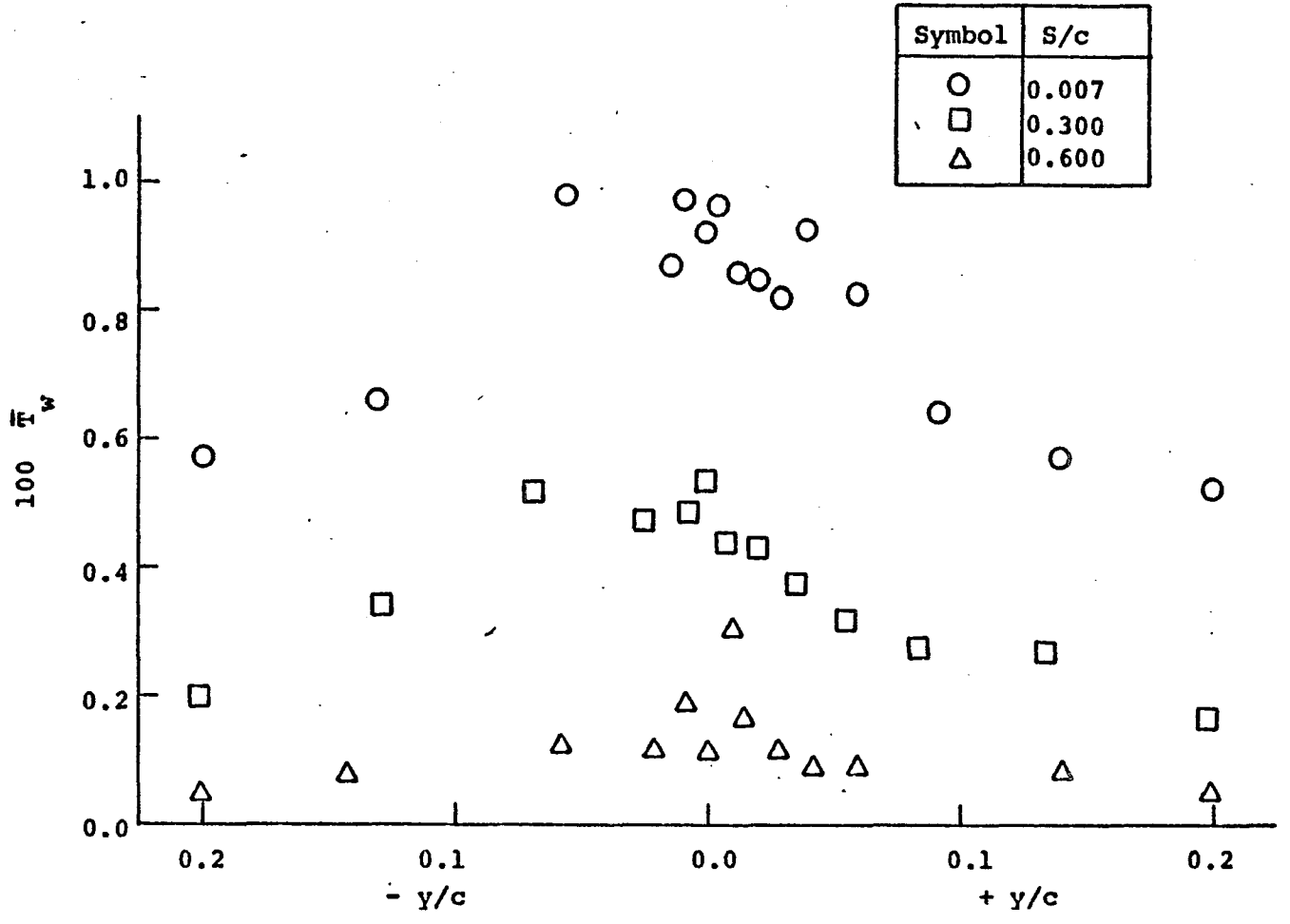

Figure 7.11(d) Variation of Normal Component of Turbulence Intensity Across the Wake ($x_1/c = 0.88$, $z/c = 0.01$)

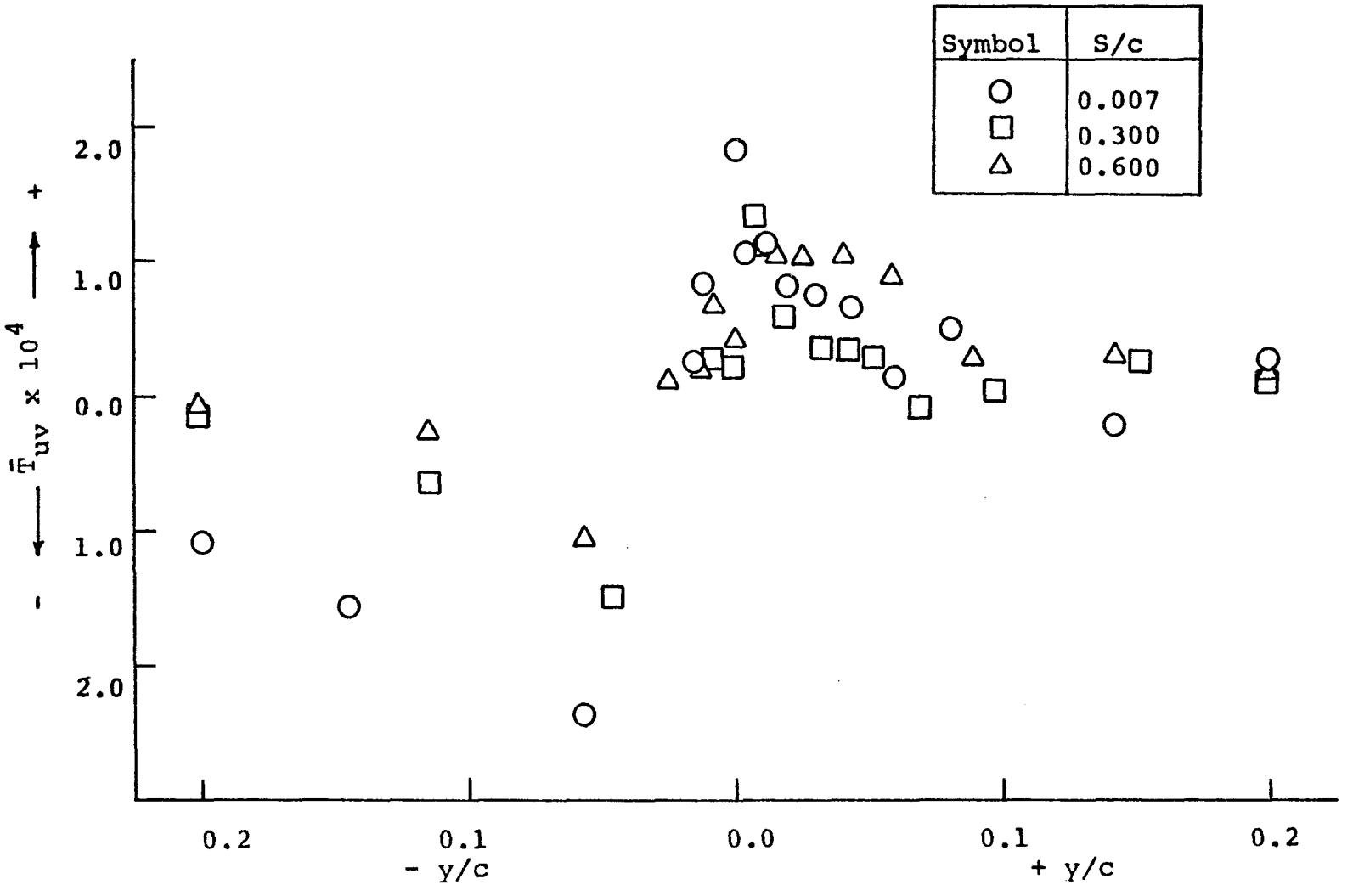

Figure 7.12(a) Variation of Reynolds Stress Component, $\bar{T}_{uv}$, Across the Wake ($x_{1/c} = 0.68$, $z/c = 0.026$)

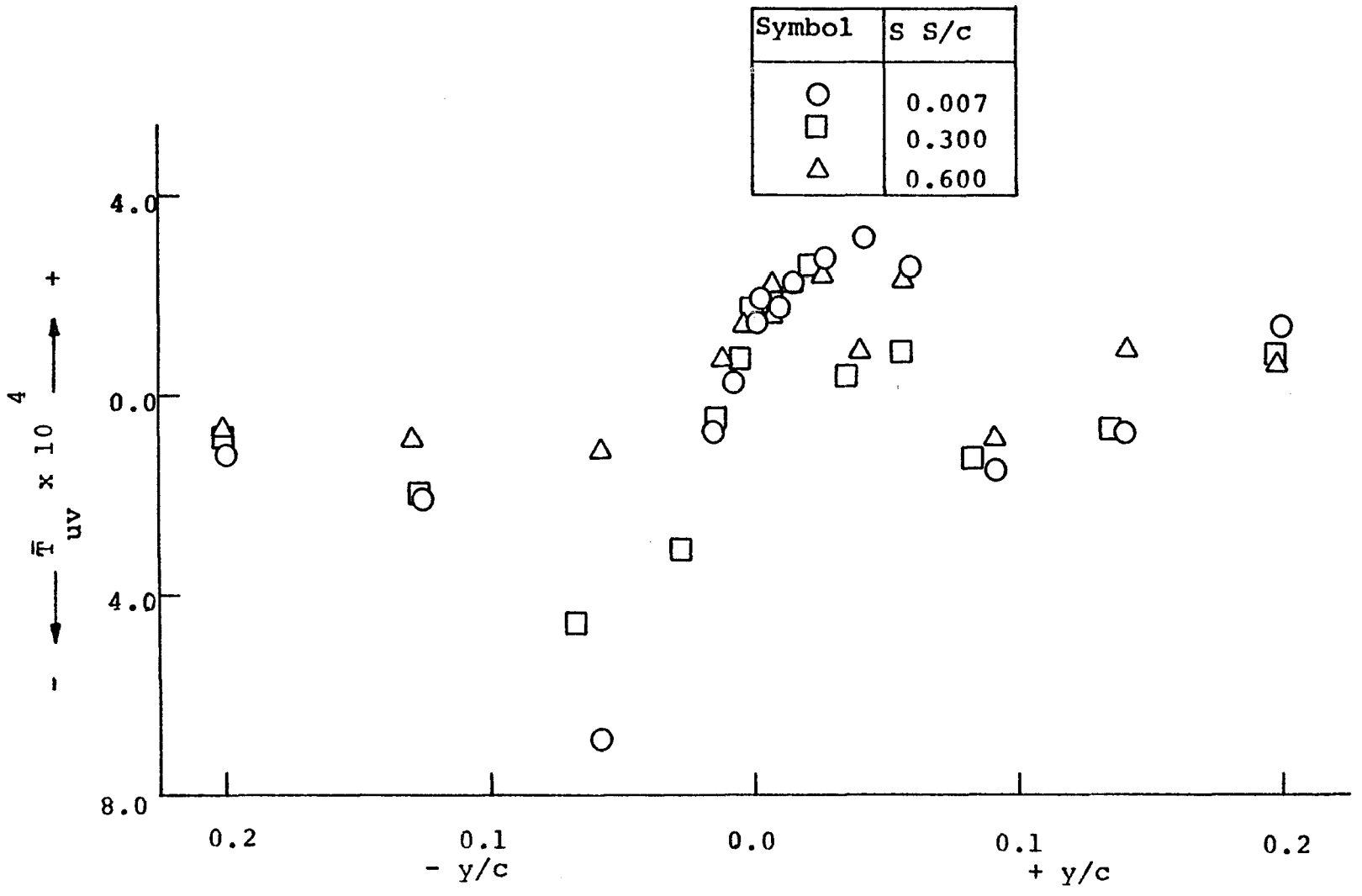

Figure 7.12(b) Variation of Reynolds Stress Component, $\bar{T}_{uv}$, Across the Wake ($x_1/c = 0.68$, $z/c = 0.01$)

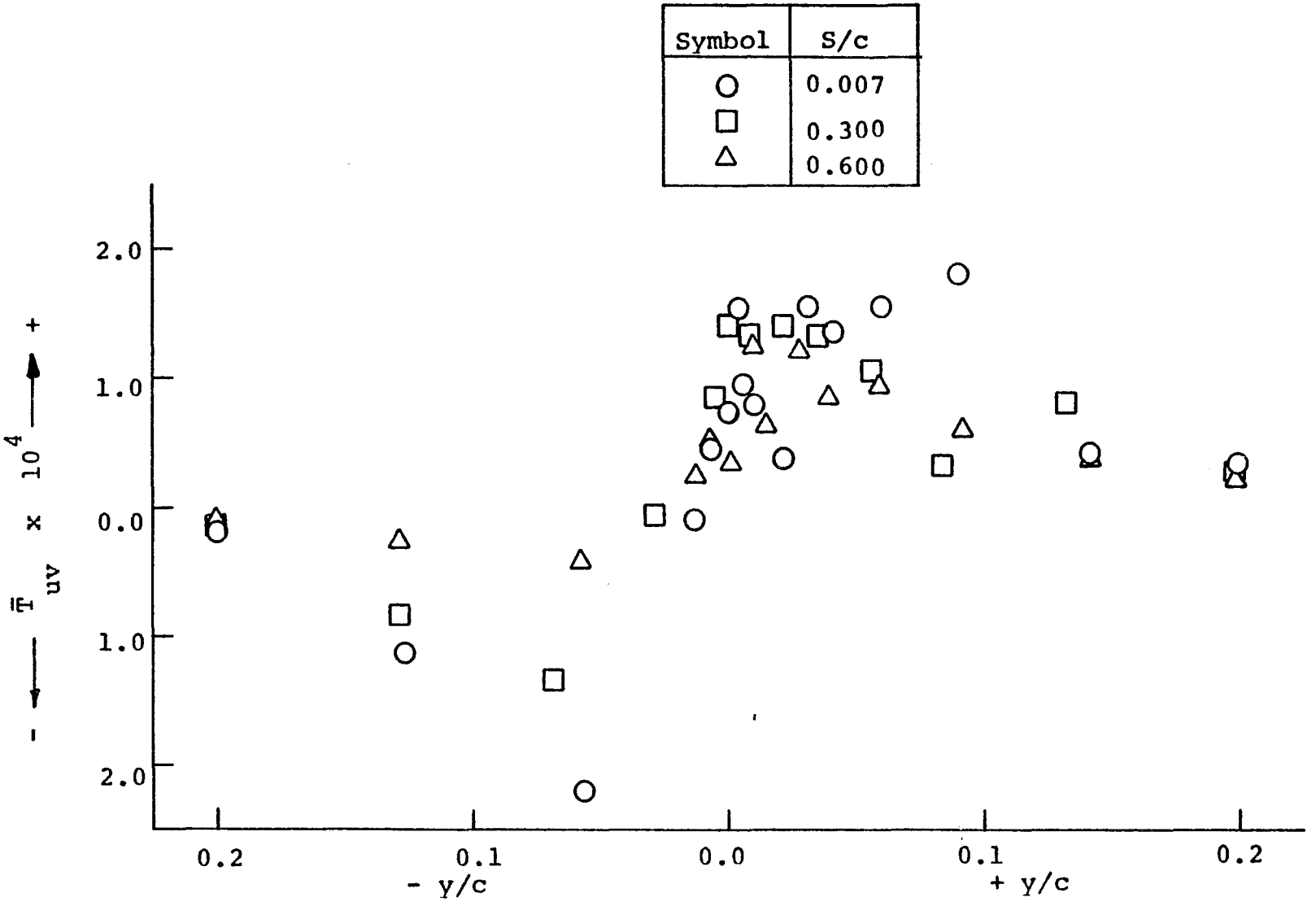

Figure 7.12(c) Variation of Reynolds Stress Component, $\bar{T}_{uv}$, Across the Wake ($x_1/c = 0.88$, $z/c = 0.026$)

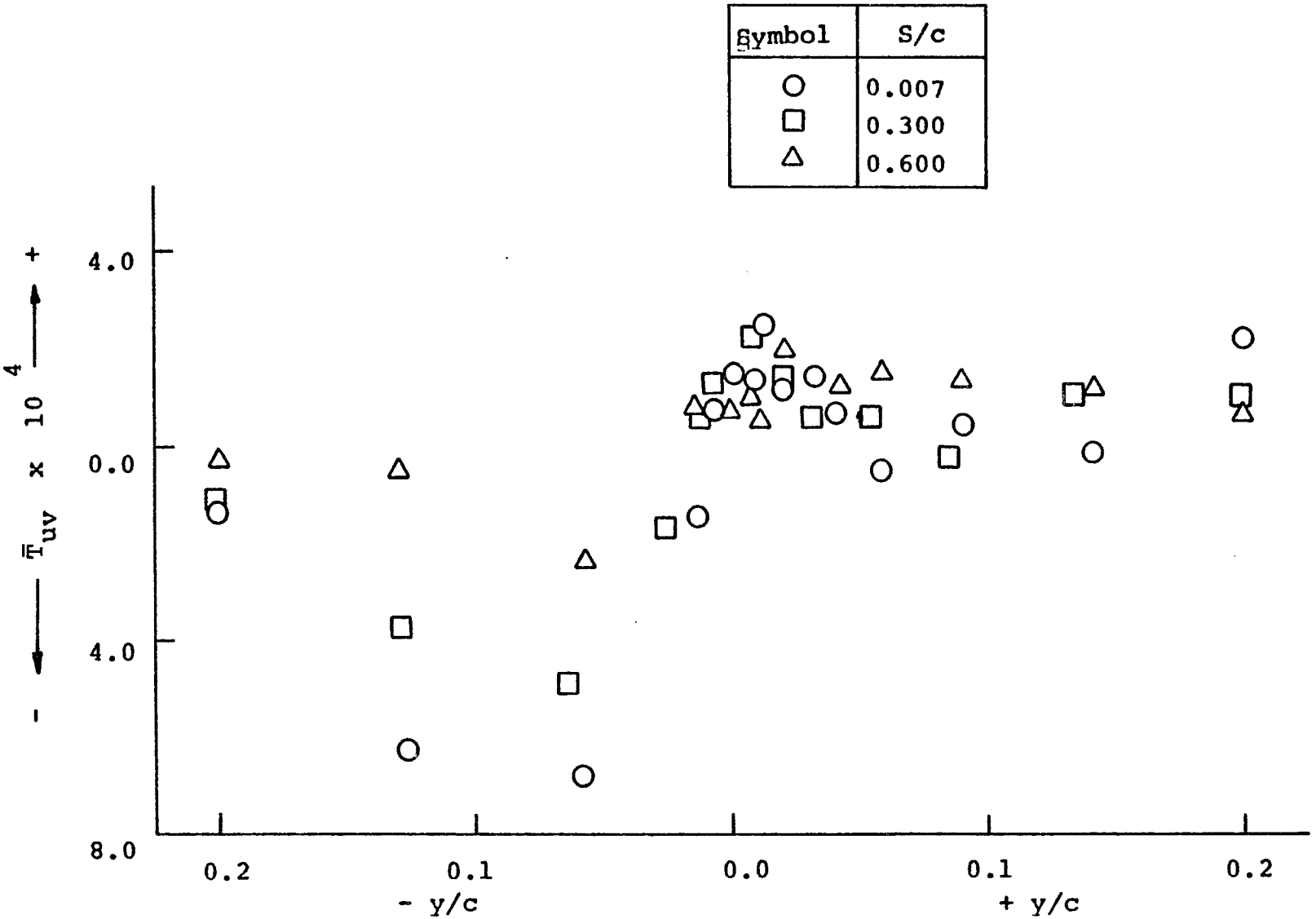

Figure 7.12(d) Variation of Reynolds Stress Component, $\bar{T}_{uv}$, Across the Wake ($x_1/c = 0.88$, $z/c = 0.01$)

increase in spacing.

The Reynolds stress distribution of $\overline{T}_{vw}$ component [Figures 7.13(a) to (d)] does not change sign about the wake center line but is slightly asymmetrical about the wake center line. Its value decreases with the increase in spacing and increases towards the inner region. Its value at the outer edge of the wake in any region is higher for $S/c \sim 0.007$ and lower for $S/c \sim 0.3$.

The Reynolds stress distribution of $\overline{T}_{wu}$ component [Figures 7.14(a) to (d)] changes sign about the wake center line. The trend is similar to the distribution of $\overline{T}_{uv}$ component.

The maximum value of the Reynolds stress components occurs at or in the vicinity of the occurrence of the maximum value of turbulence intensity components. The occurrence of these maximum values shifts away from the wake center line with the increase in downstream distance and with the increase in spacing, which is related to the wake spread.

In the outer region of the interacted boundary layer, $\overline{T}_{uv}$ and $\overline{T}_{vw}$ are of the same order of magnitude, while $\overline{T}_{wu}$ is about one third of $\overline{T}_{uv}$. In the inner region of the interacted boundary layer, $\overline{T}_{uv}$ is nearly 1.5 times $\overline{T}_{vw}$ and $\overline{T}_{wu}$ remains about one third of $\overline{T}_{uv}$.

The maximum value of the three components of

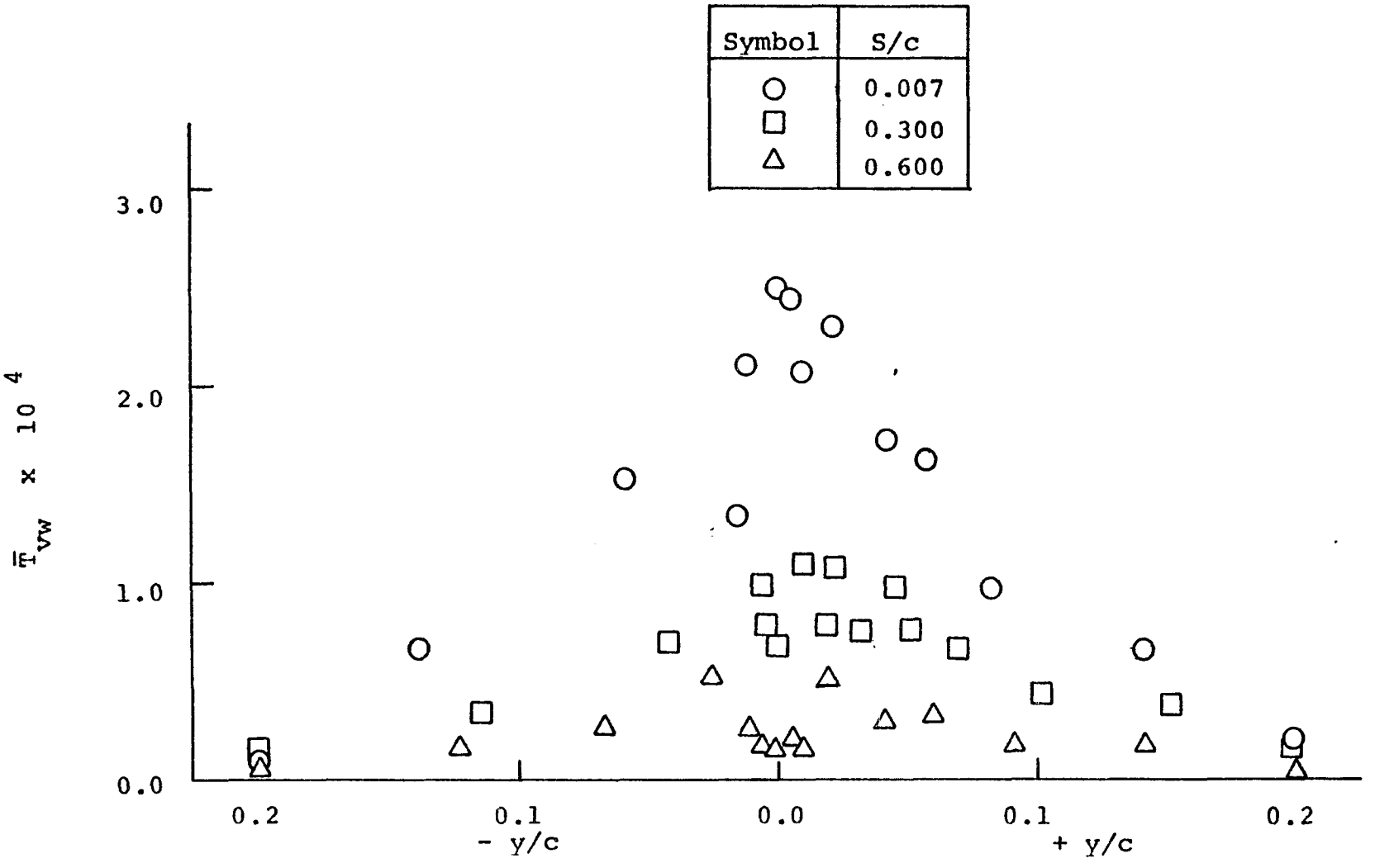

Figure 7.13(a) Variation of Reynolds Stress Component , $\bar{T}_{vw}$, Across the Wake ($x_1/c = 0.68$, $z/c = 0.026$)

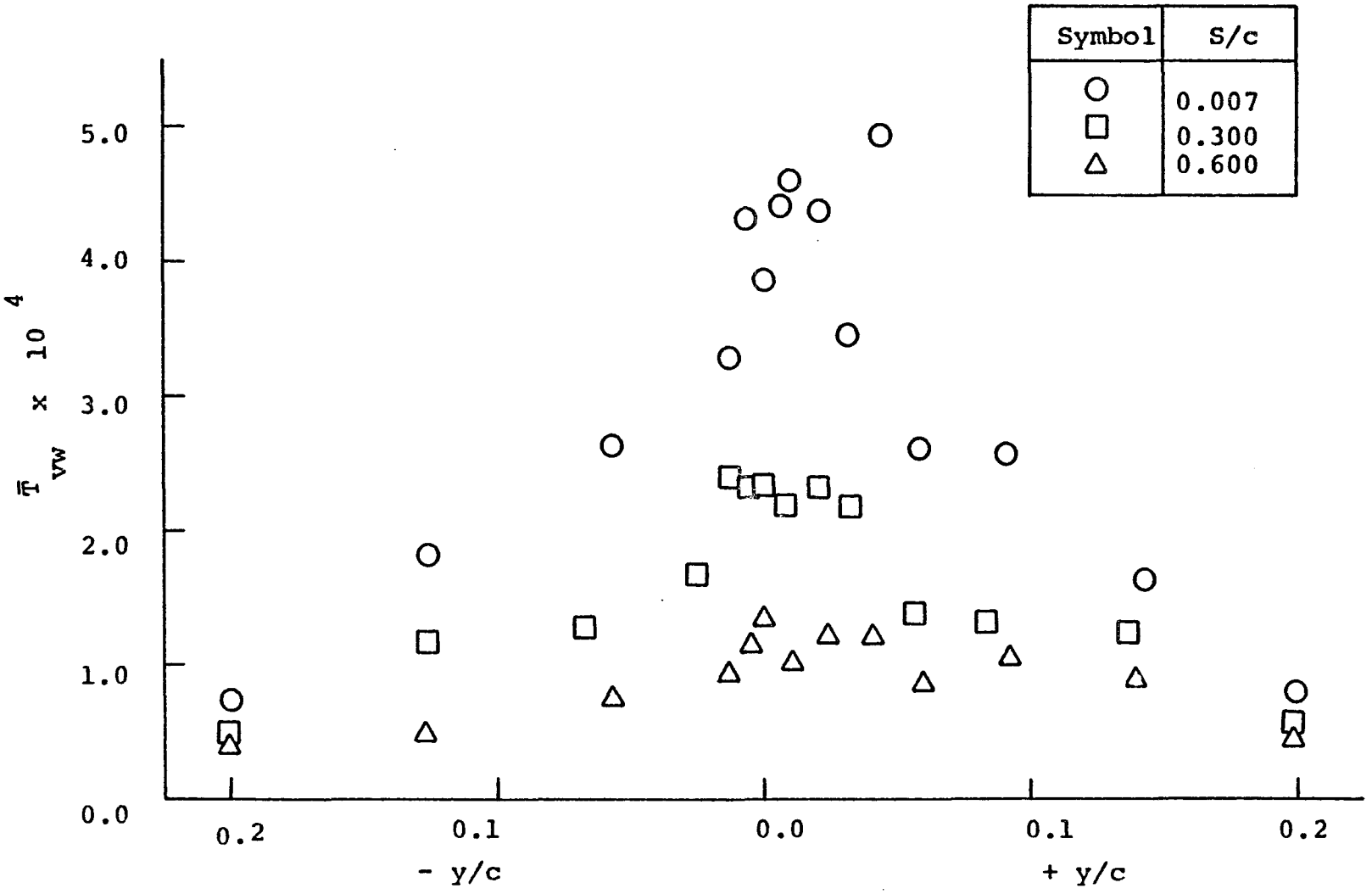

Figure 7.13(b) Variation of Reynolds Stress Component, $\bar{T}_{vw}$, Across the Wake ($x_1/c = 0.68$, $z/c = 0.01$)

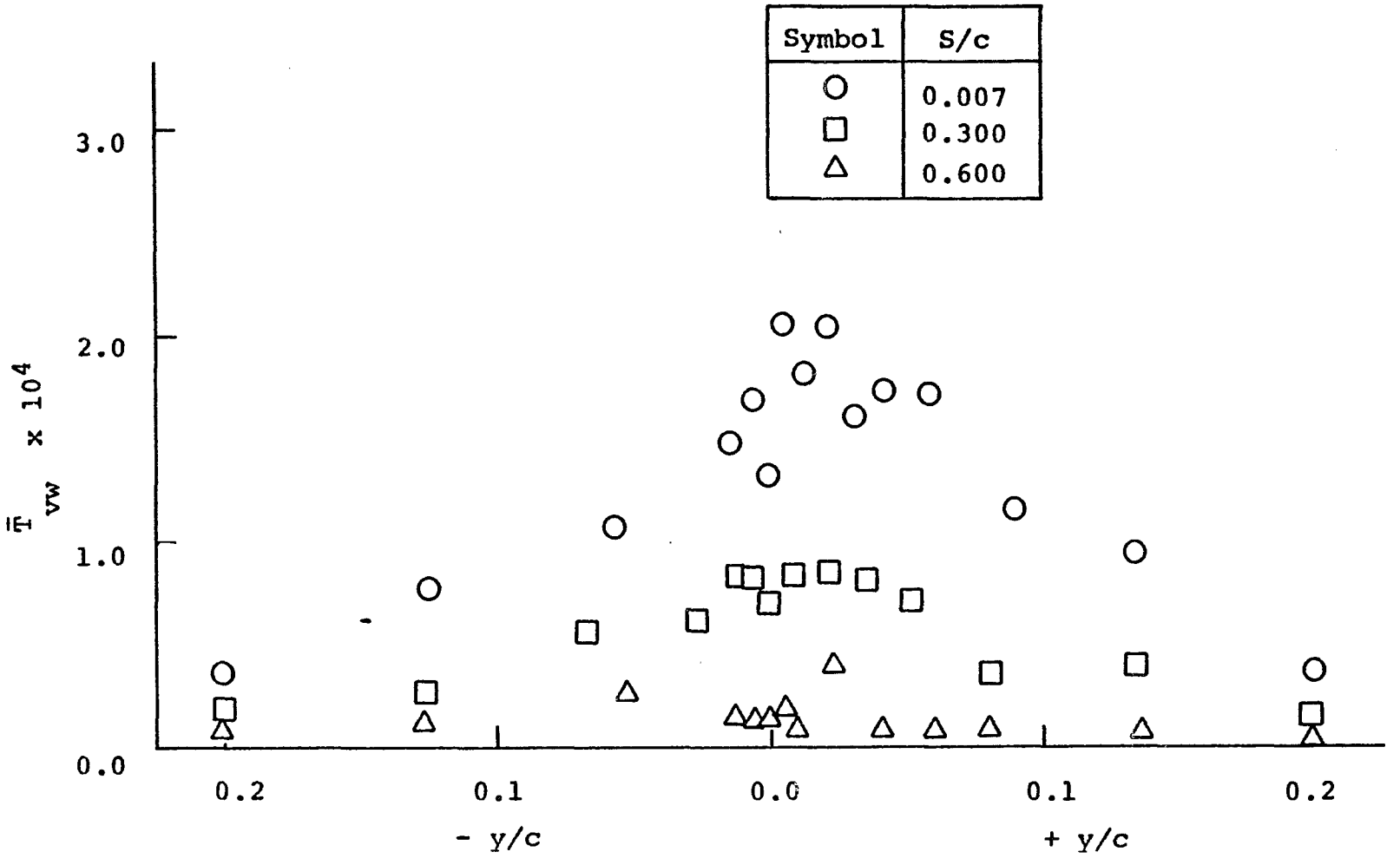

Figure 7.13(c) Variation of Reynolds Stress Component, $\bar{T}_{vw}$, Across the Wake ($x_1/c = 0.88$, $z/c = 0.026$)

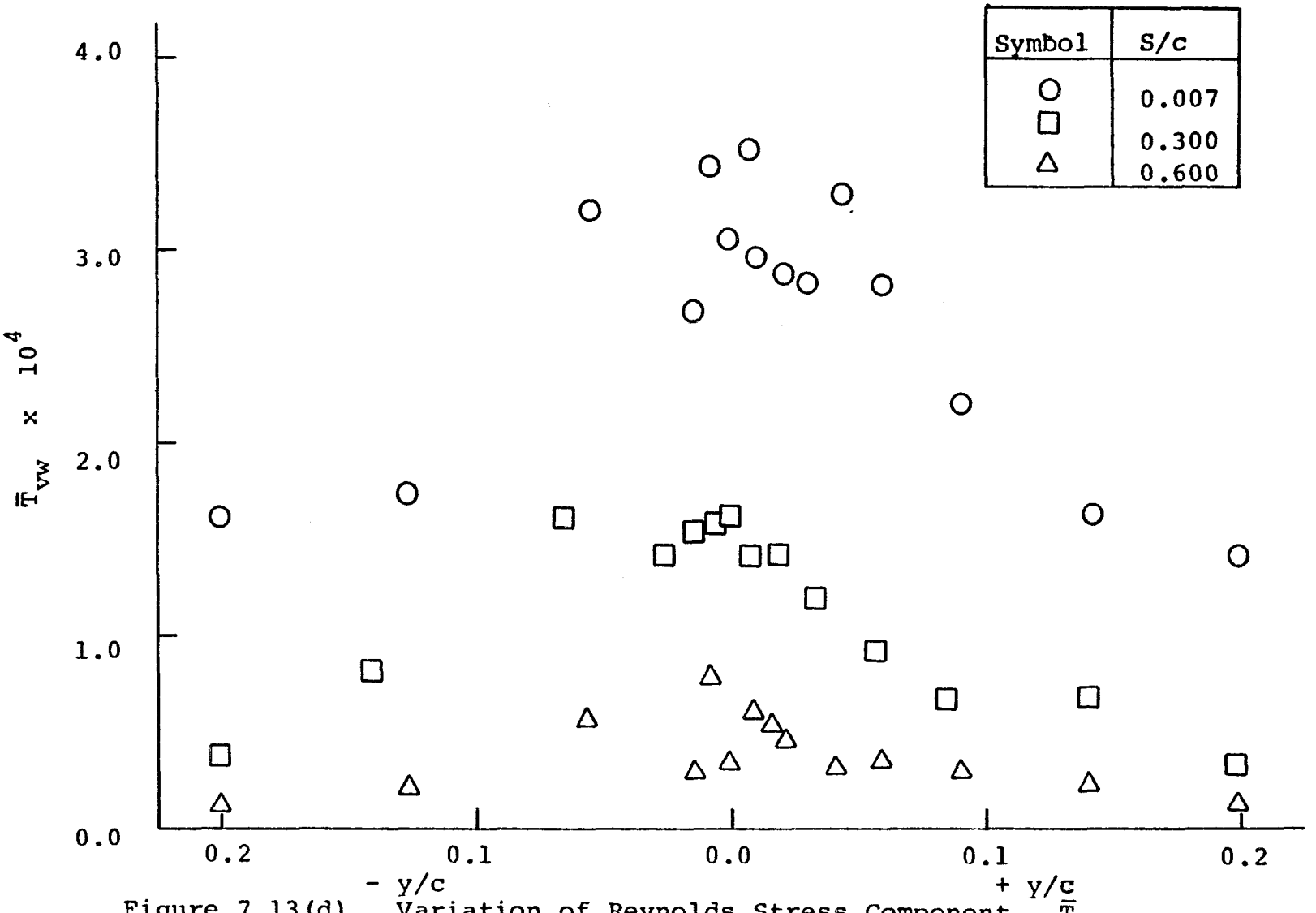

Figure 7.13(d) Variation of Reynolds Stress Component, $\bar{T}_{vw}$, Across the Wake ($x_1/c = 0.88$, $z/c = 0.01$)

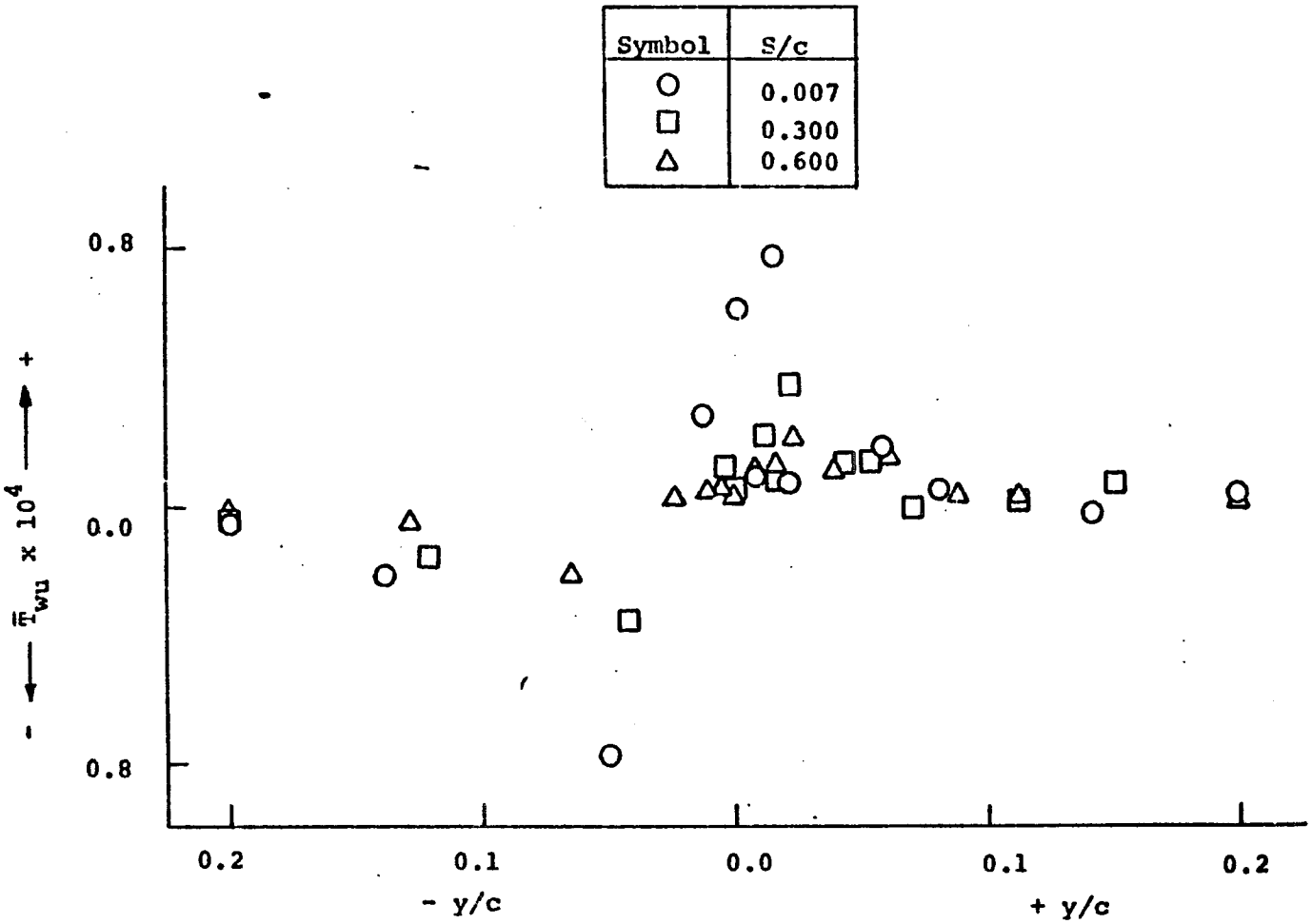

Figure 7.14(a) Variation of Reynolds Stress Component, $\bar{T}_{wu}$, Across the Wake ($x_1/c = 0.68$, $z/c = 0.026$)

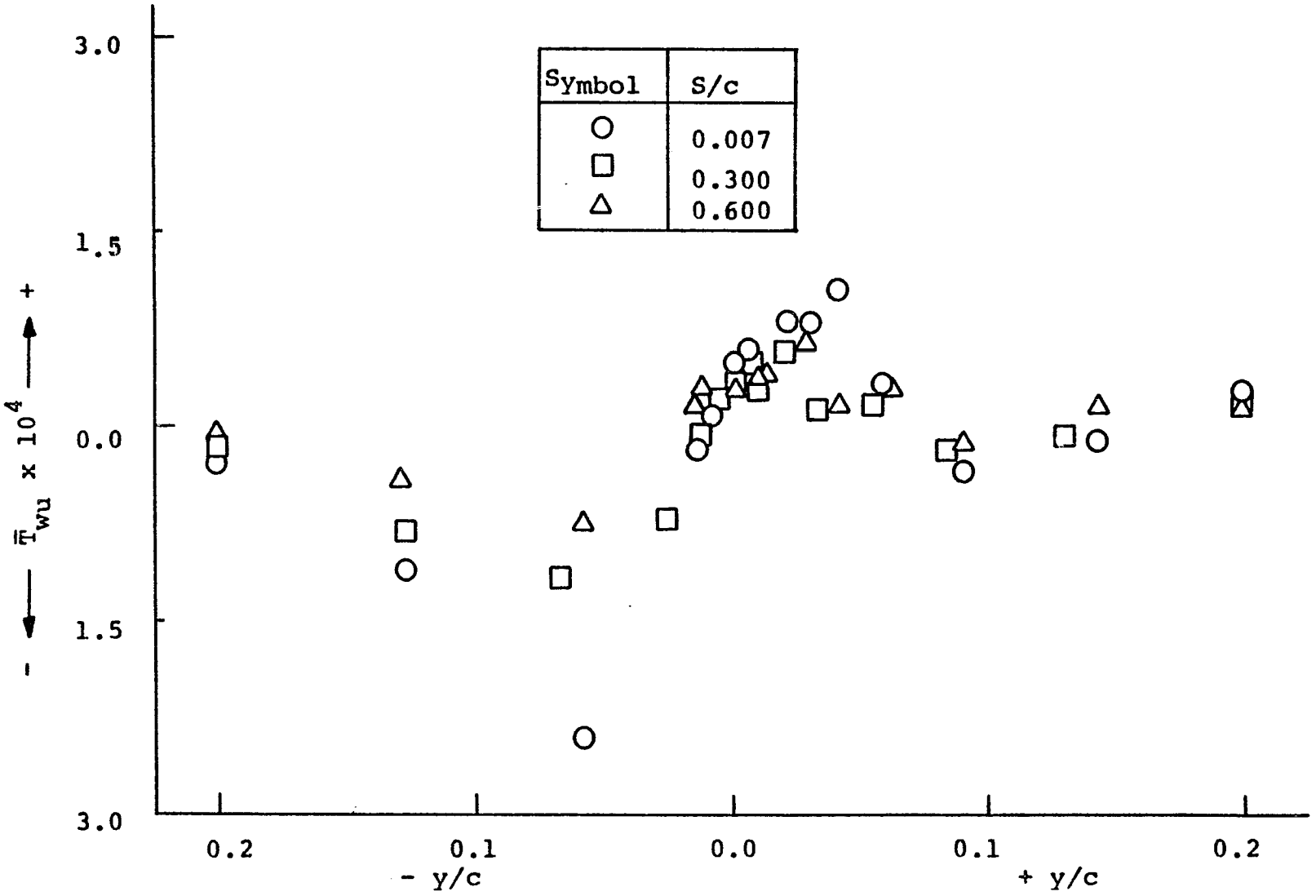

Figure 7.14(b) Variation of Reynolds Stress Component, $\bar{T}_{wu}$, Across the Wake ($x_1/c = 0.68$, $z/c = 0.01$)

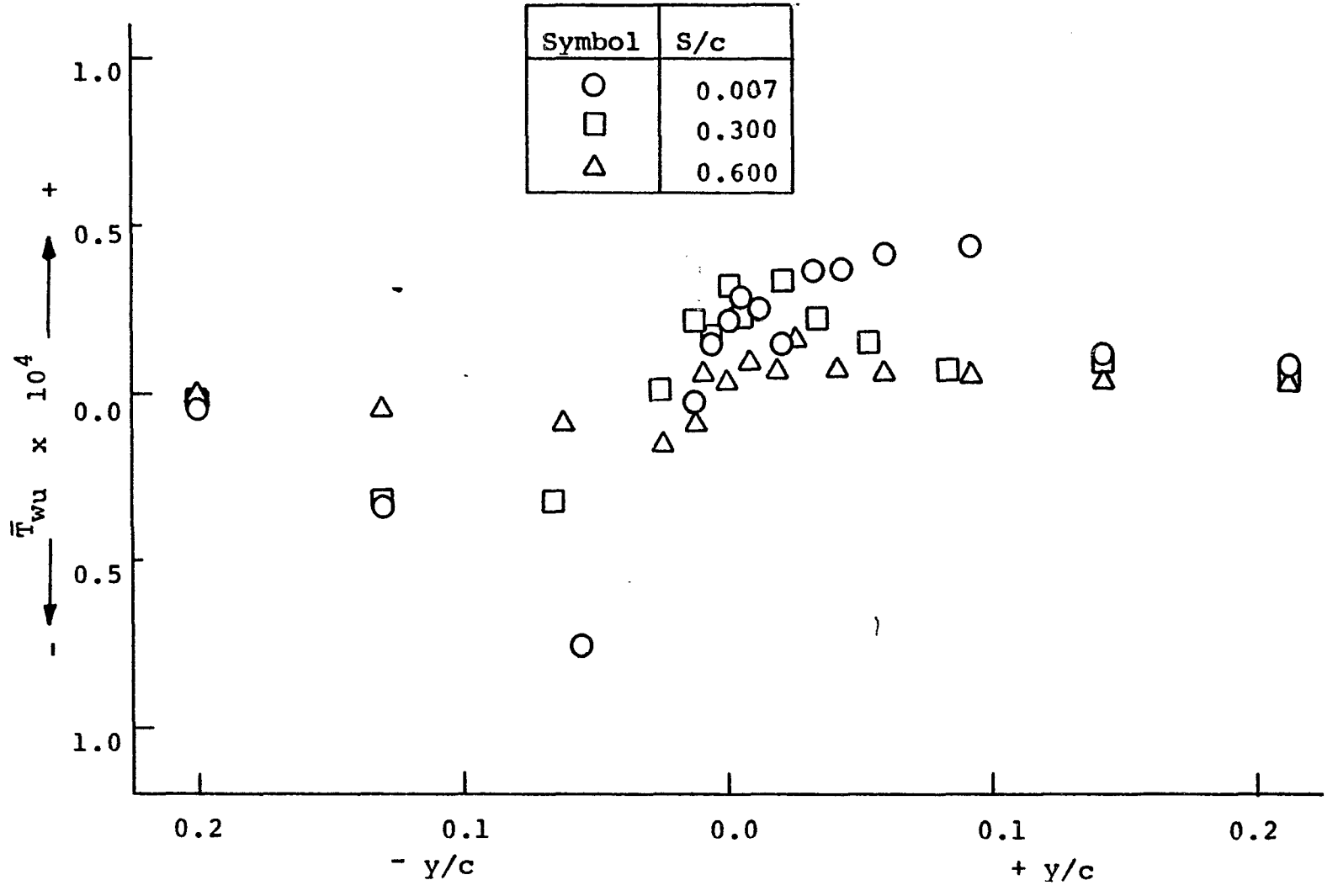

Figure 7.14(c) Variation of Reynolds Stress Component, $\bar{T}_{wu}$, Across the Wake ($x_1/c = 0.88$, $z/c = 0.026$)

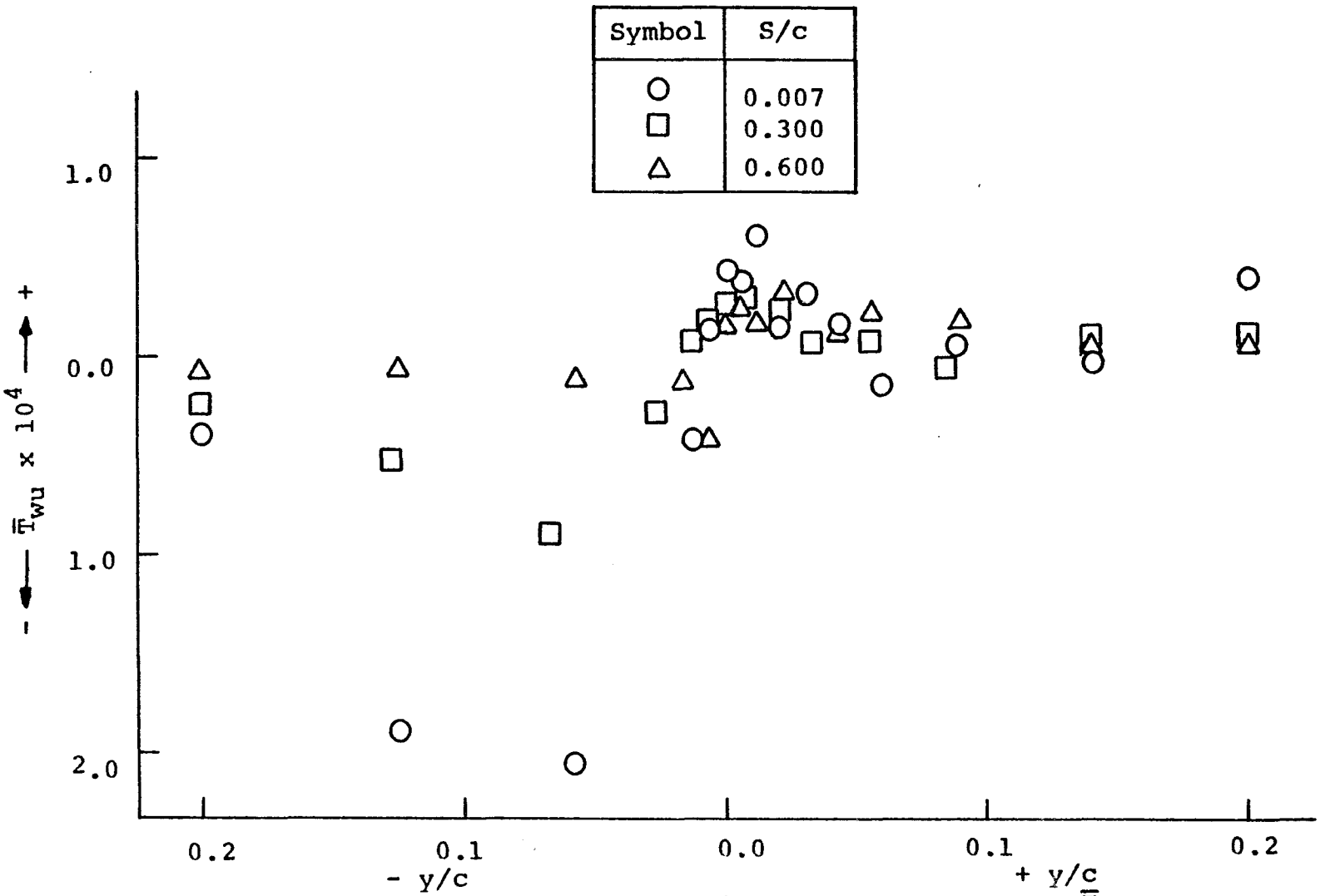

Figure 7.14(d) Variation of Reynolds Stress Component, $\overline{T}_{wu}$, Across the Wake (x_1/c = 0.88, z/c = 0.01)

turbulence intensity at stations I and II with the increase in spacing is shown in Figures 7.15(a) and (b), respectively. The maximum values of the components of turbulence intensity decrease with the increase in spacing because of the weaker interaction of the wake and the boundary layer, with the increase in spacing. The value of the components of turbulence intensity at any spacing increase towards the wall because of the stronger influence of the boundary layer over the constant influence of the wake. $(\overline{T}_u/\overline{T}_v)_{max}$ decreases from 1.28 to 1.01 with the variation of S/c from 0.007 to 0.6. $(\overline{T}_u/\overline{T}_w)_{max}$ varies from 3.8 to 7.0 with the variation of S/c from 0.007 to 0.6. The unequality in the maximum value of the components of turbulence intensity is due to anisotropy of the flow.

Figures 7.15(c) and (d) show the variation of the maximum values of the three components of Reynolds stress at stations I and II, respectively. The value of the components of Reynolds stress decreases with the increase in spacing because of the far wake interaction. The values increase towards the wall because of the stronger velocity gradients. In the outer region of the interacted boundary layer, $(\overline{T}_{uv}/\overline{T}_{vw})_{max}$ is of the order of 1.5 while in the inner region, it varies from 1.4 to 2.1. In the outer region of the interacted boundary layer, $(\overline{T}_{uv}/\overline{T}_{wu})_{max}$ varies from 3.0 to 6.0, while in the inner region, it varies from 2.7 to 4.0 with the variation of S/c from 0.007 to 0.6.

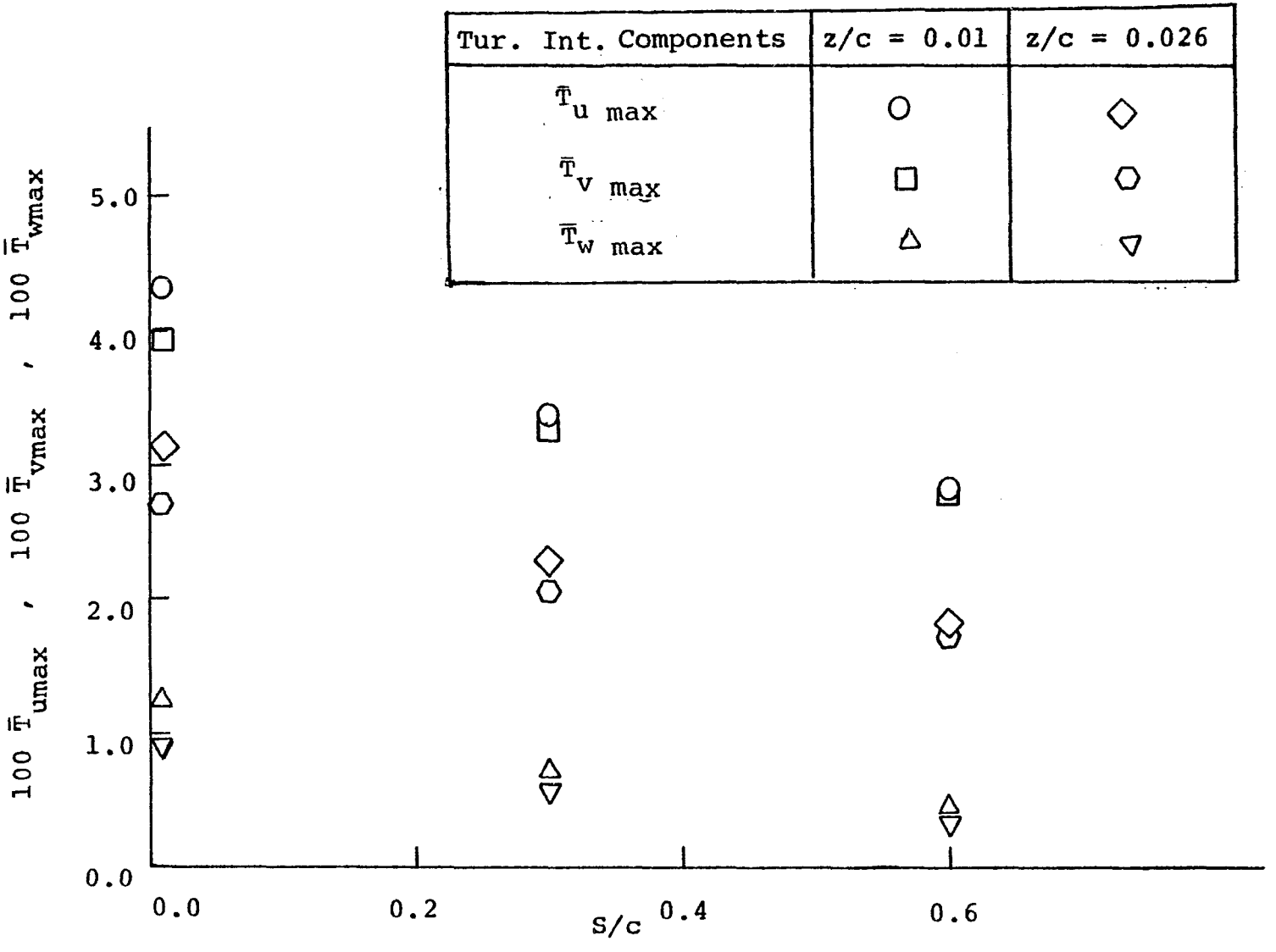

Figure 7.15(a) Variation of Maximum of Axial, Lateral and Normal Components of Turbulence Intensity With S/c Ratio ($x_1/c = 0.68$)

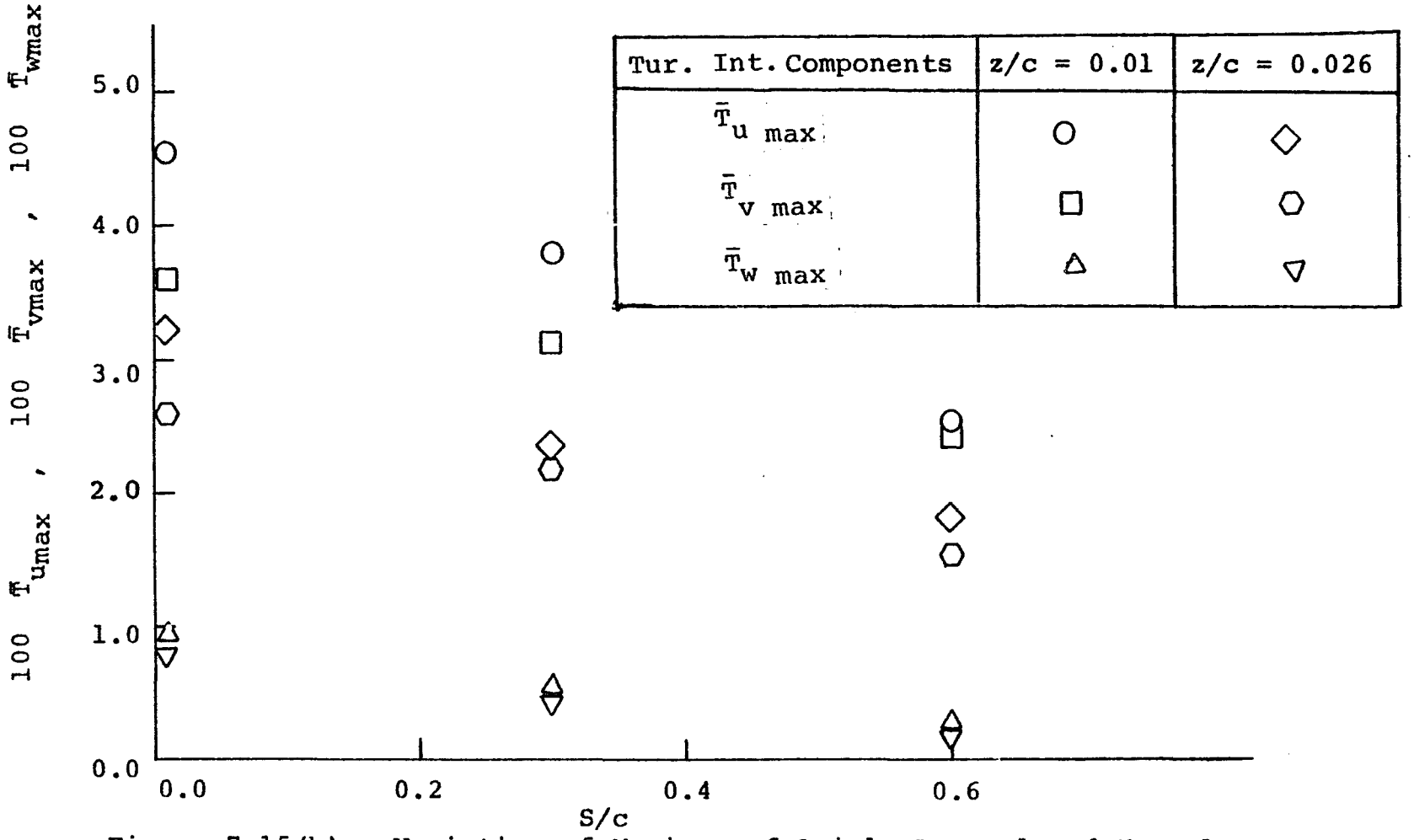

Figure 7.15(b) Variation of Maximum of Axial, Lateral and Normal Components of Turbulence Intensity With S/c Ratio ($x_1/c = 0.88$)

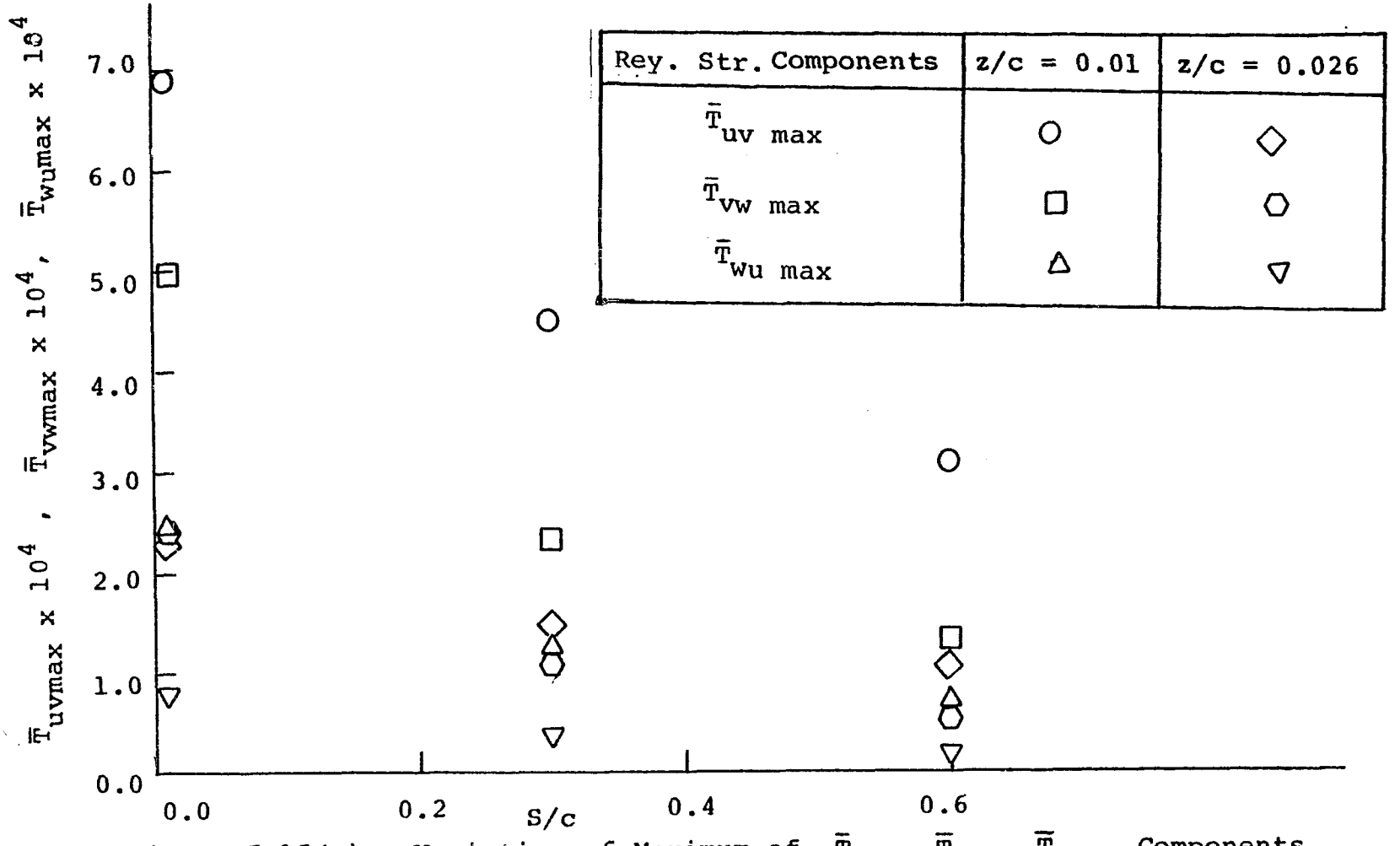

Figure 7.15(c) Variation of Maximum of $\bar{T}_{uv}$, $\bar{T}_{vw}$, $\bar{T}_{wu}$ Components of Reynolds Stress With S/c Ratio ($x_1/c = 0.68$)

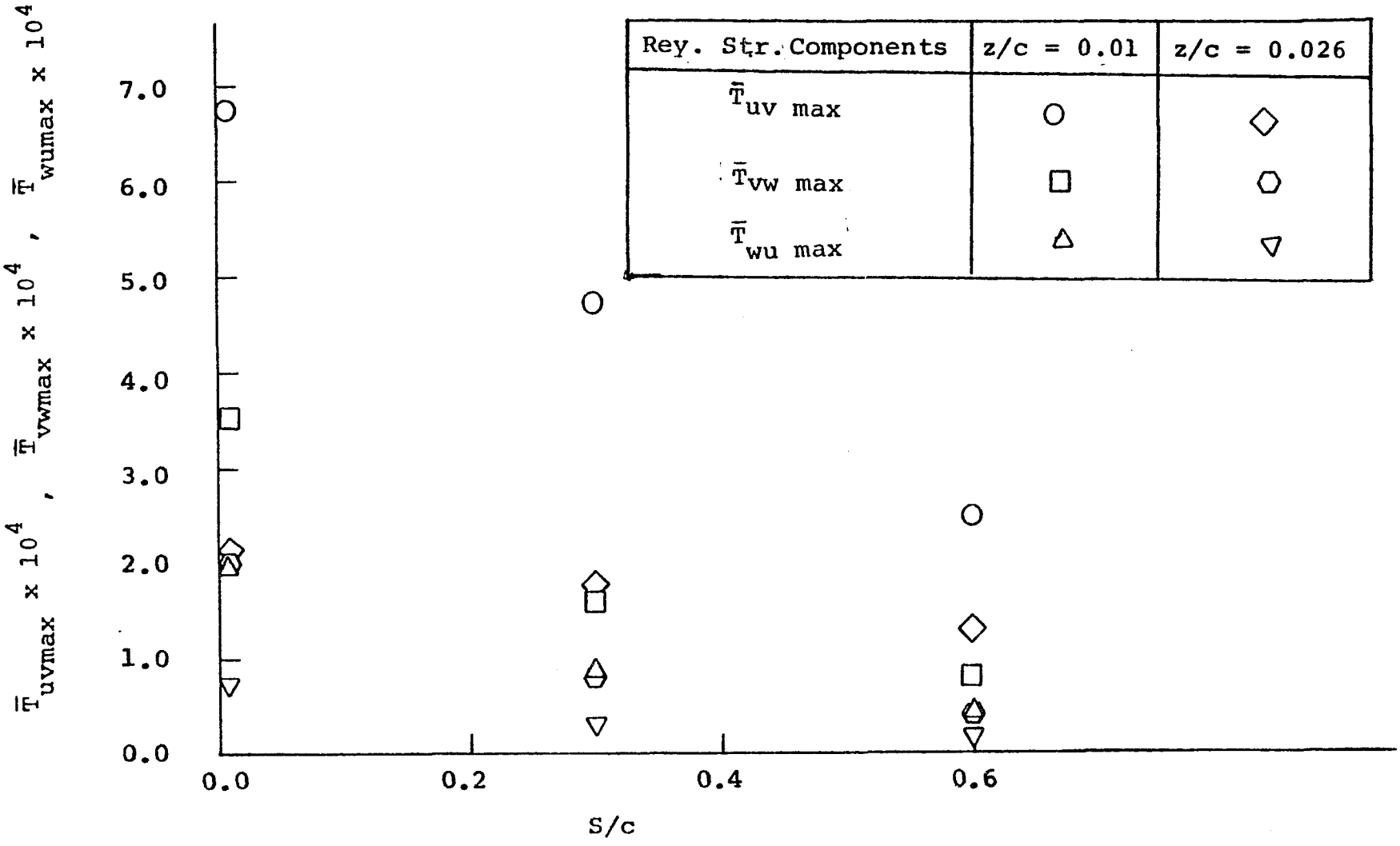

Figure 7.15(d) Variation of Maximum of $\bar{T}_{uv}$, $\bar{T}_{vw}$, $\bar{T}_{wu}$ Components of Reynolds Stress With S/c Ratio ($x_1/c = 0.88$)

7.2.3 Decay or Growth of Turbulence Quantities:

Based on the correlations developed for the mean velocity defect, an effort is made to combine the data for the maximum values of the components of turbulence intensities and Reynolds stress into a single curve.

The logarithmic variation in the peak values of the axial, lateral and normal components of turbulence intensity for two stations, at the inner and outer regions, is shown in Figures 7.16(a), (b) and (c), respectively. The semi-empirical correlations representing the logarithmic variation in turbulence intensity components are written as follows:

$$T_{u\ max} = \overline{K}_5 \left[\left(\frac{x - S}{c} \right)^{-\frac{1}{2}} e^{-\eta^2} \right]^{0.772} \quad \ldots(7.10)$$

$$T_{v\ max} = \overline{K}_6 \left[\left(\frac{x - S}{c} \right)^{-\frac{1}{2}} e^{-\eta^2} \right]^{0.986} \quad \ldots(7.11)$$

$$T_{w\ max} = \overline{K}_7 \left[\left(\frac{x - S}{c} \right)^{-\frac{1}{2}} e^{-\eta^2} \right]^{0.97} \quad \ldots(7.12)$$

The value of η is obtained in the same manner as discussed in Section 7.1.2. $\overline{K}_5$, $\overline{K}_6$, and $\overline{K}_7$ are the constants depending upon the spacing and are given in Table VI, page 241. These constants can also be expressed as:

$$\overline{K}_i = a \left(K_i' \right)^b \quad , \quad i = 5 \text{ to } 7 \quad \ldots(7.13)$$

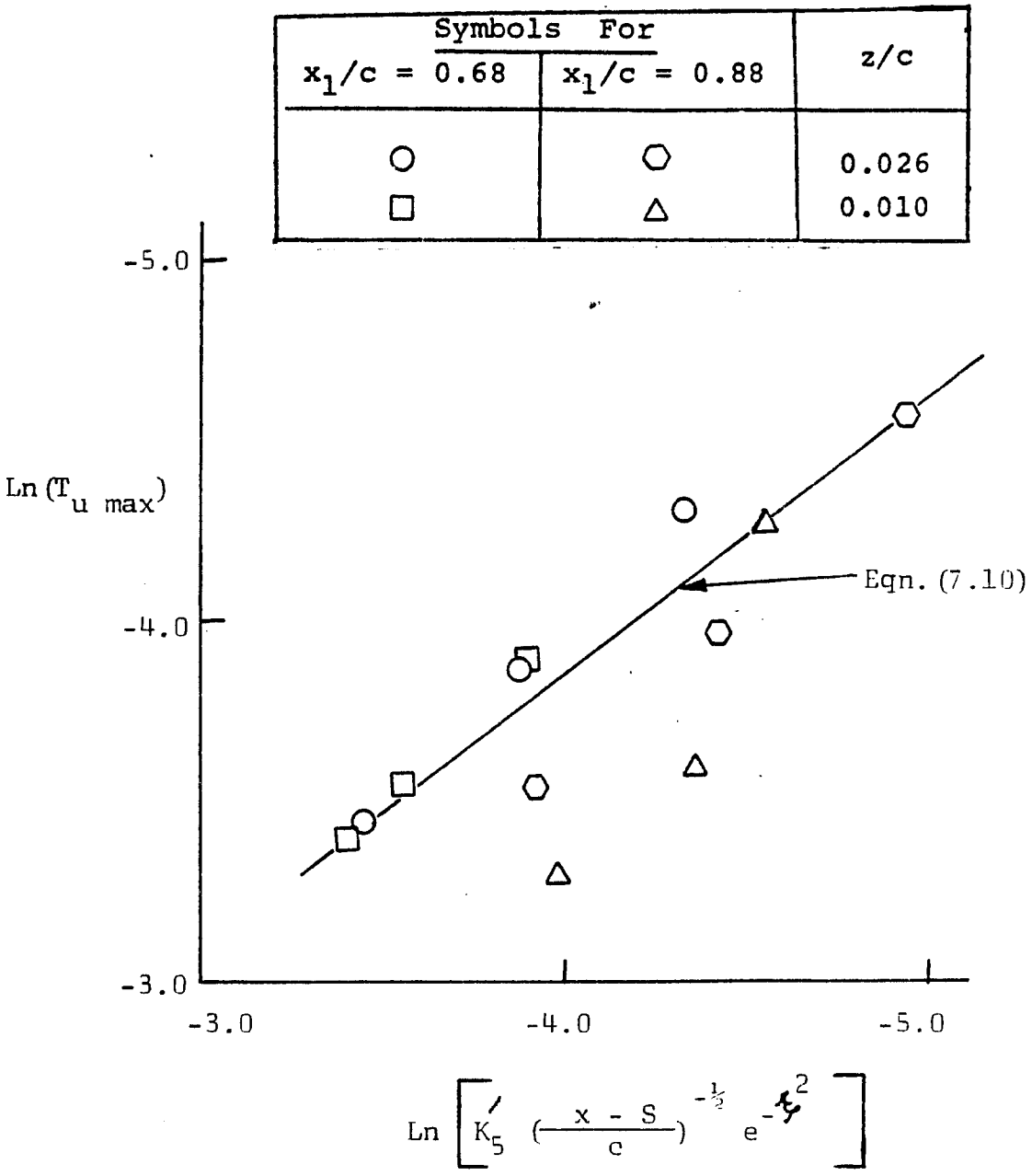

Figure 7.16 (a) Decay Characteristics of Maximum of Axial Component of Turbulence Intensity With Downstream Distance

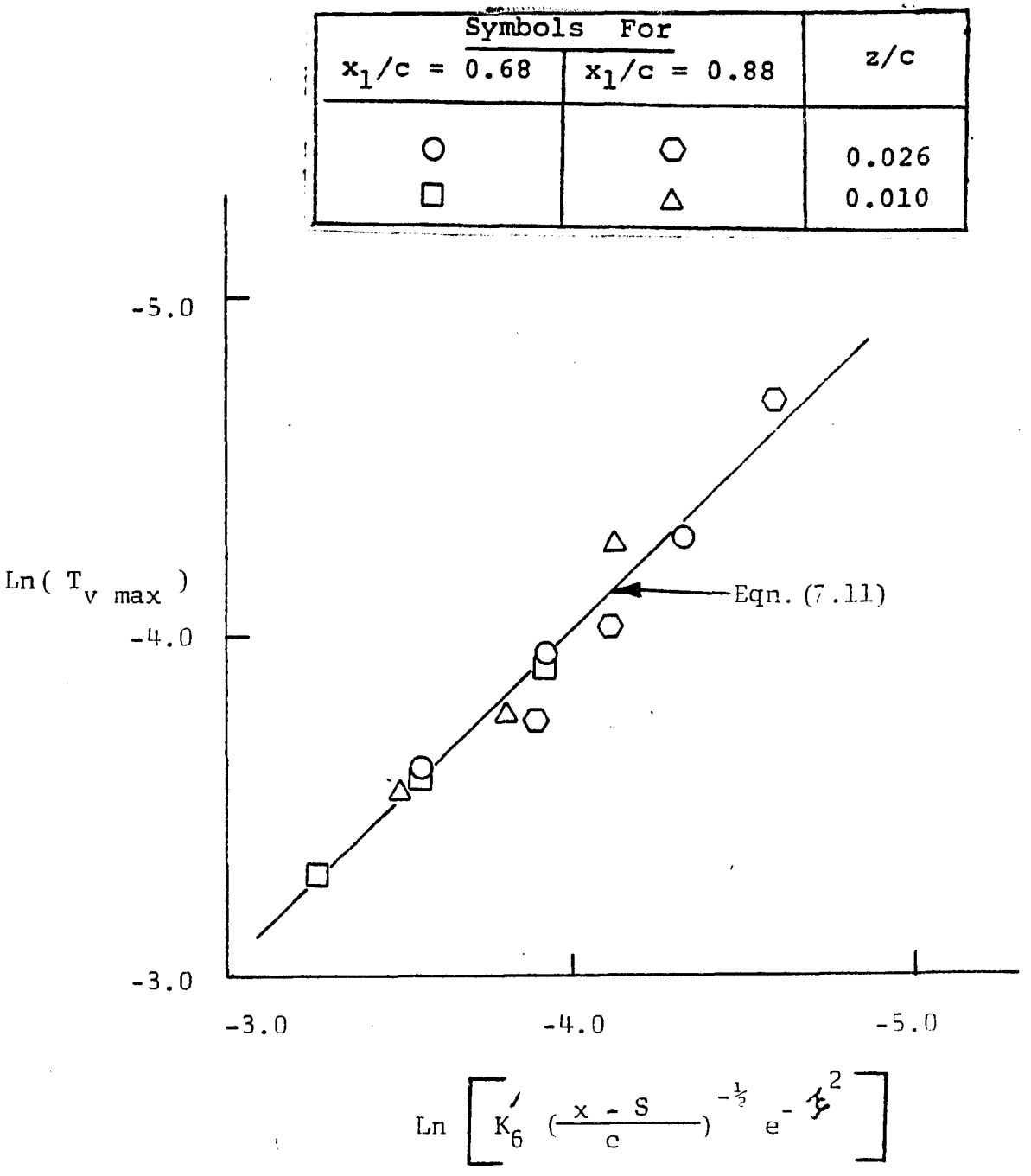

Figure 7.16(b) Decay Characteristics of Maximum of Lateral Component of Turbulence Intensity With Downstream Distance

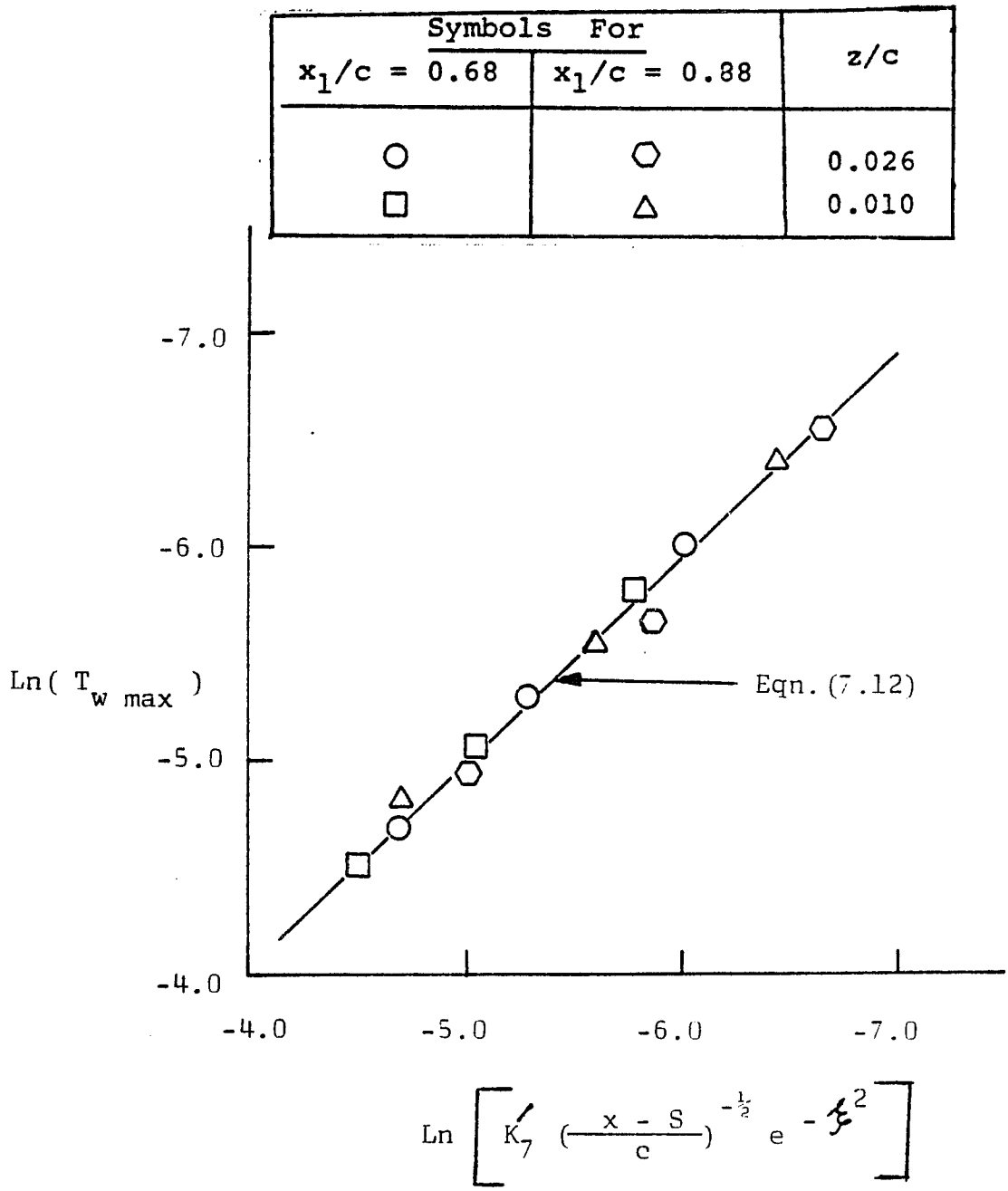

Figure 7.16(c) Decay Characteristics of Maximum of Normal Component of Turbulence Intensity With Downstream Distance

where K_5' , K_6' and K_7' are the constants used in Figures 7.16(a), (b) and (c), respectively. The values of the constants a and b are given in Table VI.

It can be concluded that the decay rate of the maximum values of the normal and lateral components of turbulence intensity is faster when compared to the axial component of turbulence intensity, because of the least effect of interaction with downstream distance. The agreement between the semi-empirical correlations and the experimental data is favorable.

The maximum values of longitudinal and lateral components of turbulence intensity in the interacting region are higher as compared to the non-interacted region but for smaller spacing (S/c = 0.007) ratio. The opposite is true for $S/c \geqslant 0.3$. This means that the decay rate of the peak values of the longitudinal and lateral components of turbulence intensity in the interacting region increases with the increase in spacing.

Logarithmic variation in the peak values of the components of Reynolds stress for two stations at the inner and outer regions is shown in Figures 7.17(a), (b) and (c), respectively. The semi-empirical correlations representing the logarithmic variation in Reynolds stress components are written as follows:

$$T_{uv\ max} = \bar{K}_8 \left[\left(\frac{x - S}{c} \right)^{-\frac{1}{2}} e^{-\eta^2} \right]_{..}^{0.905} \quad ..(7.14)$$

Symbols For $x_1/c = 0.68$	Symbols For $x_1/c = 0.88$	z/c
○	⬡	0.026
□	△	0.010

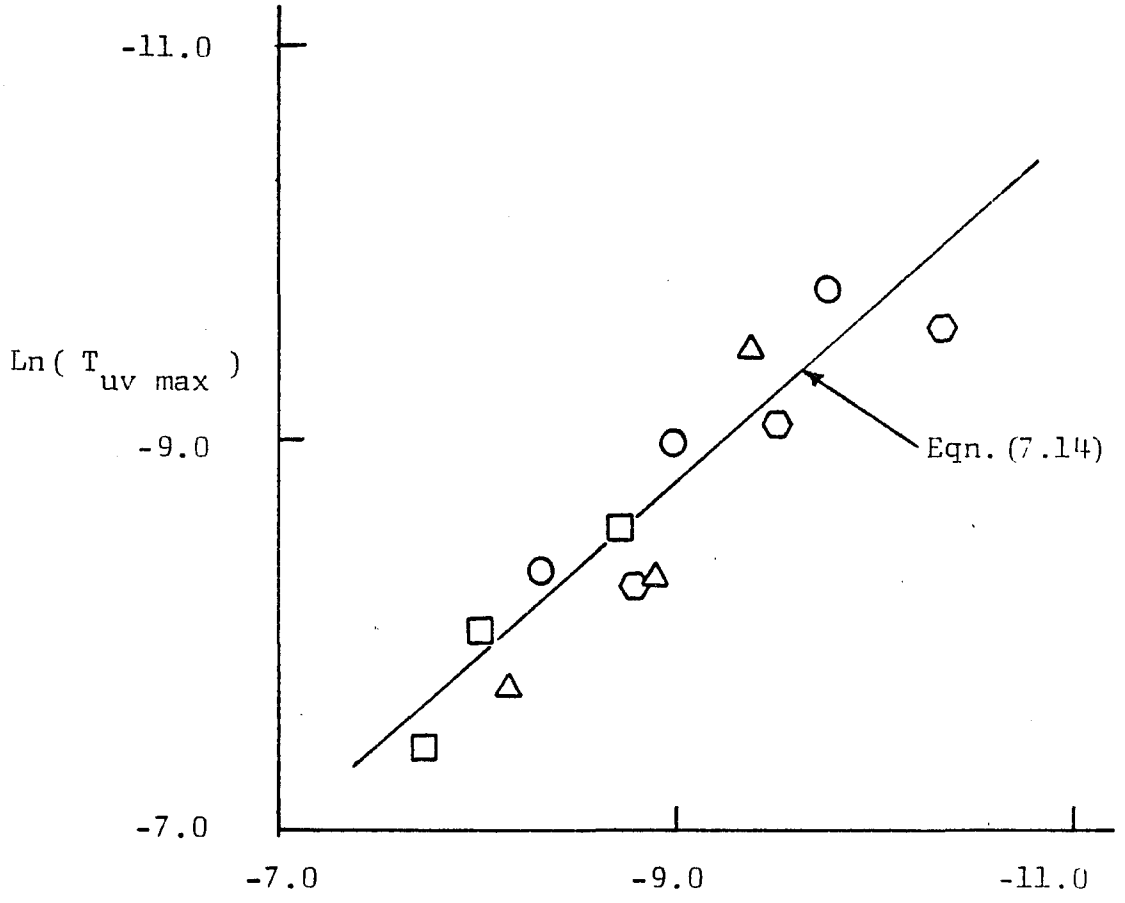

Figure 7.17 (a) Decay Characteristics of Maximum of Reynolds Stress Component, T_{uv}, With Downstream Distance

Symbols For x_1/c = 0.68	Symbols For x_1/c = 0.88	z/c
○	⬡	0.026
□	△	0.010

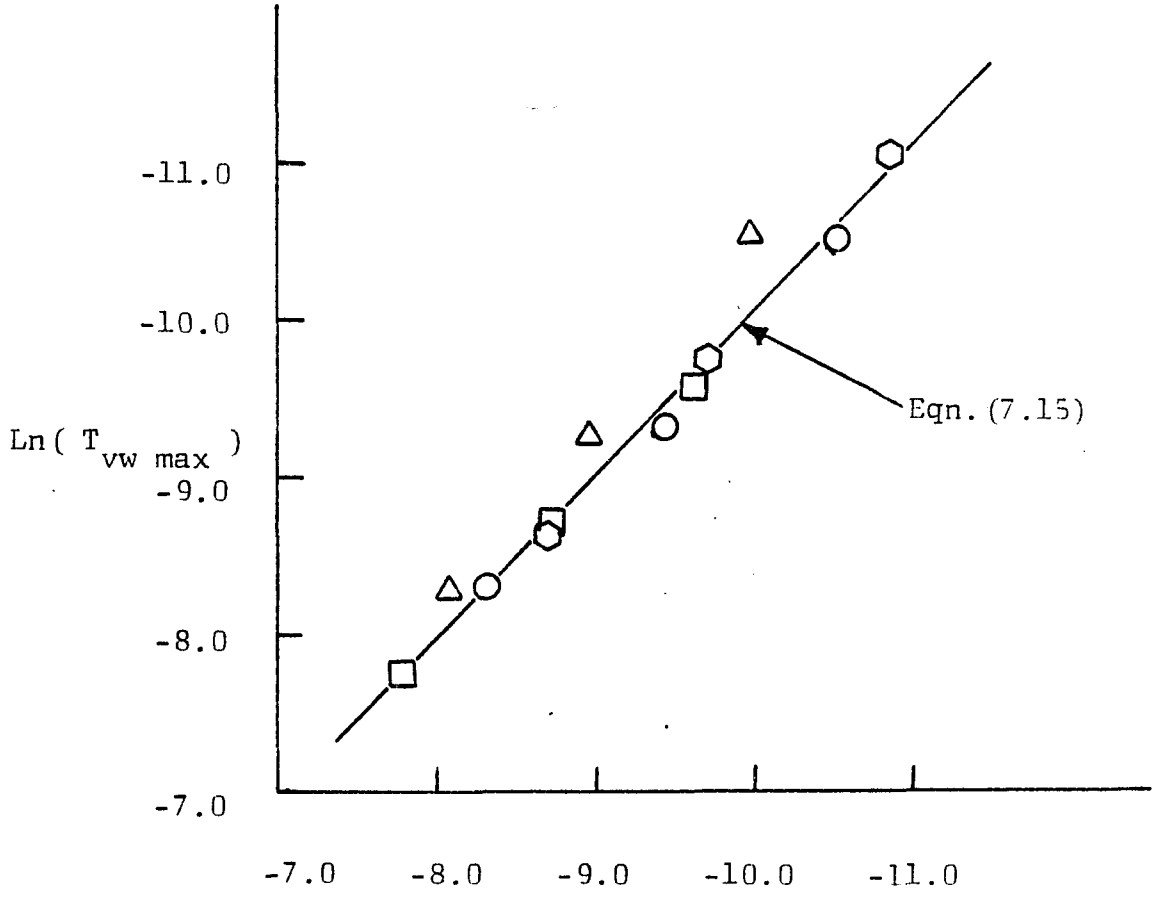

Figure 7.17 (b) Decay Characteristics of Maximum of Reynolds Stress Component, T_{vw}. With Downstream Distance

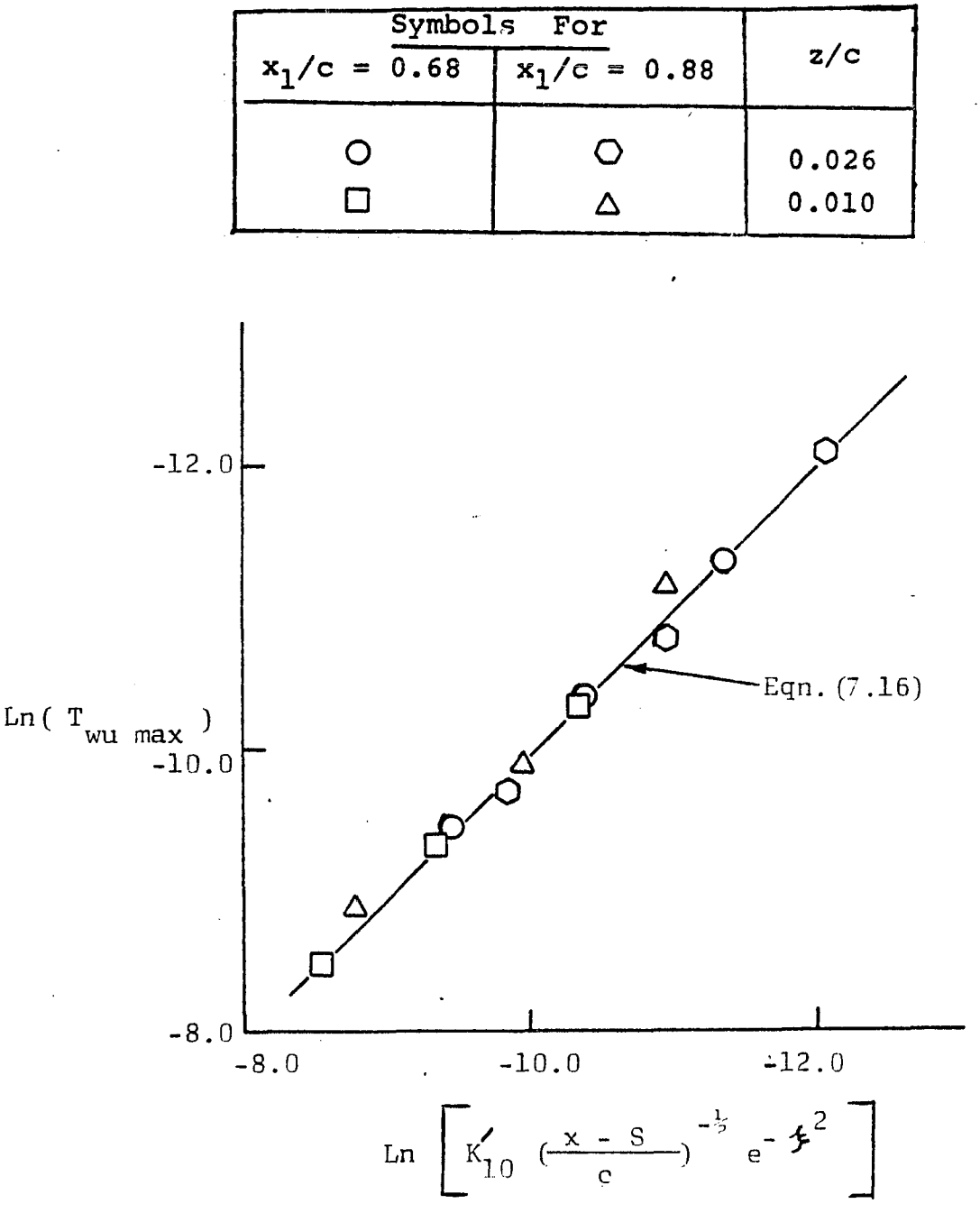

Figure 7.17(c) Decay Characteristics of Maximum of Reynolds Stress Component. T_{wu} . With Downstream Distance

TABLE VI

VALUES OF THE CONSTANTS IN TURBULENCE QUANTITIES OF WAKE BOUNDARY LAYER INTERACTION WORK

z/S	$\bar{K}_5$	$\bar{K}_6$	$\bar{K}_7$	$\bar{K}_8$	$\bar{K}_9$	$\bar{K}_{10}$
3.7143	0.0402	0.0314	0.01246	0.000134	0.000286	0.000112
0.0867	0.0357	0.0323	0.00857	0.000156	0.000129	0.000055
0.0430	0.0334	0.0372	0.00700	0.000078	0.000076	0.000033
1.4286	0.0687	0.0468	0.0206	0.001276	0.000556	0.000393
0.0333	0.0674	0.0497	0.1391	0.000955	0.000308	0.000205
0.0167	0.0617	0.059	0.0095	0.000628	0.000207	0.000106
$\bar{K}_i = a\,(K_i')^b$ i = 5 to 10						
a	0.465	0.934	0.874	0.533	1.419	1.278
b	0.772	0.986	0.970	0.905	1.040	1.020

$$T_{vw\ max} = \bar{K}_9 \left[\left(\frac{x - S}{c} \right)^{-\frac{1}{2}} e^{-\xi^2} \right]^{1.04} \quad \ldots(7.15)$$

$$T_{wu\ max} = \bar{K}_{10} \left[\left(\frac{x - S}{c} \right)^{-\frac{1}{2}} e^{-\xi^2} \right]^{1.02} \quad \ldots(7.16)$$

The value of ξ is obtained in the same manner as discussed in Section 7.1.2. The value of the constants $\bar{K}_8$, $\bar{K}_9$ and $\bar{K}_{10}$ for a variable spacing is listed in Table VI. The value of the constants K_8', K_9' and K_{10}' used in Figures 7.17(a), (b) and (c), respectively can be calculated by Eqn.(7.13) and the corresponding constants a and b are given in Table VI.

It can be concluded that the decay rate of the $T_{vw\ max}$ is faster than that of $T_{wu\ max}$, while the decay rate of $T_{wu\ max}$ is faster than that of $T_{uv\ max}$. The agrement between the semi-empirical correlations and the experimental data is quite favorable.

The maximum value of the T_{uv} component is higher in the interacting region as compared to that of the non-interacted region for $S/c = 0.007$. But the opposite is true for $S/c \gtrsim 0.3$. This means that the decay rate of the peak values of the T_{uv} component for the interacting region increases with the increase in spacing.

7.2.4 Total Correlation Coefficient:

The variation of the total correlation

coefficient defined as the ratio of the total maximum Reynolds stress to the maximum turbulence energy ($\bar{R}_{ij} = |\tau_{max}| / \rho\, q^2_{max}$) is plotted against downstream distance for two locations in the inner and outer regions of the interacted boundary layer at each location in Figure 7.18(a); while the spacing effect on the total correlation coefficient of the maximum values is shown in Figure 7.18(b).

The value of the total correlation coefficient usually increases in the inner region of the interacted boundary layer as compared to the outer region which is due to the increase in total Reynolds stress when compared to the increase in the total turbulence intensity. The increase in Reynolds stress is associated with the increase in velocity gradients towards the wall. The value of the total correlation coefficient usually decreases with the increase in downstream distance because of the faster decay of Reynolds stress components. The total correlation coefficient varies from 0.16 to 0.25 in the interacted region investigated.

The total correlation coefficient decreases for $S/c \gtrsim 0.3$ as compared to $S/c = 0.007$, except at $x_1/c = 0.88$, where the opposite trend is found to be observed.

7.3 Spectral Distribution in the Interacting Region:

The frequency spectra for the far wake

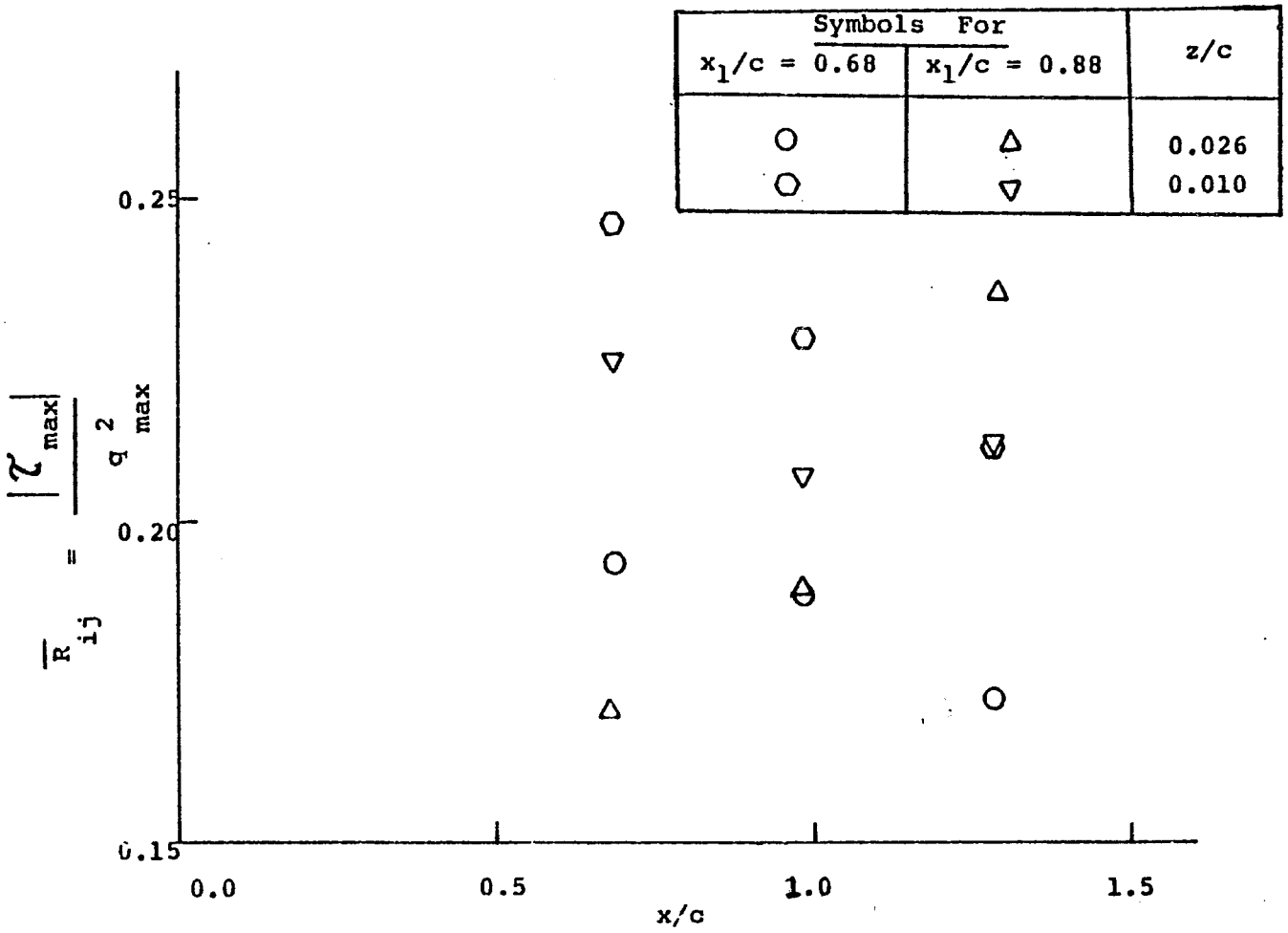

Figure 7.18(a) Variation of Correlation Coefficient ($\overline{R}_{ij}$) With Downstream Distance

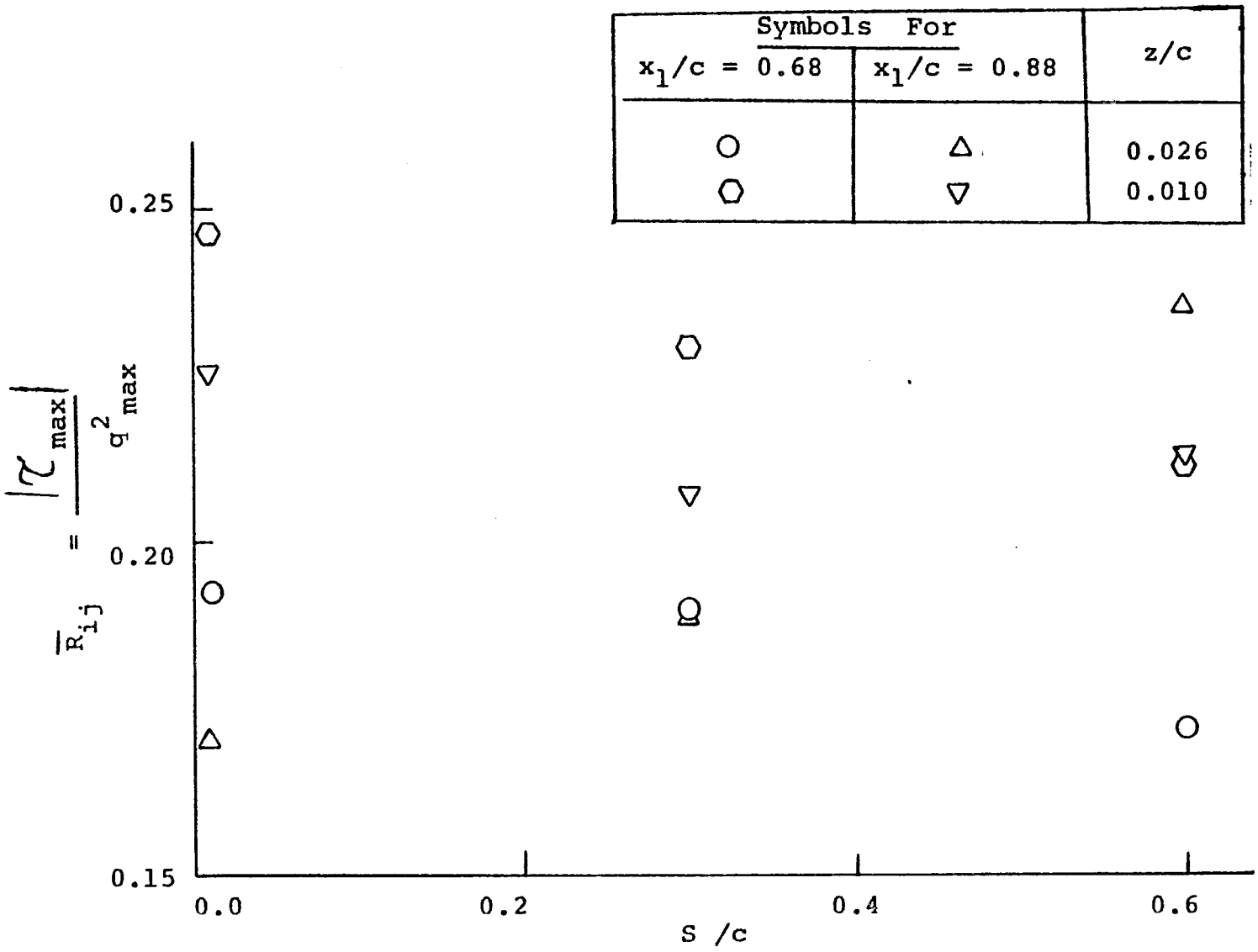

Figure 7.18(b) Variation of Correlation Coefficient ($\overline{R}_{ij}$) With S/c Ratio

interaction with variable spacing ratio in the interacting region near the wall is shown in Figures 7.19(a) to (f). Their representation in the wave number domain (For details, see Chapter V) is plotted in Figure 7.20.

The axial, normal and lateral locations of the stations, sweep width factor, frequency range and the frequency where the spectrum first drops to zero, for the spectra shown in Figures 7.19(a) through (f) are given in Table VII. The rising portions of the spectra in Figures 7.19(a) through (f) should not be considered as physicially significant. They are due to the experiment. Spectral energy decreases with the increase in spacing because of the reduced shearing effect.

Energy fall-off frequency is the same at station II for S/c ratios of 0.3 and 0.6.

Figure 7.20 shows the spectral energy distribution for the wake interacted boundary layer. The boundary layer turbulence spectrum, [Reference (51)] in the wave number domain is also shown in this figure. It can be concluded from this comparison that the spectral energy for the wake interacted boundary layer region is larger than that of only the boundary layer. Increase in energy is more pronounced for the low wave number range in comparison to the high wave number range. In both the cases, the effect of isotropy and shear yielding the

See Table VII for x-axis scale

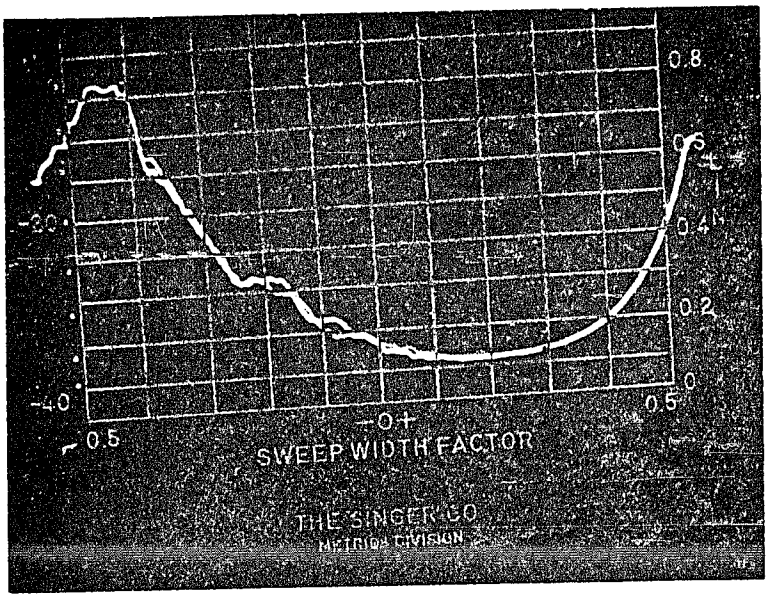

Figure 7.19(a) Frequency Spectrum at $x_1/c = 0.68$, $z/\delta = 0.1$ and $S/c = 0.007$

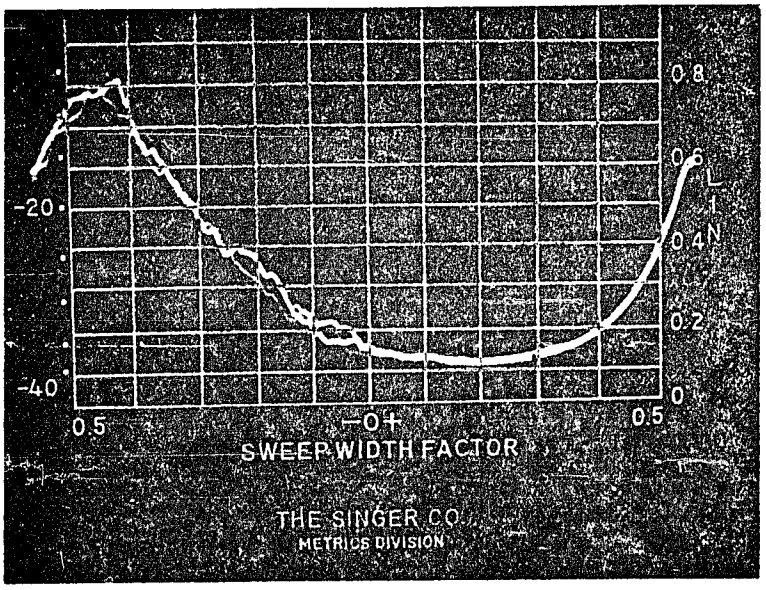

Figure 7.19(b) Frequency Spectrum at $x_1/c = 0.88$, $z/\delta = 0.1$ and $S/c = 0.007$

See Table VII for x-axis scale

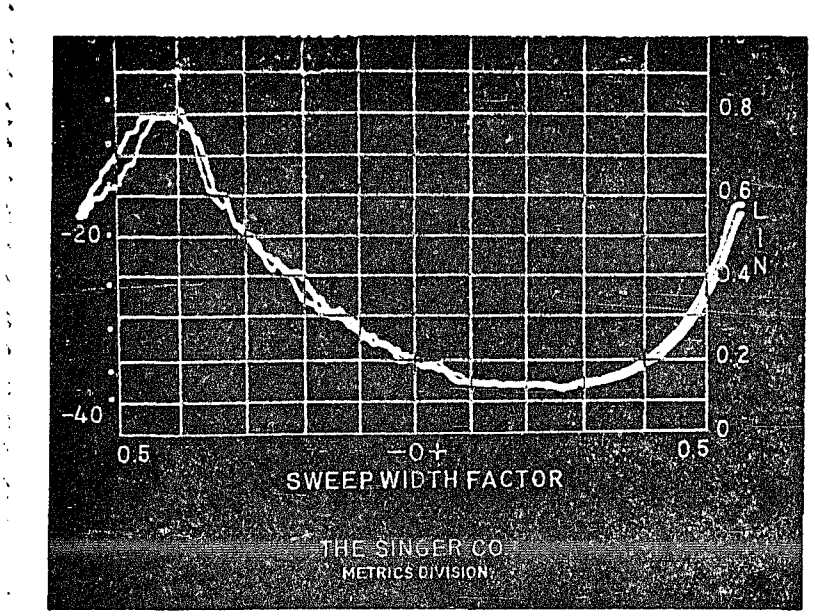

Figure 7.19(c) Frequency Spectrum at $x_1/c = 0.68$, $z/\delta = 0.1$ and $S/c = 0.30$

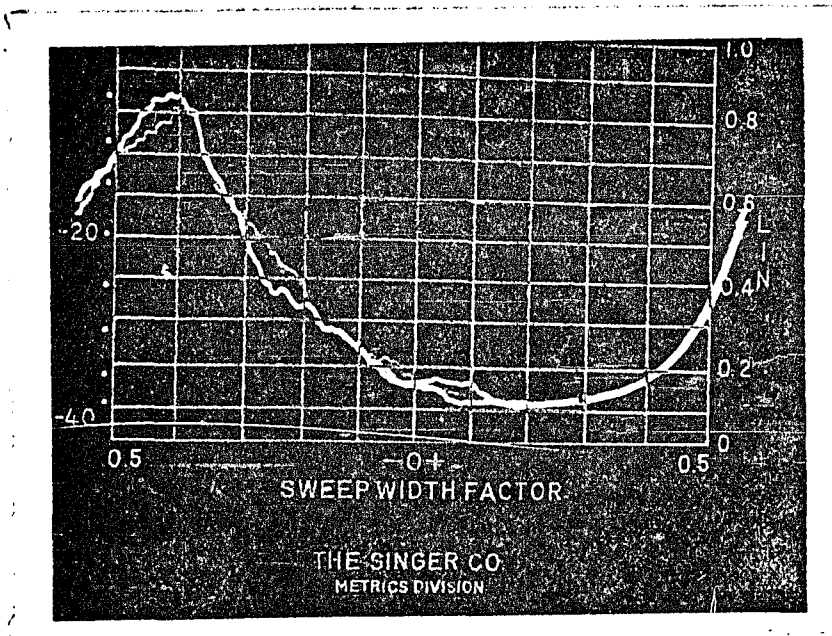

Figure 7.19(d) Frequency Spectrum at $x_1/c = 0.88$, $z/\delta = 0.1$ and $S/c = 0.30$

See Table VII for x-axis scale

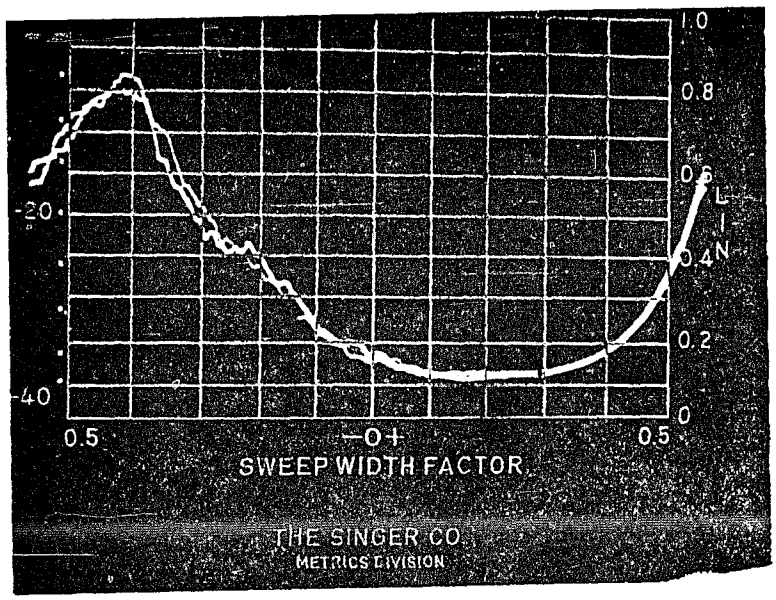

Figure 7.19(e) Frequency Spectrum at $x_1/c = 0.68$, $z/\delta = 0.1$ and $S/c = 0.60$

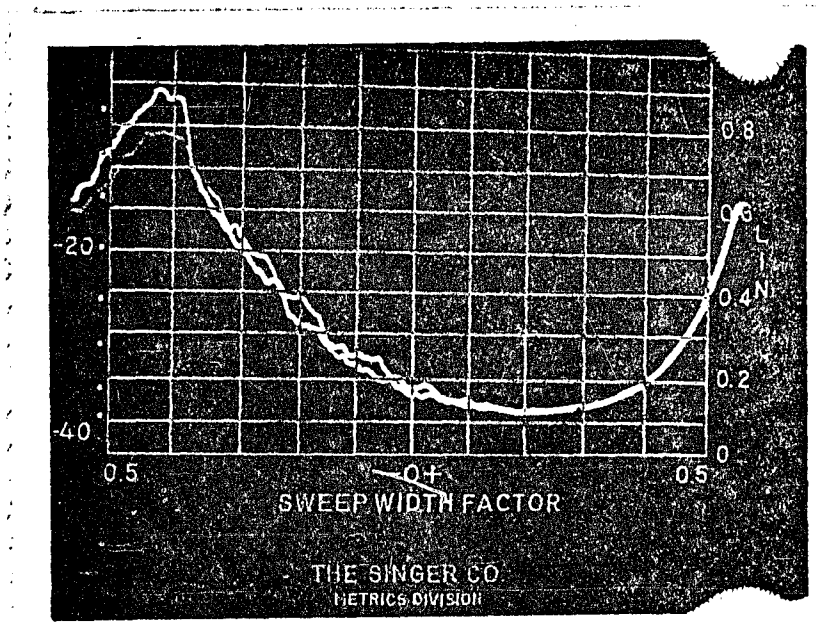

Figure 7.19(f) Frequency Spectrum at $x_1/c = 0.88$, $z/\delta = 0.1$, and $S/c = 0.60$

TABLE VII

DETAILS ON FREQUENCY SPECTRA

Figure No.	Locations of the Stations at the Wake Center line			Sweep Width Factor	Frequency Range	Frequency Where the Spectrum First Decays
	S/c	x_1/c	z/δ			
7.19(a)	0.007	0.68	0.10	-0.43 to 0.41	0 to 25 KHz	17560 Hz
7.19(b)	0.007	0.88	0.10	-0.43 to 0.41	0 to 25 KHz	18150 Hz
7.19(c)	0.300	0.68	0.10	-0.43 to 0.41	0 to 25 KHz	16370 Hz
7.19(d)	0.300	0.88	0.10	-0.42 to 0.42	0 to 25 KHz	16815 Hz
7.19(e)	0.600	0.68	0.10	-0.41 to 0.41	0 to 25 KHz	15180 Hz
7.19(f)	0.600	0.88	0.10	-0.42 to 0.42	0 to 25 KHz	16815 Hz

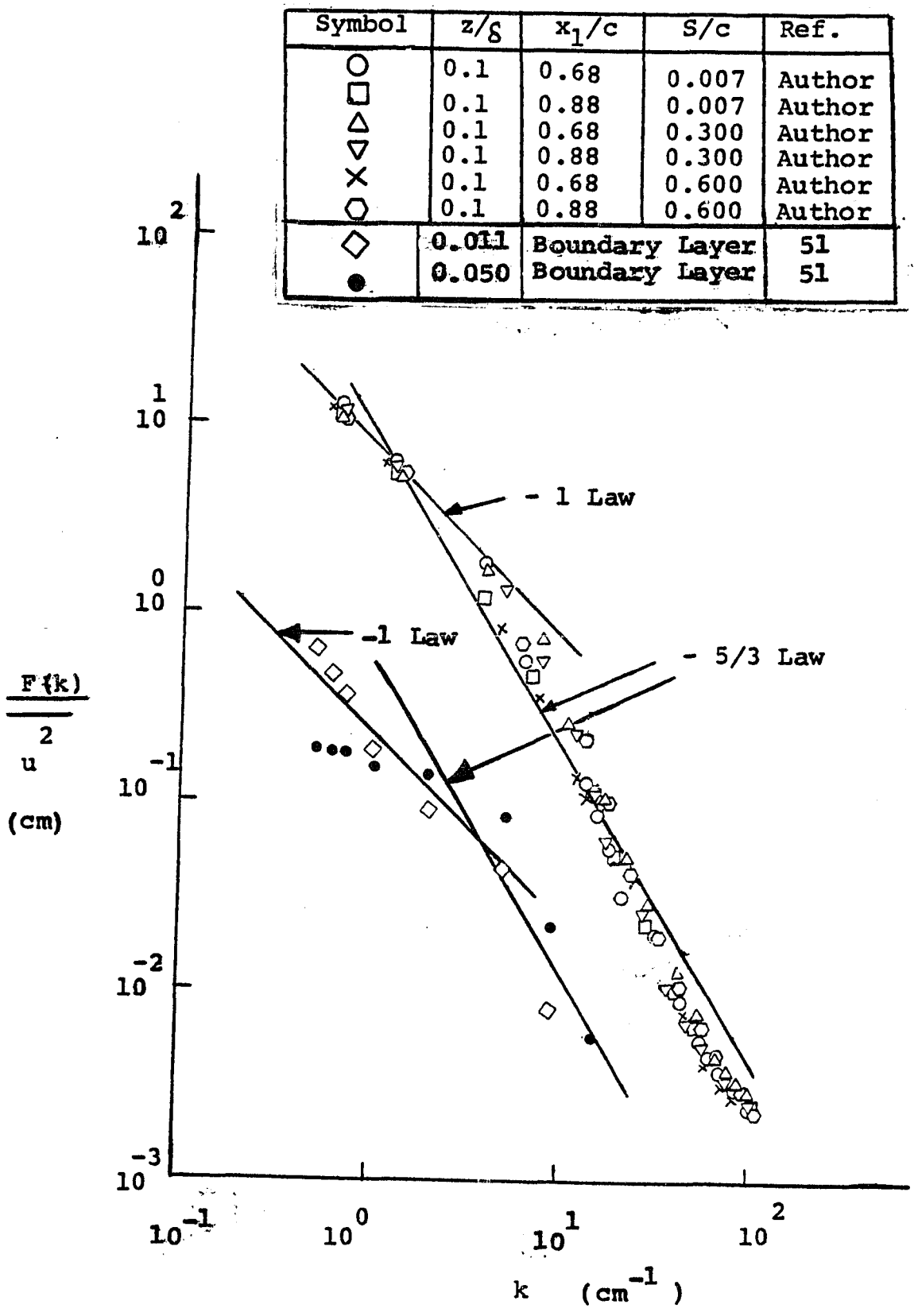

Figure 7.20 Energy Spectral Distribution in Wave Number Domain

- 5/3 law and - 1 law, respectively is found.

For a wave number less than 5.0, the spectral energy varies as k^{-1} instead of $k^{-5/3}$ for the equilibrium range. Thus, for smaller wave number range ($k < 5.0$) production, advection, convection and dissipation effects are equally important and spectral energy is far from equilibrium. This trend is in good agreement with the theoretical prediction of Tchen(5). The spectral energy variation can be closely represented by $k^{-5/3}$ for a wave number greater than 5.0, although this law increases its power with the increase in wave number. Thus, the wave number range from 5.0 to 50.0 can be classified as the equilibrium range. For $k > 50.0$, negative power of the wave number increases but it does not reach the -7 law. Absence of isotropy and homogeneity can be the additional factors from the departure of high wave number spectra from the - 7 law.

In a three-dimensional complex flow, the measurements of the spectrum are made in a one-dimensional mode with a single wire probe. Thus, the results presented in this section are of qualitative nature, but a a good insight of complex interacting flow is obtained because the one-dimensional spectrum is still an integral effect of three-dimensional spectra.

CHAPTER VIII

CONCLUSIONS

The investigation discussed in earlier Chapters can be summarized under two main headings:

8.1 Free Stream Turbulence Work:

The theoretical and experimental study (Chapter III and Chapter VI, respectively) of free stream turbulence on the characteristics of a turbulent wake leads to the following conclusions:

8.1.1 Mean Quantities:

1. Mean velocity profiles are observed to be nearly symmetrical in the presence of free stream turbulence.

2. Similarity in the mean velocity profiles is maintained to a good extent when the profiles are normalized with respect to analytically derived turbulence dependent parameters Φ_1 and Φ_2.

3. The higher the free stream turbulence, the greater is the recovery of the wake center line velocity. The decay law for the wake center line velocity defect due to free stream turbulence is well described by Eqn.(3.18).

4. The higher the free stream turbulence, the greater is the increase in length scale. The growth law of length scale with downstream distance due to free stream turbulence is well described by Eqn.(3.20).

5. The behavior of the turbulence parameters Φ_1 and Φ_2 is inverse in character, tends to unity for far wake ($x/c > 1.0$) and is given by Eqn.(3.17).

6. The displacement thickness of the wake increases with the increase in free stream turbulence level and can be predicted by Eqn.(6.8). A similar trend is observed in momentum thickness and is predicted by Eqn.(6.10).

7. Increase in free stream turbulence reduces the shape factor and the shape factor approaches unity towards the far wake regions. The higher the turbulence level, the greater is the decrease in shape factor as observed from the decay law given by Eqn.(6.11).

8. Free stream turbulence energizes the flow by producing the turbulent kinetic energy and thus increasing the energy thickness and is given by Eqn.(6.13).

8.1.2 Turbulence Quantities:

1. Longitudinal and lateral components of turbulence intensity are nearly symmetrical about the wake center line even in the presence of free stream turbulence. Both of these intensities increase with the increase in free stream turbulence level.

2. Reynolds stress is asymmetric about the wake center line and changes sign at the wake center line. Reynolds stress increases with the increase in free stream turbulence.

3. The higher the free stream turbulence, the greater the lateral distance from the wake center line to a point where the maximum value of the turbulence quantities occur.

4. The maximum values of the components of turbulence intensity occur in the vicinity of the occurrence of the maximum Reynolds stress.

5. Decay laws for the maximum values of the longitudinal and lateral components of turbulence intensity and shear stress are in good agreement with the correlation Eqns.(6.16 to 6.18), obtained from self-preservation and scaling considerations.

6. The value of the correlation coefficient obtained

from the maximum values of the turbulence quantities is 0.39 to 0.48.

7. The higher the free stream turbulence, the higher is the value of P, given by Eqn.(6.15).

8. Eddy viscosity increases with the increase in free stream turbulence.

8.2 Wake Boundary Layer Interaction:

The theoretical and experimental study (Chapter IV and Chapter VII, respectively) of wake boundary layer interaction leads to the following conclusions:

8.2.1 Mean Quantities:

1. Total velocity defect in axial, lateral and normal components of mean velocity decreases towards the inner region as well as with the increase in spacing and distance downstream the interaction. Decay laws for the axial, lateral and normal components of mean velocity are given by the semi-empirical correlation Eqns.(7.1), (7.2) and (7.3), respectively.

2. Length scale increases towards the wall, with the increase in downstream distance and with the increase in spacing. The semi-empirical correlation for the length scale is given by Eqn.(7.4).

3. Similarity in the total axial component of mean velocity profile is maintained to a good extent when the profiles are normalized with respect to the analytically derived turbulence interaction parameters.

4. The behavior of the turbulence interaction parameters, $\bar{\Phi}_i$ and $\bar{\Psi}_i$, is inverse in character and is dependent upon the interaction of the wake with the boundary layer.

8.2.2 Turbulence Quantities:

1. Axial, lateral and normal components of turbulence intensity increase towards the inner region and decrease towards the outer edge of the wake and with the increase in spacing.

2. $\bar{T}_{uv}$ and $\bar{T}_{wu}$ components of Reynolds stress change sign about the wake center line. The magnitude of these components increases towards the wall and decreases towards the outer edge of the wake and with the increase in spacing.

3. The $\bar{T}_{vw}$ component does not change sign about the the wake center line and its magnitude decreases with the increase in spacing. It increases towards the inner region and decreases towards the outer edge of the wake.

4. Peak values of the components of Reynolds stress occur in the vicinity of the occurrence of the peak values of the components of turbulence intensity. The occurrence of the peak values shifts away from the wake center line with the increase in downstream distance and with the increase in spacing.

5. It was found possible to represent all the data on the decay and growth of turbulence intensities and Reynolds stress through single lines for each of the components and for all of the points of measurements. Decay in the normal and lateral components of turbulence intensity is faster than that of the axial component. Decay in the $T_{vw\ max}$ component is faster than that of the $T_{uv\ max}$ and $T_{wu\ max}$ components.

6. Correlation coefficient increases towards the inner region and decreases with the increase in downstream distance and with the increase in spacing. The correlation coefficient varies from 0.16 to 0.25 in the interacted region investigated.

7. Spectral energy increases due to interaction and decreases with the increase in wave number. Spectral energy varies as k^{-1} for $k < 5.0$ and $k^{-5/3}$ for $5.0 < k < 50.0$ and power law increases with the increase in wave number.

CHAPTER IX

REFERENCES

1. Raj, R. and Lakshminarayana, B., " Characteristics of the Wake behind a Cascade of Airfoils, " J. of Fluid Mechanics, Vol. 61, part 4, 1973, pp. 707 - 730.

2. Tennekes, H. and Lumley, J. L., A First Course in Turbulence, Sixth Edition, The MIT Press, June 1980.

3. Raj, R., " Pressure Gradient Velocity Correlations for Flows with Two and Three Dimensional Turbulence, " Physics of Fluids, Vol. 20, No. 12, Dec. 1977.

4. Hinze, J. O., Turbulence, Second Edition, Mc Graw-Hill Series, 1975.

5. Tchen, C. M., " On the Spectrum of Energy in the Turbulent Shear Flow, " J. of Research of the National Bureau of Standards, Vol. 50, No. 1, Jan. 1953, pp. 51 - 62.

6. Coles, Donald, " The Law of the Wake in the Turbulent Boundary Layer, " J. of Fluid Mechanics, Vol. 1, 1956, pp. 191 - 226.

7. Mc Donald, Henry and Kreskovsky, John P., " Effect of Free Stream Turbulence on the Turbulent Boundary Layer, " Int. J. of Heat and Mass Transfer, Vol 17, 1974, pp. 705 - 716.

8. Evans, R. L. and Horlock, J. H., " Calculation of the Development of Turbulent Boundary Layers with a Turbulent Free Stream, " Trans. of the ASME, Dec. 1974, pp. 348 - 352.

9. Junkhan, G. H. and Serovy, G. K., " Effect of free Stream Turbulence and Pressure Gradient on Flat Plate Boundary Layer Velocity Profiles and on Heat Transfer," J. of Heat Transfer, 1967, pp. 169.

10. Charnay, G., Comte-Bellot, G. and Mathieu, J.," Development of a Turbulent Boundary Layer on a Flat Plate in an External Turbulent Flow, " AGARD CP 93, Paper No. 27, 1971.

11. Huffman, G. D., Zimmerman, D. R. and Bennet, W. A., " The Effect of Free Stream Turbulence Level on Turbulent Boundary Layer Behavior, " Paper No. I-5, AGARDograph No. 164, 1972.

12. Schlichting, H. and Das, A., " On the Influence of Turbulence Level on the Aerodynamic Losses of Axial Turbomachines, " Flow Research on Blading, Edited by L.S. Dzung, Elsevier, New York, 1950, pp. 243 - 274.

13. Bradshaw, P., " Effect of Free Stream Turbulence on Turbulent Shear Layers, " I.C. Aero. Report, Oct.1974.

14. Meier, H.U. and Kreplin, H. P., " Influence of Free Stream Turbulence on Boundary Layer Development, "

AIAA Journal, Vol.18, No. 1, Jan. 1980, pp. 11 - 15

15. Mc Donald, H. and Fish, R. W., " Practical Calculations of Transitional Boundary Layer, " Int. J. of Heat and Mass Transfer, 16 (9), 1973, pp. 1729 - 1744.

16. Kestin, J., " The Effect of Free Stream Turbulence on Heat Transfer Rates, " Advances in Heat Transfer, Edited by T. F. Irvine and H.P. Hartnett, Vol. 3, 1966, pp. 1 - 32.

17. Dryden, H. L., " Transition from Laminar to Turbulent Flow, " Turbulent Flows and Heat Transfer, Edited by C.C. Lin, Princeton University Press, Princeton, N. J. 1959, pp. 3 - 74.

18. Kline, S. J., Lisin, A. V. and Waitman, B. A., " A Preliminary Experimental Investigation of Effect of Free Stream Turbulence on Turbulent Boundary Layer Growth, " N.A.S.A., TND - 368, 1960.

19. Frenkiel, F. N., " The Decay of Isotropic Turbulence, " Trans. of the A.S.M.E., Vol. 70, 1948, pp. 311.

20. Bains, W. D. and Peterson, E. G., " An Investigation of Flow through Screens, " Trans. of the A. S. M. E., July 1951, pp. 467 - 480.

21. Robertson, James, M. and Holt, Charles, F., " Stream Turbulence Effects on Turbulent Boundary Layer, " Proceedings of A. S. C. E., Vol. 98, No. HY6, June

1972, pp. 1095 - 1099.

22. Green, G. E., " On the Influence of Free Stream Turbulence on a Turbulent Boundary Layer as it Relates to Wind Tunnel Testing at Subsonic Speeds, " AGARD Report No. 602, April 1973.

23. Nash, J. F. and Mac Donald, A.G.J., " A Turbulent Skin Friction Law for use at Subsonic and Transonic Speeds, " ARC CP No. 948, 1966.

24. Hall, A.A. and Hislop, G. S., " Experiments on the Transition of the Laminar Layer on a Flat Plate, " Aero. Res. Comm. Rep. Memo. 1843, 1938.

25. Taylor, G. I., " Some recent Developments in the Study of Turbulence, " Proc. 5th Int. Cong. Appl. Mech., John Wiley and Sons, Chichester, 1938.

26. Schubauer, G. B., " The Effect of Turbulence on Transition on the Boundary Layer of an Elliptic Cylinder, " Proc. 5th Int. Cong. Appl. Mech., John Wiley and Sons, Chichester, 1938.

27. Hall, D. J. and Gibbings, J. C., " Influence of Free Stream Turbulence and Pressure Gradient upon Boundary Layer Transition, " J. of Mech. Engr. Science, Vol. 14, No. 2, 1972, pp. 134 - 146.

28. Michel, R., " Effects of Flow Turbulence and Noise on

Aerodynamic Phenomena and Wind Tunnel Results, " AGARD Report No. 615, June 1974.

29. Tsuji, Tukaka and Iida, Shuske, " Influence of Free Stream Turbulence on Mean Velocities of Turbulent Boundary Layer without Pressure Gradient, " Trans. Japan Soc. Aero. Space Sci., Vol. 15, No. 29, 1972, pp. 105 - 116.

30. Eagleson, P. S., Huval, C.J. and Perkins, F. E., " Turbulence in the Early Wake of a Fixed Plate, " MIT Hydrodynamic Lab., TR No. 46, Feb. 1961.

31. Chevray, Rene and Kovasznay, Leslie, S. G., " Turbu - lence Measurements in the Wake of a Thin Flat Plate, " AIAA J., Vol. 7, No. 8, Aug. 1969, pp. 1641 - 1643.

32. Komoda, H., " On the Effect of Free Stream Turbulence on the Structure of Turbulent Wake, " J. Japan Society, Aero. Engr., Oct. 1957, pp. 274 - 279.

33. Eskinazi, Salamon, " Mixing of Wakes in a Turbulent Shear Flow, " NASA TN D-83, Sept. 1959.

34. Pal, S. and Raj, R., " Wake Behavior in the Presence of Free Stream Turbulence, " Presented at the 25th International Gas Turbine Conference, March 1980, New Orleans and to be published in the J. of Engineering for Power, 1981.

35. Pal, S. and Raj, R., " Characteristics of Wake

Turbulence due to Free Stream Turbulence Environment," AIAA Paper No. 1079, Presented at 16th Joint Propulsion Conference, Hartford, Connecticut, June-July 1980.

36. Love, R. M., " An Investigation of the Effect of the Wall Boundary Layer on the Wake of an Obstacle Protruding from the Wall, " U.S. Government Report No. 613625, 1963.

37. Armilli, R. V., " The Interaction of a Turbulent Flat Plate Boundary Layer with the Wake of a Circular Cylinder Mounted Normal to the Plate, " Ph. D. Thesis, VPI, July 1973.

38. Gartshore, I. S., " The Interaction between Turbulent Wakes and Boundary Layer, " C.A.S.I., Trans. Vol. 5, No. 2, Sept. 1972, pp. 49 - 55.

39. Counihan, J., Hunt, J.C.R. and Jackson, P. S., " Wakes Behind Two Dimensional Surface Obstacles in Turbulent Boundary Layers, " J. Fluid Mechanics, Vol. 64, part 3, 1974, pp. 529 - 563.

40. Bradshaw, P., Dean, R. B. and Mc Eligot, D. M., " Calculation of Interacting Turbulent Shear Layers: Duct Flow, " J. of Fluid Engineering, June 1973, pp. 214 - 220.

41. Morel, T. and Torda, T. P., " Calculation of Free Turbulent Mixing by Interaction Approach, " AIAA, J.,

Vol. 12, No. 4, April 1974, pp. 533 - 540.

42. Raj, R., " Formulation of a Generalized Mathematical Model for Computation of Boundary Layer and Wake in Turbomachines, " J. Tensor, N.S. (Japan), Vol. 31, 1977, pp. 235 - 248.

43. Silverstein, A., Katzoff, S. and Bullivant, W., " " Downwash and Wake behind Plain and Flapped Airfoils," NACA TR No. 651, 1939.

44. Schlicting, H., Boundary Layer Theory, Mc Graw-Hill Book Company, Seventh Edition, 1976.

45. Raj, R. and Lakshiminarayana, B., " Three Dimensional Characteristics of Turbulent Wakes Behind Rotors of Axial Flow Turbomachinery, " J. of Engineering for Power, Vol. 98, No. 2, 1976, pp. 218 - 228.

46. Raj, R., " On the Investigation of Cascade and Turbomachinery Rotor Wake Characteristics, " Ph. D. Thesis, Department of Aerospace Engineering, The Pennsylvania State University, Nov. 1974.

47. Friehe, C. A. and Schwarz, W. H., " Deviations from the Cosine Law for Yawed Cylindrical Anemometer Sensor, " J. Applied Mechanics, Dec. 1968, pp.655-662.

48. Champagne, F. H., Sleicher, C. A. and Wehrmann, O. H., " Turbulence Measurement with Inclined Hot-Wires, " Part I, J. Fluid Mechanics, Vol 28, 1967.

49. Bradshaw, P., An Introduction to Turbulence and Its Measurement, Pergamon Press, First Edition, 1971.

50. Reynolds, A. J, " Observations on Distorted Turbulent Wakes, " J. Fluid Mechanics, Vol. 13, 1962, pp. 333.

51. Klebanoff, P. S., " Characteristics of Turbulence in a Boundary Layer with Zero Pressure Gradient, " NACA Report No. 1247, 1955.

APPENDIX - A

CALCULATION PROCEDURE OF TURBULENCE QUANTITIES FOR TRIPLE SENSOR HOT-WIRE ANEMOMETRY

To obtain the turbulence quantities from the measured data, the procedure outlined below is followed.

Rewriting Eqn.(5.4),

$$E_i^2 - E_{0i}^2 = D_i \, U_i^{n_i} \quad , \quad i = 1, 2 \text{ and } 3 \quad \ldots(A\text{-}1)$$

Resolving velocity and voltage into mean and fluctuating parts:

$$U_i = \bar{U}_i + u_i \quad \ldots(A\text{-}2)$$

$$E_i = \bar{E}_i + e_i \quad \ldots(A\text{-}3)$$

where $\bar{E}_i$, $\bar{U}_i$, e_i and u_i are the mean voltage, mean velocity, fluctuating voltage and fluctuating velocity of the sensor i, respectively.

Time averaging Eqn.(A-1),

$$\overline{E_i^2} - \overline{E_{0i}^2} = D_i \, \overline{U_i^{n_i}} \quad \ldots(A\text{-}4)$$

Substituting Eqn.(A-2) and (A-3) in Eqn.(A-1), taking binomial expansion; subtracting Eq.(A-4) and rearranging,

$$2 \, \bar{E}_i \, e_i = (\overline{E_i^2} - \overline{E_{0i}^2}) \, n_i \, u_i / \bar{U}_i \quad \ldots(A\text{-}5)$$

Squaring, time averaging and rearranging,

$$\frac{\sqrt{\overline{u_i}^2}}{\overline{U}_i} = \frac{2}{n_i} \frac{\sqrt{\overline{e_i^2}}}{\overline{E}_i \left[1 - (\overline{E}_{0i}/\overline{E}_i)^2\right]} \quad \ldots(A\text{-}6)$$

$\sqrt{\overline{e_i^2}}$ was measured experimentally, thus $\sqrt{\overline{u_i^2}}$, fluctuating component of turbulent velocity (r.m.s. value) along the sensor axes was known.

Rearranging Eqn.(A-5),

$$e_i = \frac{D_i\, n_i}{2\, \overline{E}_i} \overline{U}_i^{(n_i - 1)} u_i \quad \ldots(A\text{-}7)$$

Writing Eqn.(A-7) for i =1 and 2, i.e., for e_1 and e_2; multiplying both the equations and taking the time average:

$$\overline{e_1\, e_2} = \frac{D_1 D_2 n_1\, n_2}{4} \overline{U}_1^{(n_1-1)}\, \overline{U}_2^{(n_2-1)} \frac{\overline{u_1 u_2}}{\overline{E}_1\, \overline{E}_2} \quad \ldots(A\text{-}8)$$

The left hand side of Eqn.(A-8) can also be written as:

$$\overline{e_1\, e_2} = \tfrac{1}{4} \left[\overline{(e_1 + e_2)^2} - \overline{(e_1 - e_2)^2} \right]_{\text{input}} \quad \ldots(A\text{-}9)$$

The dual summing units through which the fluctuating signals were passed, have the transfer function, G_T, as

$$G_T = \frac{e_{out}}{e_{in}} = 0.33$$

Thus, Eqn.(A-9) becomes,

$$\overline{e_1\ e_2} = \frac{1}{4\ G_T^2}\left[\overline{(e_1 + e_2)^2} - \overline{(e_1 - e_2)^2}\right]_{\text{output}} \quad \ldots(A\text{-}10)$$

Equating Eqns.(A-8) and (A-10) and rearranging

$$\overline{u_1\ u_2} = \frac{\bar{E}_1\ \bar{E}_2\ \bar{U}_1^{(1-n_1)}\ \bar{U}_2^{(1-n_2)}}{D_1\ D_2\ n_1\ n_2\ G_T^2}\left[\overline{(e_1 + e_2)^2} - \overline{(e_1 - e_2)^2}\right] \quad \ldots(A\text{-}11)$$

Similarly, $\overline{u_2\ u_3}$ and $\overline{u_3 u_1}$ can be written as,

$$\overline{u_2\ u_3} = \frac{\bar{E}_2\ \bar{E}_3\ \bar{U}_2^{(1-n_2)}\ \bar{U}_3^{(1-n_3)}}{D_2\ D_3\ n_2\ n_3\ G_T^2}\left[\overline{(e_2 + e_3)^2} - \overline{(e_2 - e_3)^2}\right] \quad \ldots(A\text{-}12)$$

and

$$\overline{u_3\ u_1} = \frac{\bar{E}_3\ \bar{E}_1\ \bar{U}_3^{(1-n_3)}\ \bar{U}_1^{(1-n_1)}}{D_3\ D_1\ n_3\ n_1\ G_T^2}\left[\overline{(e_3 + e_1)^2} - \overline{(e_3 - e_1)^2}\right] \quad \ldots(A\text{-}13)$$

The right hand side of Eqns.(A-11) to (A-13) is known. Therefore, the left hand side can be calculated, i.e., $\overline{u_1\ u_2}$, $\overline{u_2\ u_3}$ and $\overline{u_3\ u_1}$ components of Reynolds along the sensor axes are known.

Transformation of turbulent intensity and Reynolds stress components along the set-up axes from the sensor axes is carried out as follows:

Rewriting Eqn.(5.20) to (5.22) as:

$$U_x = U_1 \cos\theta_1 + \left(U_2^2 + U_3^2 \right)^{\frac{1}{2}} \sin\theta_1 \qquad \ldots(A\text{-}14)$$

$$U_y = a\left[- U_1 \sin\theta_1 + \left(U_2^2 + U_3^2 \right)^{\frac{1}{2}} \cos\theta_1 \right] \qquad \ldots(A\text{-}15)$$

$$U_z = b\left[- U_1 \sin\theta_1 + \left(U_2^2 + U_3^2 \right)^{\frac{1}{2}} \cos\theta_1 \right] \qquad \ldots(A\text{-}16)$$

where,

$$a = \cos\theta_2 \left(\sin\theta_3 + \cos\theta_3 \right) \qquad \ldots(A\text{-}17)$$

$$b = \cos\theta_2 \left(\cos\theta_3 - \sin\theta_3 \right) \qquad \ldots(A\text{-}18)$$

Resolving total velocity components into mean and fluctuating parts,

$$\left.\begin{aligned} U_x &= \bar{U}_x + u_x \\ U_y &= \bar{U}_y + u_y \\ U_z &= \bar{U}_z + u_z \end{aligned}\right\} \qquad \ldots(A\text{-}19)$$

and

$$\left.\begin{aligned} U_1 &= \bar{U}_1 + u_1 \\ U_2 &= \bar{U}_2 + u_2 \\ U_3 &= \bar{U}_3 + u_3 \end{aligned}\right\} \qquad \ldots(A\text{-}20)$$

Substituting Eqns.(A-19) and (A-20) into Eqn.(A-14), neglecting small terms,

$$\bar{U}_x + u_x = (\bar{U}_1 + u_1)\cos\theta_1 + (\bar{U}_2^2 + \bar{U}_3^2)^{\frac{1}{2}} \left[1 + \frac{u_2^2 + u_3^2 + 2\,(\bar{U}_3\, u_3 + \bar{U}_2\, u_2)}{2\,(\bar{U}_2^2 + \bar{U}_3^2)} \sin\theta_1 \right] \qquad \ldots(A\text{-}21)$$

Taking the mean of Eqn.(A-21),

$$\bar{U}_x = \bar{U}_1 \cos\theta_1 + (\bar{U}_2^2 + \bar{U}_3^2)^{\frac{1}{2}} \left[1 + \frac{\overline{u_2^2} + \overline{u_3^2}}{2(\bar{U}_2^2 + \bar{U}_3^2)} \sin\theta_1 \right] \quad \ldots(A\text{-}22)$$

Subtracting Eqn.(A-22) from Eqn.(A-21),

$$u_x = u_1 \cos\theta_1 + \sin\theta_1 \frac{2(\bar{U}_3 u_3 + \bar{U}_2 u_2) + u_2^2 + u_3^2 - \overline{u_2^2} - \overline{u_3^2}}{2(\bar{U}_2^2 + \bar{U}_3^2)^{\frac{1}{2}}} \quad \ldots(A\text{-}23)$$

Squaring, time averaging and rearranging, Eqn.(A-23),

$$\sqrt{\overline{u_x^2}} = \left[\overline{u_1^2} \cos^2\theta_1 + \frac{\bar{U}_3^2 \overline{u_3^2} + \bar{U}_2^2 \overline{u_2^2} + 2\bar{U}_3 \bar{U}_2 \overline{u_2 u_3}}{\bar{U}_2^2 + \bar{U}_3^2} \sin^2\theta_1 + \frac{\bar{U}_3 \overline{u_1 u_3} + \bar{U}_2 \overline{u_1 u_2}}{(\bar{U}_2^2 + \bar{U}_3^2)^{\frac{1}{2}}} \sin 2\theta_1 \right]^{\frac{1}{2}} \quad \ldots(A\text{-}24)$$

Similarly from Eqns.(A-15) and (A-16), it can be written as:

$$\sqrt{\overline{u_y^2}} = a \left[\overline{u_1^2} \sin^2\theta_1 + \frac{\overline{U_2^2 u_2^2} + \overline{U_3^2 u_3^2} + 2\bar{U}_2\bar{U}_3\overline{u_2 u_3}}{\bar{U}_2^2 + \bar{U}_3^2} \cos^2\theta_1 - \frac{\bar{U}_2 \overline{u_1 u_2} + \bar{U}_3 \overline{u_1 u_3}}{(\bar{U}_2^2 + \bar{U}_3^2)^{\frac{1}{2}}} \sin 2\theta_1 \right]^{\frac{1}{2}} \quad \ldots(A\text{-}25)$$

$$\sqrt{\overline{u_z^2}} = b\left[\overline{u_1^2}\sin^2\theta_1 + \frac{\overline{U_2^2}\,\overline{u_2^2} + \overline{U_3^2}\,\overline{u_3^2} + 2\,\overline{U}_2\overline{U}_3\overline{u_2u_3}}{\overline{U_2^2} + \overline{U_3^2}}\cos^2\theta_1 - \frac{\overline{U}_2\,\overline{u_1u_2} + \overline{U}_3\overline{u_1u_3}}{(\overline{U_2^2} + \overline{U_3^2})^{\frac{1}{2}}}\sin 2\theta_1\right]^{\frac{1}{2}} \quad \ldots(A\text{-}26)$$

Multiplying u_x and u_y, time averaging and and rearranging,

$$\overline{u_x u_y} = a\left[\tfrac{1}{2}\left(-\overline{u_1^2} + \frac{\overline{U_3^2}\,\overline{u_3^2} + \overline{U_2^2}\,\overline{u_2^2} + 2\,\overline{U}_2\overline{U}_3\overline{u_2u_3}}{\overline{U_2^2} + \overline{U_3^2}}\right)\sin 2\theta_1 + \frac{\overline{U}_2\,\overline{u_1u_2} + \overline{U}_3\,\overline{u_1u_3}}{(\overline{U_2^2} + \overline{U_2^2})^{\frac{1}{2}}}\cos 2\theta_1\right] \quad \ldots(A\text{-}27)$$

Similarly multiplying u_y with u_z and u_z with u_x, other components of Reynolds stress can be written as:

$$\overline{u_y u_z} = a\,b\left[\overline{u_1^2}\sin^2\theta_1 - \frac{\overline{U}_2\,\overline{u_1u_2} + \overline{U}_3\,\overline{u_1u_3}}{(\overline{U_2^2} + \overline{U_3^2})^{\frac{1}{2}}}\sin 2\theta_1 + \frac{\overline{U_2^2}\,\overline{u_2^2} + \overline{U_3^2}\,\overline{u_3^2} + 2\,\overline{U}_2\overline{U}_3\,\overline{u_2u_3}}{\overline{U_2^2} + \overline{U_3^2}}\cos^2\theta_1\right] \quad \ldots(A\text{-}28)$$

and

$$\overline{u_z\, u_x} = b\left[\tfrac{1}{2}\left(-\overline{u_1^2} + \frac{\overline{U_3^2 u_3^2} + \overline{U_2^2 u_2^2} + 2\,\bar{U}_2\bar{U}_3\overline{u_2 u_3}}{\overline{U_2^2} + \overline{U_3^2}}\right)\sin 2\theta_1 + \frac{\bar{U}_2\,\overline{u_1 u_2} + \bar{U}_3\,\overline{u_1 u_3}}{\left(\overline{U_2^2} + \overline{U_3^2}\right)^{\frac{1}{2}}}\cos 2\theta_1\right] \quad \ldots(A\text{-}29)$$

Thus, from Eqns. (A-24) to (A-29), $\sqrt{\overline{u_x^2}}$, $\sqrt{\overline{u_y^2}}$, $\sqrt{\overline{u_z^2}}$, $\overline{u_x\, u_y}$, $\overline{u_y\, u_z}$, $\overline{u_z\, u_x}$ can be calculated as the right hand side of these equations is known; giving the three components of turbulence intensity and Reynolds stress along the set-up axes, respectively.

APPENDIX B

LISTING OF THE COMPUTER PROGRAM DEVELOPED FOR THE

DATA ACQUISITION OF THREE SENSOR HOT-WIRE ANEMOMETRY

```
FORTRAN IV G LEVEL  21                MAIN                DATE = 80185          13/26/18

CCC1                  IMPLICIT REAL *4(A-H,O-Z)
CCC2                 DIMENSION Y(20),EMA(20),EMB(20),EMC(20),EFA(20),EFB(20),EFC(20),
                    1 EFACB(20),EFADB(20),EFBSC(20),EFBDC(20),EFCSA(20),EFCDA(20),
                    2  G1(20),G2(20),G3(20), A(10,10) , X(20), ALA(20),ALB(20),
                    3 ALC(20)    , Z(20) ,U(20),FE1(20),FE2(20),FE3(20),U1(20),U2(20)
                    4, U3(20)       ,COST3(20),SINT3(20),UX(20),UY(20),UZ(20),UNX(20),
                    5  UNY(20),UNZ(20),UEX(20),UEY(20),UEZ(20),UR(20), UF1(20),UF2(20),
                    6 UF3(20), US12(20),US23(20),US31(20),TA(20),TB(20),UFX(20),UFY(20)
                    7 , UFZ(20),UXUY(20),UYUZ(20),UZUX(20) ,UFXE(20),UFYE(20),UFZE(20),
                    8  UXUYE(20),UYUZE(20),UZUXE(20) ,URE(20) , UFXEN(20),UFYEN(20),
                    9 UFZEN(20),UXUYN(20),UYUZN(20),UZUXN(20),DEL1(20),DEL2(20),
                    9 DEL3(20)  , TAUT(20),TIT(20),COR(20)
          C                  APPENDIX  II
          C  THIS PROGRAM IS USED TO CALCULATE THE THREE COMPONENTS OF MEAN VELOCITY,
          C   TURBULENCE INTENSITY AND REYNOLDS STRESSFROM A THREE DIMENSIONAL HOT WIRE
          C   PROBE ( TSI MODEL 1294  CT - T 1.5 ) DATA
          C   XL = 1 7/8, X3  = C.304(0.291), SPACING  = 1MM, M = 15, WAKE
CCC3                CH  = 5.875/12.0
CCC4                READ(5,301) ENA,ENB,ENC,DA,DB,DC,F1,F2,F3
CCC5               READ(5,302) ANA,ANB,ANC,UE
CCC6          301 FORMAT(9F8.6)
CCC7          302 FORMAT(4F10.6)
CCC8                PA  = 22.0/(7.0 * 180.0)
CCC9                AK  =  0.1050
CCC10                 AKS  =  AK * AK
CCC11                    GT  = 0.33
CCC12                GTS  =  GT  *  GT
CCC13               THT2 = 45.0  *  PA
```

```
CC14              THII   = 3>.264    *  PA
CC15                YC   = 0.578
CC16                 M   = 1>
CC17               DO 12  I = 1,M
CC18              READ(5,9) Y(I),EMA(I),EMB(I),EMC(I),EFA(I),EFB(I),EFC(I),EFASB(I),
                 1 EFADB(I),EFBSC(I),EFBDC(I),EFCSA(I),EFCDA(I)
CC19               Y(I)  = Y(I)  -  YC
CC20               WRITE(6,15) Y(I),EMA(I),EMB(I),EMC(I),EFA(I),EFB(I),EFC(I),EFASB
                1 (I),EFADB(I),EFBSC(I),EFBDC(I),EFCSA(I),EFCDA(I)
CC21            15 FORMAT(3X,6(3X,F10.6)/3X,6(3X,F10.6))
CC22             9 FORMAT(13F6.4)
CC23               G1(I)  = (((EMA(I))*( EMA(I)) -((ENA) * (ENA)) - F1 )/DA) **
                1 (1.0 / ANA)
CC24               G2(I)  = (((EMB(I))*( EMB(I)) -((ENB) * (ENB)) - F2 )/DB) **
                1 (1.0 / ANB)
CC25               G3(I)  = (((EMC(I))*( EMC(I)) -((ENC) * (ENC)) - F3 )/DC) **
                1 (1.0 / ANC)
CC26               WRITE(6,78) M,G1(I),G2(I),G3(I)
CC27            78 FORMAT(3X, 'M = ', I5,3X,' GS ARE ' /3(3X,F10.6))
CC28               U(I)  = SQRT(((G1(I))*G1(I) + (G2(I)) * (G2(I)) + (G3(I)) *(G3(
                1 I)))/(2.0 + AKS ))
CC29               FE1(I) =   ARSIN(SQRT((1.0  -((G1(I))/(U(I)))**2.0 )/(1.0 - AKS )
                1 ))
CC30               FE2(I) =   ARSIN(SQRT((1.0  -((G2(I))/(U(I)))**2.0 )/(1.0 - AKS )
                1  ))
CC31               FE3(I) =   ARSIN(SQRT((1.0  -((G3(I))/(U(I)))**2.0 )/(1.0 - AKS )
                1  ))
CC32               U1(I)  = (U(I)) * ( SIN(FE1(I)))
CC33               U2(I)  = (U(I)) * ( SIN(FE2(I)))
CC34               U3(I)  = (U(I)) * ( SIN(FE3(I)))
```

```
CC35                COST3(I)  = ( SIN(FE3(I)))/(COS(FE1(I)))
CC36                SINT3(I)  = ( SIN(FE2(I)))/(COS(FE1(I)))
CC37                UX(I)=    (SQRT((U3(I)) * (U3(I)) + (U2(I)) * (U2(I)))) * ( SIN(
                   1  THT1)) + (U1(I)) * (COS(THT1))
CC38                UY(I) =    (SIN(THT2))* ((SQRT((U3(I))*(U3(I))+(U2(I))*(U2(I))))
                   1  *(COS(THT1)) - (U1(I)) *(SIN(THT1))) * ((COST3(I) ) +
                   2  (SINT3(I)))
CC39                UZ(I) =    ( COS(THT2))* ((SQRT((U3(I))*(U3(I))+(U2(I))*(U2(I))))
                   1  *(COS(THT1)) - (U1(I)) *(SIN(THT1))) * ((COST3(I) ) -
                   2  (SINT3(I)))
CC40                UR(I)  = SQRT((UX(I)) * (UX(I)) + (UY(I)) * (UY(I)) + (UZ(I)) *
                   1  ( UZ(I)))
CC41                UNX(I)  = (UX(I))/(UR(I))
CC42                UNY(I)  = (UY(I))/(UR(I))
CC43                UNZ(I)  = (UZ(I))/(UR(I))
CC44                 UE(I)  = (UX(I))/UE
CC45                 UEY(I)  = (UY(I))/UE
CC46                 UEZ(I)  = (UZ(I))/UE
CC47                URE(I) = (UR(I))/UE
CC48           12 CONTINUE
CC49                DO  14  I = 1,M
CC50                  Y(I)  = Y(I)  / CH
CC51                WRITE(6,11) Y(I),EMA(I),EMB(I),EMC(I),EFA(I),EFB(I),EFC(I),EFASB
                  1 (I),EFADB(I),EFBSC(I),EFBDC(I),EFCSA(I),EFCDA(I)
CC52           11 FORMAT(3X,13(1X,F8.4))
CC53           14 CONTINUE
CC54                DO  80  I  = 1,M
CC55                UEL(I)  = 2.0 /(ANA*(1.0 - ((ENA/(EMA(I)))**2.0)) *(EMA(I))) *
                  1 (EFA(I)) *(U1(I))
```

```
CC56          UF2(I)  = 2.0 /(ANB*(1.0 - ((ENB/(EMB(I)))**2.0)) *(EMB(I))) *
             1 (EFB(I)) *(U2(I))
CC57          UF3(I)  = 2.0 /(ANC*(1.0 - ((ENC/(EMC(I)))**2.0)) *(EMC(I))) *
             1 (EFC(I)) *(U3(I))
CC58          US12(I)  = (EMA(I)) * (EMB(I)) *((U1(I)) ** (1.0 - ANA)) * ((
             1  U2(I)) **(1.0 - ANB)) * ((EFASB(I)) * (EFASB(I)) - (EFADB(I)) *
             3 (EFADB(I)))/(DA * DB * ANA * ANB *  GTS )
CC59          US23(I)  = (EMB(I)) * (EMC(I)) *((U2(I)) ** (1.0 - ANB)) * ((
             1  U3(I)) **(1.0 - ANC)) * ((EFBSC(I)) * (EFBSC(I)) - (EFBDC(I)) *
             3 (EFBDC(I)))/(DB * DC * ANB * ANC *  GTS )
CC60          US31(I)  = (EMC(I)) * (EMA(I)) *((U3(I)) ** (1.0 - ANC)) * ((
             1  U1(I)) **(1.0 - ANA)) * ((EFCSA(I)) * (EFCSA(I)) - (EFCDA(I)) *
             3 (EFCDA(I)))/(DC * DA * ANC * ANA *  GTS  )
CC61             TA(I)  = (COS(THT2)) * (( COST3(I)) + (SINT3(I)))
CC62             TB(I)  = (SIN(THT2)) * ((COST3(I)) - (SINT3(I)))
CC63             UFX(I)  =              SQRT((((U3(I)) * (UF3(I))) **2.0 + ((U2(I)
             1   ) * (UF2(I))) ** 2.0  +  2.0  * (U3(I)) * (U2(I))  *(US23(I)))/
             2 ((U2(I)) * (U2(I)) + (U3(I)) * (U3(I))) * ( SIN(THT1)) * (SIN(
             3 THT1))  + (((UF1(I)) * (COS(THT1))) ** 2.0)  + 2.0 * ((U3(I)) *
             4  (US31(I)) + (U2(I)) *(US12(I)))/(SQRT((U2(I)) * (U2(I)) +
             5  (U3(I)) * (U3(I)))) * (COS(THT1)) * (SIN(THT1))  )
CC64             UFY(I)  = (TA(I)) *( SQRT((((U3(I)) * (UF3(I))) **2.0 + ((U2(I)
             1   ) * (UF2(I))) ** 2.0  +  2.0  * (U3(I)) * (U2(I))  *(US23(I)))/
             2 ((U2(I)) * (U2(I)) + (U3(I)) * (U3(I))) * ( COS(THT1)) * (COS(
             3 THT1))  + (((UF1(I)) * (SIN(THT1))) ** 2.0)  - 2.0 * ((U3(I)) *
             4  (US31(I)) + (U2(I)) *(US12(I)))/(SQRT((U2(I)) * (U2(I)) +
             5  (U3(I)) * (U3(I)))) * (COS(THT1)) * (SIN(THT1))  )      )
CC65             UFZ(I)  = (TB(I)) *( SQRT((((U3(I)) * (UF3(I))) **2.0 + ((U2(I)
             1   ) * (UF2(I))) ** 2.0  +  2.0  * (U3(I)) * (U2(I))  *(US23(I)))/
```

```
     2 ((U2(I)) * (U2(I)) + (U3(I)) * (U3(I))) * ( COS(THT1)) * (COS(
     3 THT1))  + (((UF1(I)) * (SIN(THT1))) ** 2.0)  - 2.0 * ((U3(I)) *
     4  (US31(I)) + (U2(I)) *(US12(I)))/(SQRT((U2(I)) * (U2(I)) +
     5  (U3(I)) * (U3(I)))) * (COS(THT1)) * (SIN(THT1))  )     )
CC66    UXUY(I) =            (TA(I)) * (((((U3(I)) * (UF3(I)))** 2.0) +
     1  (((U2(I)) * (UF2(I))) ** 2.0) + ( 2.C * ( U2(I)) * (U3(I)) * (
     2 US23(I))))/((U2(I)) * (U2(I)) + (U3(I)) * (U3(I))) * (SIN(THT1))
     3 * (COS(THT1)) - ( UF1(I)) * (UF1(I)) * ( SIN(THT1)) * ( COS(THT1)
     4 )  + ((U2(I)) * (US12(I)) + (U3(I)) * (US31(I)))/(SQRT((U2(I)) *
     5 (U2(I)) +(U3(I)) * (U3(I)))) * ((COS(THT1)) *(COS(THT1)) -(SIN(
     6 THT1)) * (SIN(THT1))))
CC67    UYUZ(I) = (TA(I))*   (TB(I)) * (((((U3(I)) * (UF3(I)))** 2.0) +
     1  (((U2(I)) * (UF2(I))) ** 2.0) + ( 2.C * ( U2(I)) * (U3(I)) * (
     2 US23(I))))/((U2(I)) * (U2(I)) + (U3(I)) * (U3(I))) * (COS(THT1))
     3 * (COS(THT1)) + ( UF1(I)) * (UF1(I)) * ( SIN(THT1)) * ( SIN(THT1)
     4 )  - ((U2(I)) * (US12(I)) + (U3(I)) * (US31(I)))/(SQRT((U2(I)) *
     5 (U2(I)) +(U3(I)) * (U3(I)))) * (2.0 * ( SIN(THT1)) * ( COS(THT1)
     6 ))  )
CC68    UZUX(I) =            (TB(I)) * (((((U3(I)) * (UF3(I)))** 2.0) +
     1  (((U2(I)) * (UF2(I))) ** 2.0) + ( 2.C * ( U2(I)) * (U3(I)) * (
     2 US23(I))))/((U2(I)) * (U2(I)) + (U3(I)) * (U3(I))) * (SIN(THT1))
     3 * (COS(THT1)) - ( UF1(I)) * (UF1(I)) * ( SIN(THT1)) * ( COS(THT1)
     4 )  + ((U2(I)) * (US12(I)) + (U3(I)) * (US31(I)))/(SQRT((U2(I)) *
     5 (U2(I)) +(U3(I)) * (U3(I)))) * ((COS(THT1)) *(COS(THT1)) -(SIN(
     6 THT1)) * (SIN(THT1))))
CC69  30 CONTINUE
CC70     WRITE(6,52 )
CC71  52 FORMAT(3X, '  U  ' , 3X, ' PHI 1 ', 4X, ' PHI2 ', 4X, 'PHI3' , 4X,
     1  '  U1 ', 3X,'U2  ', 4X, ' U 3 ' )
```

```
      DO  17  I = 1,M
   55 FORMAT(3X, 7(3X,F11.6)  )
   87 FORMAT(3X, 8(3X,F11.6)  )
   86 FORMAT(3X,6(3X,F11.6))
      WRITE( 6,55) U(I), FE1(I),FE2(I),FE3(I),U1(I),U2(I),U3(I)
   17 CONTINUE
      DO  69   I  = 1,M
      WRITE(6,86) COST3(I), SINT3(I),UX(I),UY(I),UZ(I),UR(I)
   69   CONTINUE
      WRITE(6,88)
   88 FORMAT(3X,'UX/UR ',5X,'UY/UR ',5X,'UZ/UR ',5X,'UX/UE ',5X,'UY/UE'
     1  ,5X,'UR/UE ' )
      DO  69   I  = 1,M
      WRITE(6,87) UNX(I),UNY(I),UNZ(I),UEX(I),UEY(I),UEZ(I) ,URE(I)
     1  , Y(I)
   69  CONTINUE
      DO  97  I  = 1,M
      WRITE(6,86) UF1(I),UF2(I),UF3(I),  US12(I),US23(I),US31(I)
   97 CONTINUE
      DO 99  I  = 1,M
      WRITE(6,55) UFX(I),UFY(I),UFZ(I),UXUY(I),UYUZ(I),UZUX(I), Y(I)
   99 CONTINUE
      DO  101 I = 1,M
      UFXE(I)  =(UFX(I)) / UE
      UFYE(I)  = (UFY(I) )/UE
      UFZE(I)  =  ( UFZ(I)  )/UE
      UXUYE(I)   = (UXUY(I)) / ( UE  *  UE )
      UYUZE(I)   =  ( UYUZ(I)  ) / ( UE * UE )
      UZUXE(I)  = ( UZUX(I)  ) / ( UE * UE )
```

```
C099      101 CONTINUE
C100          WRITE(6,91)
C101       91 FORMAT(3X,'UFXE/UE',5X,'UFYE/UE ',5X,' UFZE/UE ',5X,' UXUYE/UE',
     1    5X,'UYUZE/UE ',5X,'UZUXE/UE ', 3X,  '  Y/C  ' )
C102          DO  105   I  = 1,M
C103          WRITE(6,55 )  UFXE(I), UFYE(I), UFZE(I), UXUYE(I),UYUZE(I),
     1  UZUXE(I), Y(I)
C104      105 CONTINUE
C105           TOS  = 1.0
C106           UE  =  TOS
C107          DO  121  I  = 1,M
C108          UFXEN(I)  =(UFXE(I)  )/UE
C109          UFYEN(I)  = (UFYE(I) )/UE
C110          UYUZN(I)  = (UYUZE(I))/(UE * UE )
C111          UFZEN(I)  = (UFZE(I)) /UE
C112          UXUYN(I)  = (UXUYE(I)) / ( UE * UE )
C113          UZUXN(I)  = (UZUXE(I)) /(UE * UE )
C114      121 CONTINUE
C115          WRITE(6,91)
C116          DO  122  I  = 1,M
C117          WRITE(6,55) Y(I),UFXEN(I),UFYEN(I),UFZEN(I),UXUYN(I),UYUZN(I),
     1  UZUXN(I)
C118      122 CONTINUE
C119          WRITE(6,224)
C120      224 FORMAT(3X, ' Y/C =  ', 3X, ' DISPLACEMENT THICKNES =  ', 3X, '
     1 MOMENTUM TH. = ', 3X, ' ENERGY TH. = ' )
C121          DO  222 I = 1,M
C122          DEL1(I) = (1.0  - (UEX(I) ) )
C123          DEL2(I) = (1.0  - (UEX(I))) * ( UEX(I))
```

```
C124              DEL3(I)  =  (1.0  - (UEX(I))   * (UEX(I))) * (UEX(I))
C125              WRITE(6,223)  Y(I),DEL1(I), DEL2(I),DEL3(I)
C126         223 FORMAT(3X,4(3X,F10.6))
C127         222 CONTINUE
C128               WRITE(6,107)
C129         107  FORMAT(3X,'TOTAL REYNOLDS STRESS',3X,'TOTAL TURBULENCE INTENSITY
                1  ',3X, ' CORRLATION COEFF. ' )
C130               DO   29  I  = 1,M
C131                  UXUYE(I)  = (UXUYE(I)  ) * 10000.0      * 100.0
C132                  UYUZE(I)  = (UYUZE(I)  ) * 10000.0      * 100.0
C133                  UZUXE(I)  = (UZUXE(I)  ) * 10000.0      * 100.0
C134               UFXE(I)  =  ( UFXE(I) )  *  100.0
C135               UFYE(I)  =  ( UFYE(I) )  *  100.0
C136               UFZE(I)  =  ( UFZE(I) )  *  100.0
C137               TAUT(I)  = SQRT (( UXUYE(I))**2.0)  + ((UYUZE(I)) ** 2.0) +
                1  (( UZUXE(I)) ** 2.0 ))
C138              TIT(I) = ((UFXE(I)) **2.0)  + ((UFYE(I)) ** 2.0) + ((UFZE(I))
                1  ** 2.0)
C139               COR(I)  =  (TAUT(I))/(TIT(I))  /100.0
C140          29  WRITE(6,59)     TAUT(I), TIT(I),COR(I)
C141          59  FORMAT(3X,3(3X,F10.6))
C142               STOP
C143               END
```